# Mean-Field Approach to Collective Excitations in Deformed sd-Shell Nuclei Using Realistic Interactions

# Abstract

Realistic nucleon-nucleon interactions transformed via the Unitary Correlation Operator Method (UCOM) or the Similarity Renormalization Group (SRG) have proven to be a suitable starting point for the description of closed-shell nuclei via mean-field methods like Hartree-Fock (HF). This allows the treatment of a number of heavy nuclei with realistic nucleon-nucleon interactions, which would otherwise only be possible with phenomenological interactions. To include three-nucleon forces in an approximate way, the UCOM or SRG transformed interactions can be augmented by a three-body contact interaction, which is necessary to reproduce measured charge radii.

However, many interesting nuclei, including those near the neutron drip line, are far away from closed shells. These nuclei are of great importance for modeling nucleosynthesis processes in the universe, but experiments can only be performed at a few research facilities.

In this work, the Hartree Fock (HF) approach with realistic interactions is extended to light deformed nuclei. Pairing correlations are not taken into account. A crucial step in this process is to allow deformed ground states on the mean-field level, as only nuclei with at least one closed shell can be described with spherical HF ground states. To restore the rotational symmetry in the lab frame, exact angular-momentum projection (AMP) is implemented. Constrained HF calculations are used for an approximate variation after projection approach. The AMP-HF description of open-shell nuclei is on par with the pure HF description of closed-shell nuclei. Charge-radii and systematics of binding energies agree well with experiment. However, missing correlations, lead to an underestimated absolute value of the binding energy. Projection on higher angular momenta approximately reproduces the energy systematics of rotational bands.

To describe collective excitations, the Random Phase Approximation (RPA) constitutes a well tested approach, which can also be extended to deformed HF states. In this case, the angular-momentum projection is implemented on the level of transition amplitudes. A strong effect of the AMP is only seen for the electric isoscalar monopole transition, where it improves the agreement with experiment. For deformed HF states, the RPA shows a much stronger fragmentation of the collective states than in the spherical case. Intrinsic transition densities are used to assess the amount of spurious center-of-mass or rotational contaminations to excitations calculated in the RPA framework.

Another approach to excited states is given by the Multi-Configuration Hartree-Fock method, where preliminary studies show very promising results.

# Zusammenfassung

Mittels der Methode der unitären Korrelatoren (UCOM) oder der Ähnlichkeits-Renormierungsgruppe (SRG) transformierte realistische Nukleon-Nukleon-Wechselwirkungen haben sich als geeigneter Ausgangspunkt für die Beschreibung von Kerne mit abgeschlossenen Schalen mittels Mean-Field-Methoden wie Hartree-Fock (HF) erwiesen. Dies ermöglicht die Beschreibung von einer Reihe von schweren Kernen mit realistischen Nukleon-Nukleon Wechselwirkungen, die sonst nur mit phänomenologischen Wechselwirkungen möglich wäre. Als Näherung für Dreinukleonenkräfte, kann die UCOM oder SRG transformiert Zweiteilchenwechselwirkungen um eine Dreiteilchenkontaktwechselwirkung erweitert werden. Dies ist erforderlich, um gemessen Ladungsradien zu reproduzieren.

Allerdings sind viele interessante Kerne, insbesondere in der Nähe der Neutronendripline, von Schalenabschlüssen weit entfernt. Diese Kerne sind zwar von großer Bedeutung für eine Modellierung der Nukleosynthese im Universum, Experimente können aber nur an wenigen Forschungszentren durchgeführt werden.

In dieser Arbeit wird die Hartree-Fock (HF) Methode mit realistischen Wechselwirkungen auf leichte, deformierte Kerne ausgedehnt. Pairing-Korrelationen werden nicht berücksichtigt. Ein entscheidender Schritt in diesem Prozess ist es, deformierte Grundzustände auf der Mean-Field Ebene zuzulassen, da nur Kerne mit mindestens einer abgeschlossenen Schale mit einem sphärischen HF Grundzustand beschrieben werden können. Die Rotationssymmetrie im Laborsystem wird mittels exakter Drehimpulsprojektion wiederhergestellt. Für eine approximative Variation-nach-Projektion wird HF-Minimierung unter Nebenbedingungen verwendet. Die drehimpulsprojizierte HF-Beschreibung von Kernen ohne Schalenabschluss ist der reinen HF Beschreibung von Kernen mit abgeschlossenen Schalen gleichwertig. Ladungsradien und die Systematik der Bindungsenergien stimmen gut mit gemessenen Werten überein, allerdings führen fehlende Korrelationen zu unterschätzten Absolutwerten der Bindungsenergie. Projektion auf höhere Drehimpulse reproduziert in guter Näherung die Energiesystematik der Rotationsbanden.

Die Random Phase Approximation (RPA) ist ein wohl etablierter Ansatz, um kollektive Anregungen zu beschreiben. Sie kann ebenfalls auf deformierte HF Zustände erweitert werden. In diesem Fall wird die Drehimpulsprojektion für Übergangsamplituden durchgeführt. Ein starker Effekt der Drehimpulsprojektion ist nur für den elektrischen isoskalaren Monopolübergang zu sehen, wobei sich die Übereinstimmung mit dem Experiment verbessert. Für deformierte HF Zustände zeigt die RPA deutlich stärkere Fragmentierung der kollektiven Zustände als für den sphärischen Fall. Um Kontaminationen durch spuriose Schwerpunkts- oder Rotationsanregungen festzustellen, werden intrinsische Übergangsdichten im Rahmen der RPA berechnet.

Einen weiteren Ansatz, um angeregte Zuständen zu beschreiben, bietet das Multi-konfigurations Hartree-Fock Verfahren, für das vorläufige Studien viel versprechende Ergebnisse zeigen.

# Contents

# 1. Introduction

Although discovered more than 100 years ago, atomic nuclei are still in the focus of current research and many aspects are not yet fully understood. Measured data can be put into a consistent picture within phenomenological models, but if no or very few experimental data exists, e.g. for very unstable nuclei, where experiments are difficult to perform, accurate predictions are often not possible. However, nuclei far from stability are crucial in understanding the abundance of the elements in the universe. The observed abundances of heavy elements are consistent with production by rapid neutron capture near the neutron drip line (at neutron separation energy $S_n \approx 2\,\mathrm{MeV}$). However, the astrophysical site of this process is still a matter of discussion (candidates are core-collapse supernovae or neutron-star mergers). A complete theoretical ab initio treatment is therefore desirable, but has only recently become possible for light nuclei.

The reason for this unsatisfactory situation lies in the nature of the nuclear force. Nucleons are not elementary particles like electrons or photons, but are made of quarks and gluons. Quarks and gluons interact mainly by the strong interaction, which is described by quantum chromodynamics (QCD). The nucleon-nucleon (NN) interaction is the residual interaction caused by the interaction of the constituent particles. It is in that way similar to the Van der Waals force between molecules, but more complex. QCD has two features that are not present in other field theories like quantum electrodynamics: asymptotic freedom and confinement. Asymptotic freedom means that QCD is perturbative only at high energies. A perturbative treatment of the low energy region, which is the relevant regime for nuclear physics where a NN interaction could be derived, is not possible. Confinement describes the empirical observation that quarks and gluons never occur alone. In addition to the electric charge, quarks and gluons have a *color*—similar to the electric charge—but observable objects are always color-neutral (or *white*). Color-neutral particles appear as baryons and mesons, with nucleons and pions being the lightest. One way to derive an effective interaction from QCD is to treat nucleons and pions as degrees of freedom of an effective field theory, taking into account all relevant symmetries of QCD, most notably the chiral symmetry. This is referred to as chiral effective field theory ($\chi$EFT) and is under active development [ENG+02, EM03, EGM05, ME10]. Since the interaction of nucleons and pions can not be completely derived from QCD at present, additional experimental data has to be provided in the form of NN-scattering phase-shifts and the properties of few nucleon systems like the deuteron.

An alternative way to the relatively new QCD-based approaches is the use of realistic NN interactions. These interactions include both: terms motivated by QCD and purely phenomenological terms. They are fitted to the same properties as $\chi$EFT interactions. Examples for realistic NN interactions are the Argonne V18 [WSS95] (AV18), the CD-Bonn [Mac01] or the Nijmegen [SKTdS94] potential. Since the free parameters are not

fitted to nuclei but to NN scattering data and properties of few-nucleon systems, the use of interactions based on $\chi$EFT or realistic NN interactions can still be regarded as an ab-initio approach with respect to nuclear structure calculations.

However, both approaches—NN potentials based on $\chi$EFT and realistic NN potentials—share similar problems, which arise from the structure of the nuclear force. The repulsive core and the strong tensor force induce short-range correlations, which require large model spaces to be described accurately. For an harmonic oscillator (HO) basis, this corresponds to the mixing of states with high and low energy. In momentum space, this leads to the coupling of high and low momenta. For light nuclei, these model spaces are still manageable, but their size quickly grows beyond any reasonable limit. If one restricts the model space to a single Slater determinant, like in Hartree-Fock (HF) theory, the situation is even worse. Correlations can not be described by a single Slater determinant. Therefore, Hamiltonians with strongly correlated eigenstates lead to unbound nuclei.

One way to handle this problem and to obtain interactions more suitable for nuclear structure calculations, including the Hartree-Fock method, is to use a unitary transformation to address the correlations, which can be either applied to the states or to the Hamiltonian [RNF10]. If we take the point of view of a transformed Hamiltonian, all transformations that do not change the defining properties of the potential, i.e. the scattering phase shifts and deuteron properties, can be used just as well as the original, untransformed interaction. However, if a suitable transformation is used, the high- and low-lying states decouple and the resulting transformed interaction already leads to well converged results in considerably smaller model spaces. The Unitary Correlation Operator Method (UCOM) takes an approach motivated by the underlying physics of the problem. The transformation is defined through generators, which keep the nucleons apart and induce the short-range correlations. The Similarity Renormalization Group (SRG) approach uses a Renormalization Group flow equation to pre-diagonalize the interaction with respect to a certain basis. If a suitable generator for the flow equation is used, SRG transformed interactions are phase-shift invariant and preserve the deuteron properties. Although very different in their motivation, both approaches, UCOM and SRG, yield similar results.

The unitary transformation leads to a much improved convergence behavior of the interaction. For the No-Core Shell Model (NCSM), i.e. direct matrix diagonalization, the required basis size is reduced drastically [RNF10]. Since the short-range correlations are treated by the unitary transformation, HF calculations no longer lead to unbound nuclei. As mean-field approaches like HF are a common approach to deal with all known nuclei, unitary transformations provide convenient access to the complete chart of nuclei, without resorting to a phenomenological treatment. On top of the HF solution, refinements that go beyond the pure mean field can be added to improve certain aspects of the solution. Bulk properties like radii or quadrupole moments tend to be well described in the pure mean-field approach. For the ground-state energy, Many-Body Perturbation Theory can be used to improve the description [RNF10]. To treat collective excitations like giant resonances, the Random Phase Approximation (RPA) [Row70] constitutes a well tested approach and has been successfully applied with realistic interactions [PPHR06]. In the case of a symmetry-breaking HF solu-

tion, projection methods have to be employed to restore the broken symmetry. This happens for nuclei with ground-state quadrupole (or higher) moments, where the HF solutions are no longer eigenstates of the squared total angular-momentum operator. These nuclei are often referred to as *deformed nuclei*. Angular-momentum projection is used to restore the broken rotational symmetry and can also be used to treat excitations corresponding to the broken symmetry, i.e. rotational bands.

Mean-field techniques like HF and RPA have all been employed in nuclear structure calculations since many decades, but not with realistic NN interactions. Originally, these methods have been used with phenomenological interactions, where an ansatz for the Hamiltonian with some free parameters is constructed based on general properties of the NN interaction and computational requirements—the tensor force is often neglected—and then fitted to measured properties of mostly stable and spherical nuclei. The predictive power of such a framework, especially for the very interesting nuclei near the drip lines, is at best doubtful.[1] Moreover, since such interactions are specifically tailored for the HF method, any improved many-body calculation beyond HF leads to overbinding. Two popular phenomenological interactions are the Skyrme force [Sky59] (a recent parameterization has been published in [TGPO00]) and the Gogny D1S interaction [DG80]. A summary of recent work in this field is given in [Dob11]

In this work, we extend the HF and RPA studies, which have already been carried out for spherical nuclei [RPP+06, PPHR06], to deformed nuclei, namely $^{12}$C, $^{20}$Ne, $^{28}$Si and $^{32}$S.

Chapter 2 discusses the nuclear Hamiltonian. We start with a short review of the AV18 interaction. The main part of the chapter deals with unitary transformations, where short introductions to the UCOM and the SRG are given. This is followed by a discussion of the specific Hamiltonians used in this work. Finally, we discuss transformed observables and phenomenological three-body corrections.

Chapter 3 deals with axially deformed mean-field states. First, basic concepts and notations are introduced. The main part of the chapter is dedicated to the angular-momentum projection. We discuss the angular-momentum projected ground state together with its rotational band and continue with the treatment of transition amplitudes. The chapter concludes with a discussion of how to treat a Hamiltonian with a three-body contact term in the angular-momentum projection.

Chapter 4 is concerned with the HF method. We start with a short discussion of the formalism and how axial deformation is included in the approach. The application of the angular-momentum projection within the HF framework is discussed in this chapter. Finally, we give an outline of how a complete HF calculation with angular-momentum projection is carried out.

In Chapter 5, we present the results obtained with angular-momentum projected HF. First, we compare our results with those published by other authors. After a study of the convergence with respect to basis size and oscillator length, we look at the systematics of the binding energies and charge radii, which are compared to measured values. A large part of the chapter is concerned with the effect of the

---

[1]Some authors seem to disagree [HG07].

angular-momentum projection on the ground-state energies and the nuclear deformation. Finally, we present results for rotational bands.

Chapter 6 discusses the RPA formalism and the transition amplitudes derived in this framework. First, the RPA formalism is introduced, with a focus on the application to systems with axial deformation. We continue with a discussion of electromagnetic transitions in the RPA framework, where we focus on the angular-momentum projected transition amplitudes. We finish the chapter with a short discussion of transition densities.

Results obtained by the RPA approach are presented in chapter 7. We start by comparing our results with those published by other authors and with results obtained by an RPA code for spherical nuclei. After studying the convergence with respect to basis size and oscillator length, we present transition strengths for the electric isoscalar monopole, isoscalar dipole, isovector dipole and isoscalar quadrupole transitions. Centroids of the strengths and their widths are compared with measured values. The chapter is concluded with a discussion of the oscillation modes in terms of transition densities and how they contribute to different transitions.

In chapter 8, we present a brief proof-of-concept study of the multi-configuration Hartree Fock (MCHF) method. The MCHF is applied on top of a set of HF solutions and can be used to obtain a better approximation for the ground state and low-lying excited states, including rotational bands. The results are very promising, but can be improved in a number of ways.

We conclude this thesis with a short summary and an outlook on further development possibilities. Where possible, we give a general outline of the necessary steps and point out where major obstacles could be encountered.

Calculations which are deemed too long or of too little significance are discussed in the appendix.

# 2. Nuclear Hamiltonian

In this chapter, we discuss the Hamiltonian used for HF, RPA and MCHF (chapters 4 to 8). We start with a short overview of the Argonne V18 NN interaction, which we use as the basis of the transformed interactions. This is followed by a discussion of the unitary transformations, namely the UCOM and SRG transformations. The chapter is concluded by a short discussion of a phenomenological three-body correction, which is used in some of the transformed interactions.

Since the NN interaction is not the main topic of this thesis, the discussion is kept general and references to the relevant works are given.

## 2.1. Realistic NN Interactions

All unitarily transformed interactions used in this work are based on the AV18 potential [WSS95], a high-precision nucleon-nucleon potential fitted only to properties of two-nucleon systems, i.e. $pp$ and $np$ scattering data and deuteron properties. It consists of 18 operator components, three of which are charge dependent and one is charge asymmetric. In total, it has 40 adjustable parameters. The long-range behavior is based on meson exchange theory, while the medium- and short-range parts are purely phenomenological. As it is only fitted to two-nucleon systems, the AV18 potential is a pure two-body interaction. Three-body contributions have to be taken into account via a different approach.

Due to the short-range correlations induced by the repulsive core of the potential, its bare form is not suitable for mean-field methods like Hartree-Fock. When used together with unitary transformations, the resulting nuclei are bound, but all interactions used in this work lead to a binding energy of only about 4 MeV per nucleon.

This seems at first inferior to phenomenological interactions of Gogny or Skyrme type [DG80, Sky59, TGPO00]. However, phenomenological interactions only give reliable results for the observables used to fix their parameters. The missing binding energy is due to correlations that can not be described by a single Slater determinant and are also not corrected by the unitary transformation. Correlations can be included to some extent by going beyond the pure mean field, like with Many-Body Perturbation Theory (MBPT) [RPP+06, GRHR10] or the Random-Phase Approximation (RPA) [PPHR06].

## 2.2. Unitary Transformations

We consider the eigenvalue problem of the full Hamiltonian $\hat{H}$

$$\hat{H}|\Psi\rangle = E|\Psi\rangle \quad . \tag{2.1}$$

If the basis is well chosen, the eigenvectors $|\Psi\rangle$ have only a few strong contributions while all others are negligible. Since we are only interested in the ground state and at most a few low-lying excited states, all states with only a negligible contribution to these eigenvalues can be removed from the basis without affecting the low-lying eigenvalues. If the states with negligible contributions are known a priori, a suitable basis truncation can be introduced, leading to already well converged results in a small basis.

However, the short-range correlations present in the nuclear many-body problem are not well described by Slater determinants of harmonic oscillator states, requiring a large basis for well converged results. To overcome this problem, we can introduce a unitary transformation $\hat{U}$ to transform an unsuitable basis into a more suitable one. The eigenvalue problem then reads

$$\hat{H}\,\hat{U}|\Psi'\rangle = E\,\hat{U}|\Psi'\rangle \quad . \tag{2.2}$$

Since $\hat{U}^{-1} = \hat{U}^\dagger$, this can be reformulated to

$$\hat{U}^\dagger\,\hat{H}\,\hat{U}|\Psi'\rangle = E|\Psi'\rangle$$
$$\hat{H}_{\mathrm{ut}}|\Psi'\rangle = E|\Psi'\rangle \quad . \tag{2.3}$$

If we find a suitable unitary transformation, $\hat{H}_{\mathrm{ut}}$ has a band- or block-diagonal structure and a lot of basis states can be truncated without affecting the low-lying eigenvalues.

The slow convergence in a basis consisting of Slater determinants of harmonic oscillator states is caused by short-range correlations due to the repulsive core of the NN interaction. If the components of the Hamiltonian that induce these correlations are removed, the convergence behavior is improved. As already mentioned, short-range correlations make bare realistic NN potentials unsuitable for use in mean-field calculations, i.e. a basis consisting of a single Slater determinant. But since unitarily transformed interactions address these correlations at the Hamiltonian, they are suitable for a wide range of methods, including mean field calculations.

We employ three methods to include short-range correlations into the basis states. The Unitary Correlation Operator Method (UCOM) introduces generators with explicitly defined correlation functions, while the Similarity Renormalization Group (SRG) achieves a similar effect by attempting to transform the Hamiltonian to a band-diagonal form. As a third method, these two approaches can be combined to extract the form of the correlation functions from the SRG and then applying the UCOM. These methods are discussed extensively in the review paper [RNF10] and in various theses [Her08, Gün11, Rei08], where ample reference regarding the history

and background is provided. In this work, the matrix elements of the transformed interactions are only used as an input for the many-body methods. Therefore, we omit the technical details and focus on the main ideas and point out what approximations are being used during the process.

An exact unitary transformation does not change the eigenvalues. However, it can induce contributions of higher particle rank in the interaction, i.e. a transformed two-body force includes contributions from two-body terms up to $A$-body terms. From a formal point of view, this is best understood by expressing the unitary transformation $\hat{U}$ as the exponential of a hermitian generator $\hat{G}$

$$\hat{U} = e^{-i\hat{G}} = \sum_{k=0}^{\infty} \frac{(-i)^k}{k!} \hat{G}^k \quad , \tag{2.4}$$

where $\hat{G}$ is the sum of the correlation operators, which induce correlations between the single-particle states. If the generator is a one-body operator, i.e. $\hat{G} = \sum_{i=1}^{A} g_i$, the unitary transformation is given by $\hat{U} = \prod_{i=1}^{A} e^{-i\hat{g}_i}$. It transforms each single-particle state independently, without introducing any correlations. Therefore, the generators have to be at least two-body operators to achieve the desired effect. However, if the generator introduces correlations, it also induces contributions of higher particle rank, turning a two-body Hamiltonian into an $A$-body Hamiltonian. A transformed two-body Hamiltonian then reads

$$\hat{H}_{\mathrm{ut}} = \hat{U}^\dagger \hat{H} \hat{U} = \hat{U}^\dagger \hat{H}^{[1]} \hat{U} + \hat{U}^\dagger \hat{H}^{[2]} \hat{U} = \hat{H}^{[1]} + \sum_{n=2}^{A} \hat{H}_{\mathrm{ut}}^{[n]} \quad , \tag{2.5}$$

where $\hat{H}^{[n]}$ denotes pure $n$-body contributions from the Hamiltonian. The one-body term of the transformed Hamiltonian is identical to the untransformed one-body term, but all terms of higher particle rank are changed due to the transformation.

As the explicit treatment of forces beyond the two-body level is computationally expensive (it is possible for 3-body forces [RLC+11, Cal10, Lan10]), the induced contributions are neglected so that the transformed Hamiltonian only contains up to two-body terms. This *two-body approximation* is reasonable as long as the total contribution of many-body terms, i.e. the sum of induced and genuine many-body terms, is small.

Due to the *two-body approximation*, the transformation is no longer unitary with respect to the truncated many-body contributions. Therefore, the eigenvalues of the Hamiltonian are no longer exactly the same as in the untransformed case. This provides a test for the validity of the *two-body approximation*. If the results of No-Core Shell Model (NCSM) calculations do not change much due to the truncation, the higher order contributions are small and can be neglected.

Unitary transformations are also capable of describing long-range correlations. However, these vary strongly with the size of the nucleus and, therefore, cannot be included in a general interaction. Long-range correlations have to be described by the many-body method used.

## 2.2.1. Unitary Correlation Operator Method

The Unitary Correlation Operator Method (UCOM), is motivated by the underlying physics of the problem. As we just saw, we need at least a two-body generator to produce a meaningful unitary transformation.

An operator addressing the radial correlations has to keep two nucleons from getting too close, so that the effect of the repulsive core of the NN potential is reduced. This can be achieved with the following generator, which shifts two nucleons with distance $r$ apart

$$\hat{g}_r = \sum_{ST} \tfrac{1}{2} \left( \hat{q}_r \, s_{ST}(r) + s_{ST}(r) \hat{q}_r \right) \hat{\Pi}_{ST} \quad , \tag{2.6}$$

where $\hat{q}_r$ is the radial momentum, $s(r)$ adjusts the strength of the shift and $\hat{\Pi}_{ST}$ projects on spin and isospin. The unitary transformation in the many-body space then reads

$$\hat{C}_r = \exp\left( -i \sum_{i<j} \hat{g}_{r,ij} \right) \quad . \tag{2.7}$$

The tensor correlations are addressed by the generator

$$\hat{\boldsymbol{g}}_\Omega = \sum_T \vartheta_T(r) \, \hat{s}_{12}(\hat{\boldsymbol{r}}, \hat{\boldsymbol{q}}_\Omega) \hat{\Pi}_{1T} \tag{2.8}$$

$$\hat{s}_{12}(\hat{\boldsymbol{r}}, \hat{\boldsymbol{q}}_\Omega) = \tfrac{3}{2} \left( (\hat{\boldsymbol{\sigma}}_1 \cdot \hat{\boldsymbol{r}})(\hat{\boldsymbol{\sigma}}_2 \cdot \hat{\boldsymbol{q}}_\Omega) + (\hat{\boldsymbol{\sigma}}_1 \cdot \hat{\boldsymbol{q}}_\Omega)(\hat{\boldsymbol{\sigma}}_2 \cdot \hat{\boldsymbol{r}}) \right) \quad ,$$

with the orbital momentum operator

$$\hat{\boldsymbol{q}}_\Omega = \frac{1}{2r^2} \left( \hat{\boldsymbol{l}} \times \hat{\boldsymbol{r}} - \hat{\boldsymbol{r}} \times \hat{\boldsymbol{l}} \right) \quad . \tag{2.9}$$

The unitary transformation in the many-body space is then given by

$$\hat{C}_\Omega = \exp\left( -i \sum_{i<j} \hat{\boldsymbol{g}}_{\Omega,ij} \right) \quad . \tag{2.10}$$

We can now apply the correlation operators to the operators appearing in the NN interactions. Since the complete treatment of all relevant operators is already covered in [RNHF04, RHP$^+$05], the following discussion is limited to simple cases, which are sufficient to introduce the correlation functions. The correlated distance operator $\hat{r}$ is given by

$$\hat{C}_r^\dagger \hat{r} \hat{C}_r = R_+(\hat{r}) \quad \text{and} \quad \hat{C}_\Omega^\dagger \hat{r} \hat{C}_\Omega = \hat{r} \quad . \tag{2.11}$$

The correlated radial momentum operator $\hat{q}_r$ is given by

$$\hat{C}_r^\dagger \hat{q}_r \hat{C}_r = \frac{1}{\sqrt{R_+(\hat{r})}} \hat{q}_r \frac{1}{\sqrt{R_+(\hat{r})}} \quad \text{and} \quad \hat{C}_\Omega^\dagger \hat{q}_r \hat{C}_\Omega = \hat{q}_r - \vartheta'(\hat{r}) \, \hat{s}_{12}(\hat{\boldsymbol{r}}, \hat{\boldsymbol{q}}_\Omega) \quad . \tag{2.12}$$

We already encountered the tensor correlation function $\vartheta(\hat{r})$ in the form of $\vartheta_T(r)$ in eq. (2.8). The radial correlation function $R_+(\hat{r})$ is related to the shift strength $s(r)$ from eq. (2.6) by

$$\int_r^{R_+(r)} \frac{\mathrm{d}\xi}{s(\xi)} = +1 \quad . \tag{2.13}$$

But since $s(r)$ does not need to be defined, this is of no further consequence. The two correlation functions are sufficient to define the other correlated operators needed for the realistic NN potentials as well.

**Parametrized Correlation Functions**

Now the radial and and tensor correlation functions have to be defined. For the radial correlation function, two parameterizations are used

$$R_+^I(r) = r + \alpha_c(r/\beta_c)^{\eta_c} \exp\left(-\exp(r/\beta_c)\right) \tag{2.14}$$

$$R_+^{II}(r) = r + \alpha_c\left(1 - \exp(-r/\gamma_c)\right) \exp\left(-\exp(r/\beta_c)\right) \quad . \tag{2.15}$$

The parameters and the type of correlation function used is determined by a variational scheme (cf. [RNF10] for details). For the tensor correlation function, the following parameterization is used

$$\vartheta(r) = \alpha_t\left(1 - \exp(-r/\gamma_t)\right) \exp\left(-\exp(r/\beta_t)\right) \quad . \tag{2.16}$$

A common feature of all these correlation functions is the double exponential decay to large radii. Due to a purely repulsive potential in the $(S,T) = (0,0)$ channel, the correlation functions in this channel have long range, which is contrary to the initial idea of the UCOM. Therefore, the minimization is carried out under a range constraint of the form

$$I_{R_+}^{(0,0)} = \int \left(R_+(r) - r\right) r^2 \mathrm{d}r \quad . \tag{2.17}$$

In this work, a value of $I_{R_+}^{(0,0)} = 0.1\,\mathrm{fm}^4$ is used for the constraint. For the $(S,T) = (0,1)$ channel, the minimization is straightforward. The tensor correlations, which are only present in the $S = 1$ channel introduce long-range correlations as well, so a corresponding range constraint is introduced for the tensor correlation function

$$I_{\vartheta}^{(1,0)} = \int \vartheta_T(r) r^2 \mathrm{d}r \quad . \tag{2.18}$$

For the tensor constraint, a value of $I_{\vartheta}^{(1,0)} = 0.09\,\mathrm{fm}^3$ is used. The tensor correlation function for the $T = 1$ channel is set to zero. The values of the parameters for the interaction used in this work are summarized in tables 2.1 and 2.2.

| S | T | Param. | $\alpha$(fm) | $\beta$(fm) | $\gamma$(fm) | $\eta$ |
|---|---|--------|--------------|-------------|--------------|--------|
| 0 | 0 | II | 0.7971 | 1.2638 | 0.4621 | - |
| 0 | 1 | I | 1.3793 | 0.8853 | - | 0.3724 |
| 1 | 0 | I | 1.3265 | 0.8342 | - | 0.4471 |
| 1 | 1 | II | 0.5665 | 1.3888 | 0.1786 | - |

Table 2.1.: Parameters for the central correlation functions used for the UCOM(VAR) interaction [RNF10].

| S | T | $\alpha$ | $\beta$(fm) | $\gamma$(fm) |
|---|---|----------|-------------|--------------|
| 0 | 1 | 536.67 | 1.2608 | 1000.0 |
| 1 | 1 | 0.0 | 1.0 | 1.0 |

Table 2.2.: Parameters for the tensor correlation functions used for the UCOM(VAR) interaction [RNF10].

## 2.2.2. Similarity Renormalization Group

The starting point of the Similarity Renormalization Group method (SRG) is quite different from the physical picture of the UCOM. The goal of the SRG is to evolve the Hamiltonian to diagonal form via a flow equation

$$\frac{\mathrm{d}\hat{H}_\alpha}{\mathrm{d}\alpha} = [\eta_\alpha, \hat{H}_\alpha] \quad , \tag{2.19}$$

with the anti-hermitian generator $\eta_\alpha$, the flow parameter $\alpha$ and the evolved Hamiltonian $\hat{H}_\alpha$. With increasing $\alpha$, the initial Hamiltonian $\hat{H}_0 = \hat{H}$ is evolved towards a diagonal form. When the Hamiltonian commutes with the generator, the SRG evolution stops. Formally, the SRG evolution is a unitary transformation with

$$\hat{H}_\alpha = \hat{U}_\alpha^\dagger \, \hat{H} \, \hat{U}_\alpha \quad \text{and} \quad \frac{\mathrm{d}\hat{U}_\alpha}{\mathrm{d}\alpha} = -\hat{U}_\alpha \, \eta_\alpha \quad . \tag{2.20}$$

To get a pure two-body interaction, the SRG transformation is confined to two-body space and induced contributions of higher particle rank are, therefore, neglected. The interactions used in this work are due to a transformation with the generator

$$\eta_\alpha = (2\mu)^2 \, [\hat{T}_{\mathrm{int}}, \hat{H}_\alpha] = 2\mu \, [\hat{\boldsymbol{q}}^2, \hat{H}_\alpha] \quad , \tag{2.21}$$

where $\hat{T}_{\mathrm{int}} = \hat{T} - \hat{T}_{\mathrm{cm}} = \frac{\hat{\boldsymbol{q}}^2}{2\mu}$ is the intrinsic kinetic energy of a two-body state. The generator has the dimension $[\alpha] = \mathrm{fm}^4$. Decomposing the relative momentum operator into the radial and angular part

$$\hat{\boldsymbol{q}}^2 = \hat{q}_r + \frac{\hat{\boldsymbol{l}}^2}{r^2} \tag{2.22}$$

shows that this generator aims at a diagonalization with respect to the eigenstates of $\hat{q}_r^2$ and $\hat{l}^2$. In a partial-wave momentum-space basis ($|q(LS)JT\rangle$), the Hamiltonian is evolved towards band-diagonal form with respect to the relative momentum $(q, q')$ and orbital angular momentum $(L, L')$.

### 2.2.3. SRG Derived UCOM Correlation Functions

The traditional UCOM approach uses parameterized correlation functions, which can only vary in a few parameters. Consequently, if a certain type of correlation cannot be described by the parameterization of the correlation function, it can not be included in the basis states.

An alternative approach is the use of SRG generated correlation functions. SRG generated correlation functions are not restricted by the choice of a parameterization and, therefore, can provide more flexible correlation functions. First, the SRG evolution of the bare Hamiltonian $\hat{H}$ is carried out and the two-body problem is solved for the evolved Hamiltonian $\hat{H}_\alpha$. The two-body solution of $\hat{H}_\alpha$ is then mapped to the solution of $\hat{H}$ via a unitary transformation. Finally, the correlation functions for the UCOM are derived from this mapping. A detailed description of the procedure is given in [RNF10].

### 2.2.4. Center-of-Mass Corrected Kinetic Energy

Since the center-of-mass contribution to the kinetic energy destroys the translational invariance of the Hamiltonian, we have to replace the full kinetic energy with the intrinsic kinetic energy

$$\hat{T}_{\mathrm{int}} = \frac{1}{A} \sum_{ij} \frac{(\hat{p}_i - \hat{p}_j)^2}{m_N} \quad , \tag{2.23}$$

where center-of-mass contributions have been subtracted (see also [Her08]). Since the intrinsic kinetic energy can be written as a pure two-body operator, the resulting correlated Hamiltonian

$$\hat{H} = \hat{T}_{\mathrm{int}} + \hat{V} = \hat{T} - \hat{T}_{\mathrm{cm}} + \hat{V} \tag{2.24}$$

is a pure two-body operator.

The $A$-dependence of the kinetic energy implies that the correlated matrix elements also depend on $A$. However, the $A$-dependence is only due to the center-of-mass subtraction and that part is not affected by the unitary transformation [RHP$^+$05]. We can thus write the unitarily transformed Hamiltonian as

$$\hat{H}_{\mathrm{ut}} = \hat{T}_{\mathrm{int}} + (\hat{T}_{\mathrm{ut}} - \hat{T}) + \hat{V}_{\mathrm{ut}} \quad , \tag{2.25}$$

where $\hat{T}_{\mathrm{ut}} - \hat{T}$ is independent of $A$. It is convenient to absorb the unitarily transformed part of the kinetic energy into the NN potential by defining

$$\hat{V}'_{\mathrm{ut}} = (\hat{T}_{\mathrm{ut}} - \hat{T}) + \hat{V}_{\mathrm{ut}} \quad . \tag{2.26}$$

The complete transformed Hamiltonian is then given as the sum of the transformed NN potential and the untransformed kinetic energy

$$\hat{H}_{\mathrm{ut}} = \hat{T}_{\mathrm{int}} + \hat{V}'_{\mathrm{ut}} \quad . \tag{2.27}$$

## 2.2.5. Interactions Used in this Work

In this work, three different unitarily transformed interactions are used:

**UCOM(VAR)**$_{2b}$  The initial AV 18 NN potential is transformed via the traditional variational UCOM approach described in subsection 2.2.1. A detailed analysis of the interaction can be found in [Her08]. The correlation functions and parameters are given in tables 2.1 and 2.2.

**S-SRG**$_{3b}$  The initial AV 18 NN potential is transformed via the SRG transformation described in subsection 2.2.2. A detailed analysis of the interaction can be found in [GRHR10]. The prefix **S** indicates that the SRG flow equations were only solved for partial waves containing relative S-waves. The value of the flow parameter is $\alpha = 0.1\,\mathrm{fm}^4$ and the interaction has to be augmented by a phenomenological three-body interaction (see section 2.3) with $C_3 = 2000\,\mathrm{MeV\,fm}^6$.

**S-UCOM(SRG)**$_{3b}$  The initial AV 18 NN potential is transformed via the SRG based UCOM approach described in subsection 2.2.3. As for the S-SRG$_{3b}$ interaction, a detailed analysis is given in [GRHR10]. The underlying SRG flow equations were only solved for partial waves containing relative S-waves, which is indicated by the prefix **S**. The value of the flow parameter is $\alpha = 0.16\,\mathrm{fm}^4$ and the interaction has to be augmented by a phenomenological three-body interaction (see section 2.3) with $C_3 = 2200\,\mathrm{MeV\,fm}^6$.

## 2.2.6. Transformed Observables

Since a unitary transformation is equivalent to a basis change, the operators of all observables have to be transformed as well. However, the unitary transformations introduced here are designed to address short-range, high-momentum correlations. Consequently, their effect on operators which only probe long-range, low-momentum correlations is expected to be small, which justifies the use of these operators in their bare form.

Apart from the ground state energy, we study quadrupole moments (and mean-square radii), electromagnetic transitions and to some extent densities. The radii, quadrupole moments and transitions all have an $\hat{r}^\lambda$ dependence with $\lambda \geq 1$. As pointed out in [Her08, HPR11], $\hat{r}^\lambda$ is of long-range and low-momentum character. For the UCOM transformation, it has been shown in [RPP+06], that the correction in the nuclear radii due to transformed observables is very small (below 1%). The corrections to the transition operators were found to be negligible as well [PPHR06]. It is expected, that this also holds for the SRG transformation.

In principle, densities do probe short-range correlations. However, the effect on the one-body density is expected to be rather low. When we use the densities to determine the shape of a nucleus or a transition, we can, therefore, neglect the short-range correlations. When the density is used to determine an interaction strength (section 2.3, appendix B), short-range correlations can play a significant role. However, since the transformed three-body interaction is approximated by a phenomenological three-body interaction, we have to use the untransformed densities. If the phenomenological three-body force were used to model an untransformed interaction, we would have to either use transformed densities or transform the phenomenological force.

We conclude that other uncertainties, like basis truncation, the simple nature of the emulated three-body force or the inherent shortcomings of the employed many-body methods have a much stronger impact on the values of observables. We, therefore, are consistent with other works [PHPR12, Her08, HPR11, Gün11] by using the bare operators.

## 2.3. Three-Body Forces

It has been shown in [RPP⁺06] that a pure two-body interaction is not sufficient to reproduce the binding energy and charge radii of atomic nuclei at the same time. On the other hand, it has been shown in [RLC⁺11, Lan10, Cal10] that the inclusion of three-body forces in the Hamiltonian provides an improved description of atomic nuclei.

Since the inclusion of realistic or QCD based three-body forces increases the computational cost drastically, simple phenomenological three-body forces have been developed as an alternative approach [Gün11, GRHR10], which is also adopted in this work. On the RPA level, these phenomenological three-body forces shift the centroid energies to lower values, generally improving agreement with experimental data. The most successful three-body force so far is a simple zero-range interaction

$$\hat{V}_3(\hat{\boldsymbol{r}}_1, \hat{\boldsymbol{r}}_2, \hat{\boldsymbol{r}}_3) = C_3 \, \delta(\hat{\boldsymbol{r}}_1 - \hat{\boldsymbol{r}}_2) \, \delta(\hat{\boldsymbol{r}}_1 - \hat{\boldsymbol{r}}_3) \quad , \tag{2.28}$$

with the constant strength $C_3$.

Zero-range three-body forces with a constant strength have a great computational advantage when used in mean-field based calculations like HF or RPA. In the approximation of non-interacting particles, all $n$-body density matrices reduce to products of the one-body density matrix. As a consequence, the contributions of three-body forces can be reduced to density-dependent forces of lower order, reducing the computational cost significantly. The calculations relevant for this work are carried out in appendix B.

The values of the density-dependent matrix elements have to be calculated on a spatial grid. To efficiently implement the three-body interaction, the wave functions need to be cached, which limits the number of points on the grid. We use a grid with 32 points in each direction, which are evenly distributed in the interval from $-2 \cdot A^{1/3}$ fm to $+2 \cdot A^{1/3}$ fm. These values have proven to be a good compromise between accuracy and calculation speed. For the HF calculations, the discretization errors are at the

order of at most a few keV. They are larger for the RPA (chapter 7.2), but still much lower than other uncertainties.

# 3. Angular-Momentum Projection

In this chapter we discuss the angular-momentum projection, which is necessary to obtain ground states, which are eigenstates of the total angular momentum operator, from a deformed mean-field ground-state. After a short discussion of deformed nuclei, we derive the formulae for angular-momentum projected ground-state energies and transition amplitudes. The chapter is concluded with a discussion of the implementation details, i.e. how to calculate the relevant matrix elements and how to efficiently include a three-body contact interaction.

## 3.1. Deformed Nuclei

As quantum systems, atomic nuclei are required to have all the symmetries of their Hamiltonian.[1] Therefore, all atomic nuclei a spherical. However, some nuclei have non-zero quadrupole (or higher) moments and exhibit excitations with the energy signature of rotational motion. In a classical picture, this is only possible for non-spherical objects. These nuclei are referred to as *intrinsically deformed nuclei*, or sometimes just *deformed nuclei.*

In mean-field calculations, these nuclei have non-spherical ground-state densities. Therefore, the mean-field provides access to the intrinsic frame of the nucleus, where multipole moments and rotational motion are consistent with the classical picture. However, the deformed mean-field states are no longer eigenstates of the total angular momentum operator.

To obtain eigenstates of the total angular momentum operator, which are the lab frame states, a method know as *angular-momentum projection* (AMP) is employed. Since the orientation of the intrinsic frame with respect to the lab frame is arbitrary, the actual lab frame state is made up of a superposition of all possible degenerate orientations of the intrinsic state, leading to a rotationally invariant state in the lab frame.

Since the resulting state is not a single Slater determinant, but a superposition of infinitely many Slater determinants, its use in calculations seems limited at first. However, angular momentum algebra can be employed to derive manageable expressions for matrix elements involving these wave functions.

To carry out the projection, we have to distinguish two total angular-momentum projection quantum numbers. The projection of total angular momentum $J$ onto the third axis of the lab frame (the 3-axis) is denoted by $M$ (or $M_J$). The projection of total angular momentum $J$ onto the third axis of the intrinsic frame (the $z$-axis) is

---

[1]A spontaneous symmetry breaking would require the first states of rotational bands and the ground-state to be degenerate, which is clearly not the case for atomic nuclei.

denoted by $K$. When using a spherical harmonic oscillator (SHO) basis, the canonical definition of the single-particle wave-functions distinguishes the $z$-axis, but this choice is in principle arbitrary. Their relation is illustrated in figure 3.1.
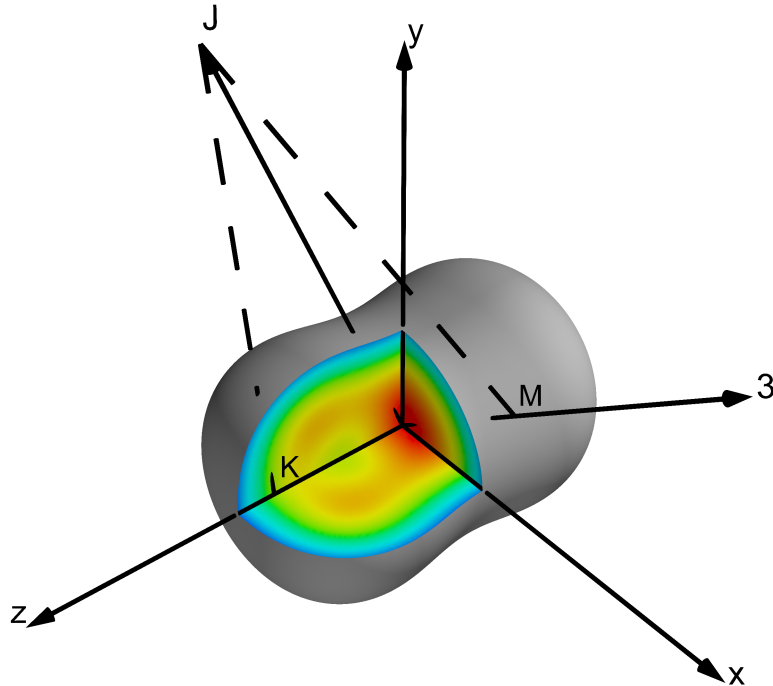


Figure 3.1.: Illustration of the relations between total angular momentum $J$, its projection $K$ onto the $z$-axis (intrinsic system) and its projection $M$ onto the 3-axis (lab system), the values are $J = \frac{3}{2}$, $K = +\frac{1}{2}$ and $M = +\frac{1}{2}$.

Single-particle states are only considered in the intrinsic frame, therefore, $m$ (or $m_j$) and $k$ are different names for the same quantum number. Which notation is used depends on the context. The $m$-notation is mainly used for HO states, while the $k$-notation is used when aspects of the angular-momentum projection are emphasized.

The treatment of deformed nuclei simplifies if we keep one symmetry axis and allow only axial deformations. As it also reduces the computational cost considerably, we study only axially symmetric nuclei in this work. In this case, a state is invariant under rotation around the symmetry axis and, therefore, a quantum-mechanical rotation around this axis is not possible. Consequently, the angular-momentum due to rotations is always perpendicular to the symmetry axis, and rotations do not contribute to the angular-momentum in the direction of the symmetry axis. Therefore, the projection of total angular momentum onto the intrinsic $z$-axis $(K)$, which is the symmetry axis, is the same in the intrinsic and the lab frame. This also holds for the single particle angular momentum projection $k$, as discussed in chapter 4.2.1.

### 3.1.1. Deformation Parameter

The deformation of atomic nuclei is usually described in terms of the deformation parameters $\beta$, ranging from 0 to $\infty$ and $\gamma$, ranging from 0° to 60° (see, for example [RS80]). The $\beta$ parameter defines the amount of deformation present in the nucleus and the $\gamma$ parameter defines the directions of the deformation, i.e. if the deformation is oblate or prolate and if it is purely axial (0° and 60°) or if it also includes triaxial deformations. The range of $\gamma$ can be expanded up to 360° to include the orientation of the nucleus in the intrinsic frame, but as the orientation of the intrinsic frame is arbitrary, this does not provide any real information. In the case of axially deformed nuclei, $\gamma$ only defines whether the deformation is oblate (60°) or prolate (0°), but since this can also be represented by the sign of $\beta$, the $\gamma$ parameter is superfluous. Oblate shapes have negative $\beta$, while a positive $\beta$ corresponds to prolate shapes. The $\beta$ parameter is related to the total intrinsic quadrupole moment $Q_0$ by [RS80, eq. 1.72]

$$\beta = \frac{\sqrt{5\pi}}{3} \frac{Q_0}{A\,R^2} \quad . \tag{3.1}$$

It further depends on the nuclear radius $R$ and the number of nucleons $A$. For details of the calculation in a harmonic oscillator basis, see appendix A.2.

Deformations of higher order than quadrupole are also present in atomic nuclei, but are not covered with the $\beta$ parameter. As a consequence, $\beta = 0$ is only a necessary condition for a spherical nucleus, but not sufficient.

### 3.1.2. Mean-Square Radius

Whenever a single value for the nuclear radius is required, we use the translationally invariant intrinsic mean-square radius of a many-body system. It is defined by [RPP+06]

$$\hat{R}_{\mathrm{ms}} = \frac{1}{A} \sum_i (\hat{\boldsymbol{x}}_i - \hat{\boldsymbol{X}}_{\mathrm{cm}})^2 = \frac{1}{2\,A^2} \sum_{ij} \hat{r}_{ij}^2 \quad , \tag{3.2}$$

with the center-of-mass position operator $\hat{\boldsymbol{X}}_{\mathrm{cm}}$.

As already discussed in chapter 2.2.6, a unitary transformation has to be applied to all observables, including radii, but it is justified to neglect this transformation.

## 3.2. Projection Operator

First, we just repeat some formulae from [RS80, p.474–475]. A wave function with good angular momentum $J$ and projection $M$ is denoted by $|JM\alpha\rangle$, where $\alpha$ collects all quantum-numbers in addition to $J$ and $M$, needed to uniquely define the state. As $\alpha$ is not affected by the angular-momentum quantum number, it is mostly neglected in the following discussion. The state $|JM\rangle$ is constructed by using the projection-like operator $\hat{P}_{MK}^J$ to project all $K$-components of the intrinsic state $|\Phi\rangle$ onto the

angular momentum values $J$ and $M$, and then finding the optimal superposition of these components

$$|JM\rangle = \sum_K g_K \, \hat{P}^J_{MK}|\Phi\rangle \quad . \tag{3.3}$$

The $g_K$ coefficients have to be determined variationally to minimize the energy expectation value. They also depend on $J$ but this dependence is omitted for brevity. Since axially symmetric intrinsic states are eigenstates of the $\hat{J}_z$ operator, $K$ is a good quantum number and, therefore, all but one of the projections vanish, resulting in trivial $g_K$ coefficients of 0 and 1.

The operator $\hat{P}^J_{MK}$ is given by

$$\begin{aligned}
\hat{P}^J_{MK} &= \frac{2\,J+1}{8\,\pi^2} \int D^{J*}_{MK}(\Omega)\,\hat{R}(\Omega)\,\mathrm{d}\Omega \\
&= \sum_\alpha |JM\alpha\rangle\langle JK\alpha| \quad ,
\end{aligned} \tag{3.4}$$

where $D^J_{MK}(\Omega)$ denotes the Wigner D-Matrix. The state $|JK\alpha\rangle$ is defined in the same way as $|JM\alpha\rangle$, but with the angular-momentum projection quantum-number of the intrinsic frame. The rotation operator $\hat{R}(\Omega)$ rotates a state by the Euler angles $\alpha$, $\beta$ and $\gamma$

$$\hat{R}(\Omega) = \mathrm{e}^{i\alpha\hat{J}_z}\,\mathrm{e}^{i\beta\hat{J}_y}\,\mathrm{e}^{i\gamma\hat{J}_z} \quad . \tag{3.5}$$

The projection operator fulfills the relations

$$\begin{aligned}
\hat{P}^J_{MK}\,\hat{P}^{J'}_{M'K'} &= \delta_{JJ'}\,\delta_{M'K}\,\hat{P}^J_{MK'} \\
\hat{P}^{J\dagger}_{MK} &= \hat{P}^J_{KM} \quad .
\end{aligned} \tag{3.6}$$

It is important to note that the angular momentum projection Operator $\hat{P}^J_{MK}$ is not a true projection operator. A true projection operator would be given by

$$\hat{P}^J_{MM} = \sum_\alpha |JM\alpha\rangle\langle JM\alpha| \quad . \tag{3.7}$$

When acting on intrinsic states with axial symmetry, (3.7) would only reproduce one $M$ component, clearly violating the rotational symmetry we wanted to restore with the projection.

## 3.3. Projected Overlaps and Matrix Elements

### 3.3.1. Hamiltonian

The projected energy expectation value $E^J$ of a non-normalized state $|JM\rangle$ with angular momentum $J$ is

$$E^J = \frac{\langle JM|\hat{H}|JM\rangle}{\langle JM|JM\rangle} = \frac{\sum_{KK'} g_K\,g_{K'}\,\langle\Phi|\hat{P}^{J\dagger}_{MK}\,\hat{H}\,\hat{P}^J_{MK'}|\Phi\rangle}{\sum_{KK'} g_K\,g_{K'}\,\langle\Phi|\hat{P}^{J\dagger}_{MK}\,\hat{P}^J_{MK'}|\Phi\rangle} \quad . \tag{3.8}$$

Since the full Hamiltonian $\hat{H}$ is rotationally invariant, it commutes with $\hat{R}(\Omega)$ and $\hat{P}_{MK}^J$. This enables us to apply (3.6) to get

$$E^J = \frac{\sum_{KK'} g_K \, g_{K'} \, \langle \Phi | \hat{H} \, \hat{P}_{KK'}^J | \Phi \rangle}{\sum_{KK'} g_K \, g_{K'} \, \langle \Phi | \hat{P}_{KK'}^J | \Phi \rangle} \quad . \tag{3.9}$$

## 3.3.2. Transitions

A transition $\hat{T}_\lambda$ of a given multipolarity $\lambda$ from an excited state given by the quantum numbers $J_2$ and $\alpha_2$ to the ground state denoted by $J_1$ and $\alpha_1$ is calculated with the reduced matrix element

$$(J_1, \alpha_1 \| \hat{T}_\lambda \| J_2, \alpha_2) \quad . \tag{3.10}$$

We follow the derivation by Mang [Man75], but add some of the less obvious steps to facilitate understanding of the resulting formulae. Although $J$ does not define a state completely, we omit the additional quantum number $\alpha$ in the following discussion. We can use the Wigner-Eckart theorem ([Suh07, 2.27] or [Edm60, 5.4.1])

$$\langle J_1 M_1 | \hat{T}_{\lambda\mu} | J_2 M_2 \rangle = (-1)^{J_1 - M_1} \begin{pmatrix} J_1 & J_2 & \lambda \\ M_1 & -M_2 & \mu \end{pmatrix} (J_1 \| \hat{T}_\lambda \| J_2) \tag{3.11}$$

to restrict the calculation to one component of the transition operator. As it simplifies some steps in the following calculations, $\mu = 0$ is a natural choice. This restriction would not be possible if $\hat{P}_{MK}^J$ were a true projection operator as in (3.7). Writing the matrix element in terms of projectors and intrinsic states yields

$$\langle J_1 M | \hat{T}_{\lambda 0} | J_2 M \rangle = N_1 \, N_2 \cdot \sum_{K_1 K_2} g_{K_1}^{(1)} g_{K_2}^{(2)} \langle \Phi_1 | \hat{P}_{MK_1}^{J_1 \dagger} \, \hat{T}_{\lambda 0} \, \hat{P}_{MK_2}^{J_2} | \Phi_2 \rangle \quad , \tag{3.12}$$

with the normalization factors

$$N_i = \sqrt{\sum_{KK'} g_K^{(i)} g_{K'}^{(i)} \langle \Phi_i | \hat{P}_{K'K}^J | \Phi_i \rangle}^{-1} \quad . \tag{3.13}$$

The $g_K$ coefficients have to be determined by an angular momentum projection of the energy expectation values.

We omit the normalization factors and continue with:

$$\sum_{K_1 K_2} g_{K_1}^{(1)} g_{K_2}^{(2)} \langle \Phi_1 | \hat{P}_{MK_1}^{J_1 \dagger} \, \hat{T}_{\lambda 0} \, \hat{P}_{MK_2}^{J_2} | \Phi_2 \rangle$$

$$= \frac{(2\,J_1 + 1)\,(2\,J_2 + 1)}{64\,\pi^4} \sum_{K_1 K_2} g_{K_1}^{(1)} g_{K_2}^{(2)} \int \int D_{MK_1}^{J_1}(\Omega_1) \, D_{MK_2}^{J_2 *}(\Omega_2)$$

$$\times \, \langle \Phi_1 | \hat{R}^\dagger(\Omega_1) \, \hat{T}_{\lambda 0} \, \hat{R}(\Omega_2) | \Phi_2 \rangle \, \mathrm{d}\Omega_1 \, \mathrm{d}\Omega_2$$

$$= \frac{(2\,J_1 + 1)\,(2\,J_2 + 1)}{64\,\pi^4} \sum_{K_1 K_2} g_{K_1}^{(1)} g_{K_2}^{(2)} \int \int D_{MK_1}^{J_1}(\Omega_1) \, D_{MK_2}^{J_2 *}(\Omega_2)$$

$$\times \, \langle \Phi_1 | \hat{R}^\dagger(\Omega_1) \, \hat{T}_{\lambda 0} \, \hat{R}(\Omega_1) \, \hat{R}^\dagger(\Omega_1) \, \hat{R}(\Omega_2) | \Phi_2 \rangle \, \mathrm{d}\Omega_1 \, \mathrm{d}\Omega_2 \quad . \tag{3.14}$$

We can now use [Edm60, 5.2.1] or [Suh07, 2.11], which we write in the form $(D^J_{MK}(\Omega) = D^{J*}_{KM}(-\Omega)$, note that $(-\Omega) = (-\gamma, -\beta, -\alpha) \neq (-\alpha, -\beta, -\gamma))$

$$\hat{R}^\dagger(\Omega)\,\hat{T}_{\lambda\mu}\,\hat{R}(\Omega) = \sum_{\mu'} \hat{T}_{\lambda\mu'}\,D^{\lambda*}_{\mu\mu'}(\Omega) \tag{3.15}$$

and get

$$\begin{aligned}
&(3.14)\\
&= \frac{(2\,J_1 + 1)\,(2\,J_2 + 1)}{64\,\pi^4} \sum_{K_1 K_2} g^{(1)}_{K_1} g^{(2)}_{K_2} \int \int D^{J_1}_{MK_1}(\Omega_1)\, D^{J_2*}_{MK_2}(\Omega_2)\\
&\quad \times \langle\Phi_1|\sum_\mu \hat{T}_{\lambda\mu}\, D^{\lambda*}_{0\mu}(\Omega_1)\,\hat{R}^\dagger(\Omega_1)\,\hat{R}(\Omega_2)|\Phi_2\rangle\,\mathrm{d}\Omega_1\,\mathrm{d}\Omega_2 \quad .
\end{aligned} \tag{3.16}$$

As the next step, we introduce a new set of Euler angles defined by $\hat{R}(\Omega) = \hat{R}^\dagger(\Omega_1)\,\hat{R}(\Omega_2)$, which we can rewrite as $\hat{R}(\Omega_2) = \hat{R}(\Omega_1)\,\hat{R}(\Omega)$. Using the relation [Edm60, below 4.6.5]

$$D^J_{M'M}(\Omega) = \sum_{M''} D^J_{M'M''}(\Omega'')\, D^J_{M''M}(\Omega') \quad \text{with} \quad \hat{R}(\Omega) = \hat{R}(\Omega'')\,\hat{R}(\Omega') \quad , \tag{3.17}$$

we can expand $D^{J_2*}_{MK_2}(\Omega_2)$ to get

$$\begin{aligned}
&(3.16)\\
&= \frac{(2\,J_1 + 1)\,(2\,J_2 + 1)}{64\,\pi^4} \sum_{K_1 K_2} g^{(1)}_{K_1} g^{(2)}_{K_2} \int \int D^{J_1}_{MK_1}(\Omega_1) \sum_{M'} D^{J_2*}_{MM'}(\Omega_1)\, D^{J_2*}_{M'K_2}(\Omega)\\
&\quad \times \sum_\mu D^{\lambda*}_{0\mu}(\Omega_1)\, \langle\Phi_1|\hat{T}_{\lambda\mu}\,\hat{R}(\Omega)|\Phi_2\rangle\,\mathrm{d}\Omega\,\mathrm{d}\Omega_1 \quad .
\end{aligned} \tag{3.18}$$

To be able to apply [Edm60, 4.6.2]

$$\begin{aligned}
&\int D^{J_1}_{M_1 K_1}(\Omega)\, D^{J_2}_{M_2 K_2}(\Omega)\, D^{J_3}_{M_3 K_3}(\Omega)\,\mathrm{d}\Omega\\
&= 8\,\pi^2 \begin{pmatrix} J_1 & J_2 & J_3 \\ M_1 & M_2 & M_3 \end{pmatrix} \begin{pmatrix} J_1 & J_2 & J_3 \\ K_1 & K_2 & K_3 \end{pmatrix} \quad ,
\end{aligned} \tag{3.19}$$

we use $D^{J*}_{MK}(\Omega) = (-1)^{M-K} D^J_{-M-K}(\Omega)$ [Edm60, 4.2.7].

$$
\begin{aligned}
(3.18) \\
&= \frac{(2\,J_1+1)\,(2\,J_2+1)}{64\,\pi^4} \sum_{\substack{K_1 K_2 \\ M'\mu}} g^{(1)}_{K_1} g^{(2)}_{K_2} (-1)^{M-K_1} \\
&\quad \times \int D^{J_1*}_{-M-K_1}(\Omega_1)\, D^{J_2*}_{MM'}(\Omega_1)\, D^{\lambda*}_{0\mu}(\Omega_1)\, \mathrm{d}\Omega_1 \\
&\quad \times \int D^{J_2*}_{M'K_2}(\Omega)\, \langle\Phi_1|\hat{T}_{\lambda\mu}\,\hat{R}(\Omega)|\Phi_2\rangle\, \mathrm{d}\Omega \\
&= \frac{(2\,J_1+1)\,(2\,J_2+1)}{8\,\pi^2} \sum_{\substack{K_1 K_2 \\ \mu}} g^{(1)}_{K_1} g^{(2)}_{K_2} (-1)^{M-K_1} \\
&\quad \times \begin{pmatrix} J_1 & J_2 & \lambda \\ -M & M & 0 \end{pmatrix} \begin{pmatrix} J_1 & J_2 & \lambda \\ -K_1 & K_1-\mu & \mu \end{pmatrix} \\
&\quad \times \int D^{J_2*}_{K_1-\mu K_2}(\Omega)\, \langle\Phi_1|\hat{T}_{\lambda\mu}\,\hat{R}(\Omega)|\Phi_2\rangle\, \mathrm{d}\Omega \qquad\qquad (3.20)
\end{aligned}
$$

The second 3j-Symbol imposes the condition $M' = K_1 - \mu$, causing the $M'$ sum to vanish.

Now we can apply the Wigner-Eckart theorem (3.11) and reorder the 3j-Symbol to get the more convenient form

$$
\begin{aligned}
(J_1 &\|\hat{T}_\lambda\| J_2) \\
&= \frac{(2\,J_1+1)\,(2\,J_2+1)}{8\,\pi^2} N_1 N_2 \sum_{\substack{K_1 K_2 \\ \mu}} g^{(1)}_{K_1} g^{(2)}_{K_2} (-1)^{J_1-K_1} \\
&\quad \times \begin{pmatrix} J_1 & \lambda & J_2 \\ -K_1 & \mu & K_1-\mu \end{pmatrix} \int D^{J_2*}_{K_1-\mu K_2}(\Omega)\, \langle\Phi_1|\hat{T}_{\lambda\mu}\,\hat{R}(\Omega)|\Phi_2\rangle\, \mathrm{d}\Omega \\
&= (2\,J_1+1)\, N_1 N_2 \sum_{\substack{K_1 K_2 \\ \mu}} g^{(1)}_{K_1} g^{(2)}_{K_2} (-1)^{J_1-K_1} \\
&\quad \times \begin{pmatrix} J_1 & \lambda & J_2 \\ -K_1 & \mu & K_1-\mu \end{pmatrix} \langle\Phi_1|\hat{T}_{\lambda\mu}\,\hat{P}^{J_2}_{K_1-\mu,K_2}|\Phi_2\rangle \quad, \qquad (3.21)
\end{aligned}
$$

which is equivalent to [RS80, 11.137].

## 3.4. Axially Symmetric Intrinsic States

In the case of axially symmetric intrinsic states $|\Phi\rangle$, all but one of the $g_K$ coefficients vanish, only the coefficient with the same $K$ as $|\Phi\rangle$ remains. A further simplification arises from a property of the Wigner functions [Edm60, eq. 4.1.12]

$$
D^J_{MK}(\alpha, \beta, \gamma) = \mathrm{e}^{iM\gamma}\, d^J_{MK}(\beta)\, \mathrm{e}^{iK\alpha} \quad, \qquad\qquad (3.22)
$$

with the reduced Wigner functions $d^J_{MK}(\beta)$. This relation enables us to split $\hat{P}^J_{MK}$ into three operators, one for each Euler angle.

$$\hat{P}^J_{MK} = \hat{p}_M \, \hat{q}^J_{MK} \, \hat{p}_K \quad , \tag{3.23}$$

where

$$\hat{p}_K = \frac{1}{2\,\pi} \int_0^{2\pi} e^{-i\gamma K} \, e^{i\gamma J_z} \, \mathrm{d}\gamma \tag{3.24}$$

$$\hat{p}_M = \frac{1}{2\,\pi} \int_0^{2\pi} e^{-i\alpha M} \, e^{i\alpha J_z} \, \mathrm{d}\alpha \tag{3.25}$$

$$\hat{q}^J_{MK} = \frac{2\,J+1}{2} \int_{-1}^1 d^J_{MK}(\beta) \, e^{i\beta J_y} \, \mathrm{d}\cos(\beta) \quad . \tag{3.26}$$

Due to the axial symmetry, the projections for $\hat{p}_K$ and $\hat{p}_M$ have no effect, leaving only the integral over $\beta$.

$$\hat{P}^J_{MK} = \frac{2\,J+1}{2} \int_{-1}^1 d^J_{MK}(\beta) \, e^{i\beta J_y} \, \mathrm{d}\cos(\beta) \quad . \tag{3.27}$$

Applying the projector (3.27) to (3.9) yields

$$E^J = \frac{\int_{-1}^1 d^J_{KK}(\beta) \, \langle \Phi | \hat{H} \, e^{i\beta \hat{J}_y} | \Phi \rangle \, \mathrm{d}\cos(\beta)}{\int_{-1}^1 d^J_{KK}(\beta) \, \langle \Phi | e^{i\beta \hat{J}_y} | \Phi \rangle \, \mathrm{d}\cos(\beta)} \tag{3.28}$$

for the ground state energy $E^J$.

For a transition operator $\hat{T}_\lambda$, we get

$$
\begin{aligned}
& (J_1 \| \hat{T}_\lambda \| J_2) \\
&= (2\,J_1 + 1)\, N_1\, N_2 \sum_\mu (-1)^{J_1 - K_1} \\
&\quad \times \begin{pmatrix} J_1 & \lambda & J_2 \\ -K_1 & \mu & K_1 - \mu \end{pmatrix} \langle \Phi_1 | \hat{T}_{\lambda\mu} \, \hat{P}^{J_2}_{K_1-\mu, K_2} | \Phi_2 \rangle \\
&= \frac{(2\,J_1 + 1)\,(2\,J_2 + 1)}{2}\, N_1\, N_2 \sum_\mu (-1)^{J_1 - K_1} \\
&\quad \times \begin{pmatrix} J_1 & \lambda & J_2 \\ -K_1 & \mu & K_1 - \mu \end{pmatrix} \int_{-1}^1 d^{J_2}_{K_1-\mu, K_2}(\beta) \, \langle \Phi_1 | \hat{T}_{\lambda\mu} \, e^{i\beta \hat{J}_y} | \Phi_2 \rangle \, \mathrm{d}\cos(\beta) \quad , \tag{3.29}
\end{aligned}
$$

with the normalization factors

$$N_i = \sqrt{\langle \Phi_i | \hat{P}^{J_i}_{K_i K_i} | \Phi_i \rangle}^{-1} = \sqrt{\frac{2\,J_i + 1}{2} \int_{-1}^1 d^{J_i}_{K_i K_i}(\beta) \, \langle \Phi_i | e^{i\beta \hat{J}_y} | \Phi_i \rangle \, \mathrm{d}\cos(\beta)}^{-1} \quad . \tag{3.30}$$

# 3.5. Matrix Elements for Angular Momentum Projection

To calculate the angular-momentum projected quantities, we have to consider three types of matrix elements:

- The matrix element of the product of a two-body operator $\hat{H}$ with the rotation operator, evaluated for equal bra and ket states

$$\langle\Phi|\hat{H}\,\mathrm{e}^{i\beta\hat{J}_y}|\Phi\rangle \quad . \tag{3.31}$$

- The matrix element of the product of a one-body operator $\hat{T}$ with the rotation operator, evaluated for different bra and ket states

$$\langle\Phi_1|\hat{T}\,\mathrm{e}^{i\beta\hat{J}_y}|\Phi_2\rangle \quad . \tag{3.32}$$

- The matrix element of the rotation operator, evaluated for equal bra and ket states

$$\langle\Phi|\mathrm{e}^{i\beta\hat{J}_y}|\Phi\rangle \quad . \tag{3.33}$$

Before we discuss the calculation of the matrix elements, we take a brief look at the rotation operator. A rotation around the $y$-axis is given by the operator

$$\mathrm{e}^{i\beta\hat{J}_y} \quad \text{with} \quad \hat{J}_y = \frac{1}{2\,i}\left(\hat{J}_+ - \hat{J}_-\right) \quad . \tag{3.34}$$

In the HO basis, the matrix elements of $\hat{J}_y$ are given by

$$
\begin{aligned}
\langle nljm|\hat{J}_y|n'l'j'm'\rangle = {}& \frac{1}{2\,i}\,\delta_{j,j'}\,\delta_{l,l'}\,\delta_{n,n'} \\
& \times \Big(\delta_{m+1,m'}\sqrt{j(j-1)-m'(m'+1)} \\
& \quad - \delta_{m-1,m'}\sqrt{j(j-1)-m'(m'-1)}\Big) \quad .
\end{aligned}
\tag{3.35}
$$

The calculation of transition strengths is more efficient if carried out in the HF basis. In this case, $\hat{J}_y$ is converted to the HF basis before calculating the exponential. The matrix exponential is calculated with the `EXPOKIT` library subroutine `DGPADM` [Sid98].

We will now come to the details of the calculation of the matrix elements. The formal points of the discussion are identical to the ones by Brink [Bri66], but we use a more recent notation and put an emphasis on the similarities to the standard density matrix formalism. In his discussion, Brink cites Löwdin [Löw55] as the original source, but due to the manner of presentation used by Löwdin, we cite Brink as our principal source.

### 3.5.1. Normalization Factor

The matrix elements needed for the normalization factors,

$$\langle\Phi|\mathrm{e}^{i\beta\hat{J}_y}|\Phi\rangle \tag{3.36}$$

can be regarded as the overlap of two arbitrary Slater determinants

$$\langle\Phi|\Phi'\rangle \quad . \tag{3.37}$$

The state $|\Phi\rangle$ is a normalized antisymmetric product state, given by

$$|\Phi\rangle = N_\Phi\,\hat{\mathcal{A}}|\Phi_0\rangle \quad , \tag{3.38}$$

with the normalization factor $N_\Phi$, the antisymmetrization operator $\hat{\mathcal{A}}$ and the simple product state $|\Phi_0\rangle = |\varphi_1\rangle...|\varphi_A\rangle$. The antisymmetrization operator $\hat{\mathcal{A}}$ is given by

$$\hat{\mathcal{A}} = \frac{1}{A!}\sum_\pi \mathrm{sgn}(\pi)\hat{P}_\pi \quad , \tag{3.39}$$

with the permutation operator $\hat{P}_\pi$. The sum runs over all possible permutations $\pi$ of single-particle states and $\mathrm{sgn}(\pi)$ denotes the sign of the permutation. With this definition, $\hat{\mathcal{A}}$ is a projection operator.

The matrix element can now be written as

$$
\begin{aligned}
\langle\Phi|\Phi'\rangle =& N_\Phi\,N_\Phi'\,\langle\Phi_0|\hat{\mathcal{A}}^\dagger\hat{\mathcal{A}}|\Phi_0'\rangle = N_\Phi\,N_\Phi'\,\langle\Phi_0|\hat{\mathcal{A}}|\Phi_0'\rangle\\
=& N_\Phi\,N_\Phi'\,\langle\Phi_0|\frac{1}{A!}\sum_\pi \mathrm{sgn}(\pi)\hat{P}_\pi|\Phi_0'\rangle\\
=& N_\Phi\,N_\Phi'\,\langle\varphi_1|...\langle\varphi_A|\frac{1}{A!}\sum_\pi \mathrm{sgn}(\pi)\hat{P}_\pi|\varphi_1'\rangle...|\varphi_A'\rangle\\
=& N_\Phi\,N_\Phi'\,\frac{1}{A!}\sum_\pi \mathrm{sgn}(\pi)\langle\varphi_1|\varphi_{\pi(1)}'\rangle...\langle\varphi_A|\varphi_{\pi(A)}'\rangle\\
=& N_\Phi\,N_\Phi'\,\frac{1}{A!}\,\det(\langle\varphi_a|\varphi_b'\rangle_M) \quad .
\end{aligned}
\tag{3.40}
$$

In the last step, we applied the definition of the determinant. The expression $\langle\varphi_a|\varphi_b'\rangle_M$ denotes the matrix populated with all scalar products $\langle\varphi_a|\varphi_b'\rangle$. The normalization factors $N_\Phi$ and $N_\Phi'$ can be determined by the condition.

$$\langle\Phi|\Phi\rangle = 1 \quad . \tag{3.41}$$

The final expression for the overlap of two arbitrary Slater determinants is

$$\langle\Phi|\Phi'\rangle = \frac{\det(\langle\varphi_a|\varphi_b'\rangle_M)}{\det(\langle\varphi_a|\varphi_b\rangle_M)\det(\langle\varphi_a'|\varphi_b'\rangle_M)} \quad .$$

The original problem (3.36) is recovered by setting $|\varphi_b'\rangle = \mathrm{e}^{i\beta\hat{J}_y}|\varphi_b\rangle$, which also leads to $\det(\langle\varphi_a|\varphi_b\rangle_M) = \det(\langle\varphi_a'|\varphi_b'\rangle_M) = 1$. Therefore, we will omit these determinants whenever convenient.

### 3.5.2. One-Body Matrix Elements

Now, we look at the matrix elements of a one-body operator given by

$$\langle \Phi_1 | \hat{T} \, e^{i\beta \hat{J}_y} | \Phi_2 \rangle \quad . \tag{3.42}$$

As in the previous case of the normalization factor, we express it as

$$\langle \Phi | \hat{T} | \Phi' \rangle \quad . \tag{3.43}$$

The one-body operator in many-body space can be expressed as a sum of operators acting in the single-particle spaces

$$\hat{T} = \sum_i \hat{t}_i \quad , \tag{3.44}$$

with the canonical definition of $\hat{t}_i$

$$\hat{t}_i = \hat{1} \otimes \hat{1} \otimes ... \otimes \hat{t} \otimes ... \otimes \hat{1} \quad . \tag{3.45}$$
$$\uparrow$$
$$i\text{th single-particle space}$$

If a single-particle state does not have the same index as $\hat{t}_i$, $\hat{t}_i$ acts as the identity-operator. For a clearer notation, we define the operator $\hat{t}_{ia}$

$$\hat{t}_{ia} = \begin{cases} \hat{t} & \text{if } i = a \\ \hat{1} & \text{else} \end{cases} \quad . \tag{3.46}$$

With this operator, $\hat{t}_i$ for an $n$-body space is given by

$$\hat{t}_i = \hat{t}_{i1} \otimes ... \otimes \hat{t}_{in} \quad . \tag{3.47}$$

The matrix element $\langle \Phi | \hat{T} | \Phi' \rangle$ can then be written as

$$
\begin{aligned}
\langle \Phi | \hat{T} | \Phi' \rangle &= N_\Phi \, N'_\Phi \, \langle \Phi_0 | \hat{\mathcal{A}}^\dagger \hat{T} \hat{\mathcal{A}} | \Phi'_0 \rangle = N_\Phi \, N'_\Phi \, \sum_i \langle \Phi_0 | \hat{t}_i \hat{\mathcal{A}} | \Phi'_0 \rangle \\
&= N_\Phi \, N'_\Phi \, \sum_i \langle \Phi_0 | \hat{t}_i \frac{1}{A!} \sum_\pi \text{sgn}(\pi) \hat{P}_\pi | \Phi'_0 \rangle \\
&= N_\Phi \, N'_\Phi \, \sum_i (\langle \varphi_1 | ... \langle \varphi_A |) \, \hat{t}_i \frac{1}{A!} \sum_\pi \text{sgn}(\pi) \hat{P}_\pi | \varphi'_1 \rangle ... | \varphi'_A \rangle \\
&= N_\Phi \, N'_\Phi \, \frac{1}{A!} \sum_i \sum_\pi \text{sgn}(\pi) \langle \varphi_1 | \hat{t}_{i\pi(1)} | \varphi'_{\pi(1)} \rangle ... \langle \varphi_A | \hat{t}_{i\pi(A)} | \varphi'_{\pi(A)} \rangle \\
&= N_\Phi \, N'_\Phi \, \frac{1}{A!} \sum_i \det(\langle \varphi_a | \hat{t}_{ib} | \varphi'_b \rangle_M) \quad .
\end{aligned}
\tag{3.48}
$$

Including the normalization factors, we get

$$\langle\Phi|\hat{T}|\Phi'\rangle = \sum_i \det(\langle\varphi_a|\hat{\mathfrak{t}}_{ib}|\varphi'_b\rangle_M) \quad . \tag{3.49}$$

At this point, it is in order to discuss what the expression $\sum_i \det(\langle\varphi_a|\hat{\mathfrak{t}}_{ib}|\varphi'_b\rangle_M)$ actually means. The matrix elements of the matrix $\langle\varphi_a|\hat{\mathfrak{t}}_{ib}|\varphi'_b\rangle_M$ are just the scalar products $\langle\varphi_a|\varphi'_b\rangle$, if $i \neq b$. In the case $i = b$, the matrix elements are given by $\langle\varphi_a|\hat{t}|\varphi'_b\rangle$.

We illustrate this at the example of a three-body system

$$\sum_{i=1}^{3} \det(\langle\varphi_a|\hat{\mathfrak{t}}_{ib}|\varphi'_b\rangle_M) = \sum_{i=1}^{3} \det \begin{pmatrix} \langle\varphi_1|\hat{\mathfrak{t}}_{i1}|\varphi'_1\rangle & \langle\varphi_2|\hat{\mathfrak{t}}_{i1}|\varphi'_1\rangle & \langle\varphi_3|\hat{\mathfrak{t}}_{i1}|\varphi'_1\rangle \\ \langle\varphi_1|\hat{\mathfrak{t}}_{i2}|\varphi'_2\rangle & \langle\varphi_2|\hat{\mathfrak{t}}_{i2}|\varphi'_2\rangle & \langle\varphi_3|\hat{\mathfrak{t}}_{i2}|\varphi'_2\rangle \\ \langle\varphi_1|\hat{\mathfrak{t}}_{i3}|\varphi'_3\rangle & \langle\varphi_2|\hat{\mathfrak{t}}_{i3}|\varphi'_3\rangle & \langle\varphi_3|\hat{\mathfrak{t}}_{i3}|\varphi'_3\rangle \end{pmatrix}$$

$$= \det \begin{pmatrix} \langle\varphi_1|\hat{t}|\varphi'_1\rangle & \langle\varphi_2|\hat{t}|\varphi'_1\rangle & \langle\varphi_3|\hat{t}|\varphi'_1\rangle \\ \langle\varphi_1|\varphi'_2\rangle & \langle\varphi_2|\varphi'_2\rangle & \langle\varphi_3|\varphi'_2\rangle \\ \langle\varphi_1|\varphi'_3\rangle & \langle\varphi_2|\varphi'_3\rangle & \langle\varphi_3|\varphi'_3\rangle \end{pmatrix} + \det \begin{pmatrix} \langle\varphi_1|\varphi'_1\rangle & \langle\varphi_2|\varphi'_1\rangle & \langle\varphi_3|\varphi'_1\rangle \\ \langle\varphi_1|\hat{t}|\varphi'_2\rangle & \langle\varphi_2|\hat{t}|\varphi'_2\rangle & \langle\varphi_3|\hat{t}|\varphi'_2\rangle \\ \langle\varphi_1|\varphi'_3\rangle & \langle\varphi_2|\varphi'_3\rangle & \langle\varphi_3|\varphi'_3\rangle \end{pmatrix}$$

$$+ \det \begin{pmatrix} \langle\varphi_1|\varphi'_1\rangle & \langle\varphi_2|\varphi'_1\rangle & \langle\varphi_3|\varphi'_1\rangle \\ \langle\varphi_1|\varphi'_2\rangle & \langle\varphi_2|\varphi'_2\rangle & \langle\varphi_3|\varphi'_2\rangle \\ \langle\varphi_1|\hat{t}|\varphi'_3\rangle & \langle\varphi_2|\hat{t}|\varphi'_3\rangle & \langle\varphi_3|\hat{t}|\varphi'_3\rangle \end{pmatrix} \quad . \tag{3.50}$$

### 3.5.3. Two-Body Matrix Elements

For the discussion of the two-body matrix elements, it is instructive to review the one-body matrix elements for the case of an invertible matrix $\langle\varphi_a|\varphi'_b\rangle_M$, which is usually not the case if $\hat{T}$ is a transition operator. We aim at bringing (3.49) into a form similar to the usual density matrix formalism for orthogonal basis states

$$\langle\Phi|\hat{T}|\Phi'\rangle = \sum_{a,b} \langle\varphi_a|\hat{t}|\varphi'_b\rangle \, \rho_{ab} \quad . \tag{3.51}$$

The expansion form of the determinant can be collapsed up to a point where one matrix element $\mathsf{A}_{ab}$ is left, and all others are absorbed into one quantity $c_{ab}$

$$\det(\mathsf{A}) = \sum_b \mathsf{A}_{ab} \, c_{ab} \quad . \tag{3.52}$$

The quantities $c_{ab}$ are referred to as matrix cofactors or signed minors. Equation (3.52) can be written as

$$\det(\mathsf{A}) \, \delta_{aa'} = \sum_b \mathsf{A}_{ab} \, c_{a'b} \quad . \tag{3.53}$$

With the cofactor matrix $\mathsf{c}$, this can be written as a matrix multiplication

$$\det(\mathsf{A}) \, \delta_{aa'} = \mathsf{A}^T \cdot \mathsf{c} \quad , \tag{3.54}$$

and if $\mathsf{A}$ is invertible

$$c_{ab} = (\mathsf{A}^{-1})_{ba} \, \det(\mathsf{A}) \quad , \tag{3.55}$$

where $(A^{-1})_{ba}$ are matrix elements of the inverse matrix of $A$. At this point, it is essential to note that it follows from equation (3.52), that the matrix cofactor $c_{ab}$ does not contain any information regarding the matrix elements of the $a$th column or the $b$th row of $A$.

We can now write (3.49) in terms of matrix cofactors

$$\langle \Phi | \hat{T} | \Phi' \rangle = \sum_{ab} \langle \varphi_a | \hat{t} | \varphi_b' \rangle \, c_{ab} \tag{3.56}$$

$$c_{ab} = (\langle \varphi_a | \varphi_b' \rangle_M^{-1})_{ba} \, \det(\langle \varphi_a | \varphi_b' \rangle_M) \quad .$$

Since the matrix elements including the operator $\hat{t}$ are not included in the cofactors, we can simply use the cofactors of the matrix $\langle \varphi_a | \varphi_b' \rangle_M$.

Getting back to eq. (3.51), we define a *generalized density matrix*

$$\tilde{\rho}_{ab} = (\langle \varphi_a | \varphi_b' \rangle_M^{-1})_{ba} \, \det(\langle \varphi_a | \varphi_b' \rangle_M) \quad . \tag{3.57}$$

For orthogonal case $(\langle \varphi_a | \varphi_b' \rangle = \delta_{ab})$, we get $\rho_{ab} = \tilde{\rho}_{ab}$. We can now express the many-body matrix element in the usual form

$$\langle \Phi | \hat{T} | \Phi' \rangle = \sum_{a,b} \langle \varphi_a | \hat{t} | \varphi_b' \rangle \, \tilde{\rho}_{ab} \quad . \tag{3.58}$$

The same techniques used for the one-body case in eq. (3.48) through (3.56) can also be applied to the two-body case. Using the second-order cofactors $c_{ab,cd}$ defined by the relation

$$\det A = \sum_{cd} A_{ac} A_{bd} \, c_{ab,cd} \quad , \tag{3.59}$$

we get the following equation for a two-body operator

$$\langle \Phi | \hat{H} | \Phi' \rangle = \tfrac{1}{2} \sum_{abcd} \langle \varphi_a, \varphi_b | \hat{H} | \varphi_c', \varphi_d' \rangle c_{ab,cd} \quad . \tag{3.60}$$

The two-body states are simple, non-antisymmetric product states.

To fully embrace the picture of generalized density matrices, we need an expression relating the first-order cofactor to the second-order cofactor—similar to the relation of the one-particle density matrix to the two-particle density matrix in the mean-field picture (i.e. $\tilde{\rho}_{abcd}^{(2)} = \tilde{\rho}_{ac} \tilde{\rho}_{bd} - \tilde{\rho}_{ad} \tilde{\rho}_{bc}$).

Since the determinant of a matrix vanishes if two rows are equal and changes sign if two rows are exchanged, we can write $(\det(A) \neq 0)$

$$\det A \, (\delta_{aa'} \, \delta_{bb'} - \delta_{ab'} \, \delta_{ba'}) = \sum_{cd} A_{ac} A_{bd} \, c_{a'b',cd} \quad . \tag{3.61}$$

After expanding with (3.53), we get

$$(\det A)^{-1} \sum_{cd} A_{ac} A_{bd} \, (c_{a'c} \, c_{b'd} - c_{b'c} \, c_{a'd}) = \sum_{cd} A_{ac} A_{bd} \, c_{a'b',cd} \quad . \tag{3.62}$$

This is equivalent to

$$c_{ab,cd} = \det(\mathsf{A})^{-1} \left( c_{ac} \, c_{bd} - c_{ad} \, c_{bc} \right) \quad , \tag{3.63}$$

which has the desired form. The corresponding relation for the *generalized density matrices* is

$$\tilde{\rho}^{(2)}_{abcd} = \det(\langle \varphi_a | \varphi'_b \rangle_M)^{-1} \left( \tilde{\rho}_{ac} \tilde{\rho}_{bd} - \tilde{\rho}_{ad} \tilde{\rho}_{bc} \right) \quad . \tag{3.64}$$

For orthogonal basis states, we have $\det(\langle \varphi_a | \varphi'_b \rangle_M) = 1$ and reproduce the well known expression.

For the two-body matrix element with antisymmetrized two-body states, we get (cf. (3.60))

$$\langle \Phi | \hat{H} | \Phi' \rangle = \tfrac{1}{2} \sum_{abcd} \langle \varphi_a, \varphi_b | \hat{H} | \varphi'_c, \varphi'_d \rangle_A \, \det(\langle \varphi_a | \varphi'_b \rangle_M)^{-1} \, \tilde{\rho}_{ac} \tilde{\rho}_{bd} \quad . \tag{3.65}$$

## 3.6. Projection of a Three-Body Contact Interaction

Some of the interactions used in this work include a three-body contact term. As shown in appendix B for the unprojected case, the contact term can be evaluated analytically, which introduces a density dependent term to the Hamiltonian. Since this provides a very efficient way to calculate the contribution of the three-body force, a way corresponding to equation (B.31) must be found to efficiently calculate the contribution of the three-body force to the projected ground-state energy. However, due to the rotated wave functions, this is a rather complicated procedure. It is, therefore, more convenient to deduce the correct formula to evaluate the contribution of the three-body contact interaction to the projected binding energy by a different approach. For even-even nuclei, it can easily be shown that the contribution of a three-body contact term to the binding energy of the HF ground state is equal to that of a density-dependent two-body force of the form

$$\hat{V}_\rho = \tfrac{1}{6} C_3 \left( 1 + \hat{P}_\sigma \right) \rho(\hat{\boldsymbol{r}}_1) \, \delta(\hat{\boldsymbol{r}}_1 - \hat{\boldsymbol{r}}_2) \quad . \tag{3.66}$$

For a two-body force, it is still possible to carry out the projection directly, without the analytical evaluation.

However, it may not be immediately clear which density one has to use in the interaction. A computationally simple approach is to use the projected density

$$\rho(\boldsymbol{r}) = \frac{\langle JM | \hat{\rho}(\boldsymbol{r}) | JM \rangle}{\langle JM | JM \rangle} \quad , \tag{3.67}$$

with the angular momentum projected wave functions $|JM\rangle$. This approach is known as the *projected-density prescription*. For the case of parity projection and arbitrary (including non-integer) powers of density dependence, it has been shown explicitly by Robledo [Rob10], that the *projected-density prescription* does not produce sensible results.

If one only considers density dependencies caused by many-body contact interactions (i.e. integer powers), it is also clear that the *projected-density prescription* does not provide the desired results. In the full three-body formulation of the Hamiltonian, the contribution of the three-body part to each integration point only depends on the values of the HF coefficients of the unrotated state and on the HF coefficients of the rotated state at that specific point and not on any other point. This behavior must be conserved for the density-dependent interaction. Since the *projected-density prescription* violates this requirement, it cannot be used.

A computationally more demanding approach is the *mixed-density prescription*. Here, one calculates a different density for each integration point

$$\rho(\boldsymbol{r},\beta) = \frac{\langle\Phi|\hat{\rho}(\hat{\boldsymbol{r}})\,\mathrm{e}^{i\beta\hat{J}_y}|\Phi\rangle}{\langle\Phi|\mathrm{e}^{i\beta\hat{J}_y}|\Phi\rangle} \quad , \tag{3.68}$$

using the intrinsic wave functions $|\Phi\rangle$.

To arrive at the formula for the projected energy (eq. (3.9)), we used the rotational invariance of the Hamiltonian. Obviously, this is not fulfilled for deformed nuclei if the Hamiltonian includes density dependent terms. However, it has been shown in [RGER02], that (3.9) still holds in the case of the *mixed-density prescription*.

The computation of the mixed densities is rather simple. One only has to replace the normal density matrix in eq. (A.19) by the generalized density matrices introduced in section 3.5.3 and take care of the normalization factor, which is unity in the unprojected case.

As it is now clear how to include a density-dependent two-body force in the angular momentum projection, we can review our three-body contact interaction. For the contribution of the three-body force to the projected binding energy, we make the ansatz

$$\langle\Phi|\hat{V}_3\,\mathrm{e}^{i\beta\hat{J}_y}|\Phi\rangle = \tfrac{1}{4}\,C_3 \int \hat{\rho}^p(\boldsymbol{r},\beta)\,\hat{\rho}^n(\boldsymbol{r},\beta)\,\hat{\rho}(\boldsymbol{r},\beta)\cdot\langle\Phi|\mathrm{e}^{i\beta\hat{J}_y}|\Phi\rangle^x\,\mathrm{d}\boldsymbol{r} \quad . \tag{3.69}$$

The power $x$ of the normalization factor $\langle\Phi|\mathrm{e}^{i\beta\hat{J}_y}|\Phi\rangle$ is determined by comparing the projected binding energy to the results obtained by the density dependent two-body interaction (3.66) in the full two-body formulation. We find $x = 2$. The contribution of the three-body force to the projected binding energy is, therefore, given by

$$\langle\Phi|\hat{V}_3\,\mathrm{e}^{i\beta\hat{J}_y}|\Phi\rangle = \tfrac{1}{4}\,C_3 \int \hat{\rho}^p(\boldsymbol{r},\beta)\,\hat{\rho}^n(\boldsymbol{r},\beta)\,\hat{\rho}(\boldsymbol{r},\beta)\cdot\langle\Phi|\mathrm{e}^{i\beta\hat{J}_y}|\Phi\rangle^2\,\mathrm{d}\boldsymbol{r} \quad . \tag{3.70}$$

# 4. Hartree-Fock Method for Deformed Nuclei

In this Chapter, we give an overview of the Hartree-Fock (HF) method. It deals with the interactions between the nuclei only via a mean-field and, therefore, fails to take into account correlations between particles. As these correlations are very important for an accurate description of atomic nuclei, the method is obviously unsuitable for a complete description of nuclei. However, in combination with unitarily transformed NN interactions, it provides a good starting point for more elaborate methods like the Random Phase Approximation (chapter 6) or Multi-Configuration Hartree-Fock (chapter 8).

First, we describe the general formalism without reference to a specific application or class of nuclei. In the next section, we consider the application to axially deformed even-even nuclei.

## 4.1. General HF Formalism

The following presentation is essentially a summary of [RS80, sections 5.2 and 5.3].

The Hartree-Fock (HF) method is based on the general variational principle. The time-independent Schrödinger Equation

$$E|\Psi\rangle = \hat{H}|\Psi\rangle \tag{4.1}$$

is equivalent to the variational equation

$$\delta E[\Psi] = 0 \quad , \tag{4.2}$$

with the energy functional $E[\Psi]$ of the many-body state $|\Psi\rangle$ given by

$$E[\Psi] = \frac{\langle\Psi|\hat{H}|\Psi\rangle}{\langle\Psi|\Psi\rangle} \quad . \tag{4.3}$$

Equation (4.2) is exact. Approximations are introduced via the choice of trial wave functions for the variation.

In the HF approximation, (4.2) is solved with a single Slater determinant of single-particle states as the trial wave function

$$|\text{HF}\rangle = \prod_{i=1}^{A} \hat{a}_i^\dagger|0\rangle \quad . \tag{4.4}$$

The variation is carried out with respect to the single-particle states created by $\hat{a}_i^\dagger$. The single-particle states are given by a unitary transformation from a reference basis, usually some kind of harmonic oscillator (HO) basis with the creation operators $\hat{c}_a^\dagger$

$$\hat{a}_i^\dagger = \sum_a \mathsf{D}_{ia}\, \hat{c}_a^\dagger \quad . \tag{4.5}$$

The index $a$ absorbs all quantum numbers needed to define a state in the reference basis (cf. section 4.2.1). The transformation $\mathsf{D}$ is not uniquely defined. Any additional unitary transformation that does not mix particle and hole states can be applied on top of $\mathsf{D}$ without changing the result, modulo an unimportant phase factor.

However, a Slater determinant wave function is uniquely defined by its single-particle density matrix

$$\rho_{aa'} = \langle \mathrm{HF}|\hat{c}_{a'}^\dagger \hat{c}_a|\mathrm{HF}\rangle = \sum_{ii'} \mathsf{D}_{ai}\, \mathsf{D}_{a'i'}^* \, \langle \mathrm{HF}|\hat{a}_{i'}^\dagger \hat{a}_i|\mathrm{HF}\rangle = \sum_i^A \mathsf{D}_{ai}\, \mathsf{D}_{a'i}^* \quad . \tag{4.6}$$

Since the HF wave function is normalized, the HF-energy, which we want to minimize in (4.2), is given by

$$E^{\mathrm{HF}}[\rho] = \langle \mathrm{HF}|\hat{H}|\mathrm{HF}\rangle \quad . \tag{4.7}$$

For a two-body Hamiltonian with the matrix elements $\mathsf{H}_{a_1 a_2 a_1' a_2'} = \langle 0|\hat{c}_{a_1}^\dagger \hat{c}_{a_2}^\dagger \hat{H} \hat{c}_{a_2'} \hat{c}_{a_1'}|0\rangle$, this reads

$$\begin{aligned}
E^{\mathrm{HF}}[\rho] &= \frac{1}{4} \sum_{a_1 a_2 a_1' a_2'} \mathsf{H}_{a_1 a_2 a_1' a_2'} \, \langle \mathrm{HF}|\hat{c}_{a_1}^\dagger \hat{c}_{a_2}^\dagger \hat{c}_{a_2'} \hat{c}_{a_1'}|\mathrm{HF}\rangle \\
&= \frac{1}{2} \sum_{a_1 a_2 a_1' a_2'} \mathsf{H}_{a_1 a_2 a_1' a_2'} \, \rho_{a_1 a_1'} \, \rho_{a_2 a_2'} \quad ,
\end{aligned} \tag{4.8}$$

where we used the relation for two-body density matrices of single Slater determinants

$$\rho^{(2)}_{a_1 a_2 a_1' a_2'} = \rho_{a_1 a_1'} \, \rho_{a_2 a_2'} - \rho_{a_1 a_2'} \, \rho_{a_2 a_1'} \tag{4.9}$$

and the antisymmetry of the Hamiltonian. As the center-of-mass corrected kinetic energy is a two-body operator (cf. chapter 2.2.4), we do not need to consider one-body operators here.

The variation of the energy is given by

$$\delta E = \sum_{aa'} \frac{E^{\mathrm{HF}}[\rho]}{\rho_{aa'}} \delta\rho_{aa'} \tag{4.10}$$

with

$$\frac{E^{\mathrm{HF}}[\rho]}{\rho_{aa'}} = \Gamma_{aa'} = \sum_{a_2 a_2'} \mathsf{H}_{aa_2 a' a_2'} \, \rho_{a_2 a_2'} \quad . \tag{4.11}$$

If the Hamiltonian also includes a three-body interaction, the following contributions have to be added to (4.8) [GRHR10, Gün11]

$$E_3^{\mathrm{HF}}[\rho] = \frac{1}{6} \sum_{a_1 a_2 a_3 a_1' a_2' a_3'} \mathsf{H}_{a_1 a_2 a_3 a_1' a_2' a_3'} \, \rho_{a_1 a_1'} \, \rho_{a_2 a_2'} \, \rho_{a_3 a_3'} \tag{4.12}$$

and to (4.11)

$$\Gamma_{aa'}^{(3)} = \frac{1}{2} \sum_{a_2 a_3 a_2' a_3'} \mathsf{H}_{a a_2 a_3 a' a_2' a_3'} \, \rho_{a_2 a_2'} \, \rho_{a_3 a_3'} \quad . \tag{4.13}$$

$\Gamma$ is the single particle potential which arises from the average over all two-body (and three-body) interactions. This is why the HF method is referred to as a mean-field approximation. In simple language, we are looking for a nucleon configuration, that is already in the ground state of its own mean-field potential.

The optimization can be formulated as an eigenvalue problem [RS80]

$$\sum_{a'} \Gamma_{aa'} \, \mathsf{D}_{a'i} = \sum_{a'} \epsilon_i \delta_{aa'} \, \mathsf{D}_{a'i} \quad . \tag{4.14}$$

The eigenvalues $\epsilon$ are the energies of the single particle states. When solving (4.14), we have to keep in mind, that $\Gamma$ depends on $\rho$ and, therefore, the eigenvalue problem is nonlinear and has to be solved by iteration. We start with some reasonable initial state, e.g., with an appropriate number of occupied harmonic oscillator states, calculate $\Gamma$ and solve (4.14) for the first time. We then use the solution of (4.14) to calculate a new $\Gamma$ and solve (4.14) again. This process is repeated until the changes from one density matrix to the next are below a certain threshold.

## 4.2. Axially Deformed Systems

The HF method has three main ingredients: the Hamiltonian, the reference basis and the initialization state. Since the objective of this work is to use Hamiltonians based on realistic nucleon-nucleon interactions (see chapter 2), we do not follow the popular approach to use Hamiltonians specifically tailored for HF calculations. However, one can modify the HF field $\Gamma$ with a Lagrange parameters to map the energy surface with respect to certain parameters. This method is crucial in the *approximate varia-tion after projection* approach discussed in section 4.3. But first, we will discuss the reference basis and initialization states.

### 4.2.1. Reference Basis

We use an *ls*-coupled spherical harmonic oscillator basis as the reference basis for the HF method. Each state is identified by the following quantum numbers: the radial quantum number $n$, the orbital angular momentum $l$, the total angular momentum $j$, its projection $m_j$ and the isospin projection $m_t$. For brevity, the $n$, $l$, $j$ and $m_j$

quantum numbers are absorbed into the index $a$. The basis is truncated at a certain single-particle energy $e$ of the harmonic oscillator states, i.e. $e = 2\,n + l \leq e_{\mathrm{max}}$, with an additional constraint for $l$ ($l \leq l_{\mathrm{max}}$).

The $ls$-coupled states are given by

$$|a\,m_t\rangle = \sum_{m_l, m_s} (l\,m_l\,\tfrac{1}{2}\,m_s | j\,m_j)\,|n\,l\,m_l\rangle \otimes |\tfrac{1}{2}\,m_s\rangle \otimes |\tfrac{1}{2}\,m_t\rangle \quad . \qquad (4.15)$$

The $ls$-coupled real space wave functions $\varphi_a(\boldsymbol{r}) \otimes |\tfrac{1}{2}\,m_t\rangle$ are given by

$$\varphi_a(\boldsymbol{r}) \otimes |\tfrac{1}{2}\,m_t\rangle = \sum_{m_l, m_s} (l\,m_l\,\tfrac{1}{2}\,m_s | j\,m_j)\,\varphi_{nlm_l}(\boldsymbol{r}) \otimes |\tfrac{1}{2}\,m_s\rangle \otimes |\tfrac{1}{2}\,m_t\rangle \quad . \qquad (4.16)$$

The uncoupled HO wave functions $\varphi_{nlm_l}$ are defined in the appendix, eq. (A.20). Since the HO wave functions do not depend on it, $m_t$ is dropped sometimes.

The variation of the single-particle states is carried out over all single-particle states of the same type of nucleons. This is in contrast to spherical HF calculations, where only variations with respect to $n$ are allowed. The HF single-particle states are given by

$$|\alpha\,m_t\rangle = \sum_a C_a^{\alpha\,m_t}|a\,m_t\rangle \quad , \qquad (4.17)$$

with the HF coefficients $C_a^{\alpha\,m_t}$. The index $\alpha$ has the same dimension as the index $a$ and defines each HF state. However, since one HF state can, in principle, contain contributions from all HO quantum numbers, any connection to the quantum numbers absorbed in $a$ is lost and $\alpha$ is reduced to a simple state index. No physical property depends on the index $\alpha$.

Since we only study nuclei with axial symmetry and symmetry with respect to the $x$-$y$ plane, the variation does not use the full freedom (4.17) allows. It only includes states with equal angular-momentum projection quantum number $m_j$ and equal parity of the orbital angular-momentum quantum number $l$. This is easily understood when considering the mean-field Hamiltonian, which we assume to have these symmetries. Any axially symmetric operator only connects states where the sums of the $m_j$ quantum numbers in the bra and in the ket are equal ($\langle m_{j1}, ..., m_{jn}|\hat{O}|m'_{j1}, ..., m'_{jn}\rangle \neq 0$ only if $\sum_i^n m_{ji} = \sum_i^n m'_{ji}$). If the operator is symmetric with respect to the $x$-$y$ plane, it only connects states with equal parity ($\langle \pi_1, ..., \pi_n|\hat{O}|\pi'_1, ..., \pi'_n\rangle \neq 0$ only if $\prod_i^n \pi_i = \prod_i^n \pi'_i$). This is a direct consequence of the spherical harmonics involved in the wave functions of the spherical harmonic oscillator basis. Since only states with equal $m_j$ and $\pi$ are connected, only these states can be mixed by the HF scheme. Therefore, all states have well defined values of the $m_j$ and $\pi$ quantum numbers. However, to keep the discussion as general as possible, we only take this into account when there is a very strong incentive to do so, as for angular momentum projection (section 3.4) and RPA (section 6.2.4). We will assume a full variation otherwise.

When a single Slater-determinant is used to describe an open-shell nucleus, the resulting many-body state is deformed and does not have good angular momentum. This

can be prevented by averaging over all $m_j$ states and only mixing states with respect to the radial quantum number, but the obtained binding energies are considerably lager if one also allows mixing with different angular momentum states.[1] However, as atomic nuclei do have good angular momentum, the deformed Slater determinant only describes an intrinsic state. The real ground state, which is spherically symmetric and has good angular momentum, is obtained by angular-momentum projection (chapter 3).

### 4.2.2. Initialization Methods

The HF method preserves symmetries that are already present in the initialization state [RS80]. This is obvious if we consider the mean-field character of the method: if a certain symmetry is present in the initial state, the mean-field potential will have the same symmetry. Consequently the symmetry will not be destroyed during the next iteration. Numerical noise is usually insufficient to prevent this behavior. If a HF calculation is initialized with a symmetry that is not present in the targeted nucleus, the resulting intrinsic state is just a stationary point and not the energy minimum.

To circumvent this problem, we use three different HF initialization methods. Each of these methods has its distinct advantages and disadvantages. All methods are based on the canonical shell-model orbitals as shown in [BM69, Fig. 2-23].

- Spherical Initialization: This method fills the orbitals in the canonical shell-model orbital order. The states are filled from low $|m|$ to high $|m|$, producing slightly prolate states for open shell nuclei. This method has the severe disadvantage, that it produces a spherical initial state for nuclei with a closed sub-shell (e.g. $^{28}$Si).

- Prolate Initialization: This method tries to begin the iteration with a prolate state. To accomplish this, all states with $m = \pm j$ are left empty in all orbitals with $j > \frac{1}{2}$. This method has no problems with metastable states, but a prolate state usually does not change into an oblate one. This means, that it is necessary to do another calculation with an oblate initialization state to check if the ground state is prolate or oblate.

- Oblate Initialization: This method tries to begin the iteration with an oblate state. This is accomplished, by leaving all states with $m = \pm\frac{1}{2}$ empty in all orbitals with $j > \frac{1}{2}$. As with the prolate initialization, there are no problems with metastable states, but since an oblate state usually does not change into a prolate one, both initializations have to be employed to find the real ground state.

Since all initialization methods produce axially symmetric states, nuclei which are not axially symmetric, like $^{12}$C or $^{24}$Mg can not be described accurately.

---

[1] In our approach about 1 MeV per nucleon.

## 4.3. Angular Momentum Projection with Constrained HF

One can apply the angular-momentum projection directly to the ground state obtained by the HF variation. This is referred to as the *projection after variation* (PAV) approach. However, in the HF scheme, the intrinsic binding energy is minimized, but the angular-momentum projected binding energy is the quantity of interest. It has been shown how to adapt HFB theory to minimize the particle-number projected binding energy in [SR00]. In principle, it is possible to use this exact *variation after projection* method for angular momentum as well, but it has not been carried out so far.

An alternative method is to minimize the projected energy via constrained HF solutions, which we refer to as *approximate variation after projection* (AVAP). For angular momentum projection, a natural choice for the constraint is the static quadrupole moment $\hat{Q}$, which is directly linked to the deformation parameter $\beta$ (section 3.1.1). A modified Hamiltonian $\hat{H}'$ is constructed by subtracting the constraint with a Lagrange parameter $\lambda$ from the original Hamiltonian $\hat{H}$

$$\hat{H}' = \hat{H} - \lambda \hat{Q} \quad . \tag{4.18}$$

The HF solution is then found by combining the HF minimization with respect to $\hat{H}'$ with a search algorithm, which optimizes $\lambda$ to find the minimum of the projected energy.

## 4.4. Outline of an AVAP-HF Calculation

In this section, we give an example how the different parts discussed in the preceding section fit together. We want to calculate the ground state of $^{20}$Ne. Since we know that $^{20}$Ne has a prolate deformation, we start with this initialization and fill the shells with 10 neutrons and 10 protons. In the case of $^{20}$Ne, the choice of the initialization does not affect the ground state, as it does not lie at a sub-shell closure and it has no local energy-minimum with oblate deformation (cf. chapter 5.3). As we expect the unconstrained ($\lambda = 0$) result to give a good approximation of $E_{\text{proj}}$, we use $\lambda = 0$ for the first HF minimization. After the HF minimization, we carry out the angular-momentum projection. We then carry out additional HF calculations (minimization with successive angular-momentum projection) for modified values of $\lambda$ (e.g. $\lambda_{\text{new}} = \lambda_{\text{old}} \pm 10$). As soon as we have a set of three projected HF energies $E_{\text{proj}}(\lambda)$ where the one with intermediate $\lambda$ has the lowest projected HF energy, we start a bisection search to determine the minimum of the projected energy $E_{\text{proj}}(\lambda)$. A minimum is considered to be found, when the deformation parameters $\beta$ of the current minimum, $\beta_0$, and of the two neighboring HF solutions, $\beta_-$ and $\beta_+$, (one with smaller $\lambda$ and one with larger $\lambda$) lie all within a certain range (we use $\max(|\beta_0 - \beta_-|, |\beta_0 - \beta_+|) < 0.002$).

# 5. Results for Hartree-Fock

In this chapter, we present results obtained with the deformed Hartree-Fock method with angular-momentum projection. We start by comparing our results to those obtained by other authors with the same method. Next, we look at ground-state parameters and the effect of the angular-momentum projection. After studying the ground-state densities of deformed nuclei, we conclude the chapter with a short section on rotational bands.

## 5.1. Comparison to Published Results

We check the implementation by using the same interactions and basis parameters as in results published by a number of other authors. Since it is not possible to exactly reproduce the conditions under which the published results were obtained, a full agreement of the results is unlikely, but we expect an agreement within about $1\,\mathrm{MeV}$.

### 5.1.1. Comparison with the Brink B1 Force

To check the implementation of the angular momentum projection, we carry out calculations with the Brink B1 force and compare our results to those of H.A.Lamme and E.Boeker [LB68]. Since this interaction is independent of the type of nucleon and only time-reversal invariant systems are considered, the basis size can be reduced by a factor of 4, if each state can be occupied by up to four nucleons. A complete agreement between the results is not to be expected due to the different calculation bases. Lamme and Boeker used a Cartesian Harmonic Oscillator basis with a total of 12 HO states, making up 3 HF states, with 4 HO states each. For a charge dependent Hamiltonian with no restriction on time-reversal invariant systems, this corresponds to a basis size of 48 states. The $e_{\max} \geq 2n + l$ truncation used in this work leads to 40 ($e_{\max} = 2$), 80 ($e_{\max} = 3$) and 140 ($e_{\max} = 4$) spherical HO states, which roughly correspond to the basis size used by Lamme and Boeker. Table 5.1 shows the intrinsic HF ground-state energy $E_{\mathrm{HF}}$, the angular-momentum projected ground-state energy $E^0$ and the energy of rotational states with $J = 2$ and $J = 4$ ($E^2$ and $E^4$). We also give the energy differences $\delta E_{\mathrm{HF}} = E_{\mathrm{HF}} - E^0$ and $\delta E^J = E^J - E^0$. As shown in table 5.1, the results agree very well for eMax = 3, within less than $0.6\,\mathrm{MeV}$. Since the basis used by Lamme and Boeker was designed to calculate deformed nuclei in a small basis, it is not surprising that a larger spherical HO basis is needed to reproduce their results. Therefore, we assume that the implementation of the exact angular-momentum projection is correct.

| Nucleus | $e_{\max}$ | $E_{\mathrm{HF}}$ | $E^0$ | $\delta E_{\mathrm{HF}}$ | $E^2$ | $\delta E^2$ | $E^4$ | $\delta E^4$ |
|---|---|---|---|---|---|---|---|---|
| $^8\mathrm{Be}^a$ | | -44.57 | -51.07 | 6.50 | -48.16 | 2.91 | -40.62 | 10.45 |
| $^8\mathrm{Be}$ | 2 | -40.56 | -46.51 | 5.95 | -43.44 | 3.07 | -34.91 | 11.60 |
| $^8\mathrm{Be}$ | 3 | -44.53 | -51.50 | 6.96 | -48.56 | 2.94 | -40.64 | 10.86 |
| $^8\mathrm{Be}$ | 4 | -45.34 | -52.47 | 7.14 | -49.55 | 2.92 | -41.73 | 10.74 |
| $^{12}\mathrm{C}^a$ | | -67.92 | -73.01 | 5.09 | -70.53 | 2.48 | -63.36 | 9.65 |
| $^{12}\mathrm{C}$ | 2 | -64.18 | -68.85 | 4.67 | -66.15 | 2.70 | -58.63 | 10.22 |
| $^{12}\mathrm{C}$ | 3 | -68.43 | -73.57 | 5.13 | -71.06 | 2.50 | -63.85 | 9.72 |
| $^{12}\mathrm{C}$ | 4 | -69.12 | -74.31 | 5.19 | -71.80 | 2.51 | -64.53 | 9.78 |

$^a$ from [LB68]

Table 5.1.: Angular momentum projected energies ($J = 0, 2, 4$) of the intrinsic HF ground state (in MeV) for the Brink B1 interaction, compared to results by H.A.Lamme and E.Boeker.

## 5.1.2. Comparison with the Gogny D1S Force

To further check the implementation, we carry out calculations with the Gogny D1S force and compare our results with those from the AMEDEE database [HG07] and other published data. Compared to the Brink B1 force, the Gogny D1S force has the benefit of including a density-dependent term. The density-dependent term can be implemented in the same way as the three-body contact-interaction used for the S-SRG$_{3b}$ and S-UCOM(SRG)$_{3b}$ interactions, which allows us to check this part of our code. However, as this force is used for Hartree-Fock-Bogolyubov (HFB) calculations, i.e. including pairing correlations, a comparison is only possible in cases, where the pairing energy is small or vanishes. This is the case for some ground-states of deformed $sd$-shell nuclei, but not for the whole $E(\beta)$ curve. Therefore, only the minima of the curves are considered. Even though $^{24}\mathrm{Mg}$ is expected to have a triaxial deformation, it is included here because there is data available for the axial-symmetric approximation. The calculations for the AMEDEE database have been carried out with a basis size of at least 8 times the number of occupied states. The basis is truncated with respect to the principle oscillator quantum number ($e_{\max}$), with $e_{\max} = 4$ for $^{12}\mathrm{C}$ and $^{16}\mathrm{O}$, and $e_{\max} = 6$ for $^{20}\mathrm{Ne}$, $^{24}\mathrm{Mg}$, $^{28}\mathrm{Si}$, $^{32}\mathrm{S}$ and $^{40}\mathrm{Ca}$. This basis size is by far insufficient for converged ground-state energies. Convergence at the level of $1\,\mathrm{MeV}$ requires at least a basis size of $e_{\max} = 10$.[1]

Our results and the corresponding values from the database are presented in table 5.2. Since some approximations have been used in determining the oscillator length in the calculations for AMEDEE, our results for at least two values of the oscillator length are shown, the optimal value for $a_{\mathrm{HO}}$ and the values best reproducing the values from the database. For the results from the AMEDEE database, we show the HFB ground-state energy $E_{\mathrm{HFB}}$, the pairing energy $E_{\mathrm{pair}}$ and the proton and neutron quadrupole

---

[1]For $^{28}\mathrm{Si}$, the HF ground-state energies are $E = -232.725\,\mathrm{MeV}$ at $e_{\max} = 8$, $E = -233.246\,\mathrm{MeV}$ at $e_{\max} = 10$ and $E = -233.304\,\mathrm{MeV}$ at $e_{\max} = 14$.

moments $Q_n$ and $Q_p$. For our results, we show the HF ground-state energy $E_{\mathrm{HF}}$, the proton and neutron quadrupole moments $Q_n$ and $Q_p$, and the oscillator length $a_{\mathrm{HO}}$. Our results are in very good agreement with the database, if a sub-optimal value for $a_{\mathrm{HO}}$ is used. The only case that can not be well reproduced is that of $^{32}$S. However, as the additionally listed values for $^{32}$S from the database show, the minimum is very flat and broad. Taking into account the non-vanishing pairing-energy for $^{32}$S, this might well account for the discrepancy. Nevertheless, if we consider our optimal oscillator lengths, the quadrupole moments differ considerably.

According to the database, two of the nuclei we study in this work ($^{20}$Ne and $^{32}$S) have a non-zero pairing-energy. For these nuclei, we also included the intrinsic ground-state energy of the AVAP minimum and the corresponding values from the database. This shows, that the pairing energy for the AVAP minimum vanishes. For the other nuclei studied in this work, $^{12}$C and $^{28}$Si, the region of zero pairing-energy is given by $Q < -6\,\mathrm{fm}^2$ and $Q < -28\,\mathrm{fm}^2$, respectively. Since the projection increases the absolute value of the deformation parameter (or quadrupole moments), it is save to assume that pairing will not play a role for these nuclei either. Therefore, the pure HF treatment is sufficient. We assume that this also holds for the realistic interactions used later on. However, as results by Rodríguez [RE10] show, this only holds on the pure HF/HFB level. For $^{24}$Mg (and probably other nuclei as well), the pairing energy does not vanish in a *variation after particle-number projection* approach.

A this point, a statement regarding the harmonic oscillator basis is necessary. For the AMEDEE database, a deformed HO basis is used, which has a different value of $a_{\mathrm{HO}}$ in each direction. This is a common choice, since the number of required oscillator shells should be lower than in a spherical basis. However, all oscillator lengths have to be determined separately for each nucleus, which is a time consuming process. Therefore, the AMEDEE database employs approximations, which have a negative impact on the obtained results, as can be seen in table 5.2. In this work, a spherical HO (SHO) basis is used, which is done for two reasons. First, determining the best relation of the different values of the oscillator length is either too time consuming, or too inaccurate. Second, a very efficient storage and retrieval system for matrix elements in the SHO basis was developed by A. Calci, J. Langhammer and R. Roth and has been integrated into the code used for this work. This scheme allows fast access to precomputed matrix elements, which enables us to carry out all Brink B1 and Gogny D1S calculations used in this section in about a day on a single office computer.[2]

Returning to the quadrupole moments, table 5.2 shows, that our calculations consistently predict a lower deformation than those published in the database. Since our results also have a lower binding energy and we can reproduce the more deformed results by increasing $a_{\mathrm{HO}}$, we conclude that our results are more accurate and that the values published in the database overestimate the deformation, most likely due to an unreliable estimate of the oscillator parameters (see also table 5.8). This also leads to the conclusion, that there are no sizable negative effects due to the SHO basis. As stated in the next section, we use a much larger basis for our actual results, which

---

[2]Intel Core2 Quad, 2.83GHz

| Nucleus | $E_{\text{exp}}$ | AMEDEE database [HG07] | | | | this work | | | |
|---|---|---|---|---|---|---|---|---|---|
| | | $E_{\text{HFB}}$ | $E_{\text{pair}}$ | $Q_p$ | $Q_n$ | $E_{\text{HF}}$ | $Q_p$ | $Q_n$ | $a_{\text{HO}}$ |
| $^{12}$C | $-92.16$ | $-87.54$ | 0 | $-13.9$ | $-13.6$ | $-87.66$ | $-10.1$ | $-10.1$ | 1.6 |
| | | | | | | $-87.56$ | $-11.9$ | $-11.9$ | 1.7 |
| | | | | | | $-87.21$ | $-14.4$ | $-14.4$ | 1.8 |
| $^{16}$O | $-127.62$ | $-128.00$ | 0 | 0 | 0 | $-128.20$ | 0.0 | 0.0 | 1.8 |
| | | | | | | $-127.62$ | 0.0 | 0.0 | 2.0 |
| $^{20}$Ne | $-160.64$ | $-155.96$ | 3.4 | 40.7 | 39.6 | $-156.23$ | 26.8 | 26.5 | 1.7 |
| | | | | | | $-156.07$ | 41.4 | 41.0 | 2.2 |
| | | $-155.65$ | 0 | 53.0 | 51.5 | $-155.10^a$ | 50.8 | 50.2 | 2.2 |
| $^{24}$Mg | $-198.26$ | $-193.19$ | 0 | 60.6 | 59.2 | $-193.68$ | 38.0 | 37.8 | 1.7 |
| | | | | | | $-193.61$ | 54.2 | 54.2 | 2.0 |
| | | | | | | $-193.14$ | 67.0 | 67.0 | 2.2 |
| $^{28}$Si | $-236.54$ | $-231.47$ | 0 | $-49.9$ | $-48.6$ | $-231.97$ | $-32.8$ | $-32.5$ | 1.7 |
| | | | | | | $-231.39$ | $-51.1$ | $-50.8$ | 2.2 |
| $^{32}$S | $-271.78$ | $-266.27$ | 4.5 | $-9.0$ | $-8.6$ | $-266.25$ | 21.4 | 20.7 | 2.0 |
| | | $-266.26$ | 4.5 | 17.9 | 17.2 | $-266.46$ | 21.6 | 20.9 | 2.2 |
| | | $-266.27$ | 0.8 | 35.8 | 34.5 | $-263.64$ | 28.9 | 28.1 | 2.4 |
| | | $-265.94$ | 0 | 44.8 | 43.1 | $-265.36^a$ | 39.4 | 38.5 | 2.2 |
| | | $-265.68$ | 0 | 53.7 | 51.8 | | | | |
| $^{40}$Ca | $-342.05$ | $-342.69$ | 0 | 0 | 0 | $-343.01$ | 0.0 | 0.0 | 1.8 |
| | | | | | | $-342.71$ | 0.0 | 0.0 | 1.9 |

$^a$ projected minumum

Table 5.2.: Unprojected HF ground state energies (all energies in MeV) and quadrupole moments (in fm$^2$) for the Gogny D1S interaction ($a_{\text{HO}}$ in fm, only applies to results from this work). Measured values from [AWT03].

further reduces any negative effects the SHO basis might have.

Unfortunately, data for angular-momentum projected ground-state energies is hard to obtain. Although these calculations are carried out and published quite frequently, authors often do not give absolute values for projected ground-state energies, but only excitation energies of rotational states (e.g. [RGER02, RE10, ER04]).[3] However, Tomás Rodríguez provided us with raw data related to his paper [RE10]. We compare his results to our calculations in table 5.3. All results are obtained with an oscillator length of $a_{\mathrm{HO}} = 1.7\,\mathrm{fm}$ and a basis truncation of $e_{\mathrm{max}} = 6$. The results agree within less than $1\,\mathrm{MeV}$. As there is a great number of details in the implementation which can affect the results, like the treatment of the kinetic energy or the evaluation of wave functions on a spatial grid, this is a reasonable agreement.

This concludes the comparison to published data and validates the implementation. The agreement is in general very good, so we conclude that our code is correct. We go on by presenting the results obtained with realistic interactions. However, at some points, we also include data fro the Gogny D1S interaction for comparison.

| Nucleus | $E_{\mathrm{exp}}$ | Rodríguez [Rod12] | | this work | |
| | | $E_{\mathrm{proj}}$ | $E_{\mathrm{HF}}$ | $E_{\mathrm{proj}}$ | $E_{\mathrm{HF}}$ |
|---|---|---|---|---|---|
| $^{24}\mathrm{Mg}$ | -198.26 | -197.10 | -193.79 | -197.37 | -193.08 |

Table 5.3.: Angular-momentum projected and intrinsic HF ground state energies (in MeV) of $^{24}\mathrm{Mg}$ for the Gogny D1S interaction.

## 5.2. Ground-State Properties

The optimal angular-momentum projected HF ground-states, which are also used for the RPA calculations, are found via an *approximative variation after projection* (AVAP) based on constrained HF (cf. chapter 4.3). Calculations are carried out for all relevant values of $a_{\mathrm{HO}}$ to determine the optimal value. However, due to the availability of matrix elements, $a_{\mathrm{HO}} = 1.6\,\mathrm{fm}$ was the smallest possible value with any relevance.

The AVAP method is compared to the *projection after variation* (PAV) approach, where the angular momentum-projection is applied to the HF state which minimizes the intrinsic ground-state energy. If not stated otherwise, the AVAP method is used.

To assess the convergence of the HF calculations, both, the ground-state energies $E_{\mathrm{proj}}$ and the deformation parameter $\beta$ are examined. Since HF is self-consistent and variational, the most important convergence measure is the ground-state energy. The state with the lowest ground-state energy generally provides the best approximation.

---

[3]This might be related to the fact, that the Gogny D1S force leads to an overbinding of a few MeV, if pairing, triaxial deformation and angular-momentum projection are included (data from [Rod12]).

| nucleus | eMax | $a_{\mathrm{HO}} = 1.6\,\mathrm{fm}$ | | $a_{\mathrm{HO}} = 1.7\,\mathrm{fm}$ | |
|---|---|---|---|---|---|
| | | $E_{\mathrm{proj}}$ | $\delta E$ | $E_{\mathrm{proj}}$ | $\delta E$ |
| $^{16}\mathrm{O}$ | 10 | $-56.299$ | 0.000 | $-56.277$ | 0.000 |
| | 12 | $-56.334$ | 0.000 | $-56.321$ | 0.000 |
| | 14 | $-56.345$ | 0.000 | $-56.339$ | 0.000 |
| $^{20}\mathrm{Ne}$ | 10 | $-69.564$ | 5.851 | $-69.511$ | 5.775 |
| | 12 | $-69.585$ | 5.777 | $-69.555$ | 5.713 |
| | 14 | $-69.583$ | 5.737 | $-69.565$ | 5.683 |
| $^{28}\mathrm{Si}_o$ | 10 | $-103.050$ | 6.274 | $-103.017$ | 6.194 |
| | 12 | $-103.113$ | 6.199 | $-103.099$ | 6.192 |
| | 14 | $-103.139$ | 6.193 | $-103.128$ | 6.208 |
| $^{40}\mathrm{Ca}$ | 10 | $-171.966$ | 0.000 | $-171.976$ | 0.000 |
| | 12 | $-172.026$ | 0.000 | $-172.034$ | 0.000 |
| | 14 | $-172.057$ | 0.000 | $-172.052$ | 0.000 |

Table 5.4.: Convergence of AMP HF ground-state energy $E_{\mathrm{proj}}$ for the UCOM(VAR)$_{2b}$ interaction, including the difference to the intrinsic HF ground state energy $\delta E = E_{\mathrm{HF}} - E_{\mathrm{proj}}$. All energies in MeV.

But since the deformation depends much stronger on the oscillator length $a_{\mathrm{HO}}$ than the energy, looking at deformation parameters provides additional information.

## 5.2.1. Convergence of the Ground-State Energy

In tables 5.4 and 5.5, we study the convergence of the ground-state energy with respect to the basis truncation $e_{\mathrm{max}}$. We examine only four nuclei, $^{16}\mathrm{O}$, $^{20}\mathrm{Ne}$, $^{28}\mathrm{Si}$ and $^{40}\mathrm{Ca}$, and only for the UCOM(VAR)$_{2b}$ and S-SRG$_{3b}$ interactions (cf. chapter 2.2.5). For the S-SRG$_{3b}$ and S-UCOM(SRG)$_{3b}$ interactions, $^{28}\mathrm{Si}$ has two degenerate states, one with oblate deformation and one with prolate deformation (cf. section 5.3). These states are denoted by $^{28}\mathrm{Si}_o$ and $^{28}\mathrm{Si}_p$. In this section, we only consider the oblate state $^{28}\mathrm{Si}_o$. As we see later, both SRG based interactions, S-SRG$_{3b}$ and S-UCOM(SRG)$_{3b}$ give very similar results and there is no reason why their convergence behavior should be any different. Doing a full convergence study of all nuclei with all interactions would consume too much computation time, without adding any relevant information. The two spherical nuclei are used to measure the effect of the number of occupied states with respect to basis truncation. The deformed nuclei $^{20}\mathrm{Ne}$ and $^{28}\mathrm{Si}_o$ are included to see whether the convergence behavior of prolate or oblate deformed nuclei is fundamentally different from that of spherical nuclei.

The calculations for all nuclei converge equally well. As can be seen, the ground-state energy is already well converged at $e_{\mathrm{max}} = 12$, but since we expect a better

| nucleus | eMax | $a_{\mathrm{HO}} = 1.6\,\mathrm{fm}$ | | $a_{\mathrm{HO}} = 1.7\,\mathrm{fm}$ | | $a_{\mathrm{HO}} = 1.8\,\mathrm{fm}$ | |
|---|---|---|---|---|---|---|---|
| | | $E_{\mathrm{proj}}$ | $\delta E$ | $E_{\mathrm{proj}}$ | $\delta E$ | $E_{\mathrm{proj}}$ | $\delta E$ |
| $^{16}$O | 10 | $-65.658$ | 0.000 | $-65.662$ | 0.000 | | |
| | 12 | $-65.665$ | 0.000 | $-65.669$ | 0.000 | | |
| | 14 | $-65.689$ | 0.000 | $-65.686$ | 0.000 | | |
| $^{20}$Ne | 10 | $-81.032$ | 4.970 | $-81.062$ | 4.880 | | |
| | 12 | $-81.131$ | 4.908 | $-81.126$ | 4.860 | | |
| | 14 | $-81.148$ | 4.858 | $-81.138$ | 4.815 | | |
| $^{28}$Si$_o$ | 10 | $-115.977$ | 4.979 | $-116.097$ | 4.973 | | |
| | 12 | $-116.167$ | 4.988 | $-116.184$ | 4.934 | | |
| | 14 | $-116.202$ | 4.931 | $-116.212$ | 4.926 | | |
| $^{40}$Ca | 10 | $-180.939$ | 0.000 | $-181.130$ | 0.000 | $-181.154$ | 0.000 |
| | 12 | $-181.162$ | 0.000 | $-181.205$ | 0.000 | $-181.205$ | 0.000 |
| | 14 | $-181.202$ | 0.000 | $-181.232$ | 0.000 | $-181.243$ | 0.000 |

Table 5.5.: Convergence of AMP HF ground-state energy $E_{\mathrm{proj}}$ for the S-SRG$_{3b}$ interaction, including the difference to the intrinsic HF ground state energy $\delta E = E_{\mathrm{HF}} - E_{\mathrm{proj}}$. All energies in MeV.

convergence of the wave functions at $e_{\mathrm{max}} = 14$, we use that value for the RPA calculations (note that we always truncate the $l$ quantum number at $l \leq 10$). For the $E(\beta)$ plots in the next section, we only use $e_{\mathrm{max}} = 10$. The calculations for these plots are time consuming and we only aim at an accuracy of about $1\,\mathrm{MeV}$, so there is no benefit in using a larger basis. In the case of $^{20}$Ne with $a_{\mathrm{HO}} = 1.6\,\mathrm{fm}$, the projected ground-state energy for $e_{\mathrm{max}} = 12$ is $2\,\mathrm{keV}$ lower than for $e_{\mathrm{max}} = 14$, but as we can see from $\delta E$, this is not true for the intrinsic ground-state energy. This is most likely an effect of the AVAP minimization, which is only accurate up to a few keV. We can also see that the energy difference from one $a_{\mathrm{HO}}$ to the next is very small. This does not pose a problem for the spherical nuclei $^{16}$O and $^{40}$Ca, but for deformed nuclei, we need to take a closer look at the deformation parameter.

## 5.2.2. Ground-State Deformation

Table 5.6 shows the deformation parameters for the ground states corresponding to different oscillator lengths. We see that although the energy difference is very small, the deformation parameter differs by up to 10% for the two oscillator lengths (excluding $^{12}$C).

The same effect can also be seen for the Gogny D1S force in table 5.2. In principle, a search algorithm for the optimal oscillator length could give a more accurate estimate of the deformation parameter. However, the possible values of $a_{\mathrm{HO}}$ are lim-

| | | $a_{\mathrm{HO}} = 1.6\,\mathrm{fm}$ | | $a_{\mathrm{HO}} = 1.7\,\mathrm{fm}$ | | $a_{\mathrm{HO}} = 1.8\,\mathrm{fm}$ | |
|---|---|---|---|---|---|---|---|
| interaction | nucleus | $E_{\mathrm{proj}}$ | $\beta$ | $E_{\mathrm{proj}}$ | $\beta$ | $E_{\mathrm{proj}}$ | $\beta$ |
| UCOM(VAR)$_{2b}$ | $^{12}$C | $-35.945$ | $-0.80$ | $-35.938$ | $-1.00$ | | |
| | $^{20}$Ne | $-69.583$ | $+0.50$ | $-69.565$ | $+0.54$ | | |
| | $^{28}$Si$_o$ | $-103.139$ | $-0.46$ | $-103.128$ | $-0.52$ | | |
| | $^{28}$Si$_p$ | $-101.150$ | $+0.61$ | $-101.136$ | $+0.70$ | | |
| | $^{32}$S | $-114.457$ | $+0.34$ | $-114.441$ | $+0.38$ | | |
| S-SRG$_{3b}$ | $^{12}$C | $-44.837$ | $-0.55$ | $-44.828$ | $-0.64$ | | |
| | $^{20}$Ne | $-81.148$ | $+0.46$ | $-81.138$ | $+0.48$ | | |
| | $^{28}$Si$_o$ | $-116.202$ | $-0.38$ | $-116.212$ | $-0.40$ | | |
| | $^{28}$Si$_p$ | $-115.964$ | $+0.49$ | $-115.972$ | $+0.53$ | | |
| | $^{32}$S | $-129.774$ | $+0.29$ | $-129.790$ | $+0.30$ | $-129.789$ | $+0.32$ |
| S-UCOM(SRG)$_{3b}$ | $^{12}$C | $-49.515$ | $-0.53$ | $-49.508$ | $-0.61$ | | |
| | $^{20}$Ne | $-90.914$ | $+0.46$ | $-90.907$ | $+0.47$ | | |
| | $^{28}$Si$_o$ | $-131.333$ | $-0.37$ | $-131.344$ | $-0.39$ | $-131.341$ | $-0.42$ |
| | $^{28}$Si$_p$ | $-131.344$ | $+0.48$ | $-131.353$ | $+0.51$ | $-131.349$ | $+0.55$ |
| | $^{32}$S | $-147.937$ | $+0.29$ | $-147.953$ | $+0.30$ | $-147.954$ | $+0.32$ |

Table 5.6.: AMP HF ground-state energies (in MeV) and deformation parameters for all interactions.

ited by the availability of matrix elements. Currently, only matrix elements for the oscillator lengths $a_{\mathrm{HO}} = (1.3, 1.6, 1.7, 1.8, 1.9, 2.0, 2.1, 2.2, 2.4)\,\mathrm{fm}$ are available. From these values, only 1.6 fm, 1.7 fm, 1.8 fm and 1.9 fm are relevant for the nuclei studied in this work. Therefore, we use the different values of $\beta$ to give an error estimate for the ground-state deformation. As already discussed in section 5.1.2, it is unlikely that a deformed oscillator basis would improve the situation. Table 5.7 shows the optimal values for $a_{\mathrm{HO}}$ and the values used to determine the error-bounds for the quadrupole moments and the deformation parameter.

**Comparison to Experiment**

Table 5.8, compares the intrinsic proton quadrupole moment, which is related to the deformation parameter (see eq. (3.1)), to published experimental data [Sto05]. Since the intrinsic quadrupole moment can not be measured directly, it has to be derived from the spectroscopic quadrupole moment and, therefore, is model-dependent. Moreover, depending on the experimental technique, the spectroscopic quadrupole moment is also a model-dependent quantity. As the theoretical models used for nuclear physics experiments are usually very simple and crude, we choose a similar approach to determine the intrinsic quadrupole moment from the spectroscopic quadrupole moment. For a rotating spheroid, the relation between the intrinsic quadrupole moment $Q$ and

| nucleus | UCOM(VAR)$_{2b}$ | | S-SRG$_{3b}$ | | S-UCOM(SRG)$_{3b}$ | |
|---|---|---|---|---|---|---|
| | $a_{\text{HO}}$ | $a_{\text{HO}}^{\text{err}}$ | $a_{\text{HO}}$ | $a_{\text{HO}}^{\text{err}}$ | $a_{\text{HO}}$ | $a_{\text{HO}}^{\text{err}}$ |
| $^{12}$C | 1.6 | 1.7 | 1.6 | 1.7 | 1.6 | 1.7 |
| $^{16}$O | 1.6 | | 1.6 | | 1.6 | |
| $^{20}$Ne | 1.6 | 1.7 | 1.6 | 1.7 | 1.6 | 1.7 |
| $^{28}$Si$_o$ | 1.6 | 1.7 | 1.7 | 1.6 | 1.7 | 1.6 |
| $^{28}$Si$_p$ | 1.6 | 1.7 | 1.7 | 1.6 | 1.7 | 1.6 |
| $^{32}$S | 1.6 | 1.7 | 1.7 | 1.8 | 1.8 | 1.7 |
| $^{40}$Ca | 1.6 | | 1.8 | | 1.8 | |

Table 5.7.: Optimal oscillator lengths ($a_{\text{HO}}$) and oscillator length used for $\delta\beta$ estimate ($a_{\text{HO}}^{\text{err}}$) for all nuclei and interactions, given in fm.

the spectroscopic quadrupole moment $Q_{J^\pi}$ of an excited state $J^\pi$ is given by the relation

$$Q = \frac{(J+1)(2J+3)}{3K^2 - J(J+1)} Q_{J^\pi} \quad .\tag{5.1}$$

Since [Sto05] gives $Q_{2^+}$, the relation simplifies to

$$Q = -\frac{7}{2} Q_{J^\pi} \quad .\tag{5.2}$$

| nucleus | UCOM(VAR)$_{2b}$ | S-SRG$_{3b}$ | S-UCOM(SRG)$_{3b}$ | experiment |
|---|---|---|---|---|
| | $Q_p$ | $Q_p$ | $Q_p$ | $Q_p$ |
| $^{12}$C | $-19.83 \pm 4.79$ | $-17.55 \pm 2.65$ | $-17.27 \pm 2.27$ | $-21 \pm 11$ |
| $^{20}$Ne | $+26.16 \pm 1.76$ | $+31.41 \pm 0.90$ | $+31.68 \pm 0.89$ | $+81 \pm 11$[a] |
| $^{28}$Si$_o$ | $-37.47 \pm 4.84$ | $-43.87 \pm 2.19$ | $-44.23 \pm 2.16$ | $-56 \pm 11$ |
| $^{32}$S | $+32.18 \pm 3.91$ | $+39.04 \pm 2.48$ | $+41.23 \pm 2.34$ | $+52 \pm 14$ |

[a] see text

Table 5.8.: Comparison of intrinsic charge quadrupole moments (in fm$^2$) to experimental data [Sto05].

All calculated values except for $^{20}$Ne agree within the given error margins. Considering the original reference for $^{20}$Ne, [Spe81], the method of determining the error seems to be very optimistic. A value of about 30 might be a better choice.

## 5.2.3. Adopted HF Ground-States

In figures 5.1 and 5.2, the binding energies of $^{12}$C, $^{16}$O, $^{20}$Ne, $^{28}$Si (oblate and prolate, denoted as $^{28}$Si$_o$ and $^{28}$Si$_p$), $^{32}$S and $^{40}$Ca are plotted for the PAV and AVAP approach. There is a small difference between the plots, but it is very hard to spot. Therefore, we

conclude that the gain of the AVAP method compared to the simpler and much faster PAV method is negligible, if one is only interested in systematics of the ground-state energies. The most dominant feature is the difference of about 4–5 MeV between the measured binding energies and the values obtained by our calculations. This shift is due to correlations which are not included in the interactions and cannot be recovered by angular momentum projection. Since the interaction includes short-range correlations, the low binding energy is most likely caused by long-range correlations, which should depend on the nuclear deformation. As deformed shapes can be very different, long-range correlations could affect the systematics. All three interactions produce similar systematics, with the least binding energy for the $UCOM(VAR)_{2b}$ interaction and the strongest binding for the $S\text{-}UCOM(SRG)_{3b}$ interaction. The angular-momentum projection has a small positive effect on the systematics, as it recovers some of the correlations only present in deformed nuclei.

Figures 5.3 and 5.4 show the rms-charge-radii, again for the PAV and AVAP approach. Since the difference between projected and intrinsic radii is less than 1%, we only show the intrinsic radii. Again, the difference between the plots is rather small, but the AVAP approach produces consistently larger radii. As expected, the $UCOM(VAR)_{2b}$ interaction underestimates the radii considerably, while the $S\text{-}SRG_{3b}$ and $S\text{-}UCOM(SRG)_{3b}$ interactions reproduce the radii of spherical nuclei almost exactly. Except for a constant offset, all three interactions give similar systematics. While the radii of $^{20}$Ne and $^{32}$S are still described rather well, the results for $^{12}$C and $^{28}$Si are about 10% above the measured radii. However, at present, we cannot determine if this is a physical effect on oblate nuclei or just random fluctuation. Studying a larger number of nuclei may give additional information on this matter.

Figures 5.1 and 5.3 also include results for the phenomenological Gogny D1S force. The ground state binding energies are reproduced almost exactly, but the radii are described only slightly better than with the $S\text{-}SRG_{3b}$ or $S\text{-}UCOM(SRG)_{3b}$ interactions. As can be seen at the small effect of the angular momentum projection, the prolate initialization produces an almost spherical state for $^{28}$Si. The ground-state energy of the oblate state of $^{28}$Si agrees better with the measured value, however, the prolate state gives a better reproduction of the radius.

The ground-state properties for well-converged calculations in a large model-space ($e_{\max} = 14$, $l_{\max} = 10$) are given in table 5.9. The results are given for the optimal oscillator length (see table 5.7).
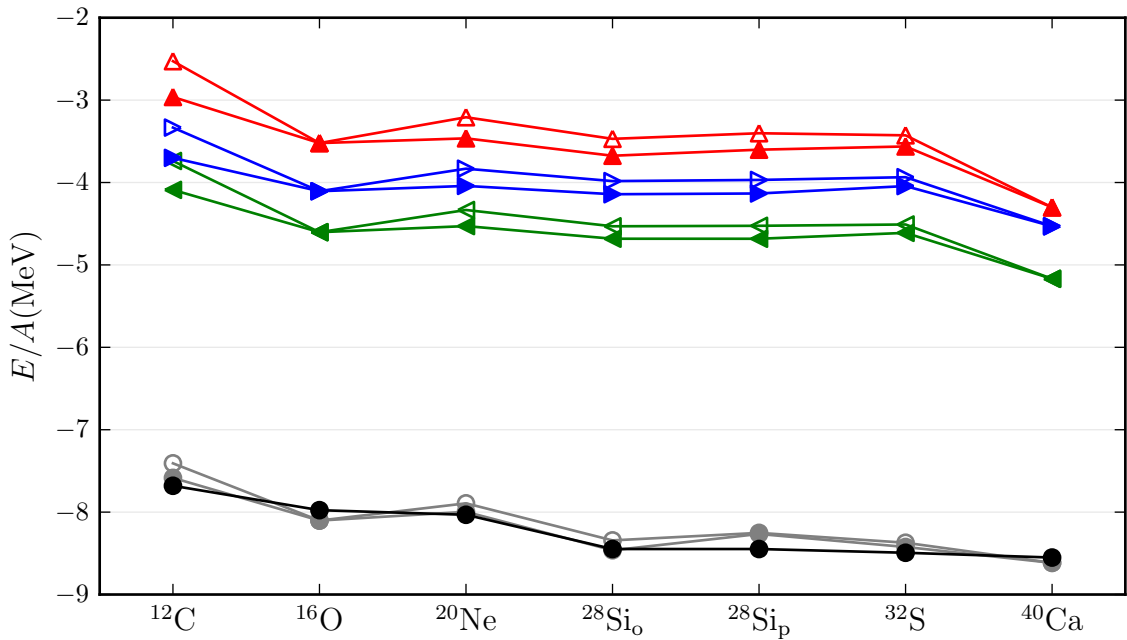
Figure 5.1.: Intrinsic (open symbols) and projected (filled symbols) ground-state energies using the PAV approach for the UCOM(VAR)$_{2b}$ (▲), S-SRG$_{3b}$ (▶) and S-UCOM(SRG)$_{3b}$ (◀) interactions, the phenomenological Gogny D1S interaction (●) and experimental ground-state energy (●) [AWT03].
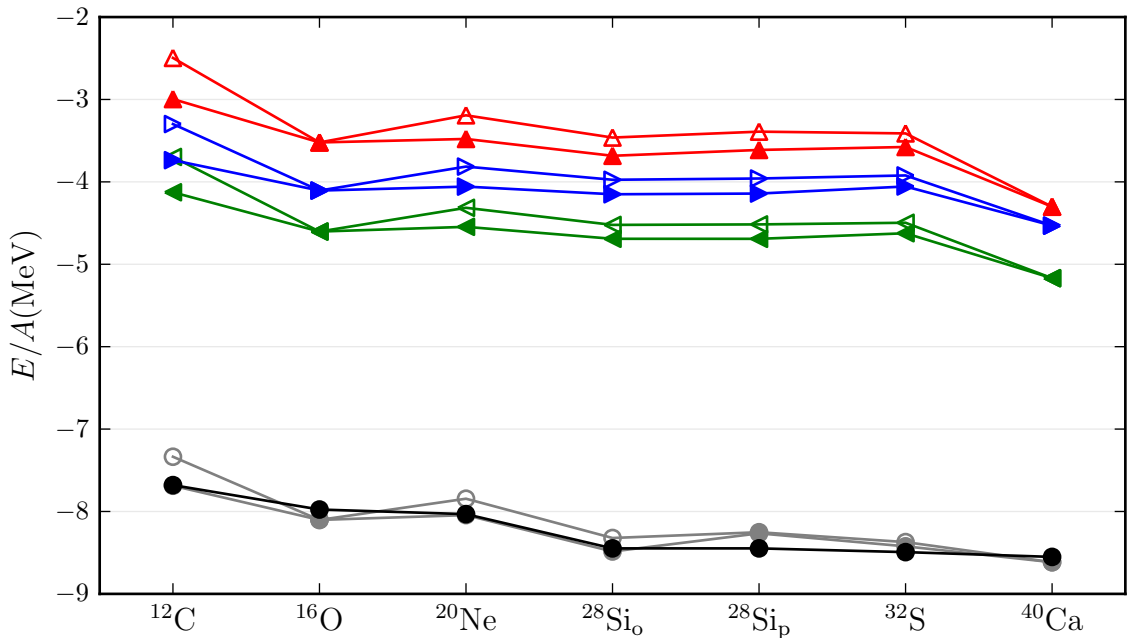


Figure 5.2.: Intrinsic (open symbols) and projected (filled symbols) ground-state energies using the AVAP approach for the UCOM(VAR)$_{2b}$ (▲), S-SRG$_{3b}$ (▶) and S-UCOM(SRG)$_{3b}$ (◀) interactions and experimental ground-state energy (●) [AWT03].
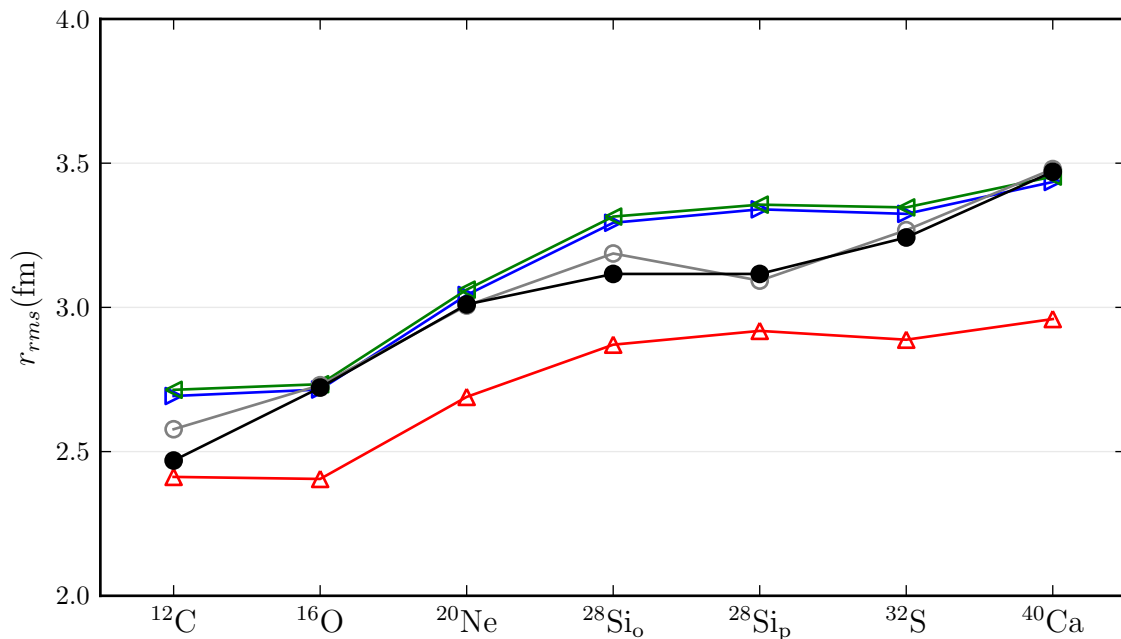
Figure 5.3.: Intrinsic rms-charge-radii using the PAV approach for the $UCOM(VAR)_{2b}$ (△), $S\text{-}SRG_{3b}$ (▶) and $S\text{-}UCOM(SRG)_{3b}$ (◀) interactions, the phenomenological Gogny D1S interaction (⊖) and experimental charge-radii (●) [VJV87, FHH$^+$92].
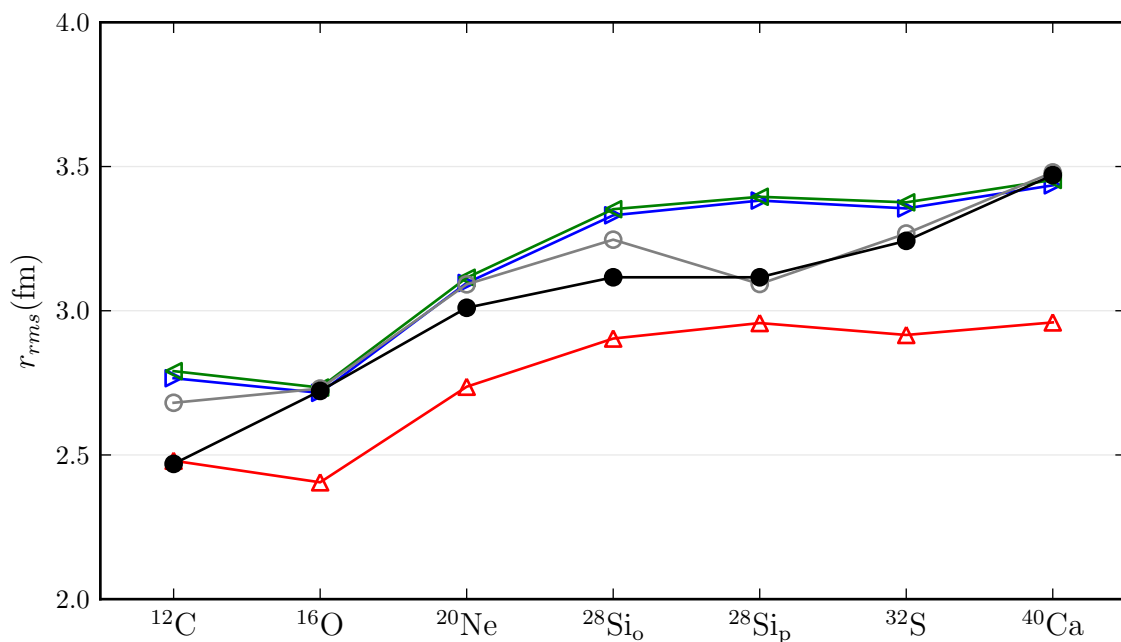


Figure 5.4.: Intrinsic rms-charge-radii using the AVAP approach for the $UCOM(VAR)_{2b}$ (△), $S\text{-}SRG_{3b}$ (▶) and $S\text{-}UCOM(SRG)_{3b}$ (◀) interactions and experimental charge-radii (●) [VJV87, FHH$^+$92].

| nucleus | interaction | min | $E_{\mathrm{int}}$ | $E_{\mathrm{proj}}$ | $\beta$ | $r_{\mathrm{rms}}$ | $Q_p$ | $Q_n$ |
|---|---|---|---|---|---|---|---|---|
| $^{12}$C | UCOM(VAR)$_{2b}$ | PAV | $-30.3320$ | $-35.5452$ | $-0.809 \pm 0.213$ | $2.269 \pm 0.000$ | $-18.85 \pm 4.92$ | $-18.98 \pm 5.04$ |
| | | AVP | $-29.9485$ | $-35.9453$ | $-0.799 \pm 0.197$ | $2.339 \pm 0.002$ | $-19.83 \pm 4.79$ | $-19.88 \pm 4.91$ |
| | S-SRG$_{3b}$ | PAV | $-40.0008$ | $-44.4091$ | $-0.529 \pm 0.088$ | $2.563 \pm 0.001$ | $-15.82 \pm 2.59$ | $-15.78 \pm 2.66$ |
| | | AVP | $-39.5782$ | $-44.8369$ | $-0.553 \pm 0.084$ | $2.638 \pm 0.002$ | $-17.55 \pm 2.65$ | $-17.43 \pm 2.71$ |
| | S-UCOM(SRG)$_{3b}$ | PAV | $-44.8636$ | $-49.0723$ | $-0.505 \pm 0.078$ | $2.586 \pm 0.001$ | $-15.37 \pm 2.34$ | $-15.33 \pm 2.40$ |
| | | AVP | $-44.3705$ | $-49.5150$ | $-0.534 \pm 0.074$ | $2.664 \pm 0.005$ | $-17.27 \pm 2.27$ | $-17.15 \pm 2.34$ |
| $^{20}$Ne | UCOM(VAR)$_{2b}$ | PAV | $-64.1585$ | $-69.2822$ | $+0.473 \pm 0.039$ | $2.554 \pm 0.001$ | $+23.60 \pm 1.92$ | $+23.08 \pm 1.96$ |
| | | AVP | $-63.8462$ | $-69.5835$ | $+0.503 \pm 0.035$ | $2.602 \pm 0.002$ | $+26.16 \pm 1.76$ | $+25.41 \pm 1.79$ |
| | S-SRG$_{3b}$ | PAV | $-76.6441$ | $-80.8238$ | $+0.420 \pm 0.015$ | $2.922 \pm 0.002$ | $+27.48 \pm 0.97$ | $+26.81 \pm 0.98$ |
| | | AVP | $-76.2906$ | $-81.1484$ | $+0.462 \pm 0.013$ | $2.975 \pm 0.000$ | $+31.41 \pm 0.90$ | $+30.51 \pm 0.89$ |
| | S-UCOM(SRG)$_{3b}$ | PAV | $-86.6683$ | $-90.5755$ | $+0.417 \pm 0.014$ | $2.941 \pm 0.001$ | $+27.61 \pm 0.94$ | $+26.95 \pm 0.95$ |
| | | AVP | $-86.2917$ | $-90.9138$ | $+0.460 \pm 0.013$ | $2.994 \pm 0.000$ | $+31.68 \pm 0.89$ | $+30.78 \pm 0.88$ |

Table 5.9.: Ground-state energies, deformation parameters, rms-radii and quadrupole moments for PAV and AVAP HF minima. Energies in MeV, radii in fm and quadrupole moments in fm$^2$.

| nucleus | interaction | min | $E_{\mathrm{int}}$ | $E_{\mathrm{proj}}$ | $\beta$ | $r_{\mathrm{rms}}$ | $Q_p$ | $Q_n$ |
|---|---|---|---|---|---|---|---|---|
| $^{28}\mathrm{Si}_o$ | UCOM(VAR)$_{2b}$ | PAV | $-97.1630$ | $-102.9042$ | $-0.444 \pm 0.059$ | $2.740 \pm 0.001$ | $-35.54 \pm 4.64$ | $-35.02 \pm 4.78$ |
| | | AVP | $-96.9452$ | $-103.1387$ | $-0.456 \pm 0.059$ | $2.773 \pm 0.002$ | $-37.47 \pm 4.84$ | $-36.81 \pm 4.97$ |
| | S-SRG$_{3b}$ | PAV | $-111.5168$ | $-115.9830$ | $-0.380 \pm 0.019$ | $3.175 \pm 0.002$ | $-41.00 \pm 2.04$ | $-40.15 \pm 2.09$ |
| | | AVP | $-111.2851$ | $-116.2116$ | $-0.396 \pm 0.020$ | $3.213 \pm 0.002$ | $-43.87 \pm 2.19$ | $-42.84 \pm 2.23$ |
| | S-UCOM(SRG)$_{3b}$ | PAV | $-126.8715$ | $-131.1031$ | $-0.377 \pm 0.019$ | $3.198 \pm 0.001$ | $-41.28 \pm 2.01$ | $-40.45 \pm 2.07$ |
| | | AVP | $-126.6191$ | $-131.3436$ | $-0.394 \pm 0.019$ | $3.235 \pm 0.002$ | $-44.23 \pm 2.16$ | $-43.22 \pm 2.20$ |
| $^{28}\mathrm{Si}_p$ | UCOM(VAR)$_{2b}$ | PAV | $-95.2581$ | $-100.8431$ | $+0.566 \pm 0.086$ | $2.790 \pm 0.001$ | $+46.85 \pm 6.97$ | $+46.51 \pm 7.22$ |
| | | AVP | $-94.9370$ | $-101.1500$ | $+0.606 \pm 0.090$ | $2.829 \pm 0.000$ | $+51.64 \pm 7.50$ | $+51.14 \pm 7.76$ |
| | S-SRG$_{3b}$ | PAV | $-111.1222$ | $-115.7283$ | $+0.488 \pm 0.030$ | $3.224 \pm 0.002$ | $+54.18 \pm 3.26$ | $+53.41 \pm 3.37$ |
| | | AVP | $-110.8561$ | $-115.9719$ | $+0.525 \pm 0.032$ | $3.267 \pm 0.002$ | $+59.86 \pm 3.66$ | $+58.92 \pm 3.77$ |
| | S-UCOM(SRG)$_{3b}$ | PAV | $-126.7081$ | $-131.1121$ | $+0.478 \pm 0.027$ | $3.241 \pm 0.001$ | $+53.59 \pm 3.04$ | $+52.83 \pm 3.14$ |
| | | AVP | $-126.4537$ | $-131.3533$ | $+0.513 \pm 0.030$ | $3.281 \pm 0.002$ | $+58.95 \pm 3.40$ | $+58.03 \pm 3.50$ |
| $^{32}\mathrm{S}$ | UCOM(VAR)$_{2b}$ | PAV | $-109.6767$ | $-113.9978$ | $+0.288 \pm 0.032$ | $2.756 \pm 0.001$ | $+26.73 \pm 2.97$ | $+26.29 \pm 3.01$ |
| | | AVP | $-109.1822$ | $-114.4566$ | $+0.339 \pm 0.042$ | $2.784 \pm 0.001$ | $+32.18 \pm 3.91$ | $+31.48 \pm 3.96$ |
| | S-SRG$_{3b}$ | PAV | $-125.9305$ | $-129.3837$ | $+0.260 \pm 0.015$ | $3.205 \pm 0.001$ | $+32.67 \pm 1.82$ | $+31.99 \pm 1.85$ |
| | | AVP | $-125.5041$ | $-129.7897$ | $+0.304 \pm 0.019$ | $3.236 \pm 0.001$ | $+39.04 \pm 2.48$ | $+38.06 \pm 2.51$ |
| | S-UCOM(SRG)$_{3b}$ | PAV | $-144.2980$ | $-147.5513$ | $+0.270 \pm 0.014$ | $3.229 \pm 0.001$ | $+34.43 \pm 1.74$ | $+33.80 \pm 1.77$ |
| | | AVP | $-143.8754$ | $-147.9539$ | $+0.317 \pm 0.018$ | $3.258 \pm 0.001$ | $+41.23 \pm 2.34$ | $+40.32 \pm 2.38$ |

Table 5.9.: Ground-state energies, deformation parameters, rms-radii and quadrupole moments for PAV and AVAP HF minima. Energies in MeV, radii in fm and quadrupole moments in fm$^2$. (continued)

## 5.3. Effect of Angular Momentum Projection

Before we can start to discuss the effect of the angular-momentum projection, it is necessary to discuss a few details about the plots used to illustrate the effect. The effect of angular momentum projection is best shown in plots of $E(\beta)$ surfaces. However, there are some subtleties about these plots, that we have to keep in mind for correct interpretation. Therefore, we discuss the method to calculate the points on these plots and its limitations. The meaning of the symbols and linestyles is as follows: Points obtained by the oblate initialization method (chapter 4.2.2) are denoted by ◀, those obtained by the spherical initialization by ●, and those obtained by the prolate initialization by ▶. If points are sufficiently close in $\beta$ ($\Delta\beta < 0.04$), they are connected by a solid line, otherwise by a dotted line. The lines are obtained by a spline approximation—true interpolations can produce very dominant artifacts, making the plots difficult to read.

Each point is calculated by a constrained HF calculation, i.e. according to eq. (4.18). As pointed out in the discussion in chapter 4.3, the deformation parameter obtained for a given constraint is not known a priori. If a specific value for $\beta$ (or $Q$) is desired, a search algorithm has to be employed—but this is not necessary if we are only interested in plotting $E(\beta)$. In this case, we can simply calculate some points and insert additional points in between if they are too far apart. The algorithm works as follows. First, a point for $\lambda = 0$ is calculated. Next, $\lambda$ is increased in each direction until the energy is more than $20\,\mathrm{MeV}$ above the ground state. Finally, additional points are inserted between existing points until they are no further apart than $\Delta\beta = 0.04$.

However, for some regions, no points can be calculated. The reason for this behavior is illustrated in figure 5.5. Introducing a linear constraint to the HF equations essentially means, that the energy-minimization is not carried out with respect to a horizontal line in $E(\beta)$ space, but with respect to a sloped line. The gradient corresponds to the value of the Lagrange parameter $\lambda$. If the sloped $\lambda Q$-line corresponds to a tangent of an inflection point of the $E(\beta)$ curve (line $a$ in the figure), any further increase in $\lambda$ probes not the absolute minimum 1, but a region in the adjacent minimum 2 (in a certain sense, the solution *falls* to minimum 2). The first point with an infinitesimal increased $\lambda$ ($\lambda = \lambda_a + \delta\lambda$) lies in the region of minimum 2, at the point where $E(\beta)$ has the same slope as line $a$ (shown by line $b$), which marks the border between regions $C$ and $B$. All points with a higher $\lambda$ lie in area $B$. Areas between the two points corresponding to $\lambda_a$ and $\lambda_a + \delta\lambda$ (areas $C$ and $D$) can, in principle, not be probed. Area $C$ could be probed if there existed an initialization procedure which would lead to a HF solution in minimum 2. But since this it not the case here, this area is inaccessible. Area $D$ may not be probed at all, since a higher slope than given by line $c$ would lead to a point in area $A$. But these strict conditions may not hold in practice, as can be seen in the plot. Since an initialization procedure exists that gives a solution in minimum 3, region $E$ is well accessible, but region $F$ should not be accessible, because a higher slope than given by line $d$ leads to a point in area $A$, like in region $D$.

In principle, there should be no points at all in regions $C$, $D$ and $F$. However,

this is only true for well converged HF calculations. The energy of a HF solution converges much faster than the density matrix. The energy is usually converged within 1 MeV after less than ten iterations, whereas about 30 iterations are needed for a well converged density matrix.[4] Using only ten iterations for the $E(\beta)$ plots, therefore, enables us to obtain a few points in regions that would not be accessible otherwise, but the number of obtainable points is often insufficient to get a close enough spacing.

Another point which may alter the above picture is the effect of the angular momentum projection. For the technical discussion above, the intrinsic HF energy $E_{\mathrm{HF}}(\beta)$ is the relevant quantity, but from a physical perspective, the projected energy $E_{\mathrm{proj}}(\beta)$ is more interesting. Since the slope of the two curves might be different at certain points, the origin of unaccessible regions might be obscured in a pure $E_{\mathrm{proj}}(\beta)$ plot.
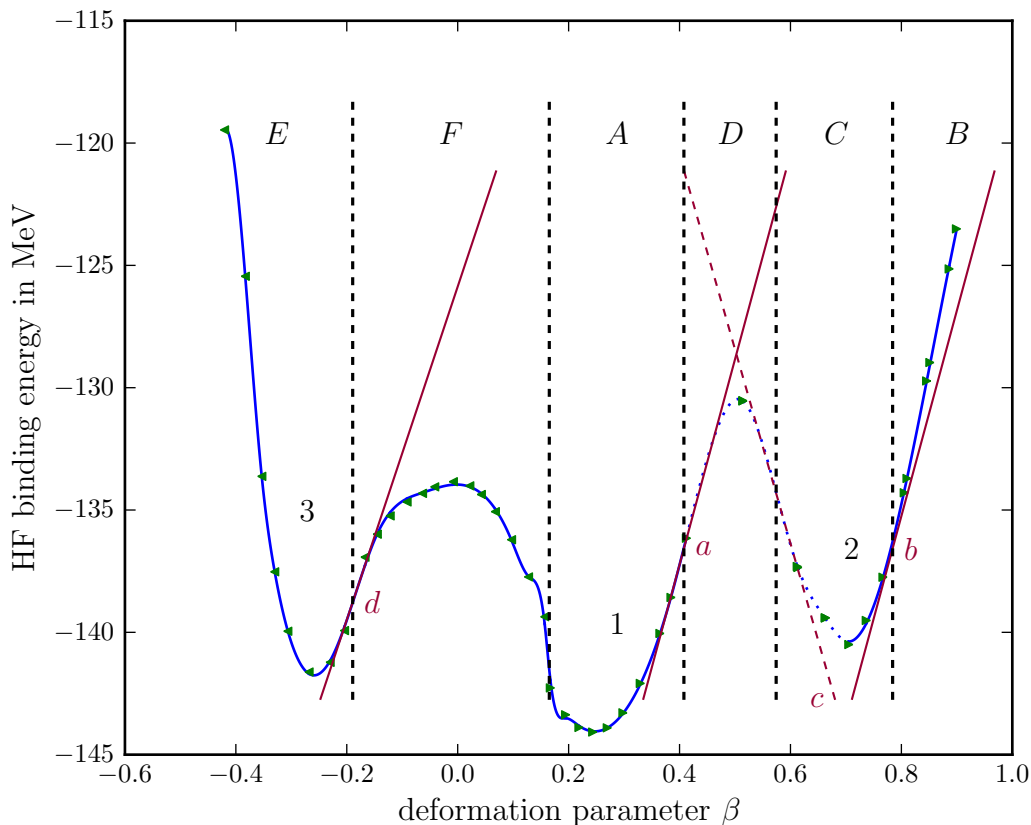


Figure 5.5.: Explanation of the $E(\beta)$ plots and the difficulties involved in their production, see text.

To study the effect of the angular momentum projection and three-body forces, we consider the binding energy in dependence of the deformation parameter for all three interactions (figures 5.6 to 5.9). No offsets have been introduced in the plots, the

---

[4]This holds only for realistic interactions, calculations for the Gogny D1S force often require 50–100 iterations or even more.

spacing of the curves is a real effect of the interactions used.

As already discussed, the oscillator length has a significant influence on the deformation parameter, even in large model spaces. Since the $E(\beta)$ plots have been calculated in a considerably smaller model space ($e_{\max} = 10$), the effect is even stronger. But as these plots are only of a qualitative nature, we do not explore this effect further. For each curve, the optimal oscillator length has been used (table 5.7). We can make the general observation, that the absolute value of the deformation parameter is reduced considerably by the inclusion of three-body forces and that it is increased, although to a lesser extent, by the angular-momentum projection. For some nuclei, the projected and the intrinsic energy are identical for $\beta = 0$. This means that the nucleus is spherical at this point, which is caused by a closed subshell. Closed subshells can occur for $^{12}$C, $^{28}$Si and $^{32}$S, but not for $^{20}$Ne.

For specific nuclei, we can make the following observations:

- $^{12}$C turns out to be extremely deformed for the UCOM(VAR)$_{2b}$ interaction. This leads to a breakdown of the calculations in the region of the oblate minimum. We study this effect more closely in subsection 5.3.1. For the other interactions, one can anticipate a similar effect, since the oblate regions with a stronger deformation than the minimum only contains very few points. The $1p\frac{3}{2}$ subshell closure only occurs for the S-UCOM(SRG)$_{3b}$ interaction.

- For $^{20}$Ne, no problems are evident, but an additional effect of the projection can be seen very clearly. Even though there are very prominent bumps in the curves for the intrinsic binding energy, they are smoothed out considerably by the projection. For the S-SRG$_{3b}$ and S-UCOM(SRG)$_{3b}$ interactions, this goes even so far, that two adjacent points with a considerable difference in $E_{\text{int}}$ have almost the same $E_{\text{proj}}$.

- For $^{28}$Si, the most prominent features are the two minima with almost identical binding energy.[5] Experiment indicates an oblate deformation for $^{28}$Si [Sto05], which is confirmed by the Gogny force [HG07, PG08]. This is confirmed to some extent the UCOM(VAR)$_{2b}$ interaction, but this could still be changed when higher order correlations are included. However, for the S-SRG$_{3b}$ and S-UCOM(SRG)$_{3b}$ interaction, the prolate and oblate solutions are degenerate within the accuracy limits of the method (0.25 MeV and 0.01 MeV respectively). As the UCOM(VAR)$_{2b}$ interaction does not include any three-body forces, this effect might be related to three-body forces. At some points, the projected energy is higher than the unprojected one. In theory, this should never occur, as the angular momentum projection always improves the binding energy. However, since the calculations are not well converged, this behavior is not totally unexpected and does not pose a problem as long as the reduction of the binding energy stays small and only occurs in regions of local maxima. In the area between the two minima, the effect of the $1d\frac{5}{2}$ sub-shell closure can be seen for the

---

[5]For the Gogny D1S interaction with pairing, both minima exist with an energy difference of about 2 MeV, but the high barrier in between vanishes almost completely [HG07].
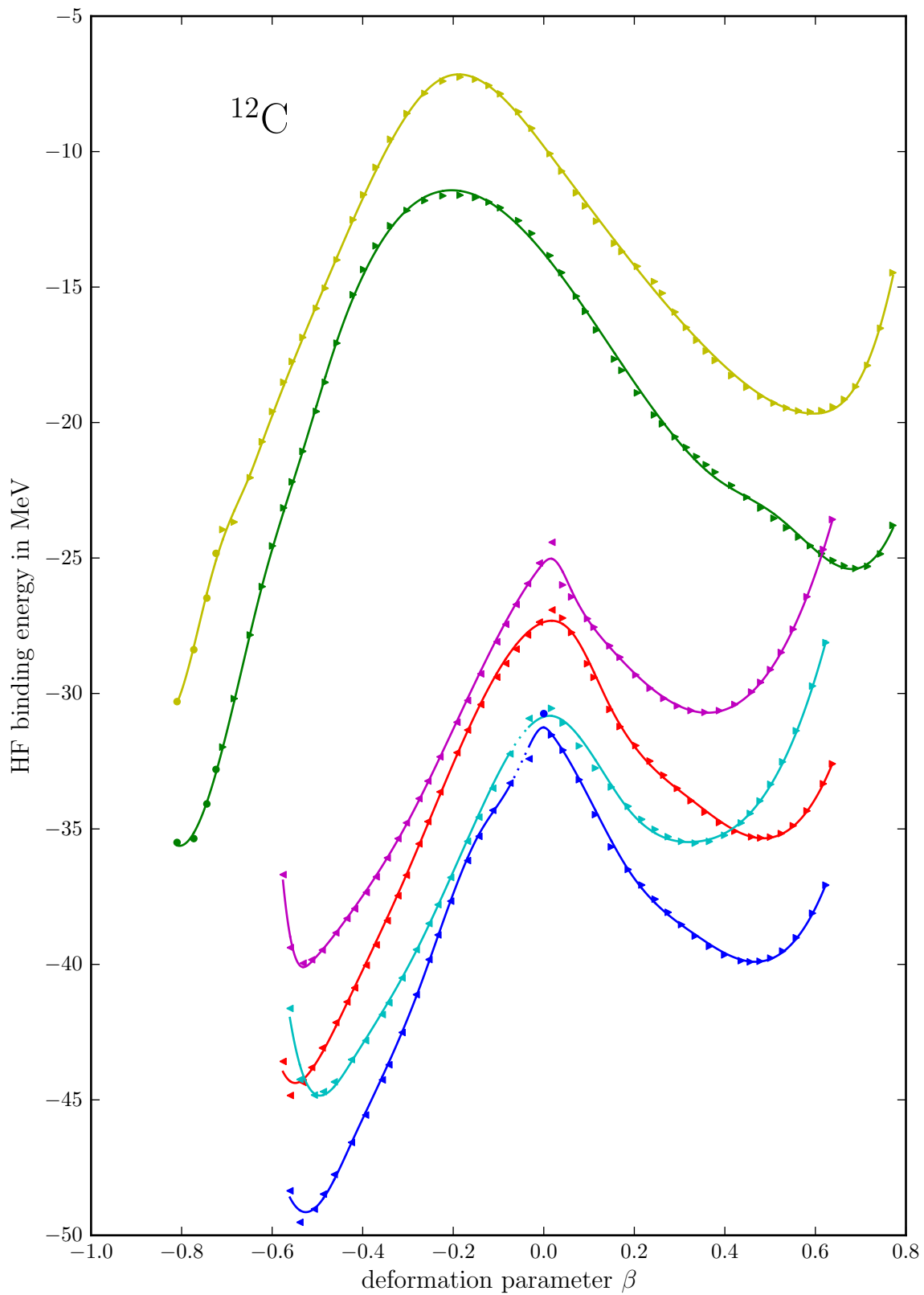
Figure 5.6.: $E_{\mathrm{int}}(\beta)$ and $E_{\mathrm{proj}}(\beta)$ of $^{12}$C for the UCOM(VAR)$_{2b}$ (⬤,⬤), S-SRG$_{3b}$ (⬤,⬤) and S-UCOM(SRG)$_{3b}$ (⬤,⬤) interactions.
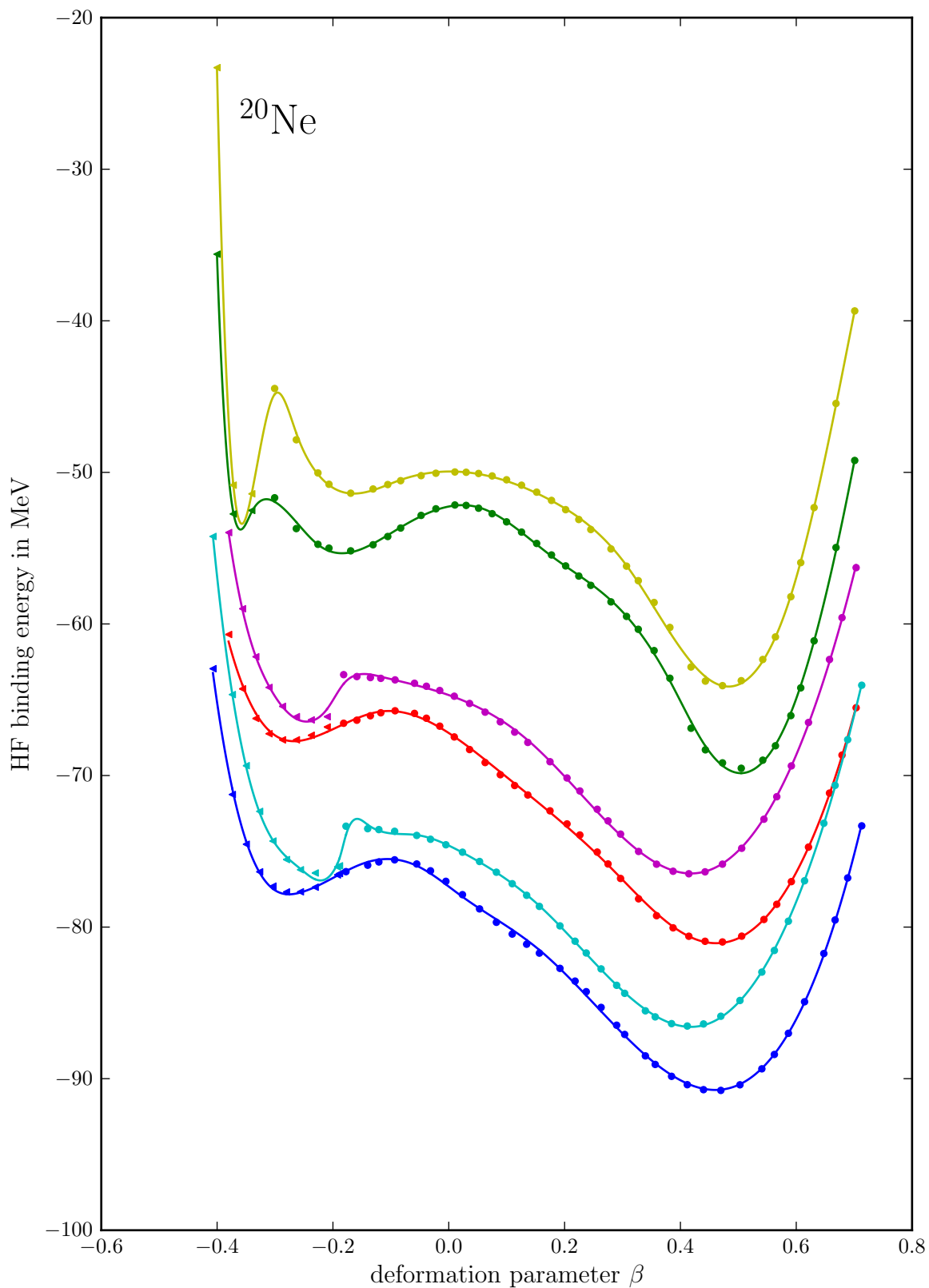
Figure 5.7.: $E_{\text{int}}(\beta)$ and $E_{\text{proj}}(\beta)$ of $^{20}$Ne for the UCOM(VAR)$_{2b}$ (—●—,—●—), S-SRG$_{3b}$ (—●—,—●—) and S-UCOM(SRG)$_{3b}$ (—●—,—●—) interactions.
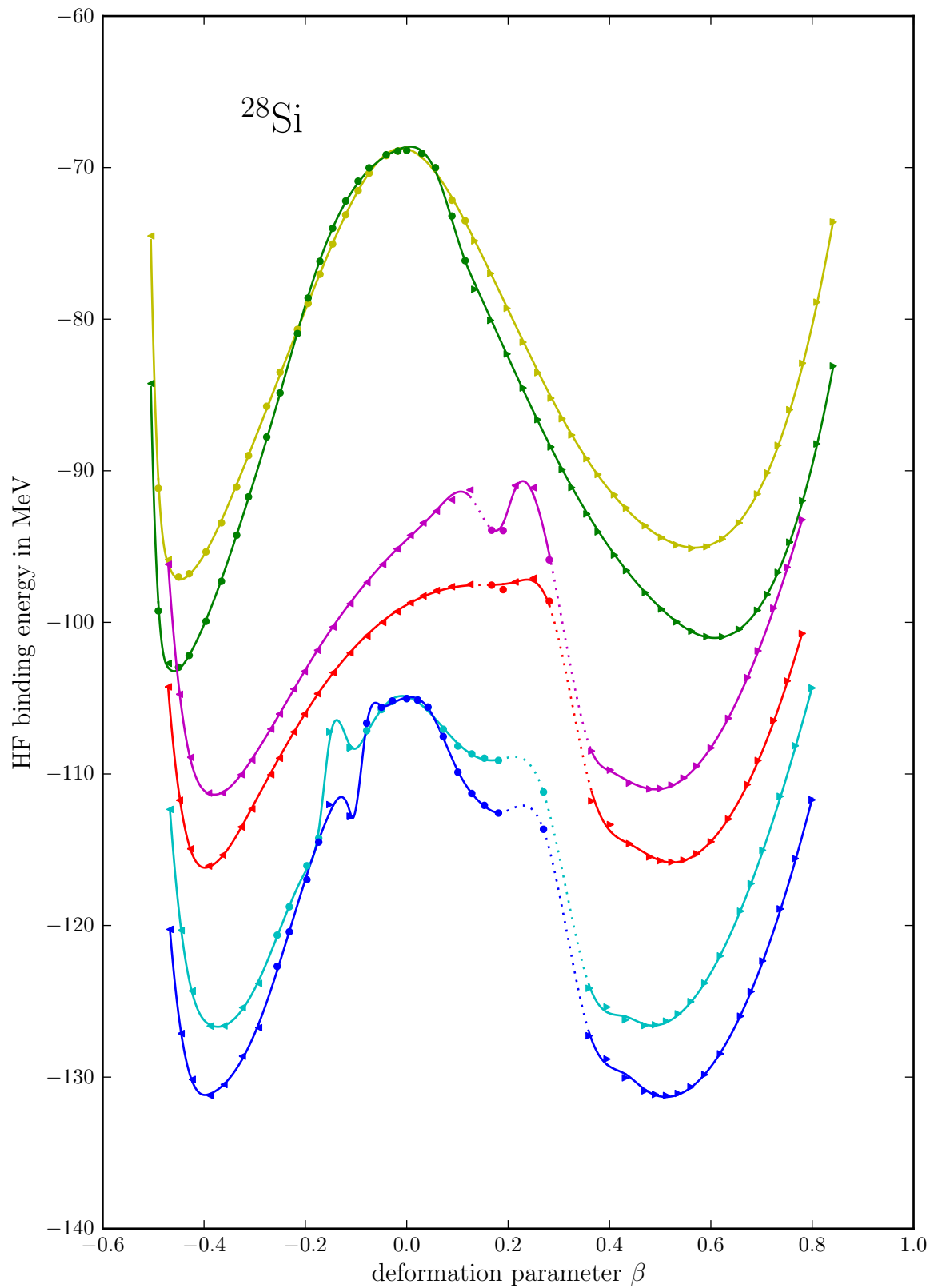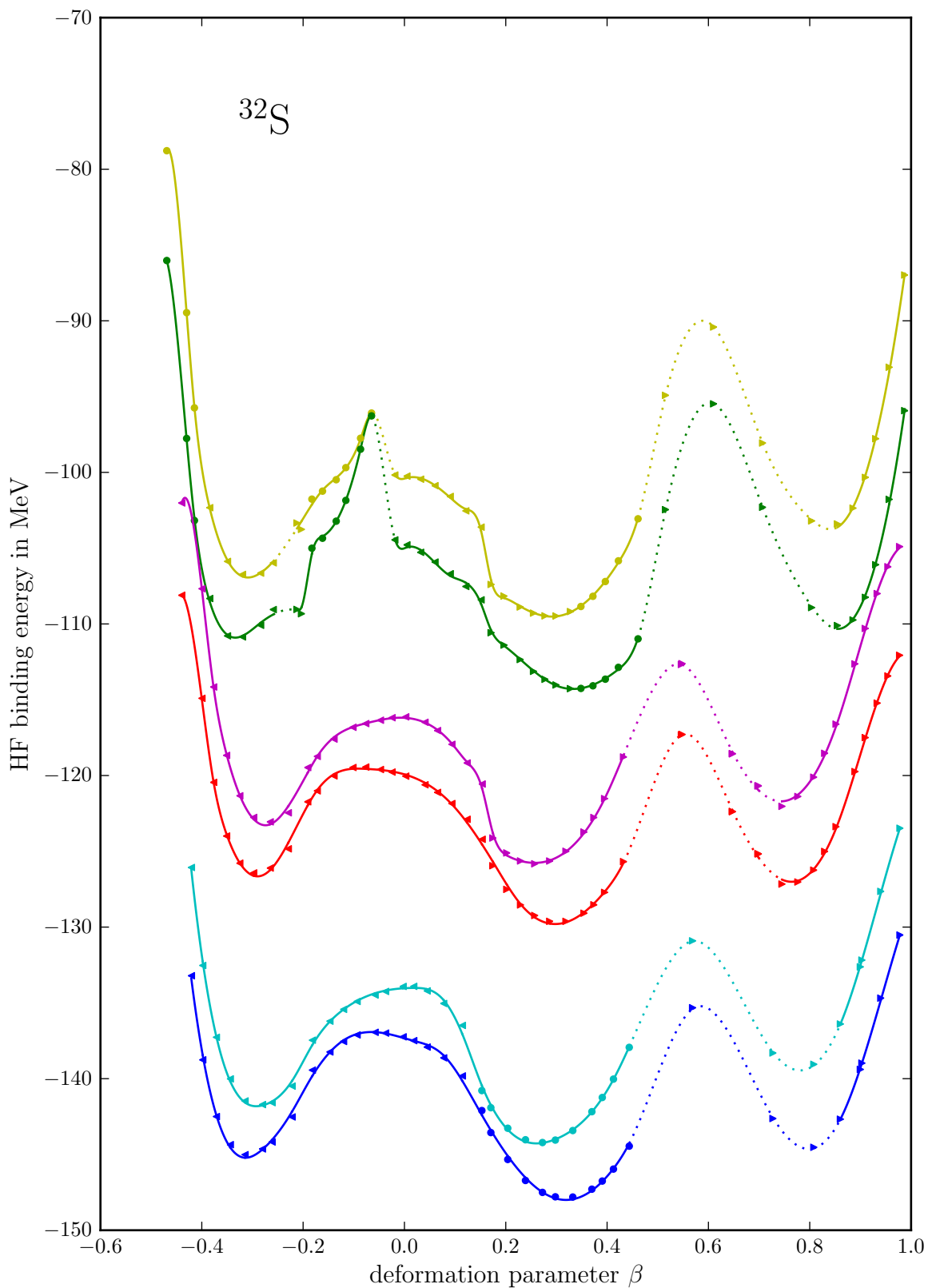
Figure 5.8.: $E_{\text{int}}(\beta)$ and $E_{\text{proj}}(\beta)$ of $^{28}$Si for the UCOM(VAR)$_{2b}$ (●,●), S-SRG$_{3b}$ (●,●) and S-UCOM(SRG)$_{3b}$ (●,●) interactions.

Figure 5.9.: $E_{int}(\beta)$ and $E_{proj}(\beta)$ of $^{32}S$ for the UCOM(VAR)$_{2b}$ (⬤—,⬤—), S-SRG$_{3b}$ (⬤—,⬤—) and S-UCOM(SRG)$_{3b}$ (⬤—,⬤—) interactions.

UCOM(VAR)$_{2b}$ and S-SRG$_{3b}$ interaction. We further note that for the S-SRG$_{3b}$ and S-UCOM(SRG)$_{3b}$ interactions, the curves look a bit erratic between the minima and the oblate side of the prolate minimum contains only very few points. This can indicate that the points found between the minima do not represent the true lower boundary for the energy. Other points with a lower energy might exist, but they are not accessible with our method.

- In the case of $^{32}$S, we have three minima. The global minimum occurs at a moderate prolate deformation and lies a few MeV lower than the other two minima. As already discussed, the oblate minimum is well accessible by the calculation, but the region between the prolate minima can not be probed very well. The $2s\frac{1}{2}$ subshell closure only occurs for the UCOM(VAR)$_{2b}$ interaction, where the curve also shows some erratic behavior in this region. For the UCOM(VAR)$_{2b}$ interaction, some points for the global minimum have been obtained by the spherical initialization. Unfortunately, the prolate initialization leaves this minimum for the more prolate minimum before the AVAP minimum is found. Therefore, the AVAP minimum has to be obtained by the spherical initialization.

## 5.3.1. The Case of $^{12}$C

Figure 5.6 shows, that $^{12}$C exhibits a strange behavior around the oblate minimum. To get a better understanding, figure 5.10 shows only the data for the UCOM(VAR)$_{2b}$ interaction and includes points that are not shown in figure 5.6.
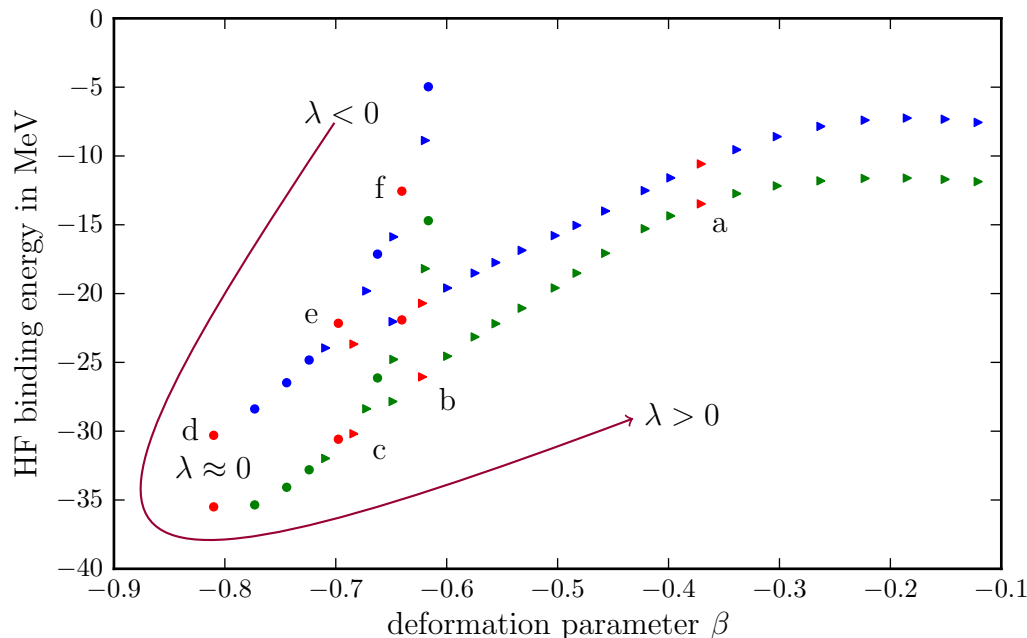


Figure 5.10.: $E_{\text{int}}(\beta)$ and $E_{\text{proj}}(\beta)$ of $^{12}$C for the UCOM(VAR)$_{2b}$ (●, ●) interaction. Points included in figure 5.11 are plotted in red (●).

Usually, $\beta(\lambda)$ is a monotonic function, but as can be seen in the plot, this is not the case for $^{12}$C with the UCOM(VAR)$_{2b}$ interaction. For $\lambda < 0$, the HF solutions are grouped in a parabola-branch like structure, but $\beta$ increases with decreasing $\lambda$. For $\lambda \approx 0$, the strongest oblate deformation is reached and now $\beta$ starts to increase with increasing $\lambda$ (the turning point lies at $\lambda \approx 0 \pm 20$ for the oblate and spherical initializations). The angular momentum projection has no effect on this behavior. What happens exactly can best be understood by looking at the 3D densities of the relevant states (see also section 5.4).

Figure 5.11 shows the intrinsic densities for the states marked from (a) to (f) in figure 5.10. Black (3D) and gray (2D) arrows indicate the symmetry axis. State (a) serves as an example of a typical oblate state, like it is also found in heavier nuclei. The surfaces are drawn at 80% of the maximum density. We start with an oblate nucleus like state (a), which has almost no higher order deformations. As the Lagrange parameter is decreased, a hexadecapole deformation develops, which reduces the density on the $z$-axis, but increases it in the off-axis region. The nuclear density assumes a slightly toroidal shape, as seen in state (b). As the Lagrange parameter is further decreased, the toroidal component gets more pronounced, as shown in state (c). Due to the toroidal deformation, the nucleus can have a very high negative quadrupole moment, without appearing as a flat disc. In state (d) (the energy minimum), the density at the origin is less than 80% of the maximum density, producing a hole in the density surface, which is even more pronounced in state (e). For very low (i.e. large negative) Lagrange parameters, the hexadecapole deformation vanishes, which can be seen at state (f), where the hole in the 80% density surface vanishes. At this point, the nucleus appears to be flatter than in state (d), even though the negative quadrupole moment is smaller.

We believe the strange behavior develops in the following way: If one uses a large negative $\lambda$, the nucleus is forced into a strongly oblate state at an early stage of the HF iterations and cannot develop any hexadecapole or toroidal deformations, which leads to a state like (f). However, if one uses smaller negative value for $\lambda$, this does not happen and the nucleus can assume a toroidal shape. The toroidal shape now allows the nucleus to attain a larger quadrupole deformation, as the hexadecapole deformation counteracts some components of the quadrupole deformation. This leads to the toroidal states like (b)–(e). The two branches develop in the following way: The algorithm starts at $\lambda = 0$ and increases $\lambda$ in both directions, until states with an energy well above the intrinsic ground state energy are found for both directions. One is found on the parabola-branch-like structure, in the region of state (f) and the other one at a prolate deformation. After these states have been found, additional points are inserted in between existing points. However, since the list of values is sorted by $\lambda$, and not by $\beta$, points for both branches are calculated. This shows, that the algorithm handles the situation very well, the problem is simply a matter of presentation—$\beta$ no longer defines a state uniquely, and, therefore, an $E(\beta)$ plot is no longer possible in a strict sense. The only problem that can arise, is that the energy minimum may be very inaccurate, but this would show itself by a large energy gap between the branch endpoints. If the strong toroidal deformations were more common, the best way to handle them would be to introduce additional constraints, like higher order
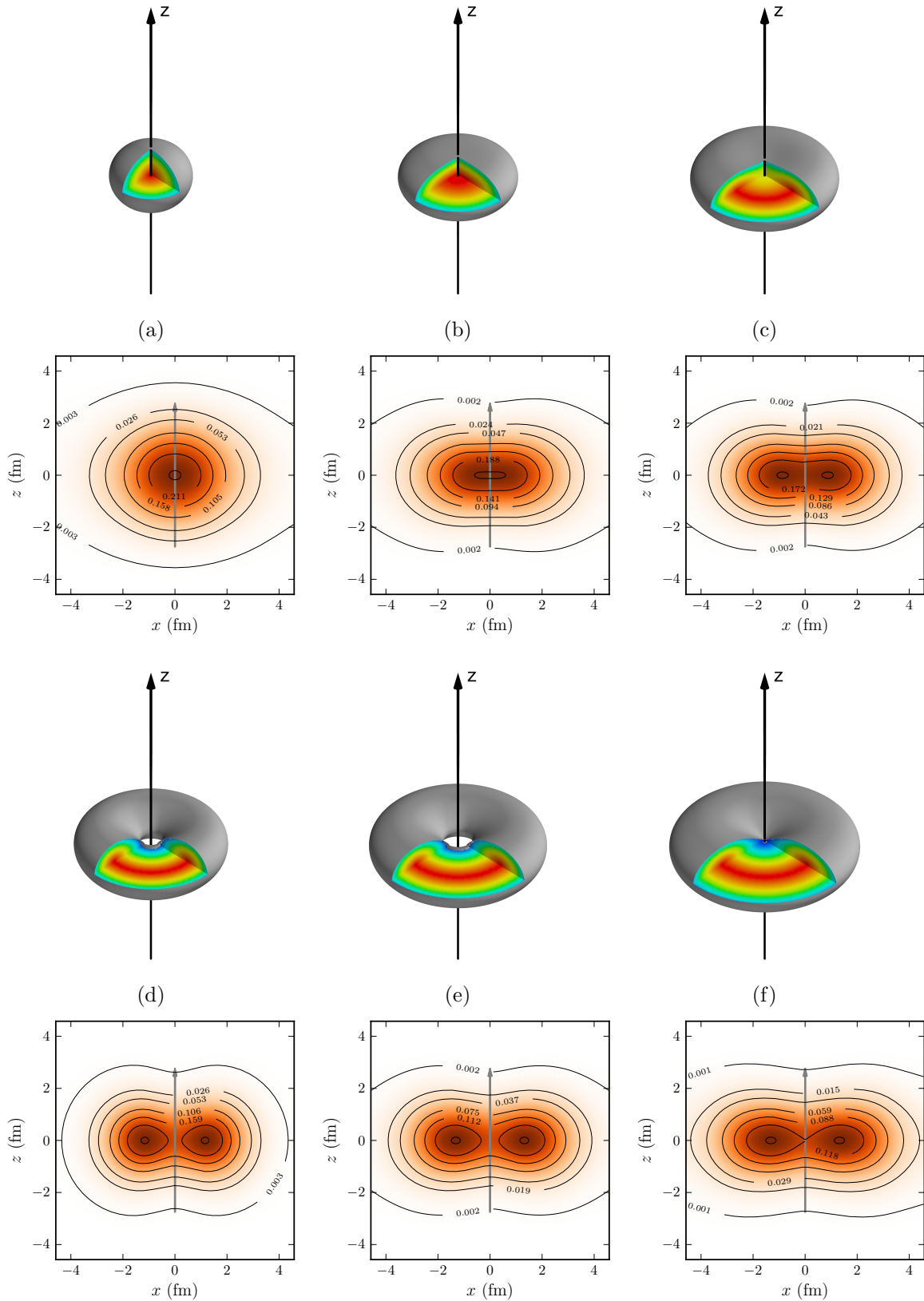
Figure 5.11.: Different deformed states of $^{12}$C for the UCOM(VAR)$_{2b}$ interactions ($x$- and $z$-axis in fm, density in nucleons/fm$^3$). Isosurfaces are at $0.8\,\rho_{\max}$, the symmetry axis is denoted by a gray (2D) or black (3D) arrow.

shape moments. But as this is the only occurrence, we consider the current treatment sufficient.

## 5.4. Ground-State Densities

Since the deformation parameter only gives a very rough idea of the shape of a nucleus —it only gives information about the static quadrupole moment—we also show density distributions and 3D-isosurface plots of the ground states (figures 5.12 to 5.16). Details of the calculation can be found in appendix A.3. The isosurfaces are drawn at $\rho = 0.4\,\rho_{\max}$. The 2D density plots are in the $x$-$z$ plane, where the $z$-axis is the symmetry axis of the nucleus. The symmetry is also denoted by a gray (2D) or black (3D) arrow. The contour lines are drawn at $(0.01, 0.1, 0.2, 0.4, 0.6, 0.8, 0.99)\,\rho_{\max}$. All plots of the same nucleus have the same scale.

We use a grid with 200 points in each direction, which are evenly distributed in the interval from $-2 \cdot A^{1/3}$ fm to $+2 \cdot A^{1/3}$ fm. For the ground-state density, using $200^3$ grid points is not a problem since each point only needs to be considered once and no caching is required.

Since the two minima of $^{28}$Si are practically degenerate, we show both ground-state densities (denoted by $^{28}$Si$_o$ and $^{28}$Si$_p$). The plots show that all nuclei have a significant hexadecapole deformation, positive for $^{20}$Ne and $^{28}$Si$_o$, and negative for $^{12}$C, $^{28}$Si$_p$ and $^{32}$S. Since the algorithm imposes good parity, deformations of uneven multipolarity (e.g. octupole) can not be present. The results for the S-SRG$_{3b}$ and S-UCOM(SRG)$_{3b}$ interactions are very similar, with a slightly lower density for the S-UCOM(SRG)$_{3b}$ interactions, which is consistent with the larger radii and a consequence of the stronger repulsive three-body force. The UCOM(VAR)$_{2b}$ interaction produces significantly smaller nuclei with a higher density, but of very similar shape, which is also consistent with the significantly lower radii and the absence of a repulsive three-body force. The maximum densities are shown in table 5.10. The density reduction for $^{28}$Si$_o$ is stronger than for the other nuclei.

| interaction | maximum density | | | | |
|---|---|---|---|---|---|
| | $^{12}$C | $^{20}$Ne | $^{28}$Si$_o$ | $^{28}$Si$_p$ | $^{32}$S |
| UCOM(VAR)$_{2b}$ | 0.250 | 0.288 | 0.332 | 0.280 | 0.280 |
| S-SRG$_{3b}$ | 0.162 | 0.178 | 0.199 | 0.168 | 0.167 |
| S-UCOM(SRG)$_{3b}$ | 0.154 | 0.169 | 0.190 | 0.162 | 0.161 |

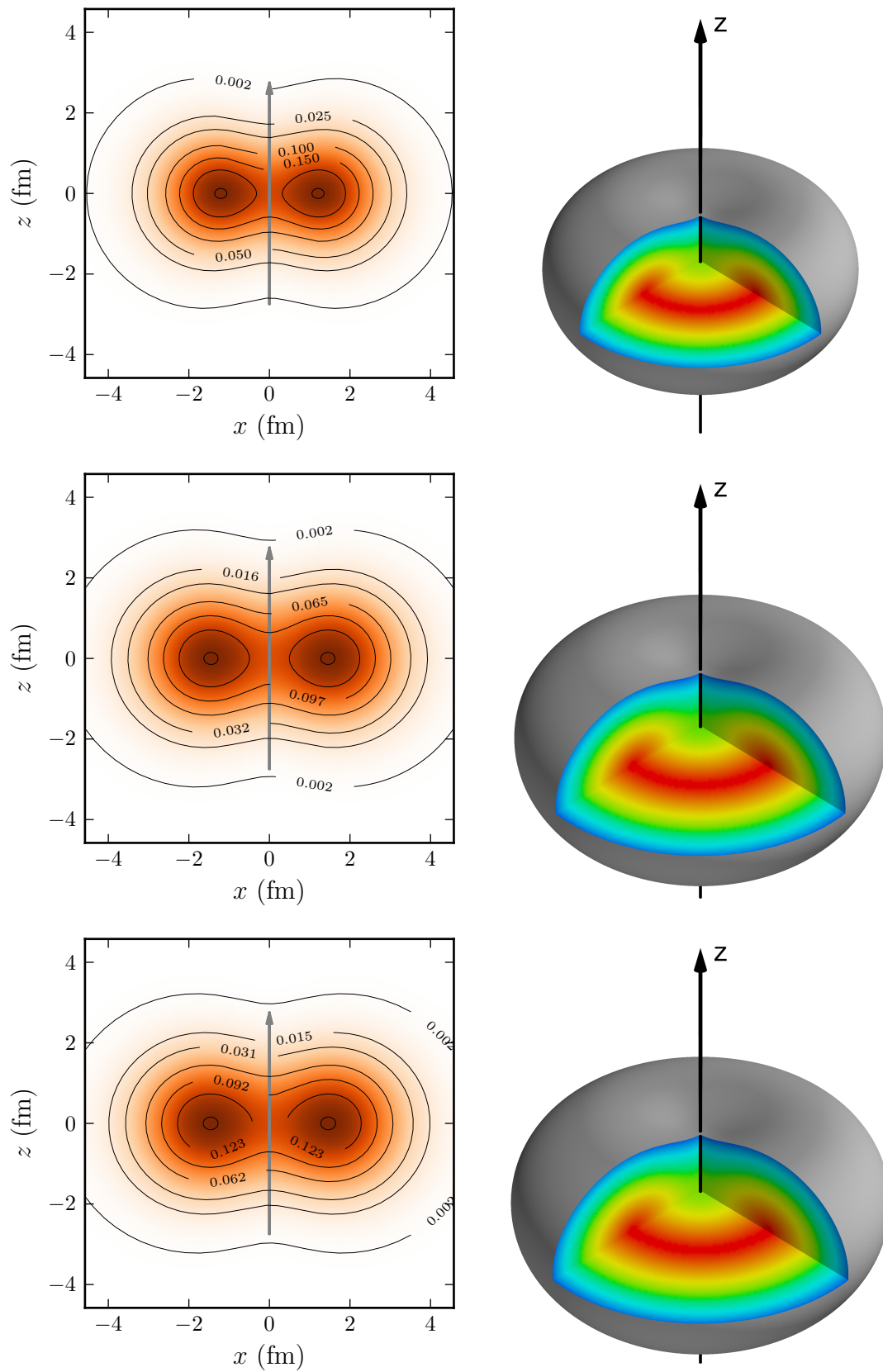Table 5.10.: Maximum densities of HF ground states, in nucleons/fm$^3$.

Figure 5.12.: Ground-state densities of $^{12}$C for the UCOM(VAR)$_{2b}$ (top), S-SRG$_{3b}$ (middle) and S-UCOM(SRG)$_{3b}$ (bottom) interactions (density in nucleons/fm$^3$).
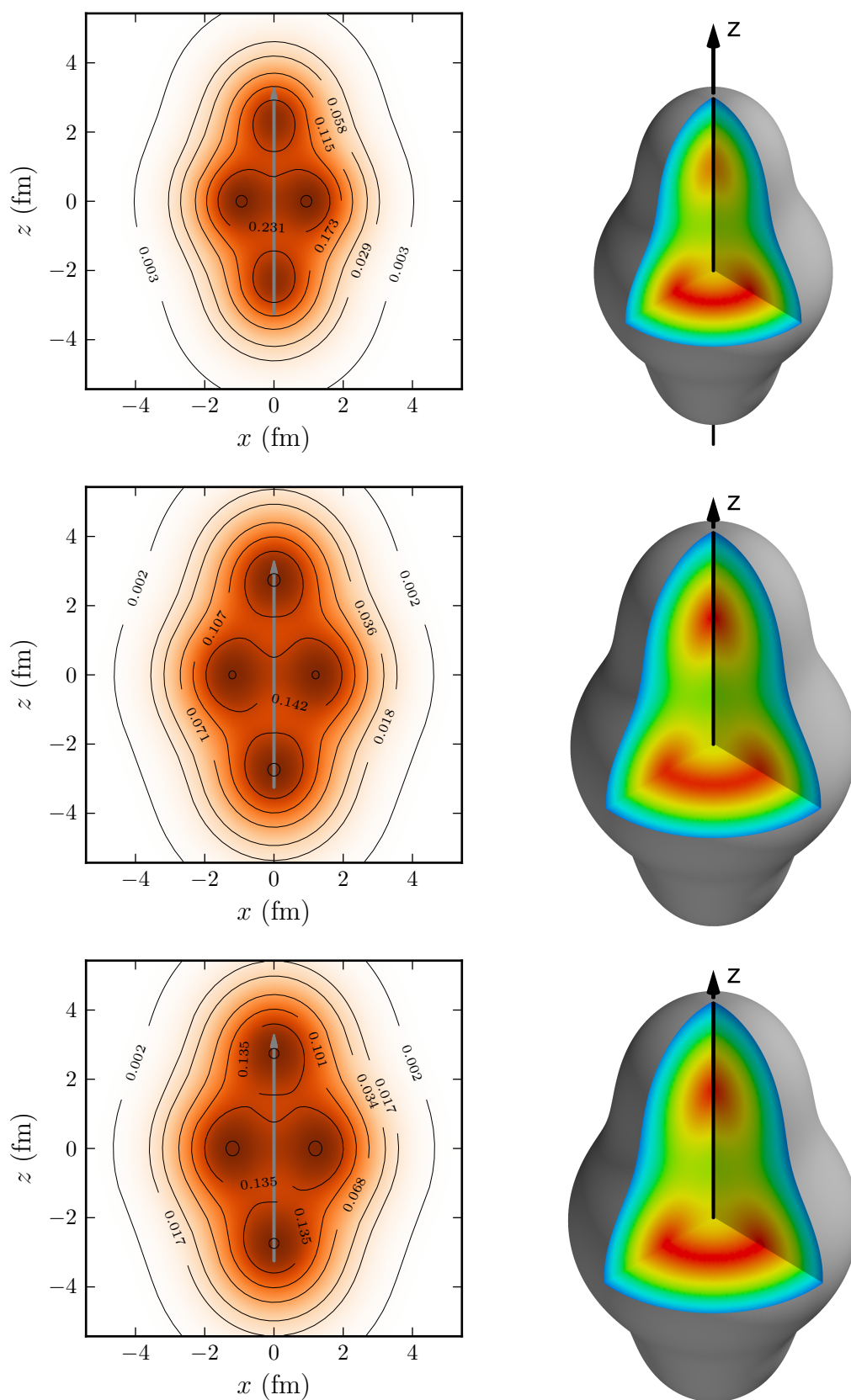
Figure 5.13.: Ground-state densities of $^{20}$Ne for the UCOM(VAR)$_{2b}$ (top), S-SRG$_{3b}$ (middle) and S-UCOM(SRG)$_{3b}$ (bottom) interactions (density in nucleons/fm$^3$).
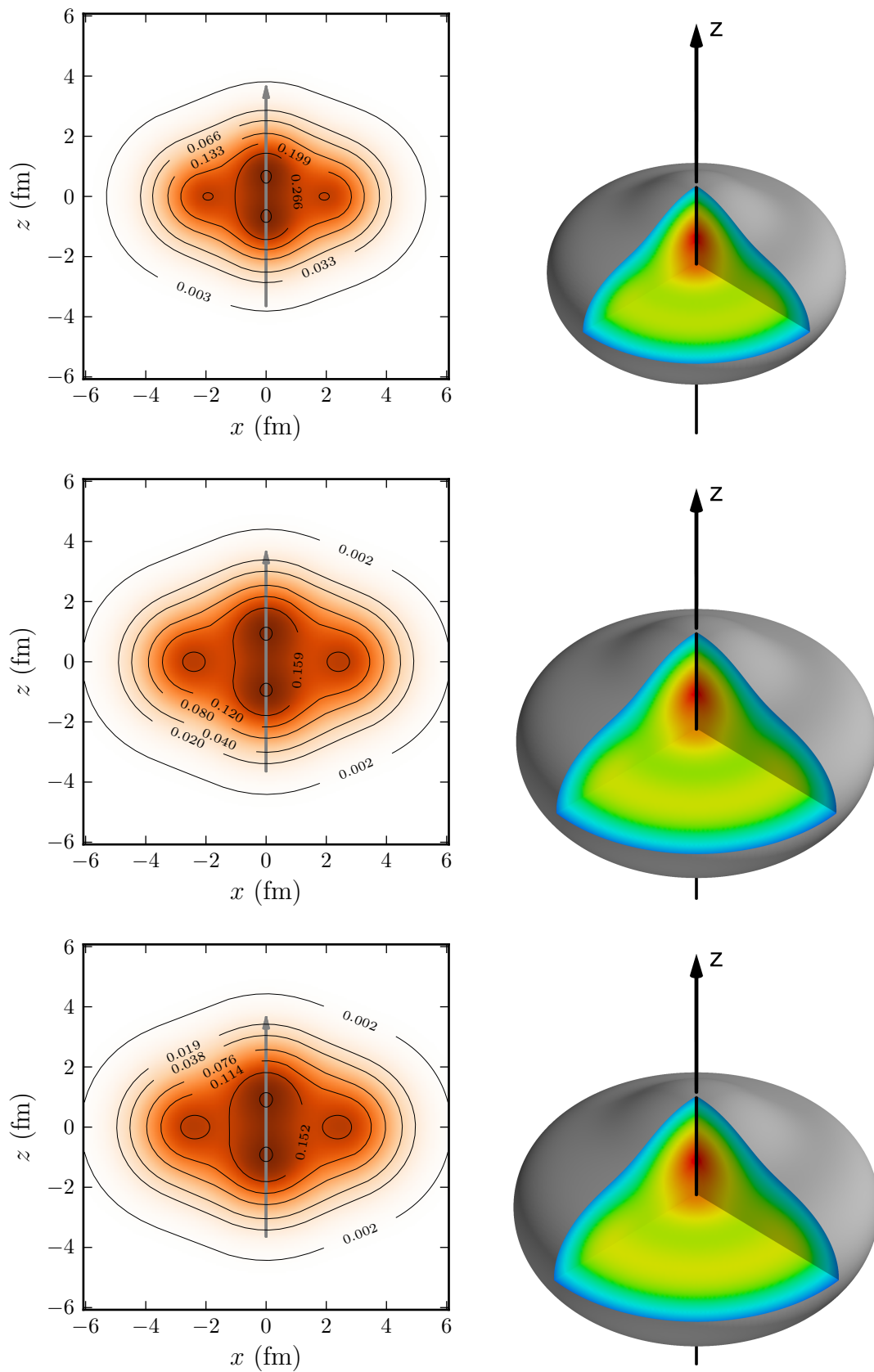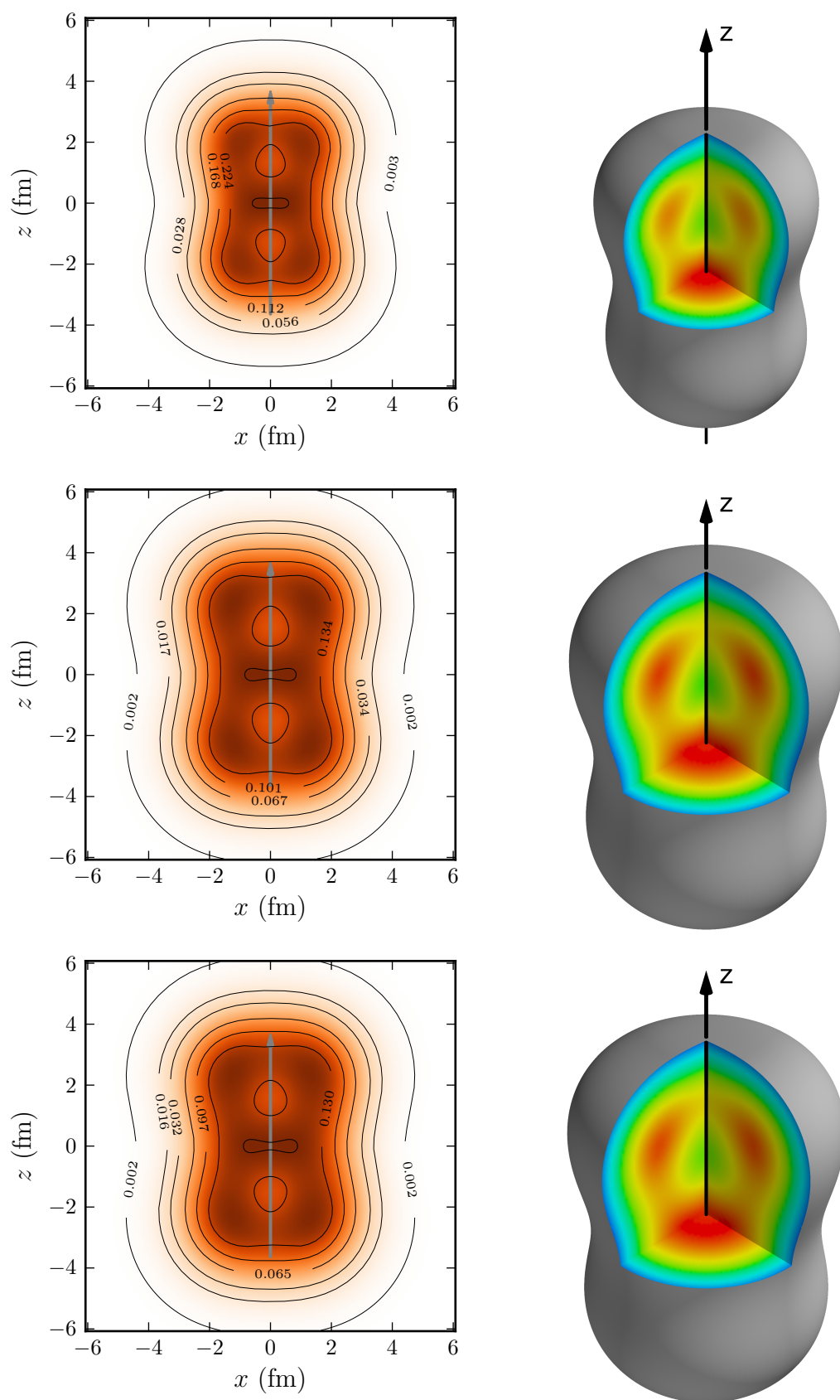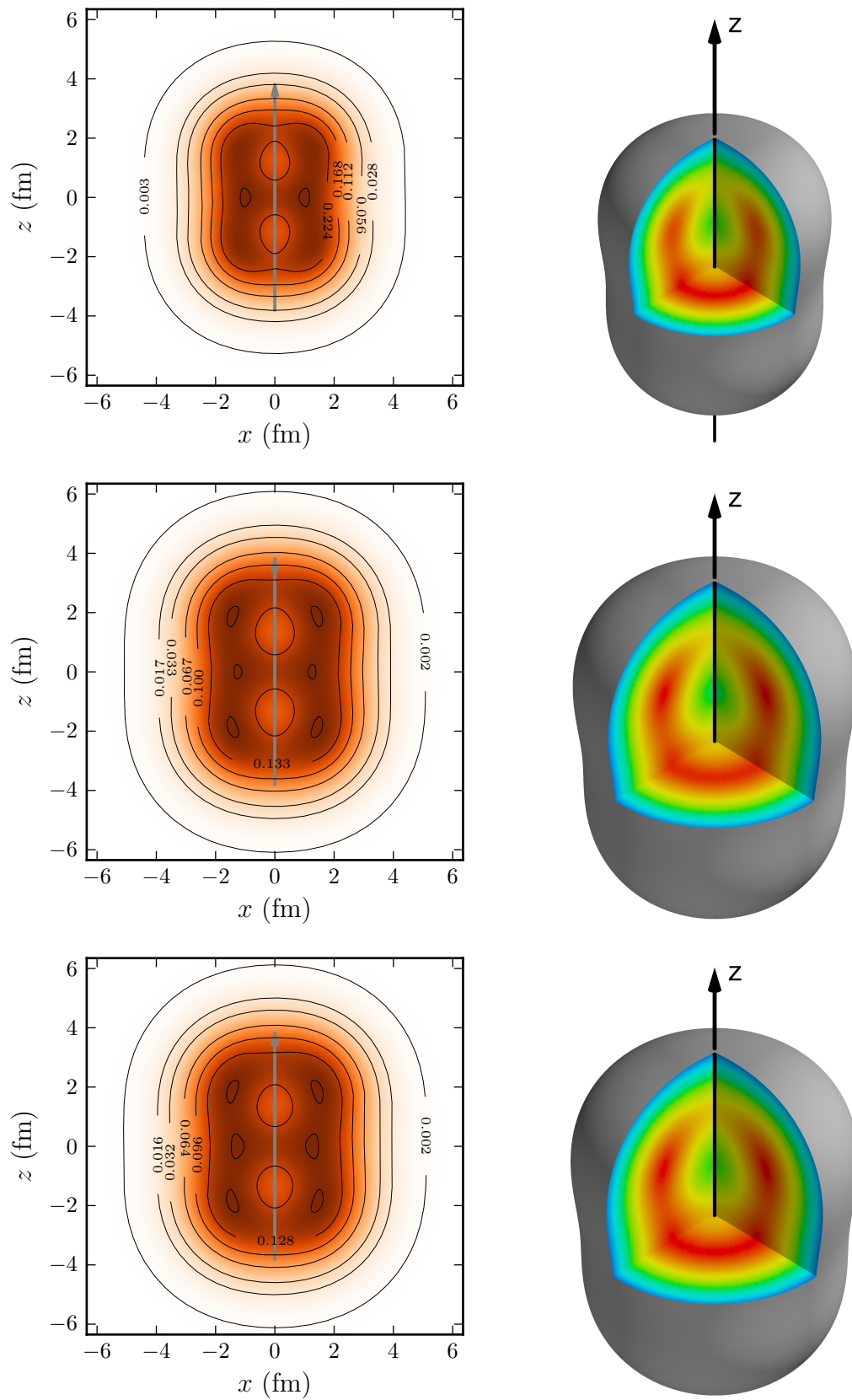
Figure 5.14.: Ground-state densities of the oblate $^{28}$Si$_o$ for the UCOM(VAR)$_{2b}$ (top), S-SRG$_{3b}$ (middle) and S-UCOM(SRG)$_{3b}$ (bottom) interactions (density in nucleons/fm$^3$).

Figure 5.15.: Ground-state densities of the prolate $^{28}\text{Si}_p$ for the UCOM(VAR)$_{2b}$ (top), S-SRG$_{3b}$ (middle) and S-UCOM(SRG)$_{3b}$ (bottom) interactions (density in nucleons/fm$^3$).

Figure 5.16.: Ground-state densities of $^{32}$S for the UCOM(VAR)$_{2b}$ (top), S-SRG$_{3b}$ (middle) and S-UCOM(SRG)$_{3b}$ (bottom) interactions (density in nucleons/fm$^3$).

# 5.5. Rotational Bands

As already mentioned, angular-momentum projection can, in theory, be used to calculate the excitation energies of rotational bands. In the limit of a rigid rotor, they are obtained simply by setting $J = 0, 2, 4, 6...$ in equation (3.28). However, it is also possible for the nucleus to have slightly different shapes for each rotational state. A lower deformation leads to a lower moment of inertia, which then leads to a lower rotational energy. If the energy-cost of the lesser deformation is lower than the energy gained by the lower moment of inertia, the lesser deformed state is favored. Therefore, a more sophisticated approach would be to assume a soft rotor and use the *approximative variation after projection* for each excited state, i.e. using equation (4.18) to minimize not the ground-state energy $E^0$, but the energy of the excited states $E^J$ with $J = 2, 4, 6$ etc.

Figures 5.17 and 5.18 show the results for the rigid approximation and the soft-rotor for all interactions. The first three excited states ($J = 2, 4, 6$) of $^{20}$Ne and the oblate and prolate states of $^{28}$Si are shown. All calculations were made with a basis truncation of $e_{\mathrm{max}} = 10$. In the rigid rotor approximation, the error due to the small basis is below 1%.

We can see that already the rigid approximation underestimates the lowest excitation energies and the soft-rotor model further decreases the energy. If we would allow triaxial deformations, the excitation energy of the soft rotor should decrease further. In this case, the nucleus could concentrate mass around the rotation axis without having to increasing the mass on a perpendicular axis, which would break axial symmetry. The underestimation of the lowest states could be related to the generally underestimated binding energies obtained with realistic interactions. Considering that we used no phenomenological input, the rotational excitations are described very well. The oblate state of $^{28}$Si is in better agreement with experimental data than the prolate state.

We also included some calculations using the phenomenological Gogny D1S interaction in the plots. Due to the bad convergence with respect to HF iterations, the values are only for the PAV minimum. As we can see, the Gogny D1S force does not perform any better than the realistic interactions. In the case of $^{20}$Ne, the level scheme is completely wrong. This shows clearly, that phenomenological interactions are only valid for the properties they have been designed to describe well, i.e. ground-state energies and radii, and have no predictive power for other observables.
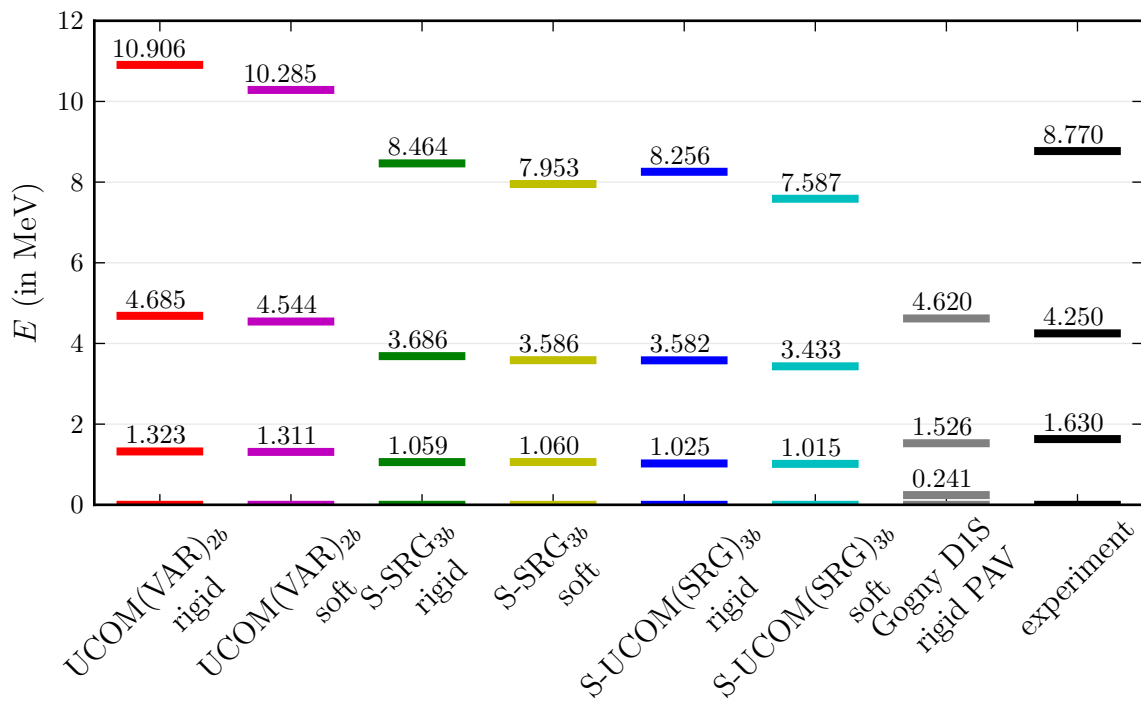
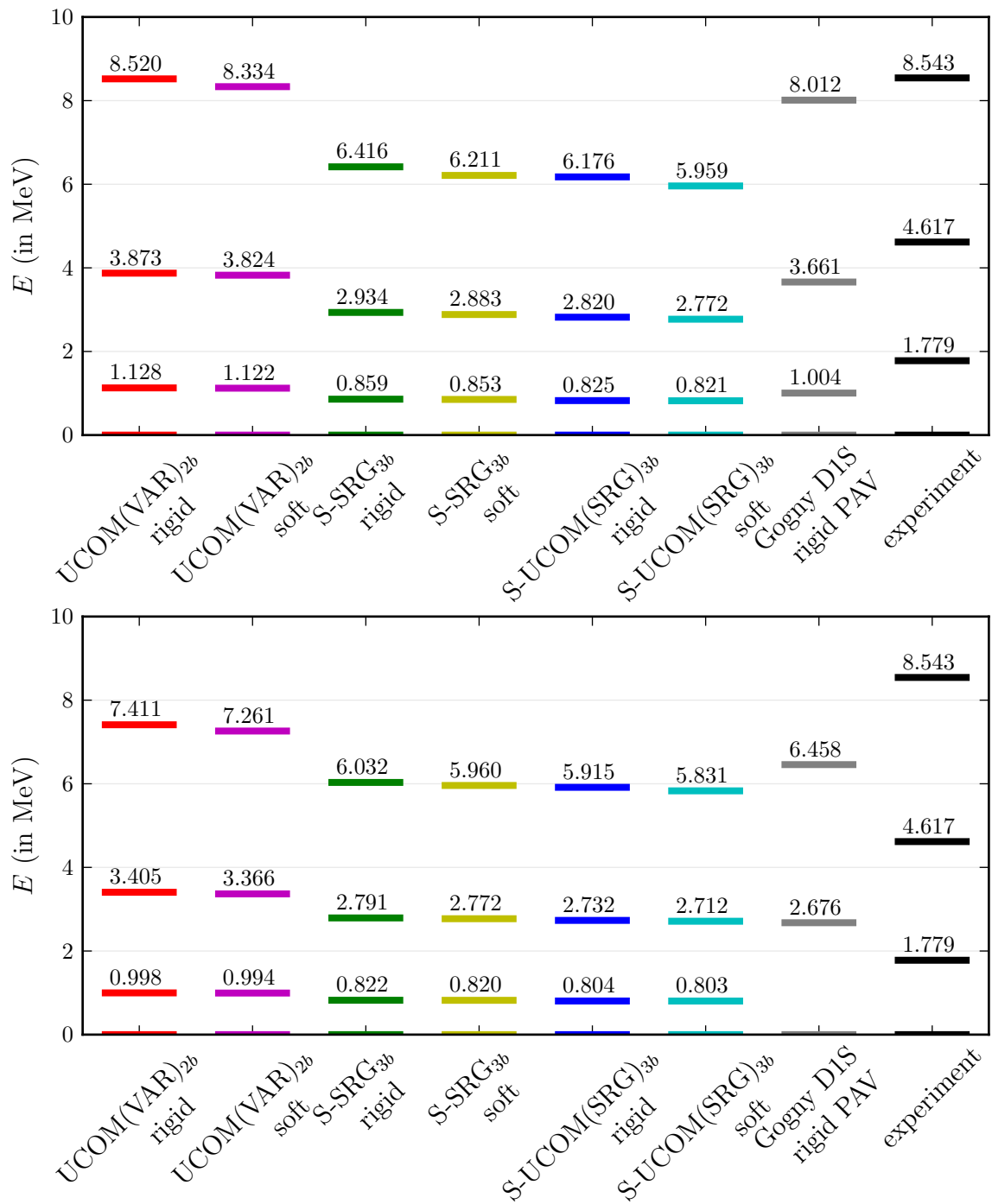Figure 5.17.: Ground-state rotational band of $^{20}$Ne. Experimental values from [SIM75].

Figure 5.18.: Ground-state rotational band of $^{28}\mathrm{Si}_o$ (top) and $^{28}\mathrm{Si}_p$ (bottom). Experimental values from [SIM75].

# 6. Collective Excitations in the RPA Framework

Electromagnetic transitions are an important observable when studying atomic nuclei —excitation spectra and transition strengths are the direct target of many experiments (for references and measured values, see chapter 7.6) and many other measurements also exploit the decay of excited states. Transition strengths are also well suited to compare different theoretical descriptions if one wants to go beyond simple bulk properties like binding energies or radii. Since transition strengths depend strongly on the wave functions of the participating states, small changes in the wave functions have a much stronger effect on the transition strengths than on bulk properties.

In this chapter, we discuss the Random Phase Approximation (RPA) and the calculation of transition strengths. We derive a method to obtain angular-momentum projected transition strengths from the RPA solutions. Finally, we discuss transition densities, which provide insight into the oscillation modes involved in the transitions.

## 6.1. RPA Method

### 6.1.1. Formalism

Excited states and ground states can be described by introducing particle-hole (ph) excitations to a HF ground state. If one allows for an infinite number of particles and holes, the expansion is exact. The Random Phase Approximation (RPA) can be seen as the first-order approximation of this expansion, the excited states are allowed to have contributions from one-particle-one-hole excitations with respect to the RPA ground state. The RPA ground state is not limited to simple one-particle-one-hole correlations on top of a HF ground state. It is the simplest method to include ground-state correlations and, therefore, is able to describe collective transitions like giant resonances, where the even simpler Tamm-Dancoff-Approximation, which retains the original HF ground state and only allows one-particle-one-hole contributions in the excited states, fails [Row70].

Since RPA with realistic interactions has already been used successfully for the description of spherical nuclei [PPHR06, Gün11] it is a natural starting point for the treatment of deformed nuclei. The RPA for deformed nuclei differs in some points from its spherical variant:

- The single-particle basis is larger than in the spherical case and the particle-hole basis cannot be reduced by coupling to a certain angular momentum. However, the particle-hole basis might still be reduced by other, remaining symmetries.

- Since the intrinsic states used to calculate transition strengths do not have good angular momentum, angular-momentum projection has to be employed to obtain observables in the lab frame.

The RPA formalism can be derived by the so called equations of motion (EOM) method. Since this method has been discussed by many authors [Row70, RS80, Suh07], only the most crucial points will be repeated here.

We start with a ground state $|0\rangle$ and an excited state $|\omega\rangle$ connected by the excitation operator $\hat{Q}_\omega^\dagger$

$$|\omega\rangle = \hat{Q}_\omega^\dagger|0\rangle \quad , \tag{6.1}$$

both satisfying the Schrödinger equation. The annihilation operator corresponding to $\hat{Q}_\omega^\dagger$ fulfills

$$\hat{Q}_\omega|0\rangle = 0 \quad , \tag{6.2}$$

which defines the ground state. The equation of motion of the excitation operator $\hat{Q}_\omega^\dagger$ is

$$[\hat{H}, \hat{Q}_\omega^\dagger]|0\rangle = (E_\omega - E_0)\hat{Q}_\omega^\dagger|0\rangle \quad . \tag{6.3}$$

Forming a commutator with the arbitrary state $\langle 0|\delta\hat{Q}$, we get

$$\langle 0|[\delta\hat{Q}, [\hat{H}, \hat{Q}_\omega^\dagger]]|0\rangle = (E_\omega - E_0)\langle 0|[\delta\hat{Q}, \hat{Q}_\omega^\dagger]|0\rangle \quad . \tag{6.4}$$

Since $\langle 0|\delta\hat{Q}$ is completely arbitrary, it spans the complete Hilbert space and the scalar product in (6.4) retains all information. Equation (6.4) is equivalent to the Schrödinger equation.

Now we leave the exact picture of the full Schrödinger equation and introduce the first approximation. We make the following ansatz for the excitation operator

$$\hat{Q}_\omega^\dagger = \sum_{mi} X_{mi}^\omega \, \hat{a}_m^\dagger \hat{a}_i - \sum_{mi} Y_{mi}^\omega \, \hat{a}_i^\dagger \hat{a}_m \quad , \tag{6.5}$$

with the HF creation and annihilation operators $\hat{a}^\dagger$ and $\hat{a}$. This ansatz is the first of the two defining features of the standard RPA—when considering higher-order RPAs (e.g. Second RPA), the excitation operator also includes higher-order particle-hole terms. The index $m$ (and later also $n$) denotes states above the Fermi level, while $i$ (and $j$,$k$) denotes the states below. The RPA ground state is then given by

$$\hat{Q}_\omega|\text{RPA}\rangle = 0 \quad . \tag{6.6}$$

The $Y$-amplitude part of $\hat{Q}_\omega^\dagger$ makes clear that the RPA ground state $|\text{RPA}\rangle$ is different from the HF ground state $|\text{HF}\rangle$, as $\hat{Q}_\omega|\text{HF}\rangle \neq 0$. Therefore, the RPA ground state has to include particle-hole correlations.

To exhaust the full subspace spanned by $\hat{Q}_\omega^\dagger$ with $\delta\hat{Q}$, we have to consider the two forms $\delta\hat{Q} = \hat{a}_m^\dagger \hat{a}_i$ and $\delta\hat{Q} = \hat{a}_i^\dagger \hat{a}_m$, leading to the following equations:

$$\begin{aligned}\langle \text{RPA}|[\hat{a}_i^\dagger\hat{a}_m, [\hat{H}, \hat{Q}_\omega^\dagger]]|\text{RPA}\rangle &= E_\omega \langle \text{RPA}|[\hat{a}_i^\dagger\hat{a}_m, \hat{Q}_\omega^\dagger]|\text{RPA}\rangle \\ \langle \text{RPA}|[\hat{a}_m^\dagger\hat{a}_i, [\hat{H}, \hat{Q}_\omega^\dagger]]|\text{RPA}\rangle &= E_\omega \langle \text{RPA}|[\hat{a}_m^\dagger\hat{a}_i, \hat{Q}_\omega^\dagger]|\text{RPA}\rangle \quad ,\end{aligned} \tag{6.7}$$

where the ground-state energy was shifted to $E_0 = 0$. In the following, $E_\omega$ always refers to the excitation energy, i.e., the energy difference between the excited state and the ground-state.

The equations (6.7) are the RPA equations of motion. Since a commutator of two operators has a particle-rank one lower than the rank of the product of the operators (the commutator of two one-body operators is a one-body operator), the dependence on two-body correlations in the ground-state wave function is reduced. This is of no importance if the exact ground-state wave functions are used, but at this point, we have to introduce the second defining feature of the RPA: the so-called *quasi-boson approximation* (QBA). We assume that all expectation values of commutators are equal to their corresponding HF values and, therefore, replace the RPA ground state with the HF ground state whenever calculating expectation values of commutators. Since HF is a mean-field method, we cannot expect the HF ground state to correctly describe two-body correlations. However, the method is suitable to deal with single-particle operators like the commutators introduced in the EOM approach.

Equation (6.7) can then be expressed as a non-hermitian eigenvalue problem, consisting of the submatrices $\mathsf{A}$ and $\mathsf{B}$.

$$\begin{pmatrix} \mathsf{A} & \mathsf{B} \\ \mathsf{B}^* & \mathsf{A}^* \end{pmatrix} \begin{pmatrix} \mathsf{X}^\omega \\ \mathsf{Y}^\omega \end{pmatrix} = E_\omega \begin{pmatrix} 1 & 0 \\ 0 & -1 \end{pmatrix} \begin{pmatrix} \mathsf{X}^\omega \\ \mathsf{Y}^\omega \end{pmatrix} \tag{6.8}$$

The matrix on the l.h.s. is called the RPA matrix and the matrix on the r.h.s. the metric matrix. The dimension of the RPA matrix is twice the number of all possible particle-hole pairs, which are defined by the indices $m$ and $i$. Construction of the particle-hole basis is the subject of the following subsection. The matrix elements of the $\mathsf{A}$ and $\mathsf{B}$ submatrices are defined by

$$\begin{aligned} A_{minj} &= \langle \mathrm{HF} | [\hat{a}_i^\dagger \hat{a}_m, [\hat{H}, \hat{a}_n^\dagger \hat{a}_j]] | \mathrm{HF} \rangle = (\varepsilon_m - \varepsilon_i) \delta_{mn} \, \delta_{ij} + \langle m, j | \hat{H} | i, n \rangle \quad, \\ B_{minj} &= -\langle \mathrm{HF} | [\hat{a}_i^\dagger \hat{a}_m, [\hat{H}, \hat{a}_j^\dagger \hat{a}_n]] | \mathrm{HF} \rangle = \langle m, n | \hat{H} | i, j \rangle \quad. \end{aligned} \tag{6.9}$$

If the Hamiltonian includes a three-body interaction, the following terms have to be added to eq. (6.9) [Tri12]

$$\begin{aligned} A_{minj}^{(3)} &= \sum_k^A \langle m, j, k | \hat{H} | i, n, k \rangle \quad, \\ B_{minj}^{(3)} &= \sum_k^A \langle m, n, k | \hat{H} | i, j, k \rangle \quad. \end{aligned} \tag{6.10}$$

## 6.1.2. Particle-Hole Basis for Axially Symmetric Nuclei

Before discussing the properties of the RPA solutions, we take a closer look at the particle-hole pairs from the excitation operator. As already discussed in chapter 4.2.1, any axially symmetric mean-field Hamiltonian only connects states where the sums of the $k$ (or $m_j$) quantum numbers in the bra and ket state are equal. If it is symmetric with respect to the $x$-$y$ plane, it only connects states with equal parity $\pi$.

The single-particle states of axially symmetric HF solutions have a well defined $k$ quantum number and parity $\pi$ (section 4.2.1). This leads to an RPA matrix (eq. (6.8)) with a block structure with respect to $\pi$ and the absolute value of $k$. The A matrix only connects equal parity ph pairs with the same $k$, while the B matrix only connects those with equal parity and opposite sign, but equal absolute value of $k$.

The single-particle states for HF ground states of even-even nuclei are degenerate with respect to the sign of $k$ due to time-reversal invariance. Consequently, for each ph pair with a certain $k_{ph}$ value there exists a corresponding ph pair with $-k_{ph}$, which is identical in all other aspects. For an excitation operator $\hat{Q}_\omega^\dagger$, where the $X$ amplitudes are associated with ph pairs with $+k_{ph}$ and the $Y$ amplitudes are associated with ph pairs with $-k_{ph}$, there also exists a second excitation operator $\hat{Q}_{\omega'}^\dagger$, where the $X$ and $Y$ amplitudes are associated with the corresponding ph pairs of opposite sign. Since these ph pairs behave identically, the excitation energies of $\hat{Q}_\omega^\dagger$ and $\hat{Q}_{\omega'}^\dagger$ are the same. As a consequence, all excitations with $k_{ph} \neq 0$ are twofold degenerate. For the special case of closed shell nuclei, the degeneracy extends over all $k$ states, and the number of degenerate excitations increases to $2J + 1$.

In the prior discussion, we did not specify the types of nucleons involved in the ph-pairs. The RPA matrix has a block structure with respect to the isospin projection quantum number of the ph-pairs $t_{ph} = t_p - t_h$, just as for the $k$ quantum number. But since we only consider charge-conserving excitations, the $|t_{ph}| = 1$ components do not contribute. Therefore, we only consider the case of $t_{ph} = 0$.

### 6.1.3. Properties of the RPA Solutions

We now review some general properties of the RPA solutions. Due to the structure of the RPA matrix, the eigenvectors are not orthogonal with respect to the unit matrix, however, they are orthogonal with respect to the metric matrix. Applying the QBA yields the orthonormality condition

$$\langle \omega | \omega' \rangle = \delta_{\omega\omega'} \approx \langle \mathrm{HF} | [\hat{Q}_\omega, \hat{Q}_{\omega'}^\dagger] | \mathrm{HF} \rangle = \sum_{mi} \left( X_{mi}^{\omega*} X_{mi}^{\omega'} - Y_{mi}^{\omega*} Y_{mi}^{\omega'} \right) \quad . \tag{6.11}$$

The unusual normalization condition of the RPA solutions has to be taken into account in the computer code.

From the structure of the RPA matrix (6.8), it is evident that the dimension of the RPA matrix is twice the dimension of the particle-hole space, which leads to the same number of solutions for the eigenvalue problem. For each eigenvector $(X^\omega, Y^\omega)$ with a positive eigenvalue $E_\omega$, there exists another eigenvector $(X^{\omega*}, Y^{\omega*})$ with the corresponding negative eigenvalue $-E_\omega$. Since $E_\omega$ denotes the excitation energy, the negative energy solutions are unphysical.

### 6.1.4. Spurious Solutions

It is possible that the RPA solutions also contain spurious states. When the HF solution violates a symmetry of the Hamiltonian, spurious states can occur. For this

work, two kinds of spurious states are relevant: spurious center-of-mass excitations and spurious rotations (which are not actually rotations). Both spurious excitations are caused by a movement of the nucleus, where the corresponding mean-field potential stays fixed. A restoring force due to the fixed potential then leads to an oscillation. The spurious rotations are, therefore, not full rotations, but only oscillations of a rigid nucleus around an axis perpendicular to the symmetry axis. Spurious center-of-mass motion can be present for E1 ($J^\Pi = 1^-$) transitions ($K = 0$ and $K = \pm 1$, $\Pi = -$) [Row70] and spurious rotational motion contributes to E2 ($J^\Pi = 2^+$) transitions ($K = \pm 1$ components only, $\Pi = +$) [BM75].

Formally, the spurious states arise when the Hamiltonian commutes with the operator generating the symmetry breaking operation, but not with the HF single-particle density operator $\hat{\rho}$ (a more elaborate discussion can be found in [Row70, RS80]). The spurious center-of-mass excitation is generated by the center-of-mass momentum operator $\hat{\boldsymbol{P}}$ and the spurious rotational excitations by the angular momentum operator $\hat{\boldsymbol{J}}$. If we have

$$[\hat{\rho}, \hat{\boldsymbol{P}}] \neq 0 \quad \text{and} \quad [\hat{H}, \hat{\boldsymbol{P}}] = 0 \quad , \tag{6.12}$$

it is clear, that a spurious solution of the RPA equation (6.7) with zero energy exists

$$\langle 0 | [\delta \hat{Q}, [\hat{H}, \hat{\boldsymbol{P}}]] | 0 \rangle = 0 \quad . \tag{6.13}$$

These solutions are not normalizable with respect to (6.11).

Due to the zero energy, the spurious modes can be identified and in principle do not contaminate the results. However, this is only true for an exact solution of the RPA eigenvalue problem in a full Hilbert space. Since the model space has to be truncated at some point, (6.13) does not hold exactly. Spurious solutions usually have a low energy and they may not be normalizable. As we see later when discussing our results, the spurious center-of-mass states have almost zero energy and are very well separated from actual excitations. For the spurious rotations, the situation is not as clear, however, states with large spurious contributions can be identified by the intrinsic transition densities.

At this point, a comment on self-consistency is in order. The RPA and HF calculations carried out in this work are fully self-consistent. This means, that the HF solution is obtained by the usual self-consistent method and that the RPA calculations use the same reference basis, truncation and Hamiltonian as the HF calculations and that there is no cutoff for the ph-basis. As discussed by a number of authors for the example of the spurious center-of-mass mode [PPHR06, AS04, CGBQ00], the impact of the spurious state is reduced if one strictly implements a self-consistent procedure. Also, it has been found that the impact of the spurious center-of-mass mode is reduced when working with realistic NN interactions [PPHR06].

## 6.2. Electromagnetic Transitions

In this section, we consider electromagnetic transitions, transition operators and their treatment in the RPA framework. Electromagnetic transitions are due to the coupling

of the nucleus to an external electromagnetic field. Expressions for the transition operators are usually derived by first-order time-dependent perturbation theory and in a *long wavelength limit*, i.e. the wavelength is large compared to the nuclear radius $r_0$ [RS80]. The *long wavelength limit* is valid as long as

$$E_\gamma \ll \frac{\hbar c}{r_0} \cdot A^{-1/3} = 197 \cdot A^{-1/3} \, \text{MeV} \quad . \tag{6.14}$$

For sd-shell nuclei, this means $E_\gamma \ll 58 \, \text{MeV}$ ($A \leq 40$). For the energy range of pygmy- and giant resonances, i.e. $E_\gamma \approx 5 - 30 \, \text{MeV}$, the validity of $E_\gamma \ll 58 \, \text{MeV}$ is certainly questionable, but it is a customary approximation [PHPR12, HPR11, Gün11, LPD$^+$10]. For heavy nuclei like $^{208}$Pb, the *long wavelength limit* is definitely not valid in a strict sense. However, considering other inaccuracies, this approximation may be justified.

Electromagnetic transition operators are classified into electric and magnetic transitions based on angular momentum $\lambda$ and parity $\pi$. We define the values of $\pi$ as 0 for even parity and 1 for odd parity; when not in a numerical context, we also use + for even and − for odd parity. Electric transitions (E$\lambda$) have $\lambda + \pi = $ even, while magnetic transitions (M$\lambda$) have $\lambda + \pi = $ odd. When the type of the transition is not fixed, it is denoted by the symbol $\sigma$, i.e. an arbitrary transition is denoted by $\sigma\lambda$. In this work, we consider electric monopole, dipole and quadrupole transitions (E0, E1, E2).

## 6.2.1. Transition Operators

In the limit of the aforementioned approximations, the transition operator for electric transitions is given by ([RS80])

$$\hat{Q}_{\lambda\mu} = \sum_i^A e_i \, \hat{r}_i^\lambda \, Y_{\lambda\mu}(\hat{\Omega}_i) \tag{6.15}$$

and the magnetic transition operator by ([RS80])

$$\hat{M}_{\lambda\mu} = \frac{\mu_N}{\hbar c} \sum_i^A \left( \frac{2}{\lambda + 1} g_l^i \, \hat{\boldsymbol{l}}_i + g_s^i \, \hat{\boldsymbol{s}}_i \right) \boldsymbol{\nabla} \, \hat{r}_i^\lambda \, Y_{\lambda\mu}(\hat{\Omega}_i) \quad . \tag{6.16}$$

Whenever the exact type of the transition is not important, the symbol $\hat{T}_{\lambda\mu}$ is used. The spin $g$-factors $g_s$ for protons and neutrons are given by

$$g_s^{\text{p}} = 5.586 \quad , \qquad g_s^{\text{n}} = -3.826 \quad , \tag{6.17}$$

and the orbital $g$-factors by

$$g_l^{\text{p}} = 1 \quad , \qquad g_l^{\text{n}} = 0 \quad . \tag{6.18}$$

It is customary to write the electric transition operator as the sum of an isoscalar and an isovector part

$$\hat{Q}_{\lambda\mu} = \frac{1}{2}\left(\hat{Q}_{\lambda\mu}^{\mathrm{IS}} + \hat{Q}_{\lambda\mu}^{\mathrm{IV}}\right) \tag{6.19}$$

$$\hat{Q}_{\lambda\mu}^{\mathrm{IS}} = e\sum_i^P \hat{r}_i^\lambda\, Y_{\lambda\mu}(\hat{\Omega}_i) + e\sum_i^N \hat{r}_i^\lambda\, Y_{\lambda\mu}(\hat{\Omega}_i) \tag{6.20}$$

$$\hat{Q}_{\lambda\mu}^{\mathrm{IV}} = e\sum_i^P \hat{r}_i^\lambda\, Y_{\lambda\mu}(\hat{\Omega}_i) - e\sum_i^N \hat{r}_i^\lambda\, Y_{\lambda\mu}(\hat{\Omega}_i) \quad. \tag{6.21}$$

For some transitions, the generic transition operators (6.15) and (6.16) can not be used. Since the first-order term of the electric monopole transition is a constant, it cannot induce transitions and the second-order term has to be used. We define the operator as

$$\hat{Q}_{00} = \sum_i^A e_i\, \hat{r}_i^2\, Y_{00}(\hat{\Omega}_i) \quad. \tag{6.22}$$

Since the electric dipole operator is potentially contaminated by spurious center-of-mass contributions (see section 6.1.4), corrected transition operators are used ([GS81] and [HvdW01])

$$\hat{Q}_{1\mu}^{\mathrm{IS}} = e\sum_i^A \left(\hat{r}_i^3 - \tfrac{5}{3}R_{\mathrm{ms}}\,\hat{r}_i\right) Y_{1\mu}(\hat{\Omega}_i) \quad, \tag{6.23}$$

$$\hat{Q}_{1\mu}^{\mathrm{IV}} = e\frac{N}{A}\sum_i^Z \hat{r}_i\, Y_{1\mu}(\hat{\Omega}_i) - e\frac{Z}{A}\sum_i^N \hat{r}_i\, Y_{1\mu}(\hat{\Omega}_i) \quad, \tag{6.24}$$

with the mean-square radius of the nucleus $R_{\mathrm{ms}}$. The corrected isoscalar operator is constructed by a superposition of leading-order and next-to-leading-order approximations, with a free parameter fixed to $\frac{5}{3}R_{\mathrm{ms}}$ by the requirement of translational invariance. The corrected operator for isovector transitions merely introduces weighting factors, which take the difference in the numbers of protons and neutrons into account. Since all nuclei considered in this work have an equal number of protons and neutrons, this does only amount to a global factor of $\frac{1}{2}$.

In principle, a unitary transformation has to be applied to the transition operators, but considering the missing higher-order correlations in the RPA and other factors (see section 2.2.6), it is justified to neglect this transformation.

## 6.2.2. Single-Particle Matrix Elements

After lengthy but straightforward calculation, one arrives at the reduced single-particle matrix elements of the transition operators (see [Suh07] for a little more detail). The state indices $a$ and $b$ contain all relevant quantum numbers, i.e. $n$, $l$, $j$ and $m_j$.

$$(a\|\hat{Q}_\lambda\|b) = e \cdot \mathcal{E}_{ab}^\lambda \cdot \mathcal{R}_{ab}^\lambda \tag{6.25a}$$

$$(a\|\hat{M}_\lambda\|b) = \frac{\mu_N}{c} \cdot \mathcal{M}_{ab}^\lambda \cdot \mathcal{R}_{ab}^{\lambda-1} \tag{6.25b}$$

We separated the radial part $\mathcal{R}_{ab}^\lambda$ from the rest of the matrix elements. The radial part is due to the $\hat{r}^\lambda$ dependence of equations (6.15) and (6.16). Since we are looking at electromagnetic transitions, the nucleons $a$ and $b$ must be of the same type. The radial part is given by (derived in appendix A.1)

$$
\mathcal{R}_{ab}^\lambda = b^\lambda \sqrt{n_a!\, n_b!\, \Gamma(n_a + l_a + \tfrac{3}{2})\, \Gamma(n_b + l_b + \tfrac{3}{2})}
$$
$$
\times \sum_{i_a, i_b=0}^{n_a, n_b} \frac{(-1)^{i_a+i_b}\, \Gamma(i_a + i_b + \frac{\lambda + l_a + l_b + 3}{2})}{i_a!\, i_b!\, (n_a - i_a)!\, (n_b - i_b)!\, \Gamma(l_a + i_a + \tfrac{3}{2})\, \Gamma(l_b + i_b + \tfrac{3}{2})} \quad , \quad (6.26)
$$

while $\mathcal{E}_{ab}^\lambda$ and $\mathcal{M}_{ab}^\lambda$ are given by (for $g$-factors see (6.17) and (6.18))

$$
\mathcal{E}_{ab}^\lambda = \frac{(-1)^{j_b+\lambda-\frac{1}{2}}}{\sqrt{4\pi}} \frac{1 + (-1)^{l_a+l_b+\lambda}}{2} \hat{\lambda}\hat{j}_a\hat{j}_b \begin{pmatrix} j_a & j_b & \lambda \\ \frac{1}{2} & -\frac{1}{2} & 0 \end{pmatrix} \tag{6.27a}
$$

$$
\mathcal{M}_{ab}^\lambda = \frac{(-1)^{j_b+\lambda-\frac{1}{2}}}{\sqrt{4\pi}} \frac{1 - (-1)^{l_a+l_b+\lambda}}{2} \hat{\lambda}\hat{j}_a\hat{j}_b \begin{pmatrix} j_a & j_b & \lambda \\ \frac{1}{2} & -\frac{1}{2} & 0 \end{pmatrix}
$$
$$
\times (\lambda - \kappa)\left( g_l\left(1 + \frac{\kappa}{1 + \lambda}\right) - \tfrac{1}{2}g_s \right) \tag{6.27b}
$$
$$
\kappa = (-1)^{l_a+j_a+\frac{1}{2}}(j_a + \tfrac{1}{2}) + (-1)^{l_b+j_b+\frac{1}{2}}(j_b + \tfrac{1}{2}) \quad .
$$

The above decomposition allows us to write the special transition operators (6.22), (6.23), (6.24) as

$$
(a\|\hat{Q}_0\|b) = e \cdot \mathcal{E}_{ab}^0 \cdot \mathcal{R}_{ab}^2 \tag{6.28}
$$
$$
(a\|\hat{Q}_1^{\mathrm{IS}}\|b) = e \cdot \mathcal{E}_{ab}^1 \cdot \left(\mathcal{R}_{ab}^3 - \tfrac{5}{3}R_{\mathrm{ms}}\,\mathcal{R}_{ab}^1\right) \tag{6.29}
$$
$$
(a\|\hat{Q}_1^{\mathrm{IV}}\|b) = e \cdot \mathcal{E}_{ab}^1 \cdot \mathcal{R}_{ab}^1 \cdot C \tag{6.30}
$$

with $C = N/A$ for protons and $C = -Z/A$ for neutrons.

The $\mu$ components of the transitions can be derived from the reduced matrix elements via the Wigner-Eckart theorem [Edm60, eq 5.4.1]

$$
\langle a|\hat{T}_{\lambda\mu}|b\rangle = (-1)^{j_a - m_a} \begin{pmatrix} j_a & \lambda & j_b \\ -m_a & \mu & m_b \end{pmatrix} (a\|\hat{T}^\lambda\|b) \quad . \tag{6.31}
$$

## 6.2.3. Transition Strengths

Since only mean lifetimes or cross sections can be observed, the matrix elements of the transition operators can not be measured directly. The transition probability (the inverse of the mean lifetime) $T$ for a transition $\sigma\lambda$ is given by [Suh07]

$$
T_{i\to f}^{\sigma\lambda} = \frac{2}{\varepsilon_0\hbar} \frac{\lambda + 1}{\lambda((2\lambda + 1)!!)^2} \left(\frac{E_\gamma}{\hbar c}\right)^{2\lambda+1} B(\sigma\lambda; J_i \to J_f) \quad , \tag{6.32}
$$

but it is customary to look at the reduced transition probability

$$
B(\sigma\lambda; J_i \to J_f) = \frac{1}{2J_i + 1}|(J_i\|\hat{T}^\lambda\|J_f)|^2 \quad . \tag{6.33}
$$

Since we only consider excitations from the ground-state of even-even nuclei ($J^{\Pi} = 0^+$) to excited states, the $J$-factor is always 1.

## 6.2.4. Transition Amplitudes in the RPA Framework

Since no publications regarding exact angular-momentum projection for RPA transition strengths are known to the author, this subject is treated in great detail.

The unprojected transition amplitudes to the RPA ground state are obtained by straightforward calculation. We start with the exact expression

$$\langle \mathrm{RPA}|\hat{T}_{\lambda\mu}|\omega\rangle = \langle \mathrm{RPA}|\hat{T}_{\lambda\mu}\,\hat{Q}_\omega^\dagger|\mathrm{RPA}\rangle = \langle \mathrm{RPA}|[\hat{T}_{\lambda\mu}, \hat{Q}_\omega^\dagger]|\mathrm{RPA}\rangle \quad , \tag{6.34}$$

apply the QBA

$$\langle \mathrm{RPA}|[\hat{T}_{\lambda\mu}, \hat{Q}_\omega^\dagger]|\mathrm{RPA}\rangle \approx \langle \mathrm{HF}|[\hat{T}_{\lambda\mu}, \hat{Q}_\omega^\dagger]|\mathrm{HF}\rangle \tag{6.35}$$

and arrive at the following result

$$\langle \mathrm{HF}|[\hat{T}_{\lambda\mu}, \hat{Q}_\omega^\dagger]|\mathrm{HF}\rangle = \sum_{mi} \left( X_{mi}^\omega \langle \mathrm{HF}|\hat{T}_{\lambda\mu}\,\hat{a}_m^\dagger \hat{a}_i|\mathrm{HF}\rangle + Y_{mi}^\omega \langle \mathrm{HF}|\hat{a}_i^\dagger \hat{a}_m\,\hat{T}_{\lambda\mu}|\mathrm{HF}\rangle \right)$$

$$= \sum_{mi} \left( X_{mi}^\omega \langle i|\hat{T}_{\lambda\mu}|m\rangle + Y_{mi}^\omega \langle m|\hat{T}_{\lambda\mu}|i\rangle \right) \quad .$$

It would be desirable to derive the projected RPA transition amplitudes in a similar manner directly from the equation for projected transition amplitudes (3.21)

$$(J_0\|\hat{T}^\lambda\|J_\omega) = (2\,J_0 + 1)\,N_0\,N_\omega \sum_{\substack{K_0 K_\omega \\ \mu}} g_{K_0}^{(0)} g_{K_\omega}^{(\omega)} (-1)^{\lambda + J_\omega + K_0}$$
$$\times \begin{pmatrix} J_0 & J_\omega & \lambda \\ -K_0 & K_0 - \mu & \mu \end{pmatrix} \langle \mathrm{RPA}|\hat{T}_{\lambda\mu}\,\hat{P}_{K_0-\mu, K_\omega}^{J_\omega}\,\hat{Q}_\omega^\dagger|\mathrm{RPA}\rangle \quad . \tag{6.36}$$

However, this is not possible in a consistent and unambiguous way. The canonical way of the RPA is to replace pairs of operators with their commutators and the RPA ground state with the HF ground state. This treatment is not possible because of the projection operator. Since the projection operator projects a fixed set of quantum numbers onto another fixed set, these quantum numbers would have to change according to the order of the operators $\hat{T}_\mu^\lambda$ and $\hat{Q}_\omega^\dagger$—otherwise the projection operator would annihilate the states. One could relax the requirement of a commutator and allow anything, that vanishes for the true RPA states, but still gives a $Y$-amplitude contribution in the QBA, to be added. Then, the quantum numbers of the projection operator could be changed to match the other operators. However, this scheme also allows the introduction of an arbitrary phase—and this freedom has to be exploited if one wants to reproduce the unprojected results for spherical nuclei. This phase is in principle arbitrary and would have to be fixed somehow, e.g. by the requirement to reproduce the unprojected results for spherical nuclei. But since this treatment is ambiguous and leaves much to be desired in terms of simplicity, we opt for a different, less ambiguous approach. For monopole transitions in spherical nuclei, which preserve

the spherical symmetry and, therefore, are not affected by the projection operator, this approach reproduces the unprojected case by construction.

To calculate the projected transition amplitudes, we again consider the unprojected intrinsic transition amplitudes. The complete transition amplitude of multipolarity $\lambda$ including normalization factors is given by

$$
\begin{aligned}
\frac{\langle \mathrm{RPA}|\hat{T}^{\lambda}|\omega\rangle}{\sqrt{\langle \mathrm{RPA}|\mathrm{RPA}\rangle \langle\omega|\omega\rangle}} &= \sum_{\mu} \frac{\langle \mathrm{RPA}|\hat{T}_{\lambda\mu}|\omega\rangle}{\sqrt{\langle \mathrm{RPA}|\mathrm{RPA}\rangle \langle\omega|\omega\rangle}} \\
&= \sum_{\mu} \frac{\langle \mathrm{RPA}|\hat{T}_{\lambda\mu}\,\hat{Q}_{\omega}^{\dagger}|\mathrm{RPA}\rangle}{\sqrt{\langle \mathrm{RPA}|\mathrm{RPA}\rangle \langle \mathrm{RPA}|\hat{Q}_{\omega}\,\hat{Q}_{\omega}^{\dagger}|\mathrm{RPA}\rangle}} \quad.
\end{aligned}
\tag{6.37}
$$

The numerator is given by eq. (6.36)

$$
\begin{aligned}
\sum_{\mu}\langle \mathrm{HF}|[\hat{T}_{\lambda\mu},\hat{Q}_{\omega}^{\dagger}]|\mathrm{HF}\rangle &= \sum_{\mu,mi}\left( X_{mi}^{\omega}\,\langle \mathrm{HF}|\hat{T}_{\lambda\mu}\,\hat{a}_{m}^{\dagger}\hat{a}_{i}|\mathrm{HF}\rangle + Y_{mi}^{\omega}\,\langle \mathrm{HF}|\hat{a}_{i}^{\dagger}\hat{a}_{m}\,\hat{T}_{\lambda\mu}|\mathrm{HF}\rangle\right) \\
&= \sum_{\mu,mi}\left( X_{mi}^{\omega}\,\langle i|\hat{T}_{\lambda\mu}|m\rangle + Y_{mi}^{\omega}\,\langle m|\hat{T}_{\lambda\mu}|i\rangle\right) \quad.
\end{aligned}
\tag{6.38}
$$

Assuming real matrix elements, we write the solution in a form that is more suitable for use in the projected formalism.

$$
\begin{aligned}
\sum_{\mu}\langle \mathrm{HF}|[\hat{T}_{\lambda\mu},\hat{Q}_{\omega}^{\dagger}]|\mathrm{HF}\rangle &= \sum_{\mu,mi}\left( X_{mi}^{\omega}\,\langle \mathrm{HF}|\hat{T}_{\lambda\mu}\,\hat{a}_{m}^{\dagger}\hat{a}_{i}|\mathrm{HF}\rangle + Y_{mi}^{\omega}\,(-1)^{\mu}\langle \mathrm{HF}|\hat{T}_{-\mu}^{\lambda}\,\hat{a}_{m}^{\dagger}\hat{a}_{i}|\mathrm{HF}\rangle\right) \\
&= \sum_{mi}\left( X_{mi}^{\omega} + (-1)^{k_{mi}}Y_{mi}^{\omega}\right) \sum_{\mu}\langle \mathrm{HF}|\,\hat{T}_{\lambda\mu}\,\hat{a}_{m}^{\dagger}\hat{a}_{i}|\mathrm{HF}\rangle
\end{aligned}
\tag{6.39}
$$

We renamed $-\mu$ to $\mu$ in the $Y$ amplitude part and used that $k$ is a well defined quantum number in axially symmetric nuclei (the parity of $k$ would be sufficient, as it is expected for triaxial even-even nuclei like $^{24}$Mg).[1]

To get the projected transition amplitudes, we simply include the $XY$-factor in the formula for the axially symmetric projected transition amplitudes (3.29) in a straight-

---

[1] We could interpret eq. (6.39) as the transition amplitude between the two states

$$
|\mathrm{HF}\rangle \quad \text{and} \quad \sum_{mi}\left( X_{mi}^{\omega} + (-1)^{k_{mi}}Y_{mi}^{\omega}\right) \hat{a}_{m}^{\dagger}\hat{a}_{i}|\mathrm{HF}\rangle \quad,
$$

and derive the projected amplitudes from these states. However, since this picture breaks down when treating the normalization factors (for both, the projected and unprojected formalism), there is no benefit to it.

forward and unambiguous way

$$
\begin{aligned}
&(\mathrm{RPA}\|\hat{T}^\lambda\|\omega) \\
&= (2\,J_0 + 1)\, N_0\, N_\omega\, (-1)^{J_0 - K_0} \sum_{mi} \left( X^\omega_{mi} + (-1)^{K_{mi}} Y^\omega_{mi} \right) \\
&\quad \times \sum_\mu \begin{pmatrix} J_0 & \lambda & J_\omega \\ -K_0 & \mu & K_0 - \mu \end{pmatrix} \langle \mathrm{HF} | \hat{T}_{\lambda\mu}\, \hat{P}^{J_\omega}_{K_0 - \mu, k_{mi}}\, \hat{a}^\dagger_m \hat{a}_i | \mathrm{HF} \rangle \quad .
\end{aligned}
\tag{6.40}
$$

We treat the normalization factors accordingly. The normalization factor from the RPA ground state is given by

$$
N_0 = \sqrt{\langle \mathrm{HF} | \hat{P}^{J_0}_{K_0 K_0} | \mathrm{HF} \rangle}^{\,-1} \quad .
\tag{6.41}
$$

For $N_\omega$, we again look at the unprojected case

$$
\begin{aligned}
\langle \mathrm{RPA} | \hat{Q}_\omega\, \hat{Q}^\dagger_\omega | \mathrm{RPA} \rangle &= \langle \mathrm{RPA} | [\hat{Q}_\omega, \hat{Q}^\dagger_\omega] | \mathrm{RPA} \rangle \approx \langle \mathrm{HF} | [\hat{Q}_\omega, \hat{Q}^\dagger_\omega] | \mathrm{HF} \rangle \\
&= \sum_{mi} \langle \mathrm{HF} | (X^\omega_{mi}\, \hat{a}^\dagger_i\, \hat{a}_m - Y^\omega_{mi}\, \hat{a}^\dagger_m\, \hat{a}_i) \sum_{nj} (X^\omega_{nj}\, \hat{a}^\dagger_n\, \hat{a}_j - Y^\omega_{nj}\, \hat{a}^\dagger_j\, \hat{a}^\dagger_n) | \mathrm{HF} \rangle \\
&\quad - \sum_{mi} \langle \mathrm{HF} | (X^\omega_{mi}\, \hat{a}^\dagger_i\, \hat{a}_m - Y^\omega_{mi}\, \hat{a}^\dagger_m\, \hat{a}_i) \sum_{nj} (X^\omega_{nj}\, \hat{a}^\dagger_n\, \hat{a}_j - Y^\omega_{nj}\, \hat{a}^\dagger_j\, \hat{a}^\dagger_n) | \mathrm{HF} \rangle \\
&= \sum_{mi,nj} \left( X^\omega_{mi}\, X^\omega_{nj} - Y^\omega_{mi}\, Y^\omega_{nj} \right) \langle \mathrm{HF} | \hat{a}^\dagger_i\, \hat{a}_m\, \hat{a}^\dagger_n\, \hat{a}_j | \mathrm{HF} \rangle \\
&= \sum_{mi} \left( X^\omega_{mi}\, X^\omega_{mi} - Y^\omega_{mi}\, Y^\omega_{mi} \right) \qquad \left( \overset{(6.11)}{=} 1 \right) \quad ,
\end{aligned}
\tag{6.42}
$$

and, therefore, use the following projected normalization factor $N_\omega$

$$
N_\omega = \sqrt{ \sum_{mi,nj} \left( X^\omega_{mi}\, X^\omega_{nj} - Y^\omega_{mi}\, Y^\omega_{nj} \right) \langle \mathrm{HF} | \hat{a}^\dagger_m \hat{a}_i\, \hat{P}^{J_\omega}_{K_{mi} K_{nj}}\, \hat{a}^\dagger_n \hat{a}_j | \mathrm{HF} \rangle }^{\,-1} \quad .
\tag{6.43}
$$

## 6.2.5. Sum Rules

Sum rules are a useful tool for the interpretation and comparison of different theoretical approaches to collective excitations. In general, sum rules are defined as

$$
S_k = \sum_\omega (E_\omega - E_0)^k |\langle \omega | \hat{T}_\lambda | 0 \rangle|^2 \quad .
\tag{6.44}
$$

The $k = 0$ sum rule is referred to as the *non energy-weighted sum rule* (NEWSR) and the $k = 1$ sum rule is referred to as the *energy-weighted sum rule* (EWSR).

The EWSR can be written as a double commutator involving the Hamiltonian [RS80].

$$
S_1 = \tfrac{1}{2} \langle 0 | [\hat{T}_{\lambda\mu}, [\hat{H}, \hat{T}_{\lambda\mu}]] | 0 \rangle
\tag{6.45}
$$

It has been shown in [Tho61] that, as long as there are no spurious solutions involved, both forms give the same results for a hermitian operator $\hat{T}$, if the RPA transition

strengths are used in (6.44) and the HF ground state in (6.45). If we keep in mind that $\hat{T}^{\dagger}_{\lambda\mu} = (-1)^{\mu}\hat{T}_{\lambda-\mu}$ and take our ph-basis into account, extension of the proof is straightforward. An intermediate state of the proof provides a more convenient way to write (6.45)

$$S_1 = \sum_{\substack{mi \\ nj}} \left( \langle m|\hat{T}_{\lambda\mu}|i\rangle\langle n|\hat{T}_{\lambda\mu}|j\rangle \, A_{minj} - (-1)^{\mu}\langle m|\hat{T}^{\lambda}_{-\mu}|i\rangle\langle n|\hat{T}^{\lambda}_{-\mu}|j\rangle \, B_{minj} \right) \quad , \quad (6.46)$$

which can be used to some extent to verify the computer code.

There are several classical sum rules, which evaluate the commutator by exploiting general algebraic relations between the transition operators and a simple approximation of the Hamiltonian, resulting in a single equation for the EWSR. Comparing the classical sum rules to the results of more elaborate theories obtained by (6.44) provides a benchmark for different theoretical models and gives insight into some features of more elaborate Hamiltonians, like momentum dependence. However, we have to keep in mind that the classical sum rules only apply for intrinsic transitions. To derive classical sum rules for projected transition strengths, one would have to make assumptions regarding the shape of the nucleus to evaluate the integrals for the projected transition strengths.

If we assume a local Hamiltonian without exchange terms, only the kinetic energy contributes to the commutator in (6.45) and the following classical forms of the EWSR can be derived [RS80]. For the isoscalar electric monopole transition, we get [2]

$$S^{\mathrm{IS}}(E0) = \frac{2\,\hbar^2\,e^2}{4\,\pi\,m}(N\,\langle R^n_{\mathrm{ms}}\rangle + Z\,\langle R^p_{\mathrm{ms}}\rangle) \quad . \quad (6.47)$$

For the isovector electric dipole transition, we arrive at the well known *Thomas-Reiche-Kuhn* (TRK) sum rule

$$S^{\mathrm{IV}}(E1) = \frac{9\,\hbar^2\,e^2}{8\,\pi\,m}\frac{N\,Z}{A} \quad . \quad (6.48)$$

Finally, the isoscalar quadrupole transition sum rule is given by

$$S^{\mathrm{IS}}(E2) = \frac{25\,\hbar^2\,e^2}{4\,\pi\,m}(N\,\langle R^n_{\mathrm{ms}}\rangle + Z\,\langle R^p_{\mathrm{ms}}\rangle) \quad . \quad (6.49)$$

Since the Hamiltonian used in this work is non-local, we do not expect the sum rules to be fulfilled exactly. For the isovector dipole sum rule (6.48), we can expect a large enhancement in the range of 100% [WKB73].

## 6.3. Intrinsic Transition Densities

To get a deeper insight into the structure of an excited state, one can investigate the shape of the nuclear vibration. Axially-symmetric deformed nuclei can either vibrate

---

[2] In [PPHR06, Her08, Gün11], the isoscalar monopole sum rule (6.47) is defined, according to the monopole transition operator, without the factor $4\pi$.

in the direction of the symmetry axis, or perpendicular to it. Vibrations along the symmetry axis, so called $\beta$-vibrations, conserve the symmetry, while vibrations along an axis perpendicular to the symmetry axis, so called $\gamma$-vibrations, destroy the axial symmetry. The shape of a vibration can be characterized by the amplitude of its density with respect to the ground-state density, i.e. the amplitude of an oscillation around the ground state. The first-order approximation of this density amplitude is called the *transition density*.

For the general derivation of the transition density, we follow [RS80]. We start by considering a wave packet consisting of the ground state $|0\rangle$ and excited states $|\omega\rangle$

$$|\psi(t)\rangle = c_0|0\rangle + \sum_\omega c_\omega|\omega\rangle \, e^{-iE_\omega t/\hbar} \quad . \tag{6.50}$$

The time-dependent density $\rho(\boldsymbol{r}, t)$ is, up to first order, given by

$$\rho(\boldsymbol{r}, t) = \langle\psi(t)| \sum_i^A \delta(\boldsymbol{r} - \hat{\boldsymbol{r}}_i)|\psi(t)\rangle$$
$$\approx \rho(\boldsymbol{r}) + \delta\rho(\boldsymbol{r}, t) \quad , \tag{6.51}$$

with the constant and vibrational parts

$$\rho(\boldsymbol{r}) = \langle 0| \sum_i^A \delta(\boldsymbol{r} - \hat{\boldsymbol{r}}_i)|0\rangle$$

$$\delta\rho(\boldsymbol{r}, t) = \sum_\omega c_\omega \, e^{-iE_\omega t/\hbar} \langle 0| \sum_i^A \delta(\boldsymbol{r} - \hat{\boldsymbol{r}}_i)|\omega\rangle \tag{6.52}$$
$$+ \sum_\omega c_\omega \, e^{iE_\omega t/\hbar} \langle\omega| \sum_i^A \delta(\boldsymbol{r} - \hat{\boldsymbol{r}}_i)|0\rangle \quad .$$

We get the transition density for a single excited state by applying a Fourier decomposition to the vibrational part

$$\delta\rho^\omega(\boldsymbol{r}) = \langle 0| \sum_i^A \delta(\boldsymbol{r} - \hat{\boldsymbol{r}}_i)|\omega\rangle \quad . \tag{6.53}$$

Equation 6.53 can be easily evaluated for the case of excited states from an RPA calculation.

$$\delta\rho^\omega(\boldsymbol{r}) = \langle\text{RPA}| \sum_i^A \delta(\boldsymbol{r} - \hat{\boldsymbol{r}}_i) \, \hat{Q}_\omega^\dagger|\text{RPA}\rangle \quad . \tag{6.54}$$

First, we follow the standard procedure by introducing a commutator and applying

the QBA

$$\delta\rho^\omega(\boldsymbol{r}) = \langle\mathrm{HF}|[\sum_i^A \delta(\boldsymbol{r}-\hat{\boldsymbol{r}}_i),\hat{Q}^\dagger_\omega]|\mathrm{HF}\rangle$$

$$= \langle\mathrm{HF}|[\sum_i^A \delta(\boldsymbol{r}-\hat{\boldsymbol{r}}_i),\sum_{nj} X^\omega_{nj}\,\hat{a}^\dagger_n\hat{a}_j - \sum_{nj} Y^\omega_{nj}\,\hat{a}^\dagger_j\hat{a}_n]|\mathrm{HF}\rangle$$

$$= \langle\mathrm{HF}|\sum_i^A \delta(\boldsymbol{r}-\hat{\boldsymbol{r}}_i)\sum_{nj} X^\omega_{nj}\,\hat{a}^\dagger_n\hat{a}_j|\mathrm{HF}\rangle$$

$$+ \langle\mathrm{HF}|\sum_{nj} Y^\omega_{nj}\,\hat{a}^\dagger_j\hat{a}_n \sum_i^A \delta(\boldsymbol{r}-\hat{\boldsymbol{r}}_i)|\mathrm{HF}\rangle \quad . \tag{6.55}$$

With the Slater rules, we get

$$\delta\rho^\omega(\boldsymbol{r}) = \sum_{nj}\left(X^\omega_{nj}\,\langle j|\delta(\boldsymbol{r}-\hat{\boldsymbol{r}})|n\rangle + Y^\omega_{nj}\,\langle n|\delta(\boldsymbol{r}-\hat{\boldsymbol{r}})|j\rangle\right)$$

$$= \sum_{nj}\left(X^\omega_{nj} + Y^\omega_{nj}\right)\langle j|\delta(\boldsymbol{r}-\hat{\boldsymbol{r}})|n\rangle \quad . \tag{6.56}$$

The matrix element is easily evaluated with the HF wave functions and we arrive at the simple expression

$$\delta\rho^\omega(\boldsymbol{r}) = \sum_{nj}\left(X^\omega_{nj} + Y^\omega_{nj}\right)\int \psi^*_i(\boldsymbol{r}')\,\psi_m(\boldsymbol{r}')\,\delta(\boldsymbol{r}-\boldsymbol{r}')\,\mathrm{d}\boldsymbol{r}'$$

$$= \sum_{nj}\left(X^\omega_{nj} + Y^\omega_{nj}\right)\psi^*_j(\boldsymbol{r})\,\psi_n(\boldsymbol{r}) \quad . \tag{6.57}$$

Since the orientation of the nucleus is not fixed in the lab frame, the intrinsic transition densities are not an observable. To compare the transition densities to experimental data, they have to be projected onto good angular momentum (see [AR08]). But as the projected transition densities are of little value in interpreting our results, we do not carry out this procedure. The intrinsic transition densities contain all information characterizing the oscillation, like the number of nodes, the main axis of the oscillation, differences in neutron and proton oscillation and the like. They can also be used to show shifts in the center-of-mass position or any rotational motion, which are a sign of contaminations from spurious modes.

# 7. Results for the Random-Phase-Approximation

In this chapter, results for electric isoscalar monopole $J^\Pi = 0^+$ (ISM), electric isoscalar dipole $J^\Pi = 1^-$ (ISD), electric isovector dipole $J^\Pi = 1^-$ (IVD) and electric isoscalar quadrupole $J^\Pi = 2^+$ (ISQ) transitions are presented. The results are show as plots of the transition strengths and as values for the centroid energies $E_\text{cent}$ and rms-widths $\Gamma_\text{rms}$. To obtain smooth strengths functions $R(E)$ from the discrete pairs of energies and transition strengths $B(E_i)$, each value is convolved with a Lorentzian

$$R(E) = \sum_i \frac{\Gamma_\text{lor}}{\pi \left( (E - E_i)^2 - \frac{\Gamma^2}{2} \right)} \cdot B_i \tag{7.1}$$

If not indicated otherwise, the Lorentzians have a width of $\Gamma_\text{lor} = 1\,\text{MeV}$.

## 7.1. Comparison to the Gogny D1S Force

To check the implementation, we carry out calculations with the Gogny D1S force and compare our results to the HFB-QRPA calculations published by Péru and Goutte [PG08]. Since their results show a vanishing pairing energy for the two nuclei in question, both results should be comparable. The relevant figures from [PG08] are shown in figure 7.1. As in chapter 5.1.2, this comparison includes $^{24}$Mg because there is data available. However, since we consider the axial symmetric approximation as unjustified for this nucleus, it is not included in our actual calculations.

Figures 7.2 and 7.3 show the corresponding results obtained with our RPA code for two relevant oscillator lengths, $a_\text{HO} = 1.7\,\text{fm}$ and $a_\text{HO} = 1.8\,\text{fm}$. The energy minimum of $^{24}$Mg lies at $a_\text{HO} = 1.7\,\text{fm}$, while that of $^{28}$Si lies at $a_\text{HO} = 1.8\,\text{fm}$. We plot both curves for both nuclei to illustrate the strong effect the oscillator length has on the relative peak height. Since Péru and Goutte use the fraction of the *energy-weighted sum-rule* for their $y$-axes, we do the same in figures 7.2 and 7.3, but we will not adopt this convention in future plots. The smoothed curves are obtained by a convolution with Lorentzian functions with a width of $\Gamma_\text{lor} = 2\,\text{MeV}$. This value for $\Gamma_\text{lor}$ differs from the one normally used in this work, which is $\Gamma_\text{lor} = 1\,\text{MeV}$.

Unfortunately Péru and Goutte do not give any information regarding the oscillator length used for the HO basis. As we will see later, even for a much larger basis a small change of the oscillator length can have a visible effect on the transition strengths.[1]

---

[1] This effect could be related to the deformation parameter $\beta$, which is very sensitive to the oscillator length. The deformation parameters for our Gogny calculations are $+0.4614$ and $+0.5114$ for $^{24}$Mg and $-0.3273$ and $-0.3572$ for $^{28}$Si (first value $a_\text{HO} = 1.7\,\text{fm}$, second $a_\text{HO} = 1.8\,\text{fm}$).
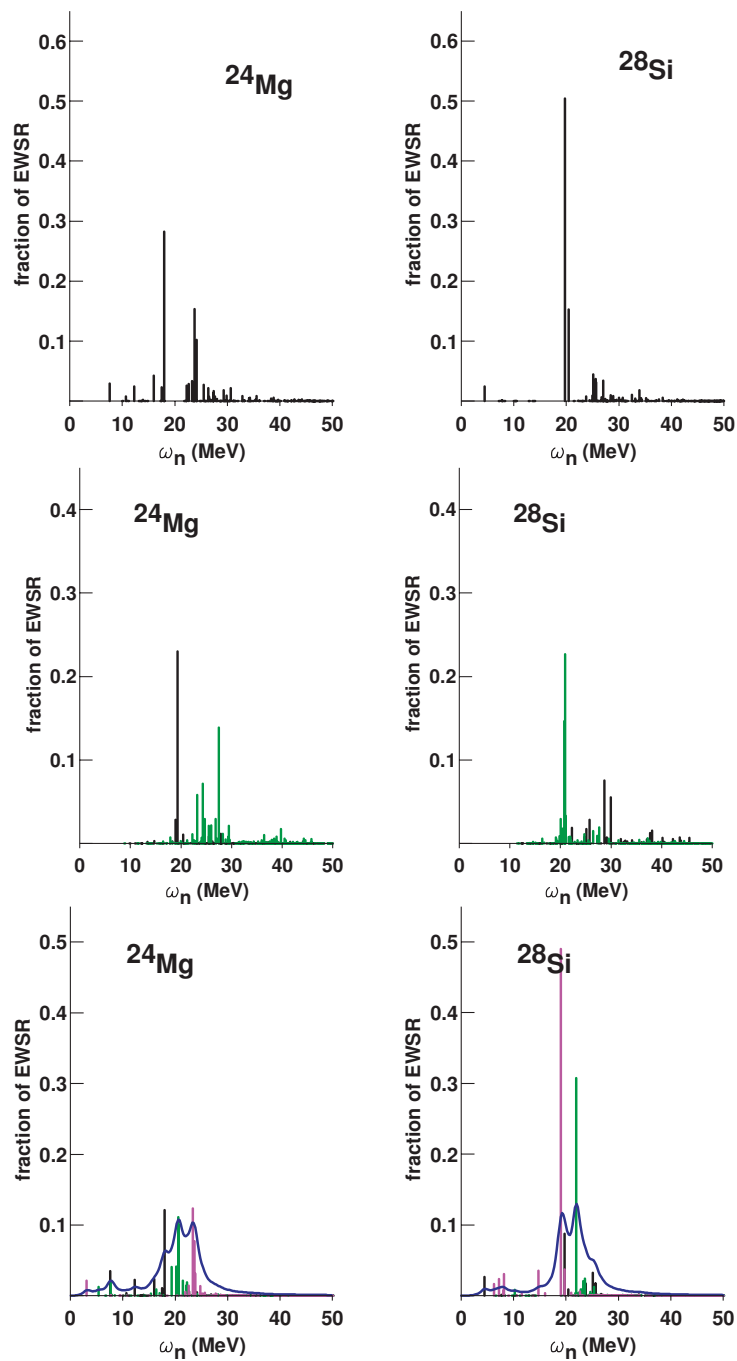
Figure 7.1.: Plots taken from [PG08]. From top to bottom: isoscalar monopole, isovector dipole, isoscalar quadrupole. The $k$-components are plotted in different colors: $k = 0$, $k = \pm 1$ and $k = \pm 2$. The convolution uses Lorentzians with a width of $\Gamma_{\mathrm{lor}} = 2\mathrm{MeV}$.
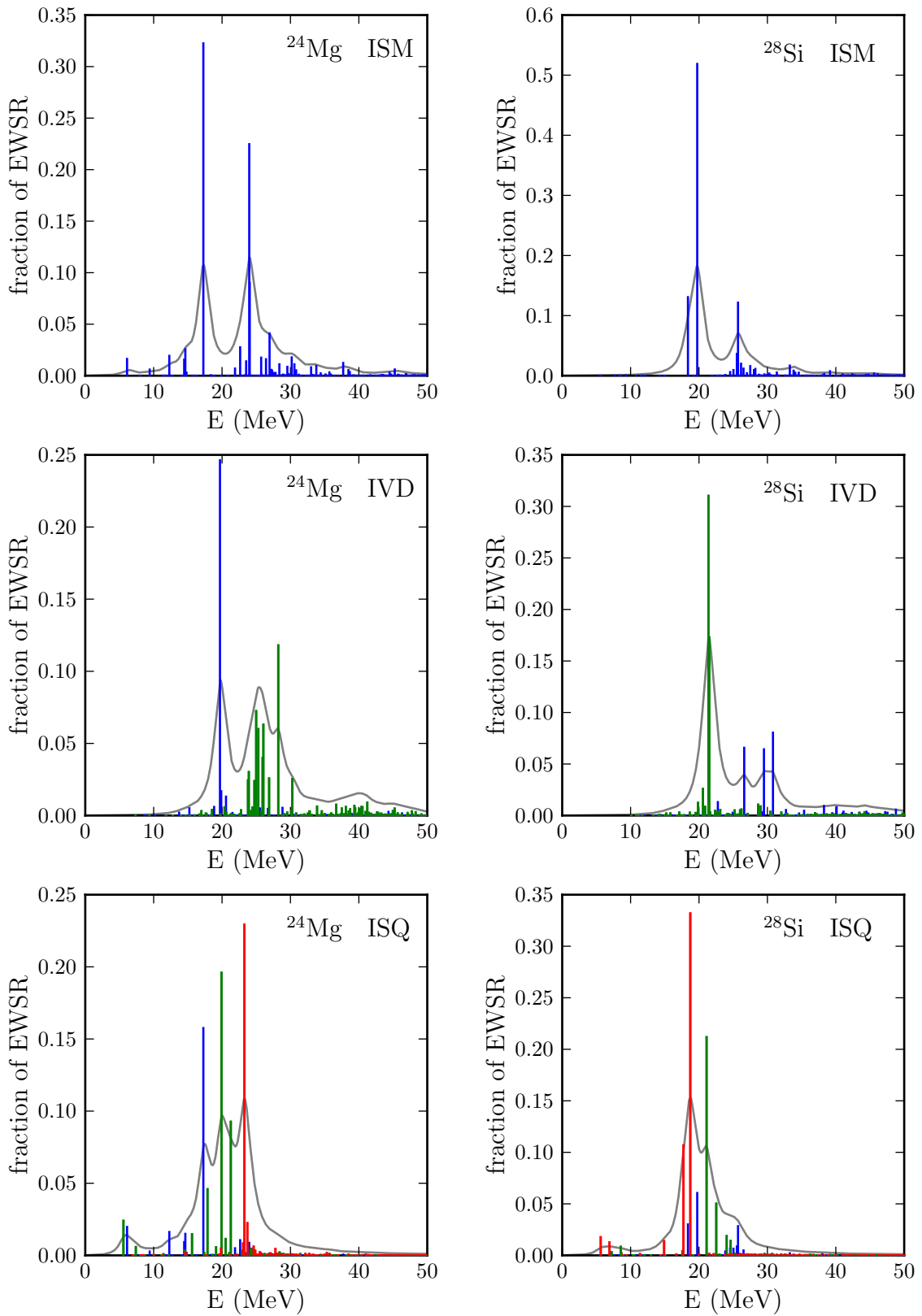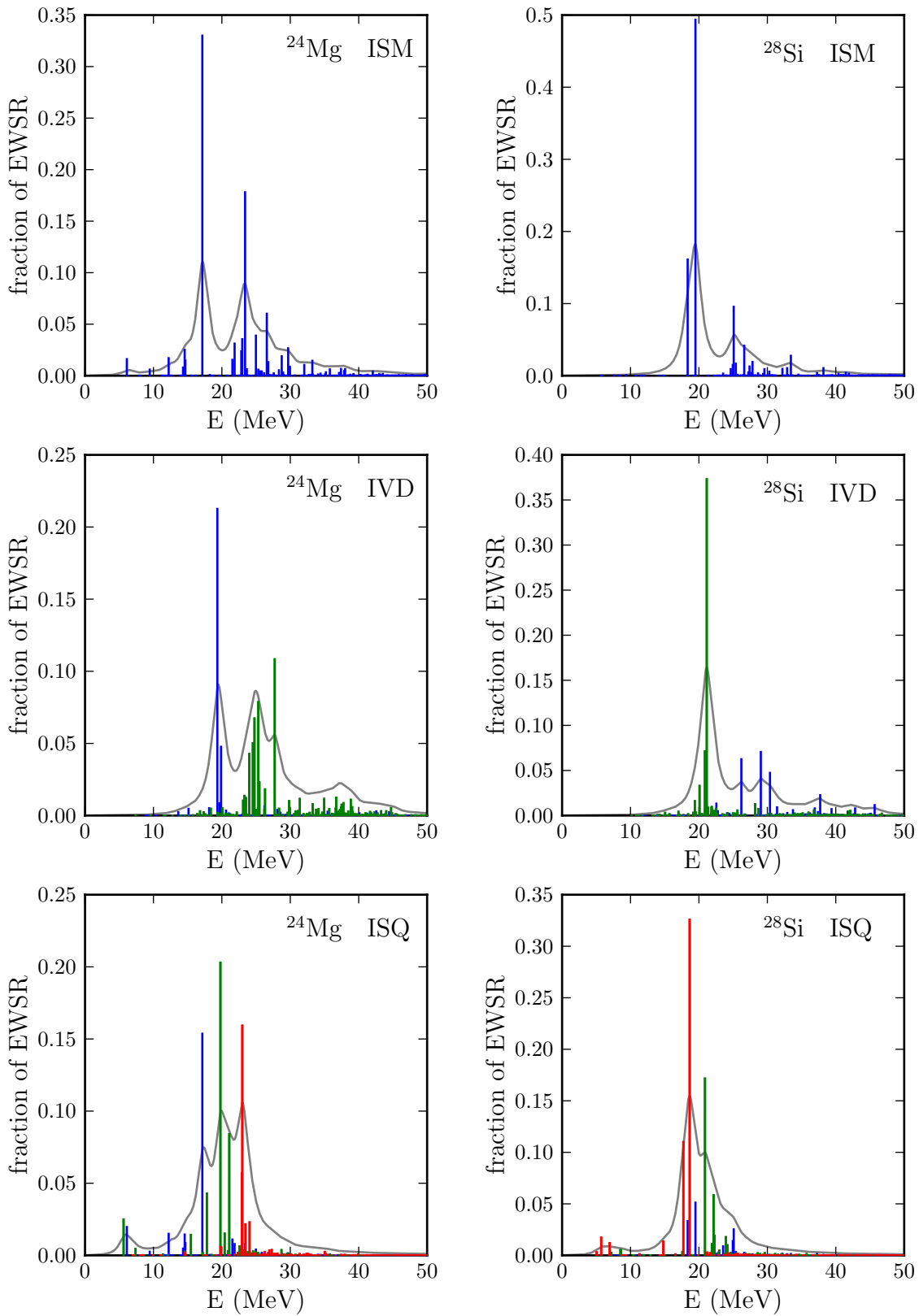
Figure 7.2.: Transition strengths for $a_{\mathrm{HO}} = 1.7\,\mathrm{fm}$. The colors of the $k$-components are: $k = 0$, $k = \pm 1$ and $k = \pm 2$. The convolution uses Lorentzians with a width of $\Gamma_{\mathrm{lor}} = 2\mathrm{MeV}$.

Figure 7.3.: Transition strengths for $a_{\mathrm{HO}} = 1.8\,\mathrm{fm}$. The colors of the $k$-components are: $k = 0$, $k = \pm 1$ and $k = \pm 2$. The convolution uses Lorentzians with a width of $\Gamma_{\mathrm{lor}} = 2\mathrm{MeV}$.

The small basis size used by Péru and Goutte, corresponding to $e_{max} = 8$, increases this effect further. They give ground-state energies of approximately 201 MeV for $^{24}$Mg and 240 MeV for $^{28}$Si. These values are not consistent with other calculations (see chapter 5.1.2) and about 3 MeV higher than the measured values.

The transition strengths agree in the general main features, however, the relative height of the peaks is sometimes changed. This happens also for the different oscillator lengths in figures 7.2 and 7.3, but not as strong as when compared to figure 7.1. The presence and approximate position of smaller features is reproduced for all cases. For both nuclei, there are two strong peaks in the ISM resonance, at about 20 and 25 MeV. For $^{24}$Mg, both are of comparable height, while for $^{28}$Si the peak at 20 MeV is notably stronger. The IVD resonance shows a narrow peak around 20 MeV and a broader structure at 25–30 MeV, which is reproduced in all calculations. We also note, that for the prolate $^{24}$Mg, the 20 MeV peak has $K = 0$, while the higher peak has $K = 1$. This is reversed for the oblate $^{28}$Si (see also section 7.7 for a discussion of the energy of the $K$ contributions). All calculations show a triple-peak for the ISQ resonance, which is located around 20–25 MeV, however, the third peak is very weak in $^{28}$Si. The same ordering with respect to the $K$-contributions is reproduced in all calculations.

Taking into account the uncertainties introduced by the unknown ground state used in [PG08], we can conclude that there is sufficient overlap between the results to rule out any major problems with our implementation. Due to the obviously different ground-states used in the calculations, a complete agreement cannot be expected.

## 7.2. Comparison to Spherical RPA

In this section, the RPA code for deformed nuclei is used to calculate spherical nuclei and the results are compared to an already well tested spherical RPA implementation [PRP07, PPRW11]. Since the deformed RPA code cannot use angular momentum coupled ph-pairs, every eigenvalue is $J$-fold degenerate and a lot of eigenvalues with zero strength appear. Therefore, we do not compare RPA eigenvalues and their corresponding transition strengths, but convolutions of the transition strengths with Lorentzian functions. As in future plots, we use Lorentzians with a width of $\Gamma_{lor} = 1$ MeV.

The comparison is shown in figures 7.4 to 7.7. For the UCOM(VAR)$_{2b}$ interaction, we have a complete agreement of the transition amplitudes obtained with the two codes. For the two other interactions, we have to take the three-body interaction into account, which is calculated on a spatial grid. As discussed in chapter 2.3, a grid fine enough to eliminate all discretization errors is not feasible. Therefore, we get some small deviations, but they have no effect on the larger features of the transition strengths. As we will see in coming sections, the errors due to the discretization are much smaller than the uncertainties introduced by the basis truncation or the choice of the oscillator length.
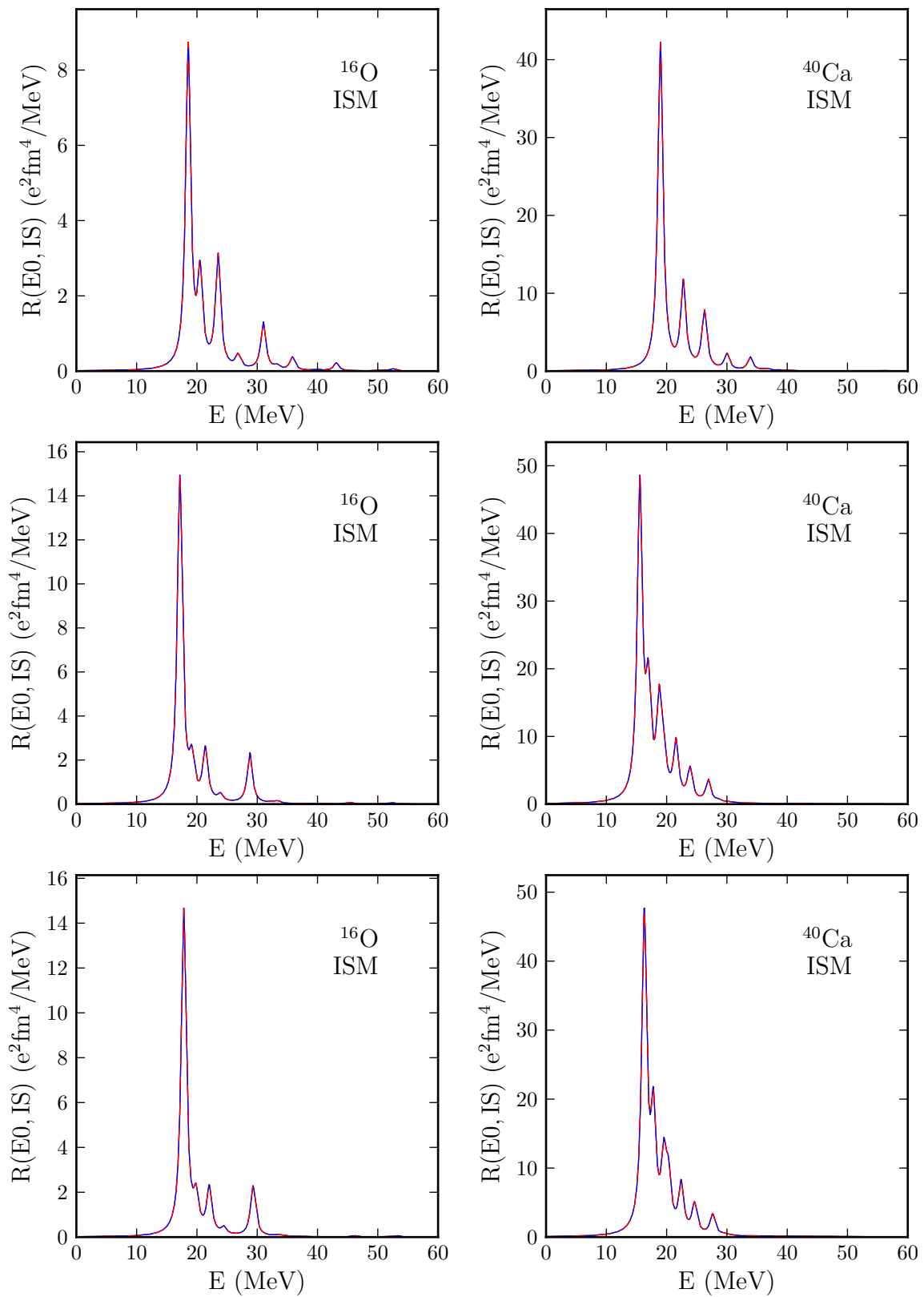
Figure 7.4.: Comparison of the deformed (——) and spherical (——) RPA codes for ISM transitions with the UCOM(VAR)$_{2b}$ (upper row), S-SRG$_{3b}$ (middle row) and S-UCOM(SRG)$_{3b}$ (lower row) interactions.
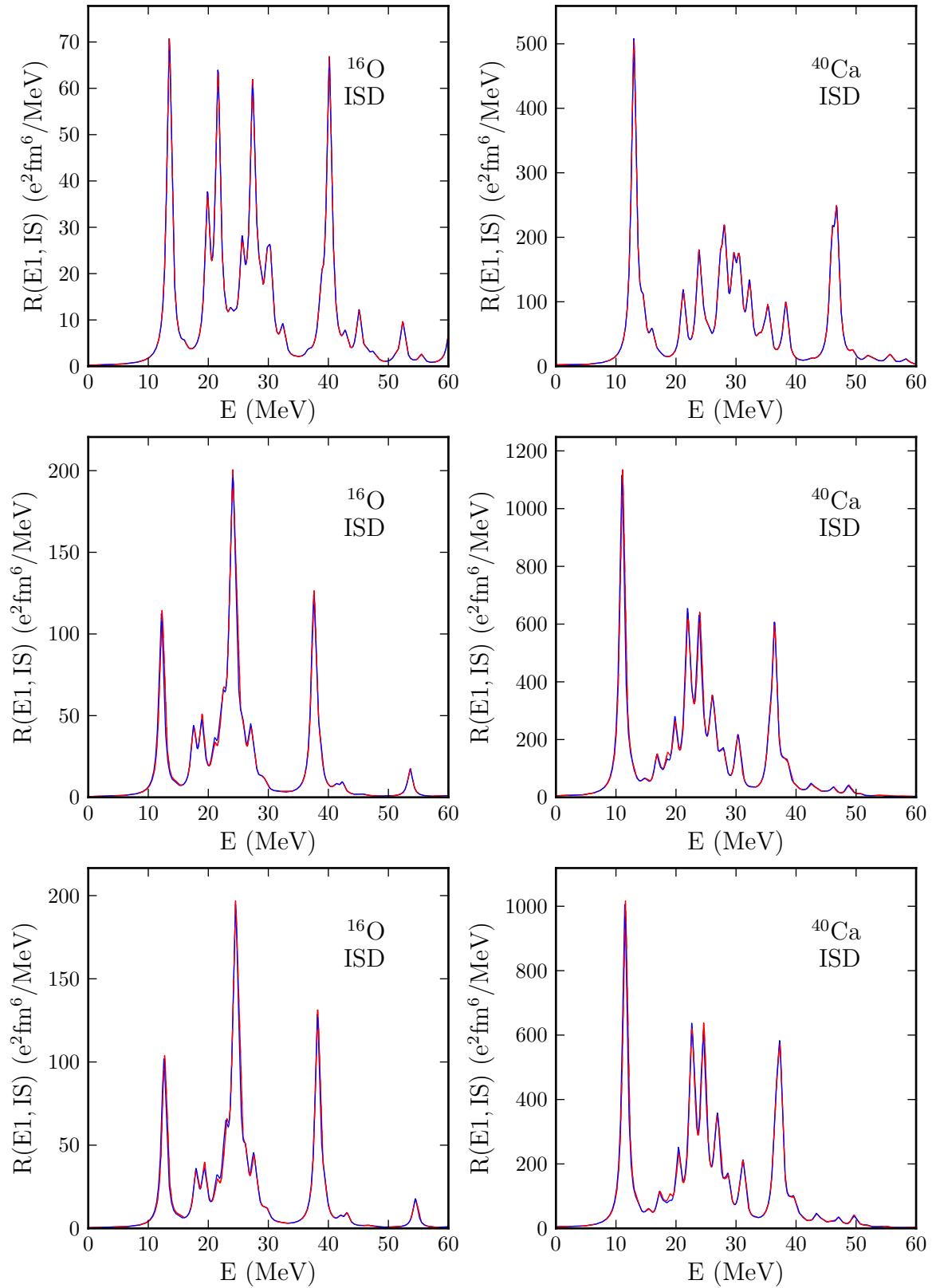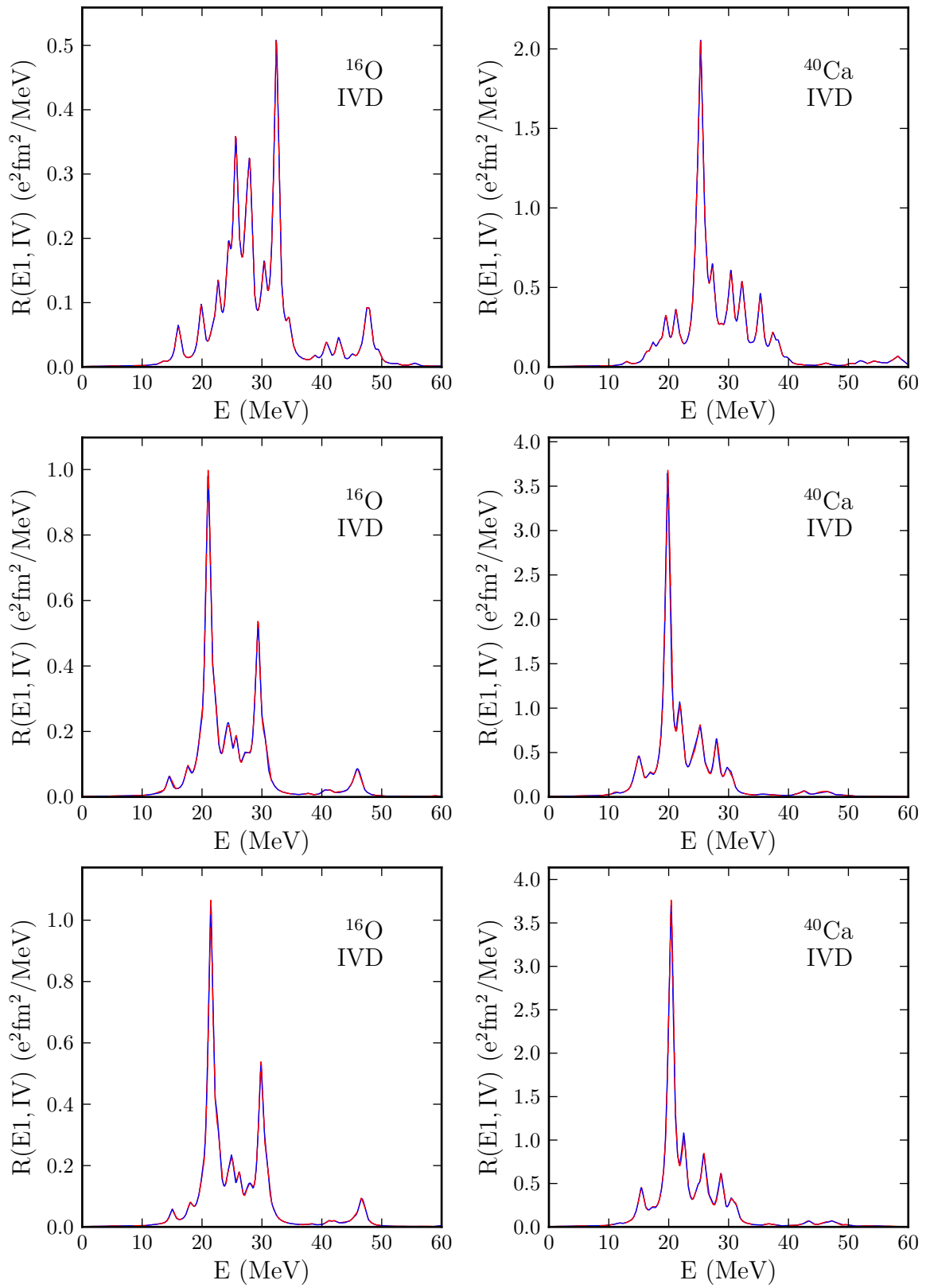
Figure 7.5.: Comparison of the deformed (———) and spherical (———) RPA codes for ISD transitions with the UCOM(VAR)$_{2b}$ (upper row), S-SRG$_{3b}$ (middle row) and S-UCOM(SRG)$_{3b}$ (lower row) interactions.
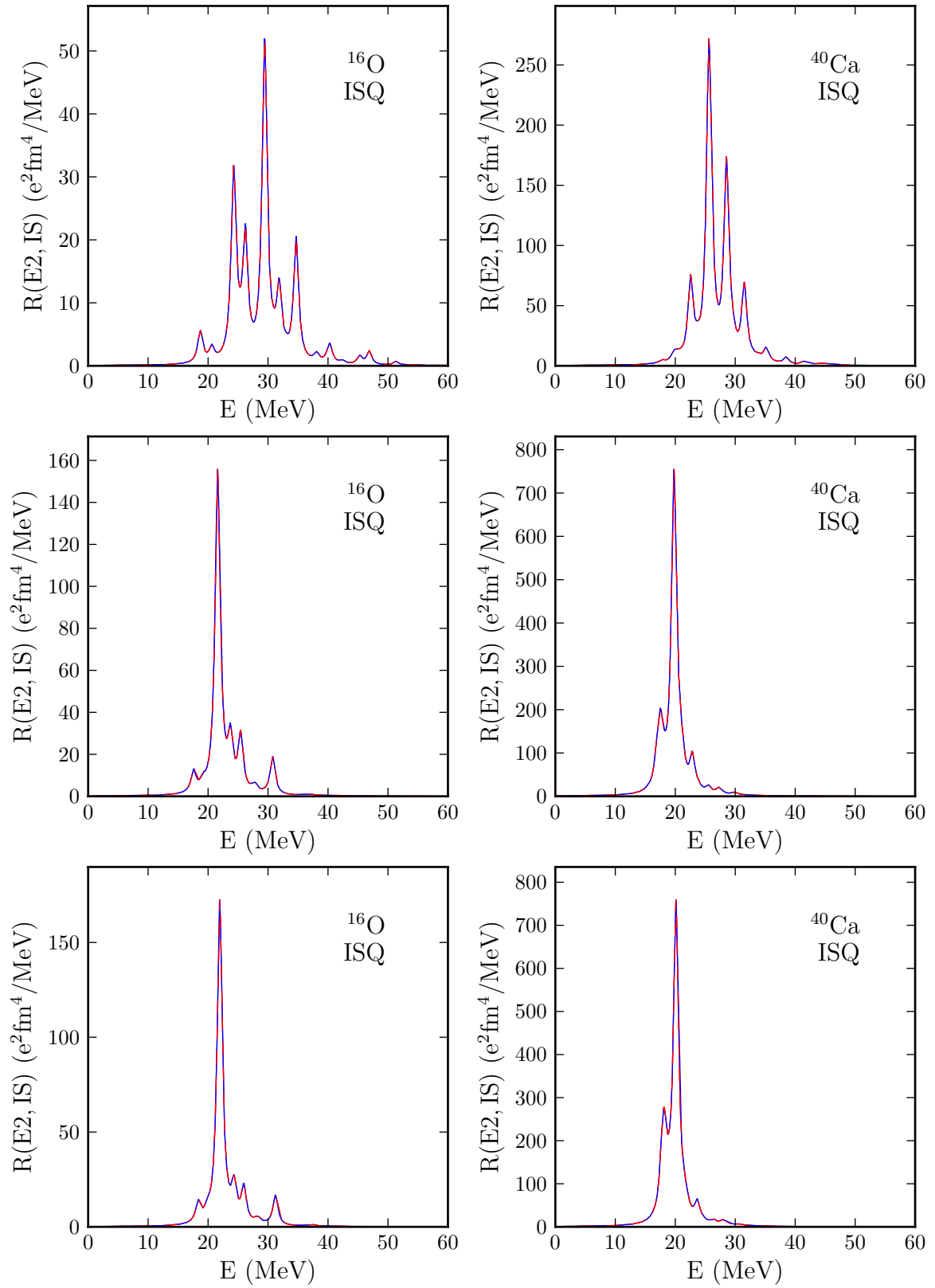
Figure 7.6.: Comparison of the deformed (——) and spherical (——) RPA codes for IVD transitions with the UCOM(VAR)$_{2b}$ (upper row), S-SRG$_{3b}$ (middle row) and S-UCOM(SRG)$_{3b}$ (lower row) interactions.

Figure 7.7.: Comparison of the deformed (——) and spherical (——) RPA codes for ISQ transitions with the UCOM(VAR)$_{2b}$ (upper row), S-SRG$_{3b}$ (middle row) and S-UCOM(SRG)$_{3b}$ (lower row) interactions.

## 7.3. Sum Rules

In table 7.1, we compare our results to the classical sum rules discussed in chapter 6.2.5. All sum rules behave as expected (cf. chapter 6.2.5). The TRK sum rule is overestimated by about 40–80%, which is due to non-local terms in the unitarily transformed interactions. The ISM sum rule is exhausted to about $100 \pm 5\%$, with no apparent differences between spherical and deformed nuclei. The ISQ sum rule is exhausted to about 100% for spherical nuclei, but for deformed nuclei, this is reduced to only 90–95%. The results for spherical nuclei are consistent with [Gün11], the small differences are due to the larger basis used in this work. There is no case, where the classical sum rules are significantly underestimated, which would indicate problems with the RPA method, like too small model spaces or unstable HF ground states. We will take up the issue of unstable HF ground states in the context of complex RPA eigenvalues in section 7.8.

The different behavior of deformed nuclei for the ISM and ISQ sum rules is connected to the oscillation patterns of the transitions. Monopole oscillations are breathing modes, which involve all nucleons, while quadrupole oscillations are surface modes, involving only those nuclei on the surface. Therefore, monopole transitions do not depend much on the shape of the nuclear surface, and deformations do not play a big role. But since deformations alter the nuclear surface, they have a great impact on quadrupole transitions. As the sum rules do not take this effect into account, their values are not reproduced as well for deformed nuclei as for spherical ones.

## 7.4. Convergence of RPA Results

In this section, the convergence behavior of the RPA calculations is investigated. As for the HF calculations, we consider the convergence with respect to two quantities: the basis truncation $e_{\max}$ and the oscillator length $a_{\mathrm{HO}}$. As before, we investigate the convergence for the nuclei $^{16}$O, $^{20}$Ne, $^{28}$Si (only oblate state $^{28}$Si$_o$) and $^{40}$Ca with the UCOM(VAR)$_{2b}$ and S-SRG$_{3b}$ interactions. For the convergence study, we only consider the amgular-momentum projected RPA transition strengths for the AVAP HF minimum.

First, we consider the convergence with respect to the basis size. The basis is truncated at $e_{\max} \geq 2\,n + l$, with $e_{\max} = 10, 12, 14$, with an additional limit for the angular-momentum quantum-number of $l \leq 10$. Figures 7.8 to 7.11 show the strength functions for the deformed nuclei. Since spherical nuclei do not behave differently from deformed nuclei, the corresponding plots are not shown. As we can see, the convergence does not depend on the type of interaction used or the type of nucleus. However, above 20 MeV, the strength of ISD transitions fluctuates notably stronger than other transitions. Peaks below 10 MeV are very well converged, the curves overlap almost completely. In the region up to 15 MeV, the peaks are not as well converged, but they still have a very large overlap. For higher energy regions, where giant resonances are located and most experiments are performed, the fine structure of the peaks is not converged.

| | nucleus | minimum | UCOM(VAR)$_{2b}$ | S-SRG$_{3b}$ | S-UCOM(SRG)$_{3b}$ |
|---|---|---|---|---|---|
| ISM | $^{12}$C | PAV | 103.22% | 95.41% | |
| | | AVAP | 102.83% | 95.66% | 93.86% |
| | $^{16}$O | | 104.44% | 94.55% | 92.10% |
| | $^{20}$Ne | PAV | 103.56% | 95.53% | |
| | | AVAP | 103.29% | 95.65% | 93.73% |
| | $^{28}$Si$_o$ | PAV | 103.73% | 95.84% | |
| | | AVAP | 103.54% | 95.89% | 94.04% |
| | $^{28}$Si$_p$ | PAV | 103.49% | 95.94% | |
| | | AVAP | 103.29% | 96.02% | 94.21% |
| | $^{32}$S | PAV | 104.02% | 95.79% | |
| | | AVAP | 103.86% | 95.84% | 93.98% |
| | $^{40}$Ca | | 104.39% | 95.64% | 93.47% |
| IVD | $^{12}$C | PAV | 163.70% | 169.63% | |
| | | AVAP | 161.70% | 167.61% | 171.67% |
| | $^{16}$O | | 170.30% | 174.66% | 179.79% |
| | $^{20}$Ne | PAV | 170.53% | 174.93% | |
| | | AVAP | 169.46% | 173.93% | 178.94% |
| | $^{28}$Si$_o$ | PAV | 174.49% | 177.51% | |
| | | AVAP | 173.61% | 176.66% | 182.08% |
| | $^{28}$Si$_p$ | PAV | 174.37% | 177.79% | |
| | | AVAP | 173.56% | 177.12% | 182.64% |
| | $^{32}$S | PAV | 175.44% | 178.03% | |
| | | AVAP | 174.82% | 177.47% | 183.11% |
| | $^{40}$Ca | | 181.35% | 182.36% | 188.50% |
| ISQ | $^{12}$C | PAV | 95.39% | 93.40% | |
| | | AVAP | 94.08% | 91.86% | 91.52% |
| | $^{16}$O | | 102.66% | 100.69% | 100.15% |
| | $^{20}$Ne | PAV | 94.67% | 93.12% | |
| | | AVAP | 92.77% | 90.88% | 90.71% |
| | $^{28}$Si$_o$ | PAV | 95.92% | 94.17% | |
| | | AVAP | 95.26% | 93.39% | 93.13% |
| | $^{28}$Si$_p$ | PAV | 93.61% | 90.54% | |
| | | AVAP | 91.97% | 88.81% | 88.64% |
| | $^{32}$S | PAV | 96.72% | 93.75% | |
| | | AVAP | 95.95% | 92.58% | 92.42% |
| | $^{40}$Ca | | 102.46% | 100.50% | 99.96% |

Table 7.1.: Exhaustion of the energy-weighted sum rules.

Figures 7.12 and 7.13 show the convergence of the centroid energies. The centroid for an arbitrary transition $\sigma\lambda$ is defined by

$$E_{\text{cent}} = \frac{\sum_i E_i\, B_i(\sigma\lambda)}{\sum_i B_i(\sigma\lambda)} \quad , \tag{7.2}$$

with the RPA eigenvalues $E_i$ and the respective strength $B_i(\sigma\lambda)$. The corresponding rms-width $\Gamma_{\text{cent}}$ is given by

$$\Gamma_{\text{cent}} = \sqrt{\frac{\sum_i (E_i - E_{\text{cent}})^2\, B_i(\sigma\lambda)}{\sum_i B_i(\sigma\lambda)}} \quad . \tag{7.3}$$

For the ISM, IVD and ISQ transitions, the centroids do not change significantly with basis size. The ISD centroid is not as well converged.

Next, we consider the oscillator length. Figures 7.14 to 7.17 show the response functions for the respective nuclei and transitions. The picture is very similar to that of the basis size, although the changes are smaller. The amount of change does not depend on the interaction, nucleus or transition. Table 7.2 shows the change of the centroid energies. Centroid energies usually decrease with increasing oscillator length, similar to an increased basis size. The change is mostly below $0.5\,\text{MeV}$, but always lower than $1\,\text{MeV}$, and the ISD transition does not behave differently from the rest.

We conclude, that our results are sufficiently converged. The position and width of giant resonance peaks is reproduced for all basis sizes and oscillator lengths, and there is an equally large amount of structure in the peaks. As the RPA neglects many important factors contributing to fine-structure of the transition strengths, like coupling to the continuum or more complex configurations, we do not expect the fine-structure to be accurately reproduced, even for fully converged calculations.
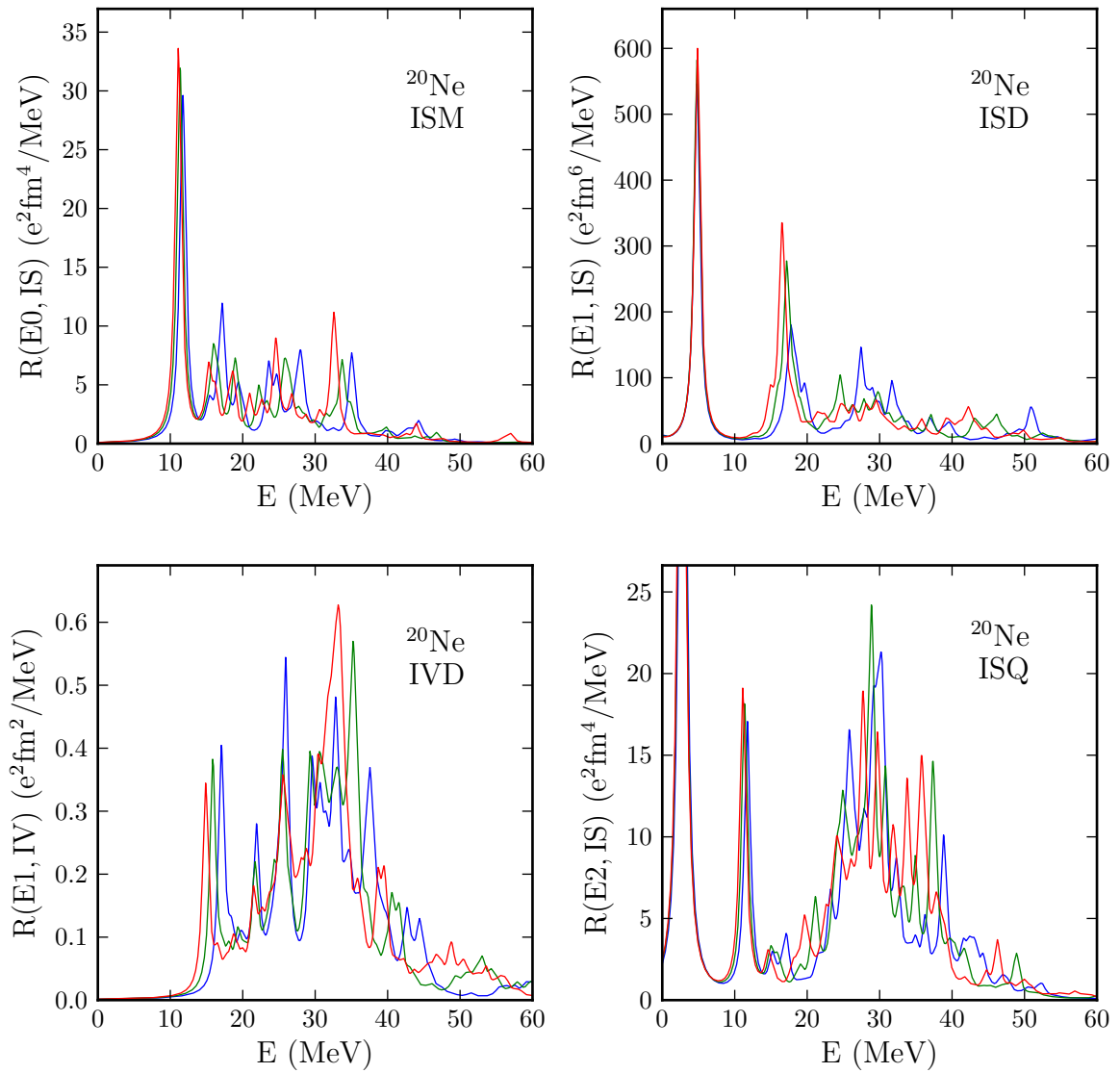
Figure 7.8.: Convergence of transition strengths with respect to basis size for $^{20}$Ne with the UCOM(VAR)$_{2b}$ interaction. Projected transition strengths for $e_{\max} = 10$ (——), $e_{\max} = 12$ (——) and $e_{\max} = 14$ (——).
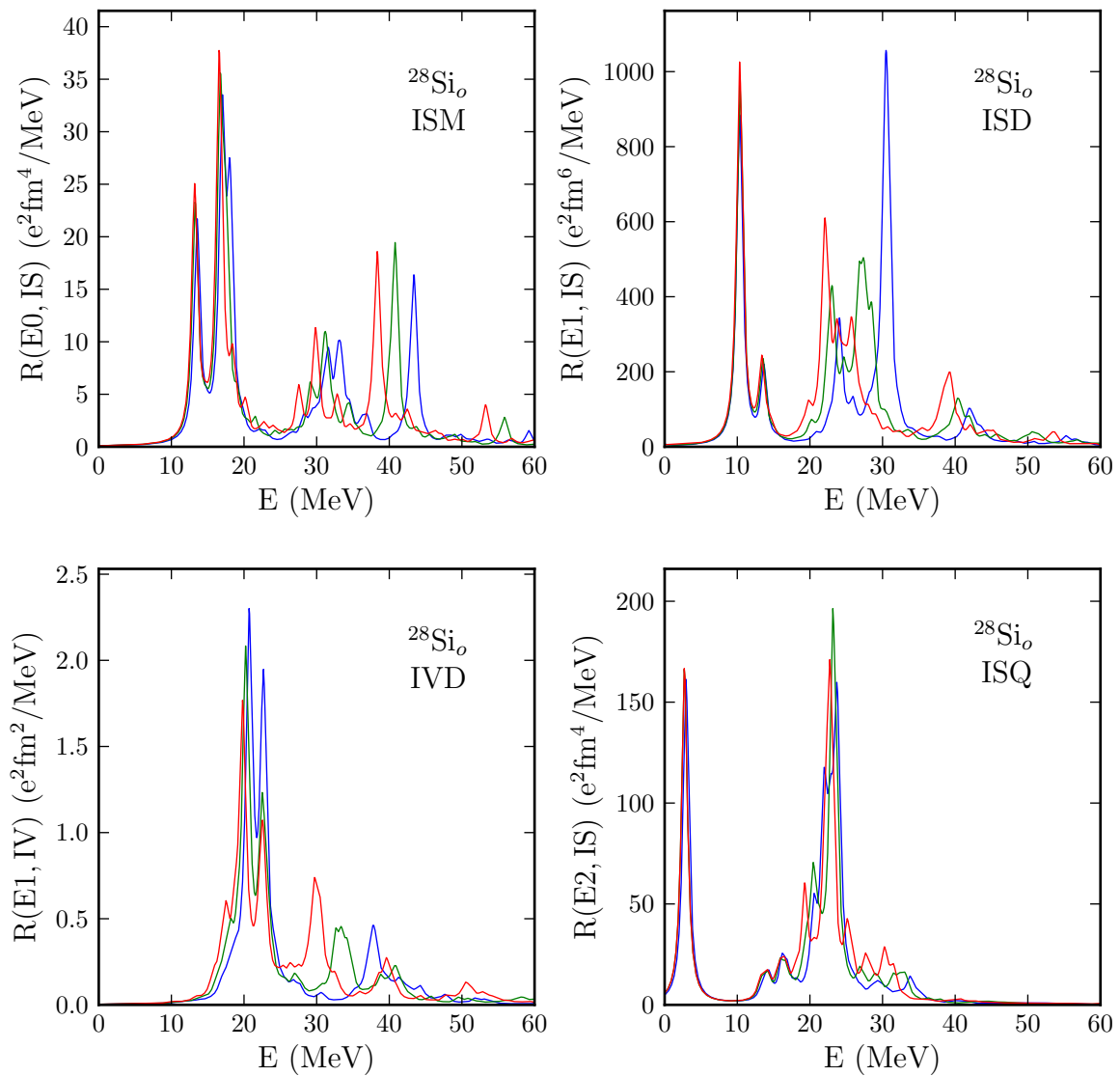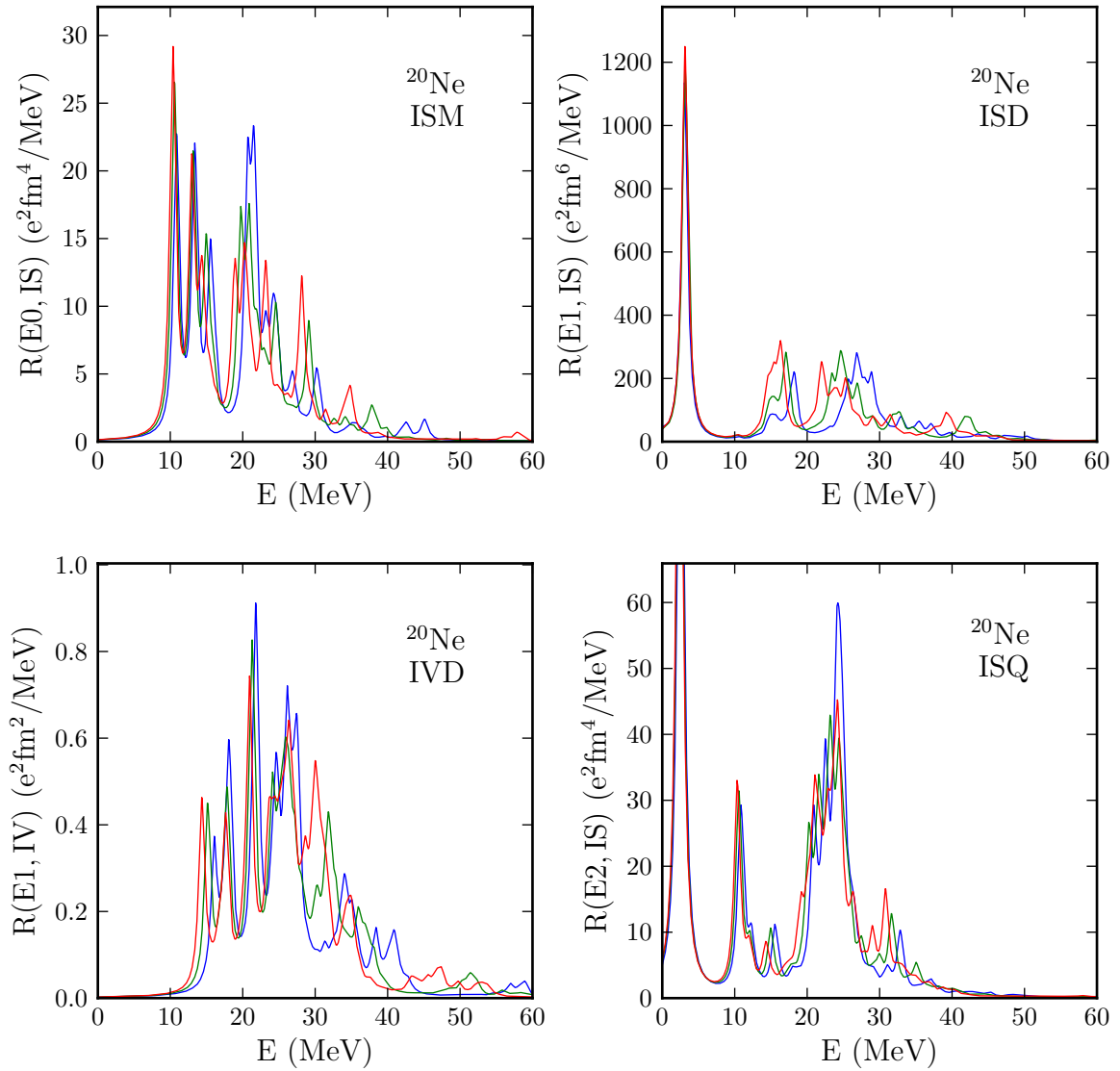
Figure 7.9.: Convergence of transition strengths with respect to basis size for $^{28}$Si with the UCOM(VAR)$_{2b}$ interaction. Projected transition strengths for $e_{\max} = 10$ (——), $e_{\max} = 12$ (——) and $e_{\max} = 14$ (——).
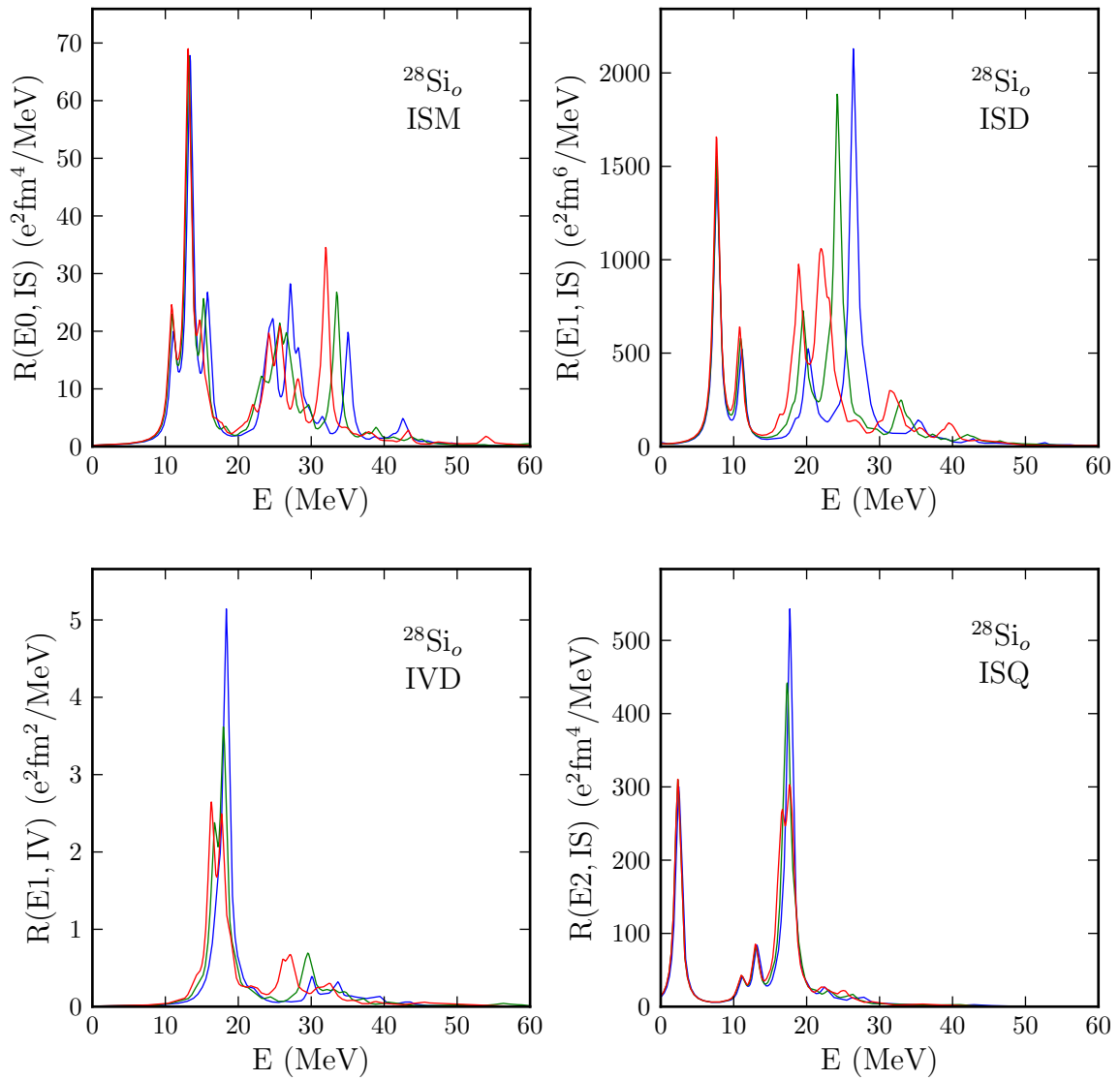
Figure 7.10.: Convergence of transition strengths with respect to basis size for $^{20}$Ne with the S-SRG$_{3b}$ interaction. Projected transition strengths for $e_{\max} = 10$ (——), $e_{\max} = 12$ (——) and $e_{\max} = 14$ (——).

Figure 7.11.: Convergence of transition strengths with respect to basis size for $^{28}$Si with the S-SRG$_{3b}$ interaction. Projected transition strengths for $e_{\max} = 10$ (——), $e_{\max} = 12$ (——) and $e_{\max} = 14$ (——).
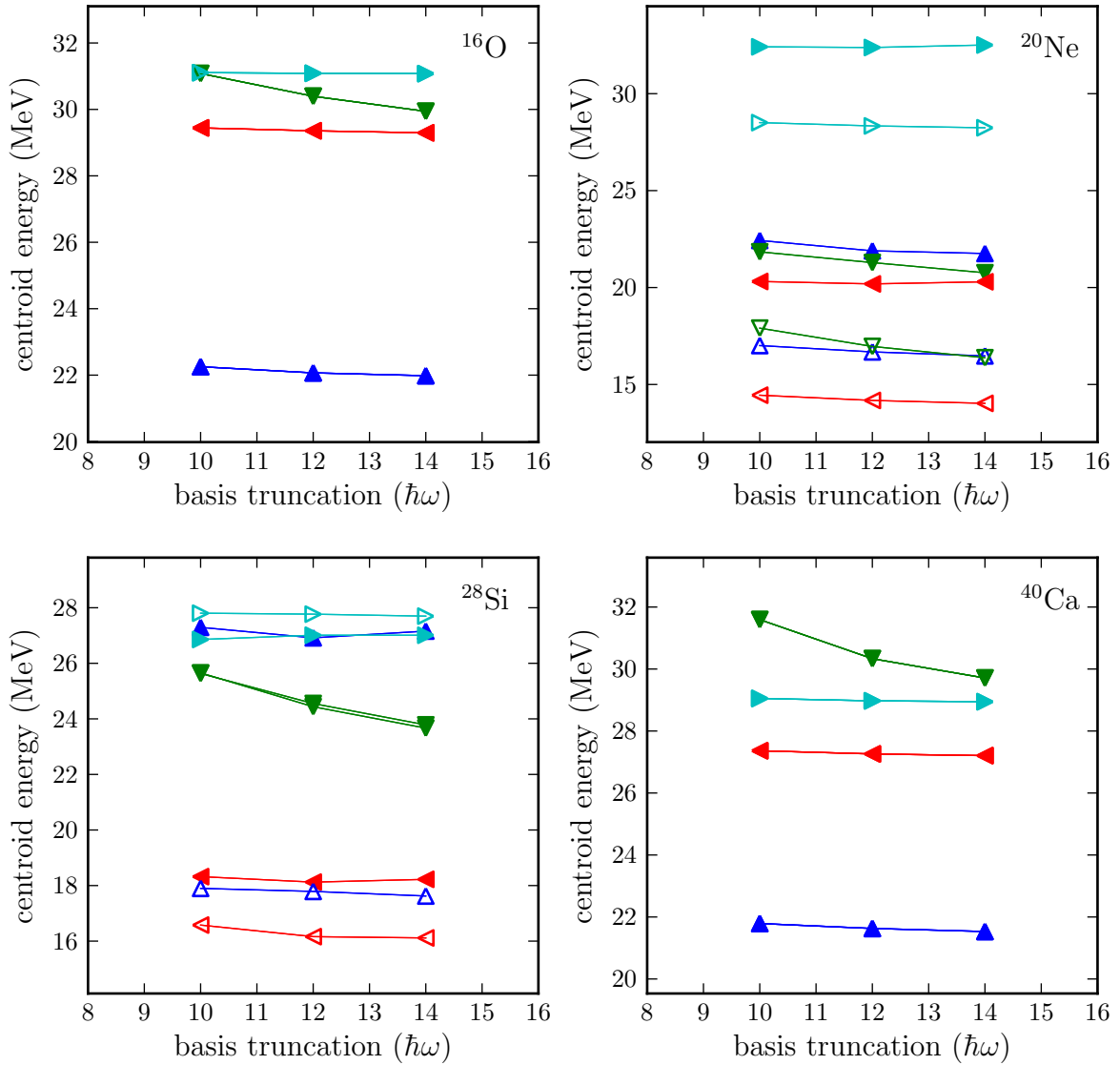
Figure 7.12.: Convergence of centroid energies with respect to basis size for the UCOM(VAR)$_{2b}$ interaction. Projected (filled symbols) and intrinsic (open symbols) centroids for the ISM (━▲━), ISD (━▼━), ISQ (━◀━) and IVD (━▶━) transitions.
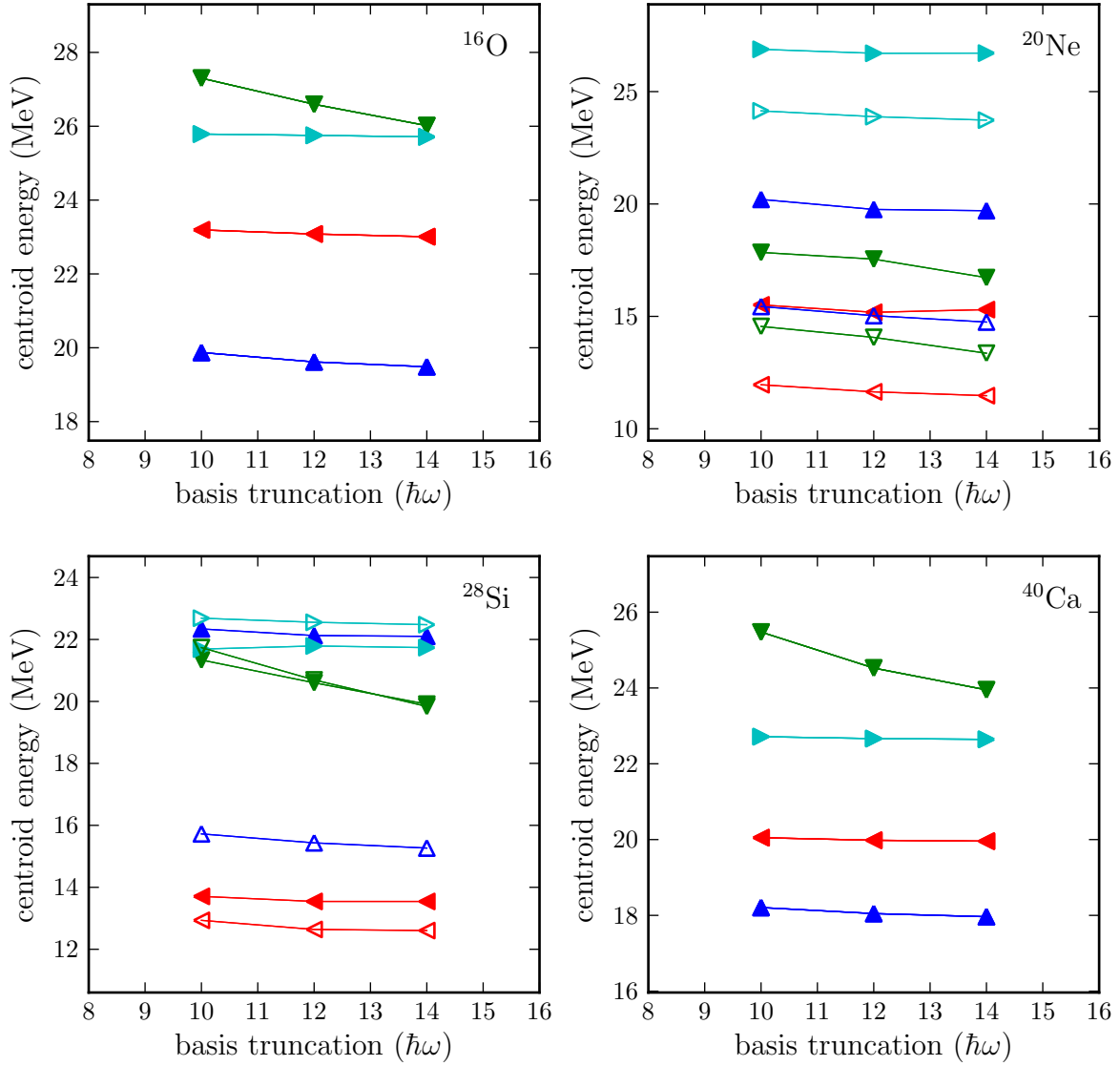
Figure 7.13.: Convergence of centroid energies with respect to basis size for the S-SRG$_{3b}$ interaction. Projected (filled symbols) and intrinsic (open symbols) centroids for the ISM (—▲—), ISD (—▼—), ISQ (—◀—) and IVD (—▶—) transitions.
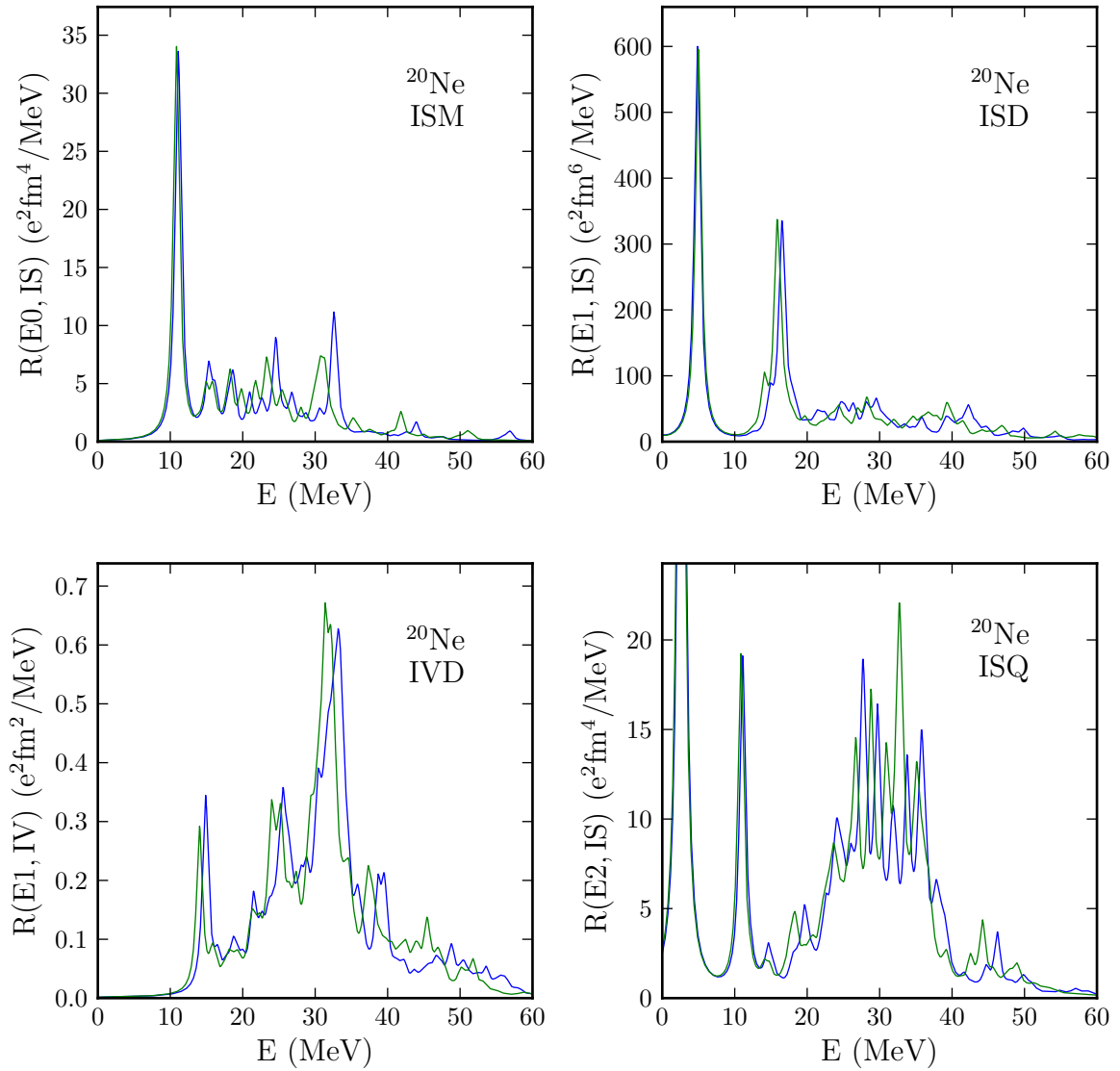
Figure 7.14.: Convergence of transition strengths with respect to oscillator length for $^{20}$Ne with the UCOM(VAR)$_{2b}$ interaction. Projected transition strengths for $a_{HO} = 1.6$ fm (——) and $a_{HO} = 1.7$ fm (——).
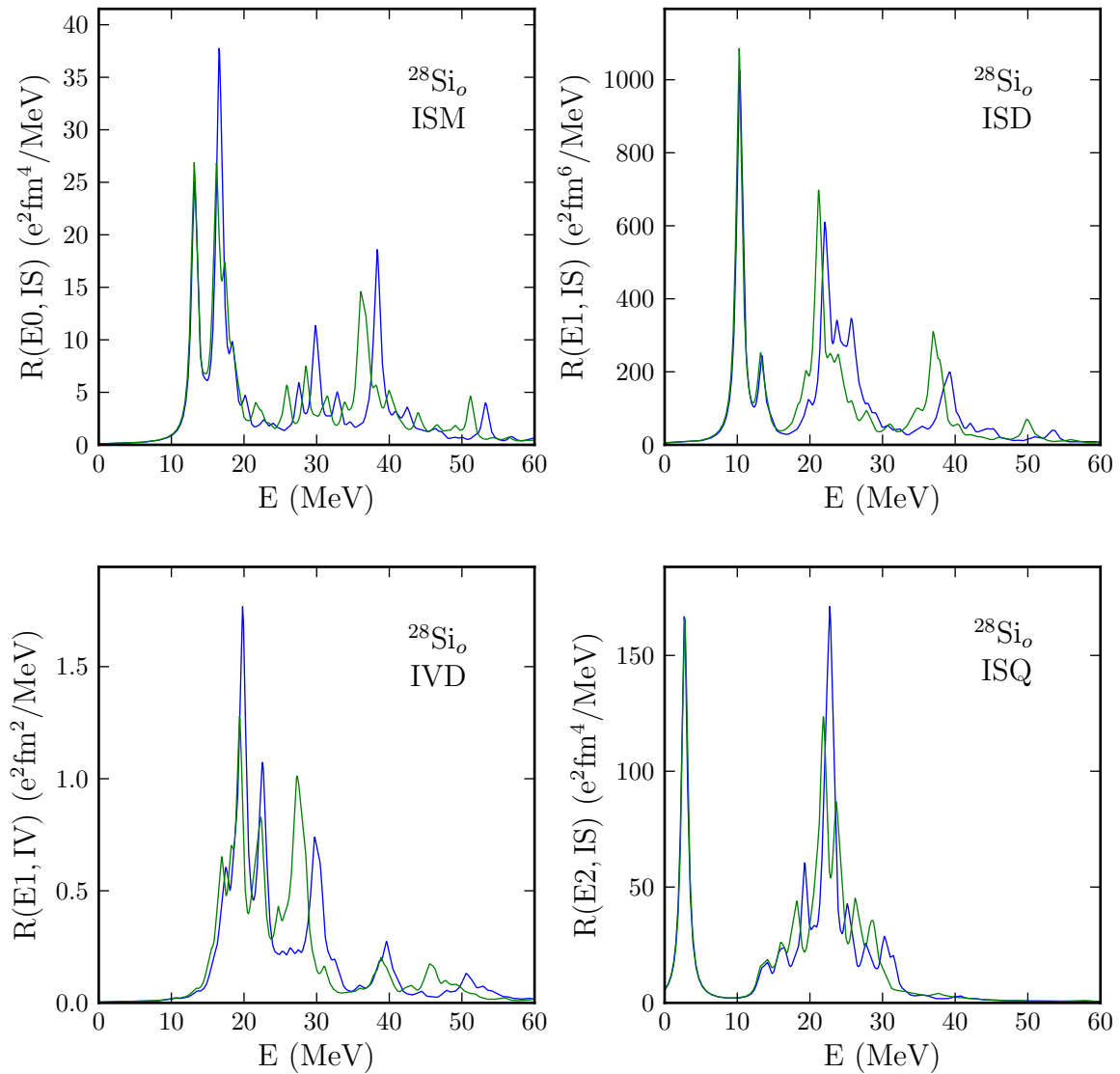
Figure 7.15.: Convergence of transition strengths with respect to oscillator length for $^{28}$Si with the UCOM(VAR)$_{2b}$ interaction. Projected transition strengths for $a_{HO} = 1.6\,\text{fm}$ (——) and $a_{HO} = 1.7\,\text{fm}$ (——).

Figure 7.16.: Convergence of transition strengths with respect to oscillator length for $^{20}$Ne with the S-SRG$_{3b}$ interaction. Projected transition strengths for $a_{HO} = 1.6$ fm (——) and $a_{HO} = 1.7$ fm (——).
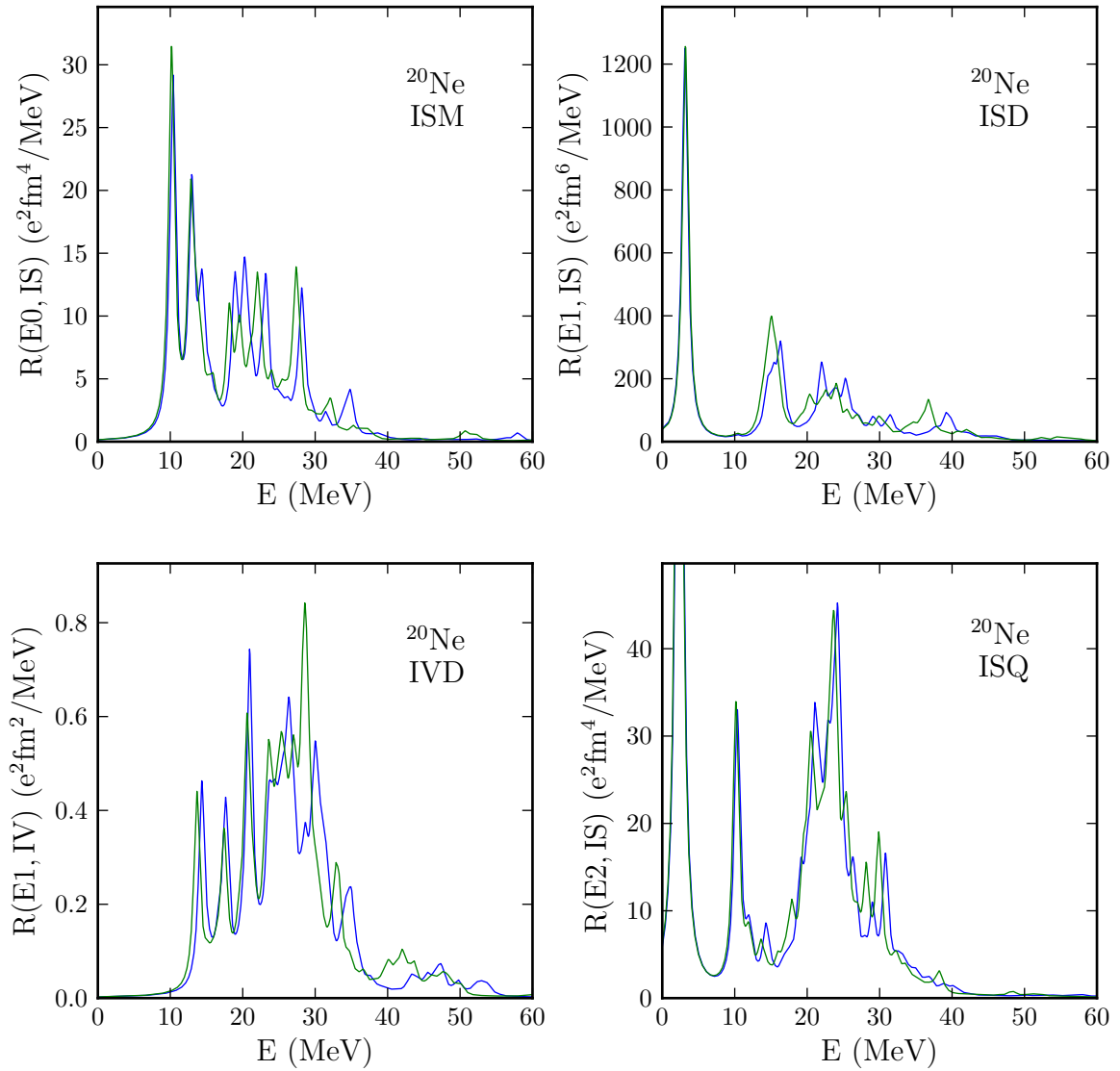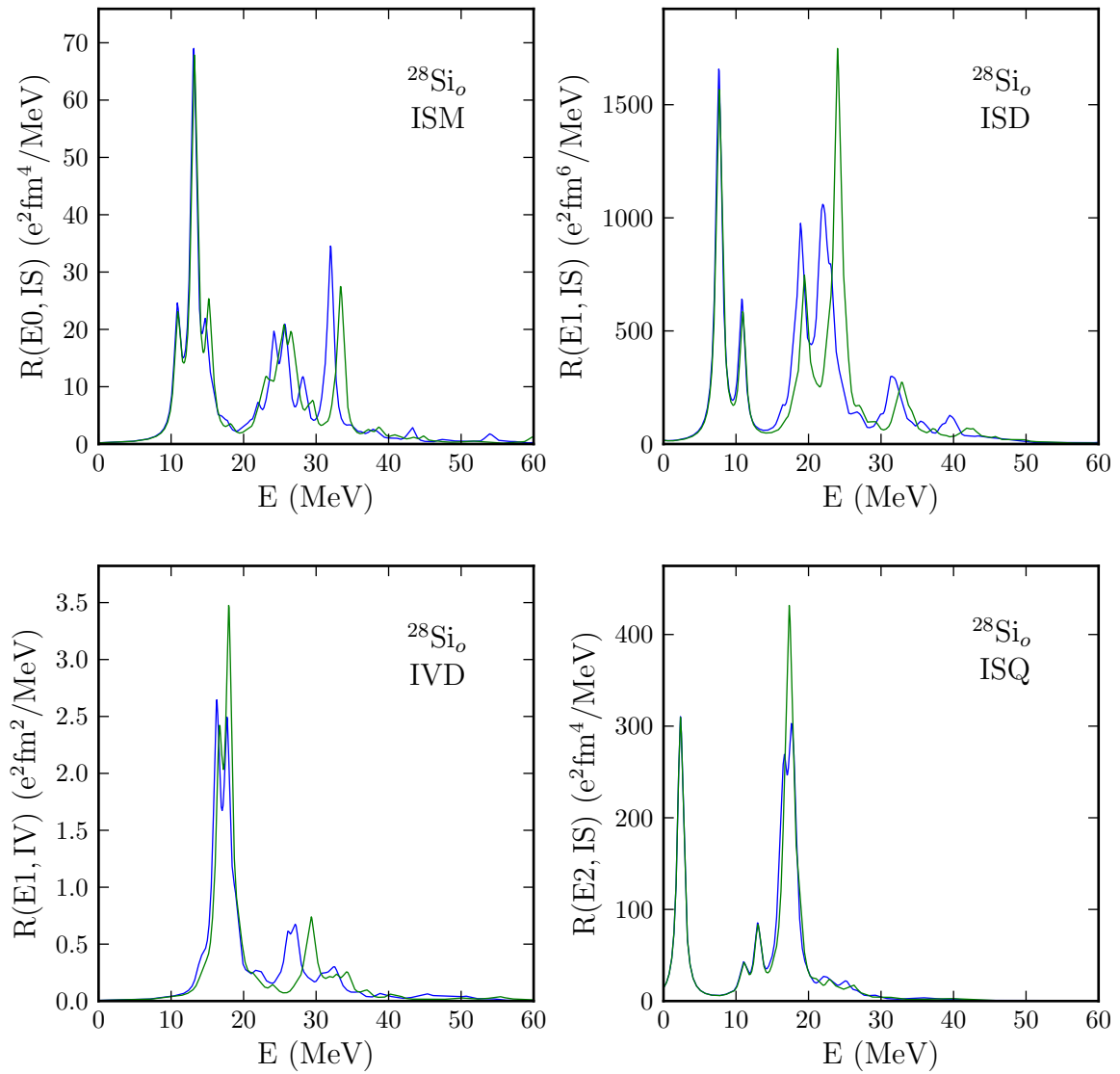
Figure 7.17.: Convergence of transition strengths with respect to oscillator length for $^{28}$Si with the S-SRG$_{3b}$ interaction. Projected transition strengths for $a_{\mathrm{HO}} = 1.7$ fm (———) and $a_{\mathrm{HO}} = 1.6$ fm (———).

| nucleus | transition | intrinsic | | projected | |
|---|---|---|---|---|---|
| | | $a_{HO} = 1.6$ | $a_{HO} = 1.7$ | $a_{HO} = 1.6$ | $a_{HO} = 1.7$ |
| $^{20}$Ne | ISM | 16.09 | 16.00 | 19.46 | 19.15 |
| UCOM(VAR)$_{2b}$ | ISD | 21.89 | 21.37 | 22.90 | 23.06 |
| | IVD | 25.29 | 24.89 | 28.72 | 28.26 |
| | ISQ | 23.67 | 23.53 | 26.73 | 26.61 |
| $^{28}$Si$_o$ | ISM | 17.29 | 17.11 | 22.78 | 22.93 |
| UCOM(VAR)$_{2b}$ | ISD | 20.65 | 20.29 | 20.80 | 20.65 |
| | IVD | 24.43 | 24.26 | 23.97 | 23.53 |
| | ISQ | 24.34 | 24.13 | 22.79 | 22.70 |
| $^{20}$Ne | ISM | 14.61 | 14.47 | 18.58 | 18.24 |
| S-SRG$_{3b}$ | ISD | 21.71 | 20.72 | 23.09 | 22.35 |
| | IVD | 22.25 | 21.97 | 24.82 | 24.62 |
| | ISQ | 19.14 | 19.06 | 21.89 | 21.77 |
| $^{28}$Si$_o$ | ISM | 15.30 | 15.13 | 20.64 | 20.45 |
| S-SRG$_{3b}$ | ISD | 19.33 | 18.83 | 19.07 | 18.70 |
| | IVD | 21.26 | 21.17 | 20.65 | 20.49 |
| | ISQ | 18.83 | 18.73 | 17.49 | 17.46 |

Table 7.2.: Convergence of centroid energies (in MeV) with respect to oscillator length (in fm).

## 7.5. Transition Strengths

The transition strengths obtained with the projected RPA approach are shown in figures 7.18–7.25. To show the effect of the different types of angular-momentum projection, the plots include the intrinsic as well as the projected transition strengths. For the transitions calculated with the UCOM(VAR)$_{2b}$ and S-SRG$_{3b}$ interactions, we also show the transition strengths obtained when using the PAV minimum of the HF calculation. Since the energy difference of the PAV- and AVAP-minima is small, we attribute the differences between the two strength functions to the different deformation parameters.

Before discussing the physical excitations, we discuss the peaks corresponding to spurious RPA solutions. For the ISD transitions in all nuclei, we see a small peak of the PAV strength at zero energy, which we identify as spurious center-of-mass modes. The modified ISD transition operator (eq. (6.23)) should suppress the strength of this state, but only does this completely for the AVAP solutions, which do not show this state. The ISQ transitions of all nuclei show a strong peak in the region of $E \approx 5$ MeV for the AVAP solutions, which is a $K = 1$ state. For the PAV solutions, there is a zero-energy RPA eigenvalue with $K = 1$ for all nuclei. For some nuclei and interactions, this state has zero-strength, while for others it is extremely strong. The state in the

PAV solutions is clearly spurious. Since the state at $E \approx 5\,\mathrm{MeV}$ is a unique feature of the AVAP solutions, and it is the first RPA eigenvalue, we also regard this state as a spurious solution. This is supported by the shape of the transition densities shown in section 7.7.

Regarding the angular-momentum projected transition strengths, we can make the following observations. The dominant transitions of the UCOM(VAR)$_{2b}$ interaction lie at higher energies than those of the S-SRG$_{3b}$ or S-UCOM(SRG)$_{3b}$ interactions. This effect has already been observed and discussed for spherical nuclei in [Gün11], where it improves the agreement with measured results (see also section 7.6). It is caused by the increased level density in the region of the Fermi energy, which is a direct consequence of the repulsive three-body interaction. The effect of the angular momentum projection depends on the type of transition considered. ISM transitions are enhanced considerably in the energy region above $20\,\mathrm{MeV}$. This effect is more pronounced for $^{12}$C and $^{20}$Ne nuclei, but also occurs for the heavier $^{28}$Si$_o$, $^{28}$Si$_p$ and $^{32}$S. For ISD transitions, the effect is much smaller. The height of some peaks is changed, but the structure of the transitions are very similar. The effect of the projection on IVD and ISQ transitions is stronger than that on ISD transitions, but not comparable to the effect on ISM transitions. A strong effect on the centroid can only be observed for ISM transitions.

Using the PAV ground state instead of the AVAP ground state only has a strong effect in the case of $^{12}$C. For the other nuclei, the effect is rather small. The fine structure is usually shifted by a few MeV, but there are no effects on the overall structure. This behavior is expected, since the PAV ground state and AVAP ground state have slightly different HF levels, which result in different RPA eigenvalues. The strengths projection on the other hand has no effect on the RPA eigenvalues and, therefore, cannot change the peak positions. It can only affect the height of the peaks —but in the case of ISM transitions, this effect can change the strength distribution completely. However, a close look at the ISD strengths for $^{20}$Ne, $^{28}$Si and $^{32}$S reveals peaks at zero-energy for the PAV ground state. These are spurious states, which emphasize the necessity for some kind of *variation after projection* approach.

Apart from the projection, we make the following observations. With increasing nuclear mass, there is a growing amount of substructure in the resonances and the resonance width increases. This is a direct consequence of the increased number of particle-hole pairs in heavier nuclei. The strengths of the S-SRG$_{3b}$ and S-UCOM(SRG)$_{3b}$ interactions look very similar. Since the RPA depends not on the absolute value of the single-particle energy levels, but on the energy gaps near the Fermi energy, the stronger binding of the S-UCOM(SRG)$_{3b}$ interaction does not affect the transition strengths. Some features, low-lying ISD and ISQ peaks, are present for all interactions. In the quadrupole case, the angular momentum projection decreases the strength of these peaks significantly. We will investigate these peaks further in section 7.7.

Figure 7.18.: Results obtained with the UCOM(VAR)$_{2b}$ (top), S-SRG$_{3b}$ (middle) and S-UCOM(SRG)$_{3b}$ (bottom) interactions. Transition strengths for intrinsic PAV (——), projected PAV (——), intrinsic AVAP (——) and projected AVAP (——).

Figure 7.19.: Results obtained with the UCOM(VAR)$_{2b}$ (top), S-SRG$_{3b}$ (middle) and S-UCOM(SRG)$_{3b}$ (bottom) interactions. Transition strengths for intrinsic PAV (—), projected PAV (—), intrinsic AVAP (—) and projected AVAP (—).
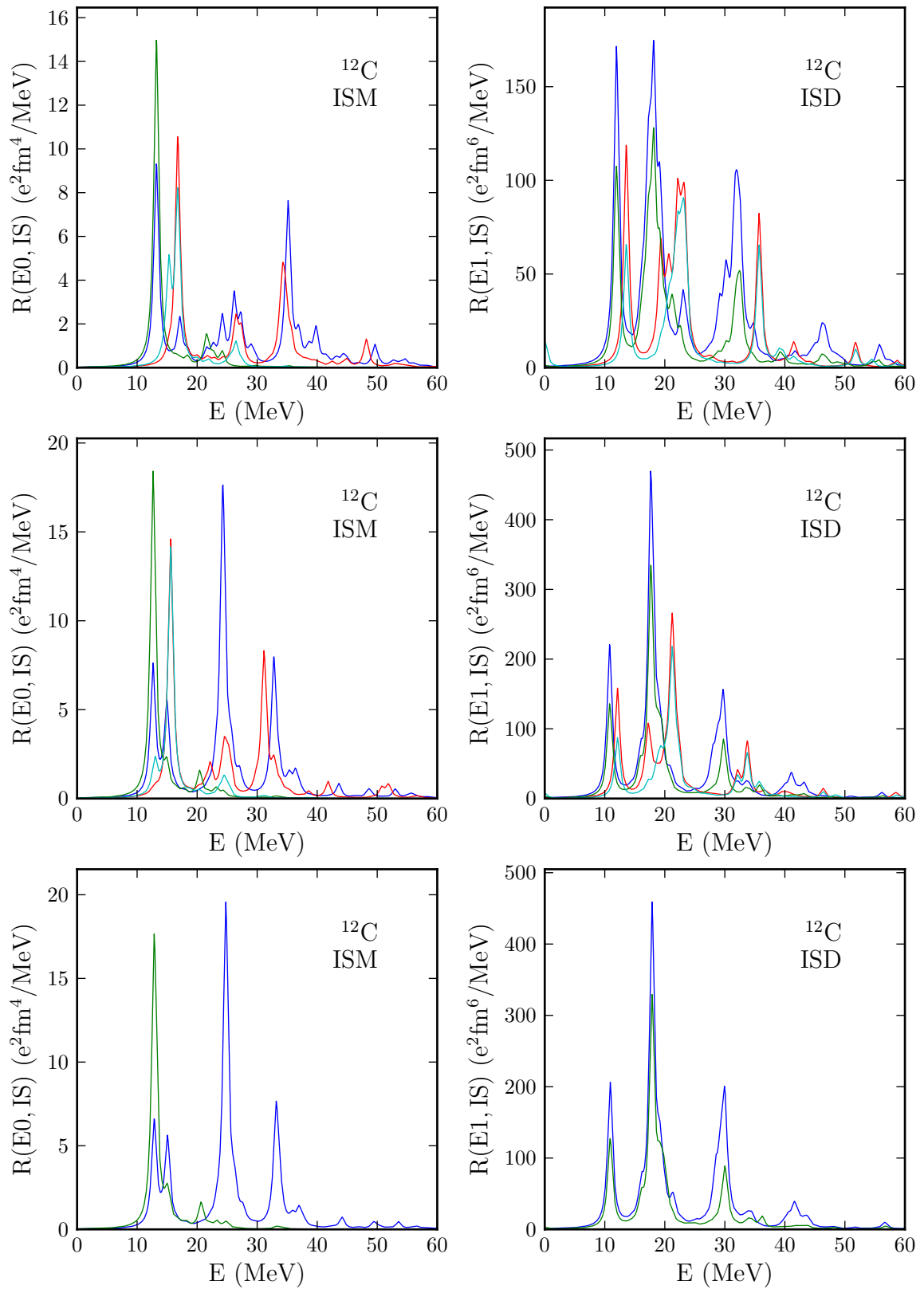
Figure 7.20.: Results obtained with the UCOM(VAR)$_{2b}$ (top), S-SRG$_{3b}$ (middle) and S-UCOM(SRG)$_{3b}$ (bottom) interactions. Transition strengths for intrinsic PAV (——), projected PAV (——), intrinsic AVAP (——) and projected AVAP (——).

Figure 7.21.: Results obtained with the UCOM(VAR)$_{2b}$ (top), S-SRG$_{3b}$ (middle) and S-UCOM(SRG)$_{3b}$ (bottom) interactions. Transition strengths for intrinsic PAV (—), projected PAV (—), intrinsic AVAP (—) and projected AVAP (—).
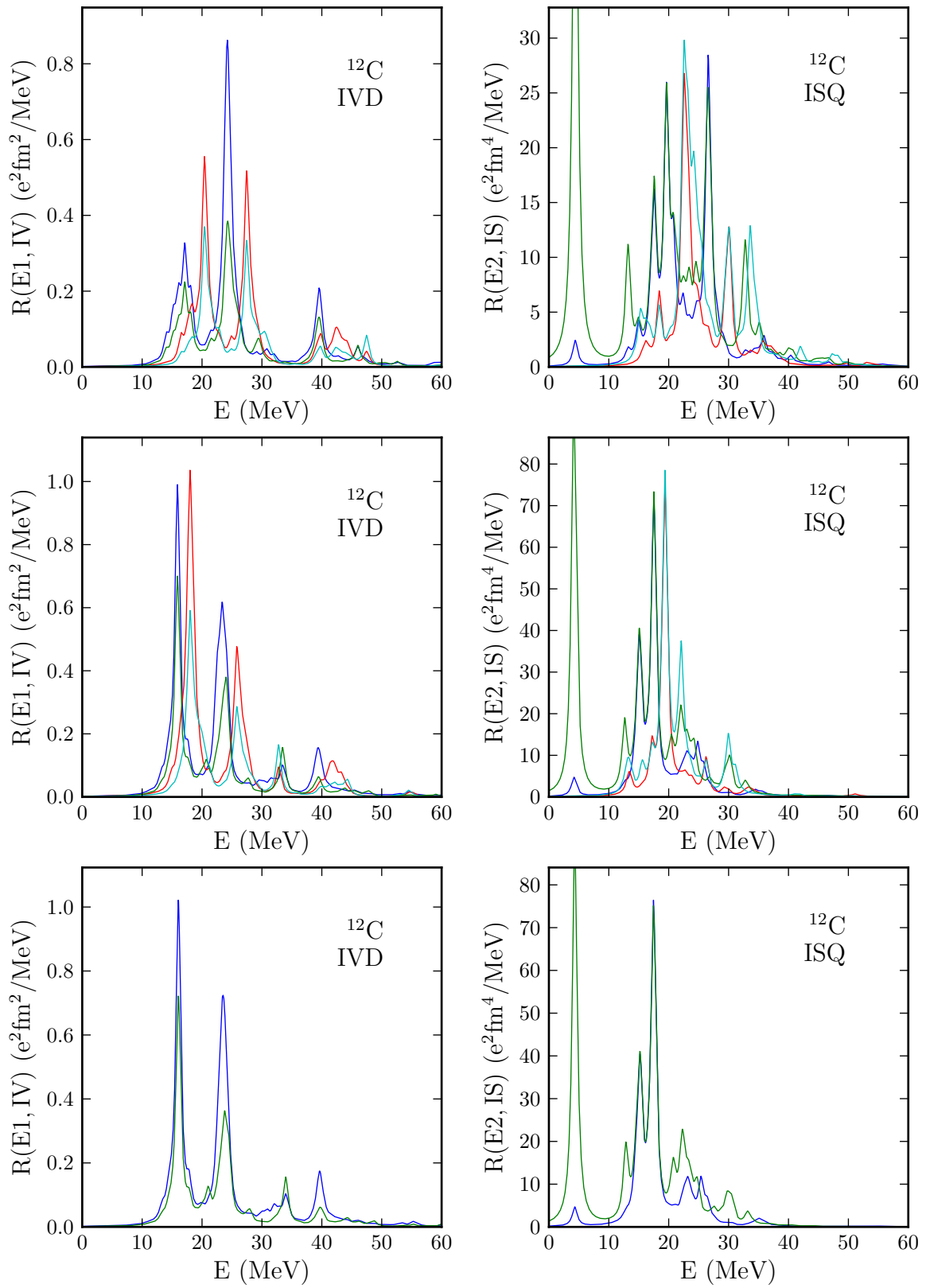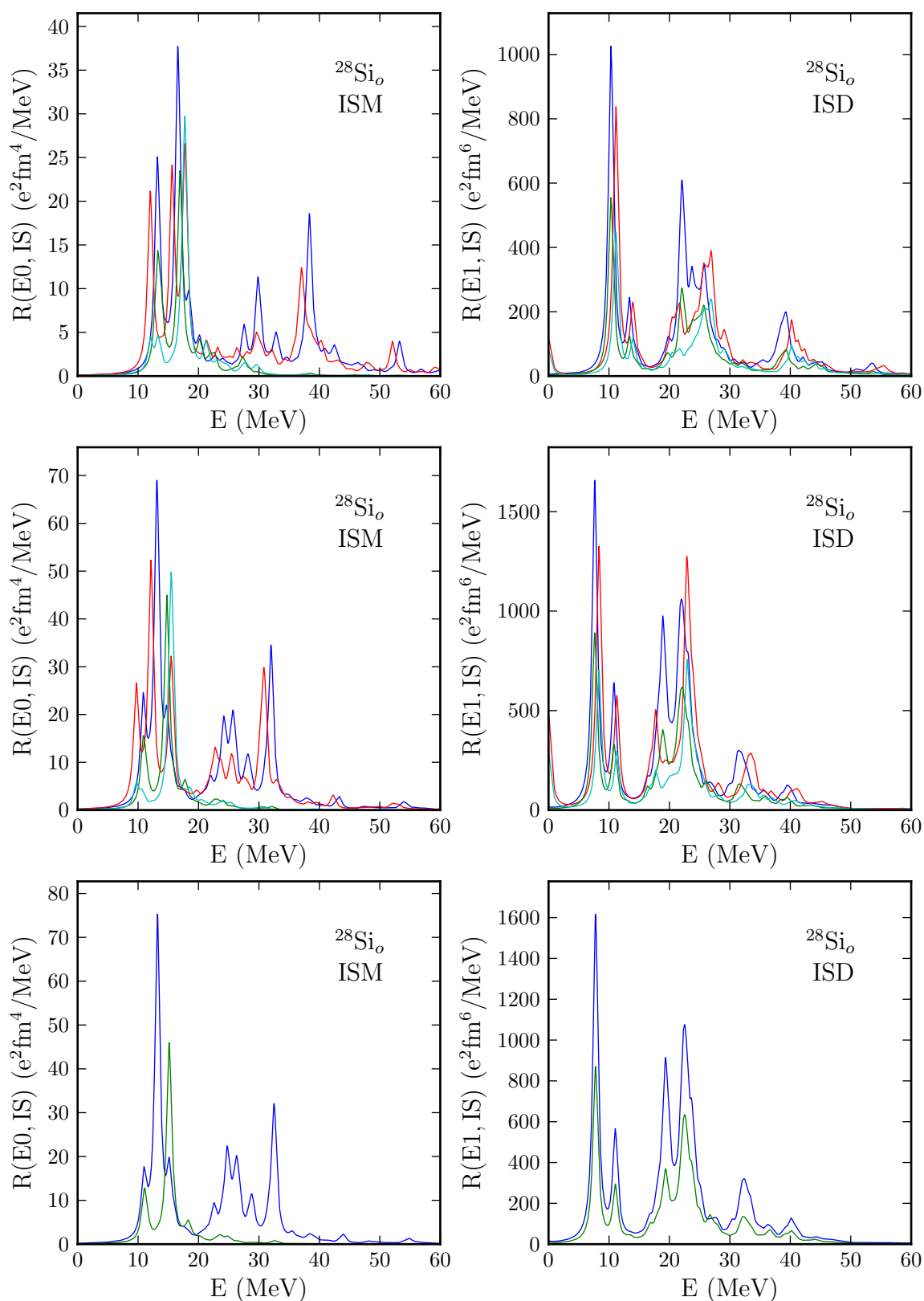
Figure 7.22.: Results obtained with the UCOM(VAR)$_{2b}$ (top), S-SRG$_{3b}$ (middle) and S-UCOM(SRG)$_{3b}$ (bottom) interactions. Transition strengths for intrinsic PAV (——), projected PAV (——), intrinsic AVAP (——) and projected AVAP (——).
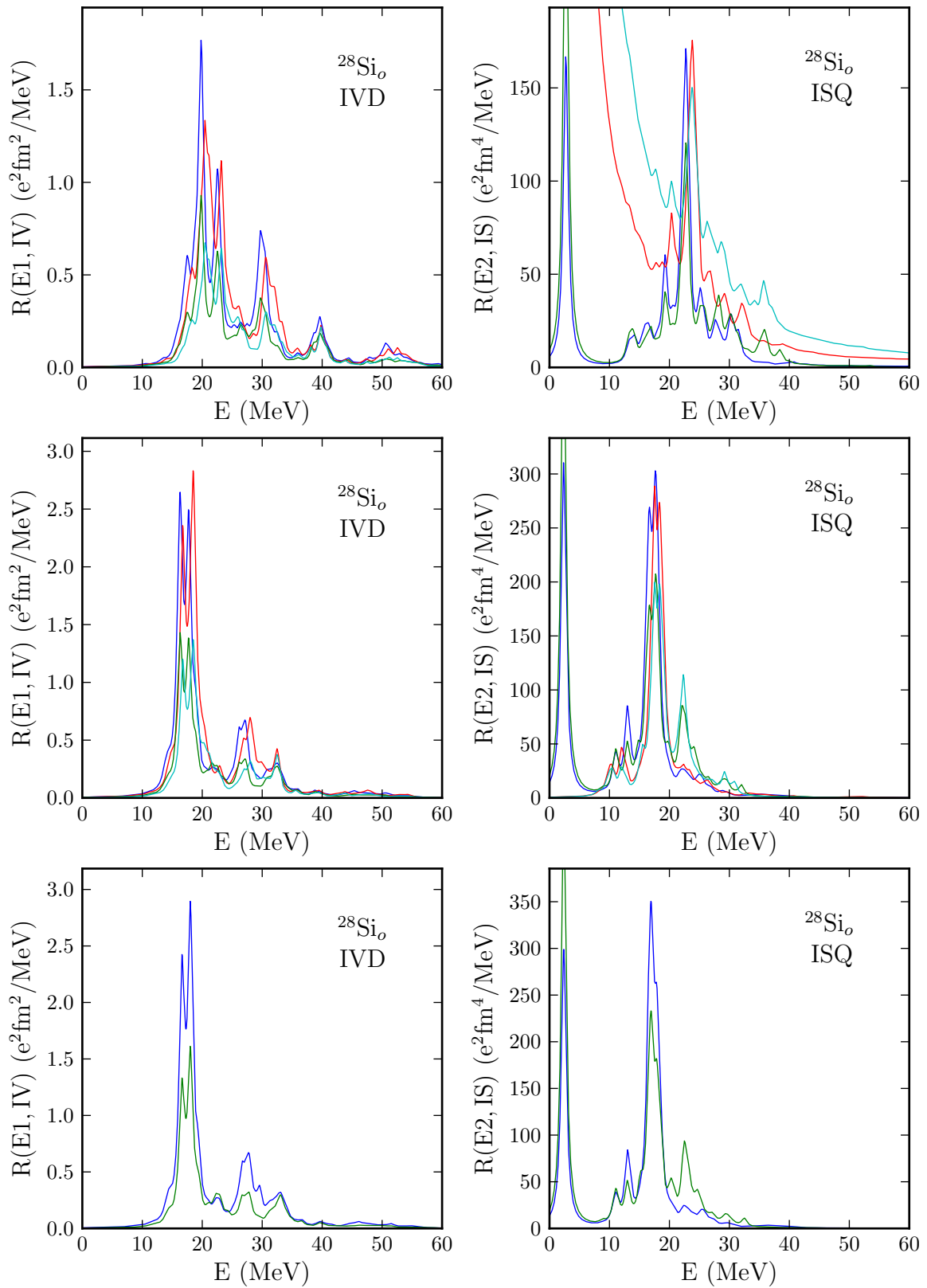
Figure 7.23.: Results obtained with the UCOM(VAR)$_{2b}$ (top), S-SRG$_{3b}$ (middle) and S-UCOM(SRG)$_{3b}$ (bottom) interactions. Transition strengths for intrinsic PAV (——), projected PAV (——), intrinsic AVAP (——) and projected AVAP (——).
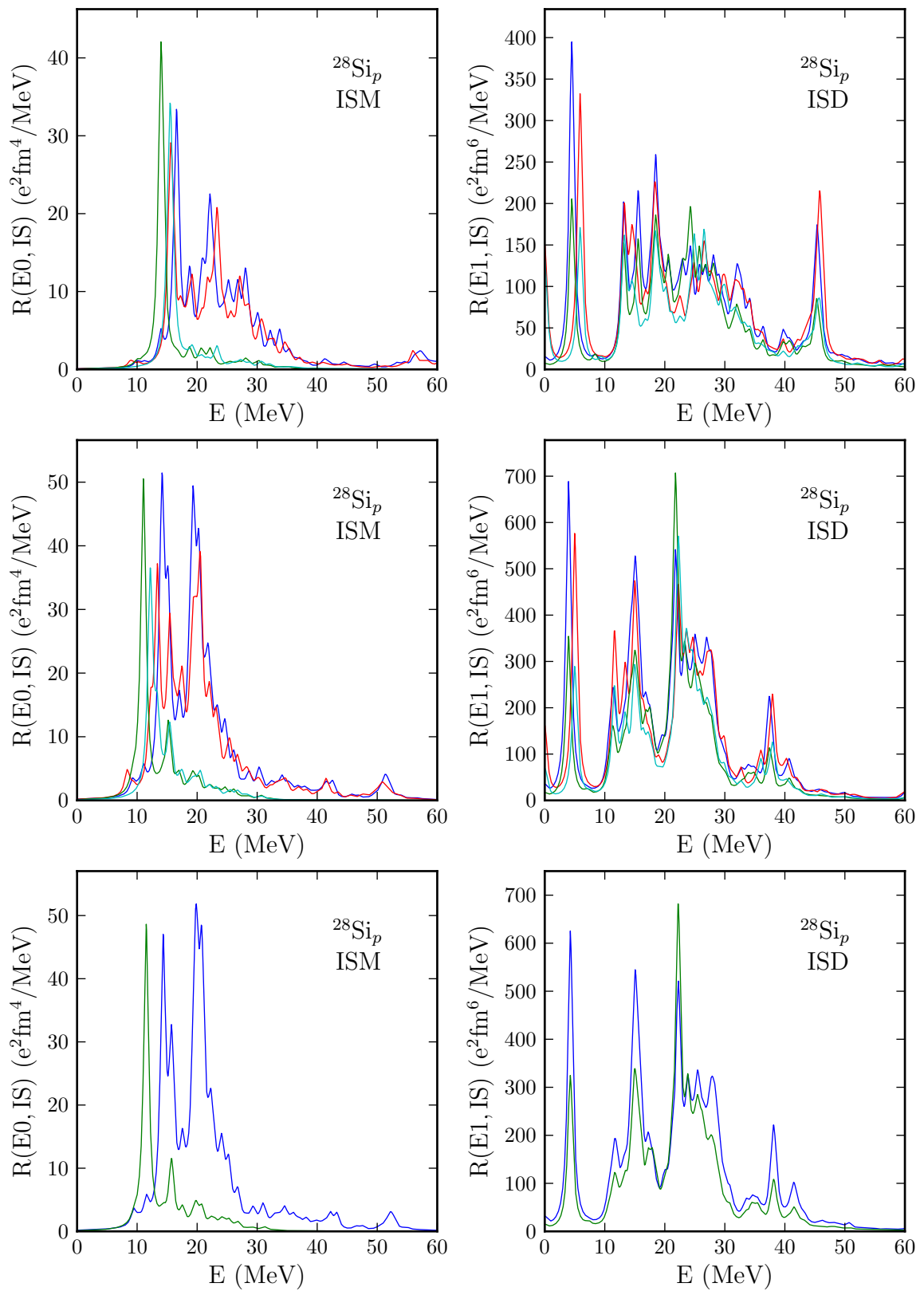
Figure 7.24.: Results obtained with the UCOM(VAR)$_{2b}$ (top), S-SRG$_{3b}$ (middle) and S-UCOM(SRG)$_{3b}$ (bottom) interactions. Transition strengths for intrinsic PAV (——), projected PAV (——), intrinsic AVAP (——) and projected AVAP (——).
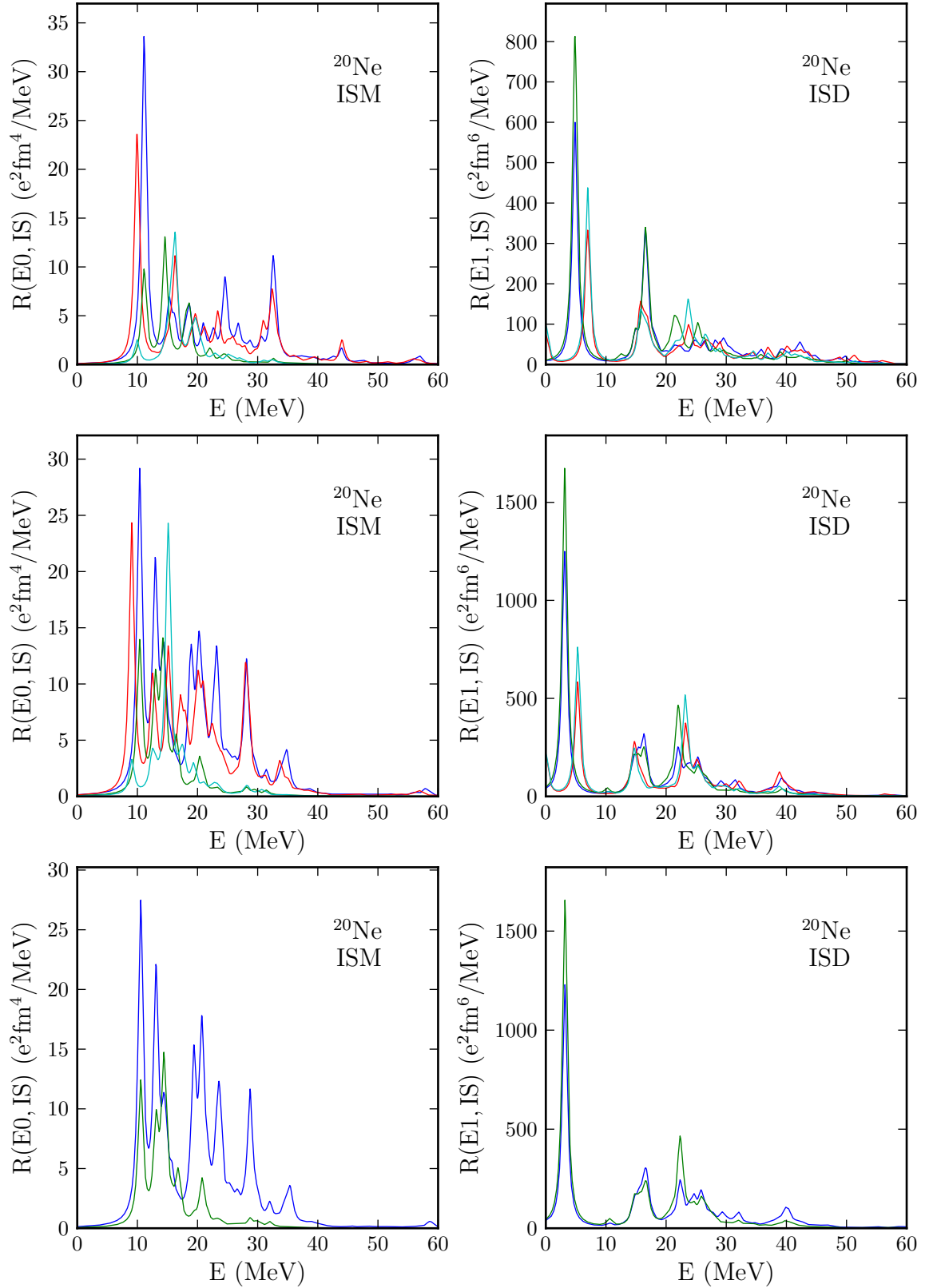
125
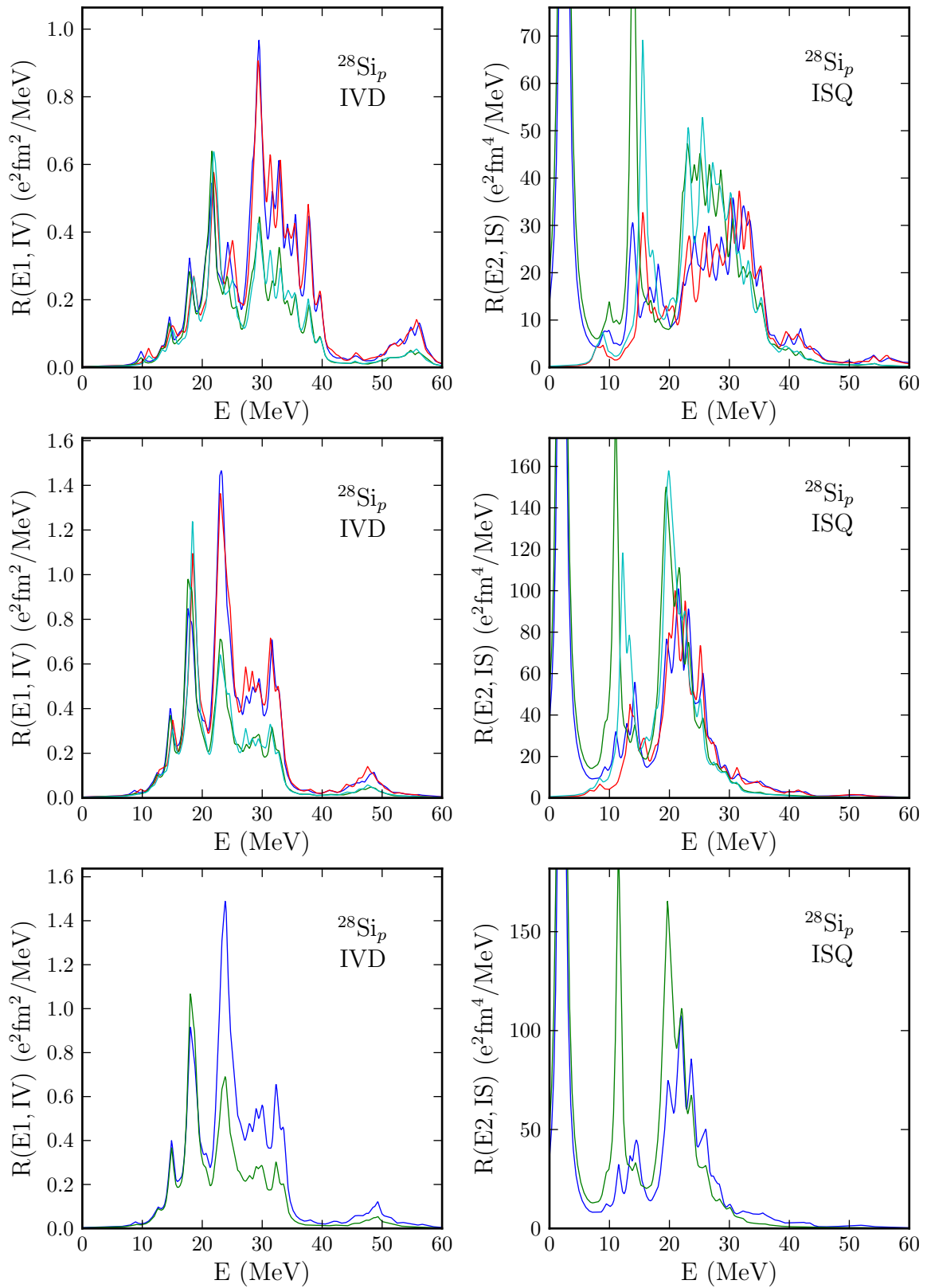
Figure 7.25.: Results obtained with the UCOM(VAR)$_{2b}$ (top), S-SRG$_{3b}$ (middle) and S-UCOM(SRG)$_{3b}$ (bottom) interactions. Transition strengths for intrinsic PAV (—), projected PAV (—), intrinsic AVAP (—) and projected AVAP (—).

Figure 7.26.: Results obtained with the UCOM(VAR)$_{2b}$ (top), S-SRG$_{3b}$ (middle) and S-UCOM(SRG)$_{3b}$ (bottom) interactions. Transition strengths for intrinsic PAV (——), projected PAV (——), intrinsic AVAP (——) and projected AVAP (——).
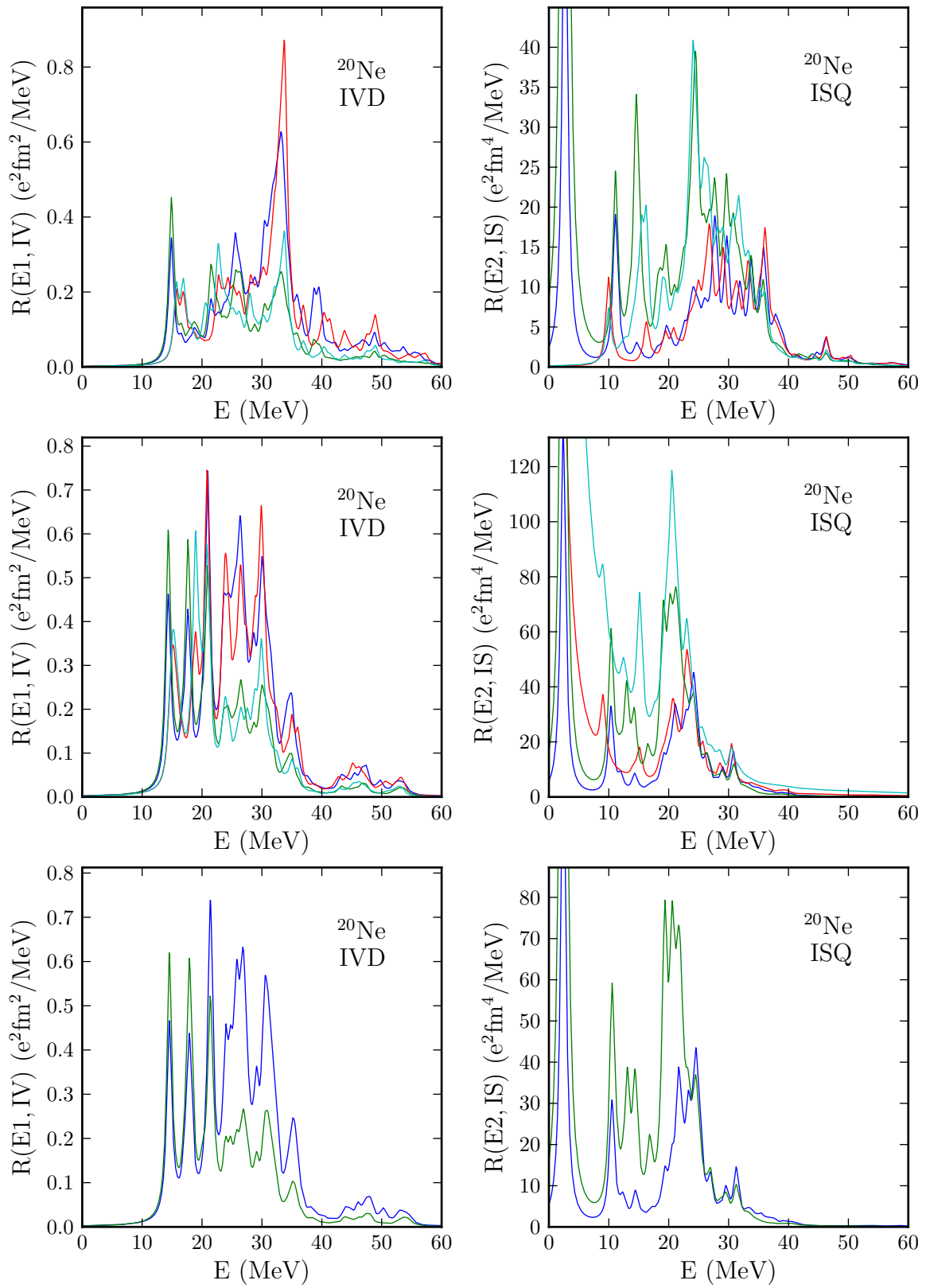
Figure 7.27.: Results obtained with the UCOM(VAR)$_{2b}$ (top), S-SRG$_{3b}$ (middle) and S-UCOM(SRG)$_{3b}$ (bottom) interactions. Transition strengths for intrinsic PAV (——), projected PAV (——), intrinsic AVAP (——) and projected AVAP (——).
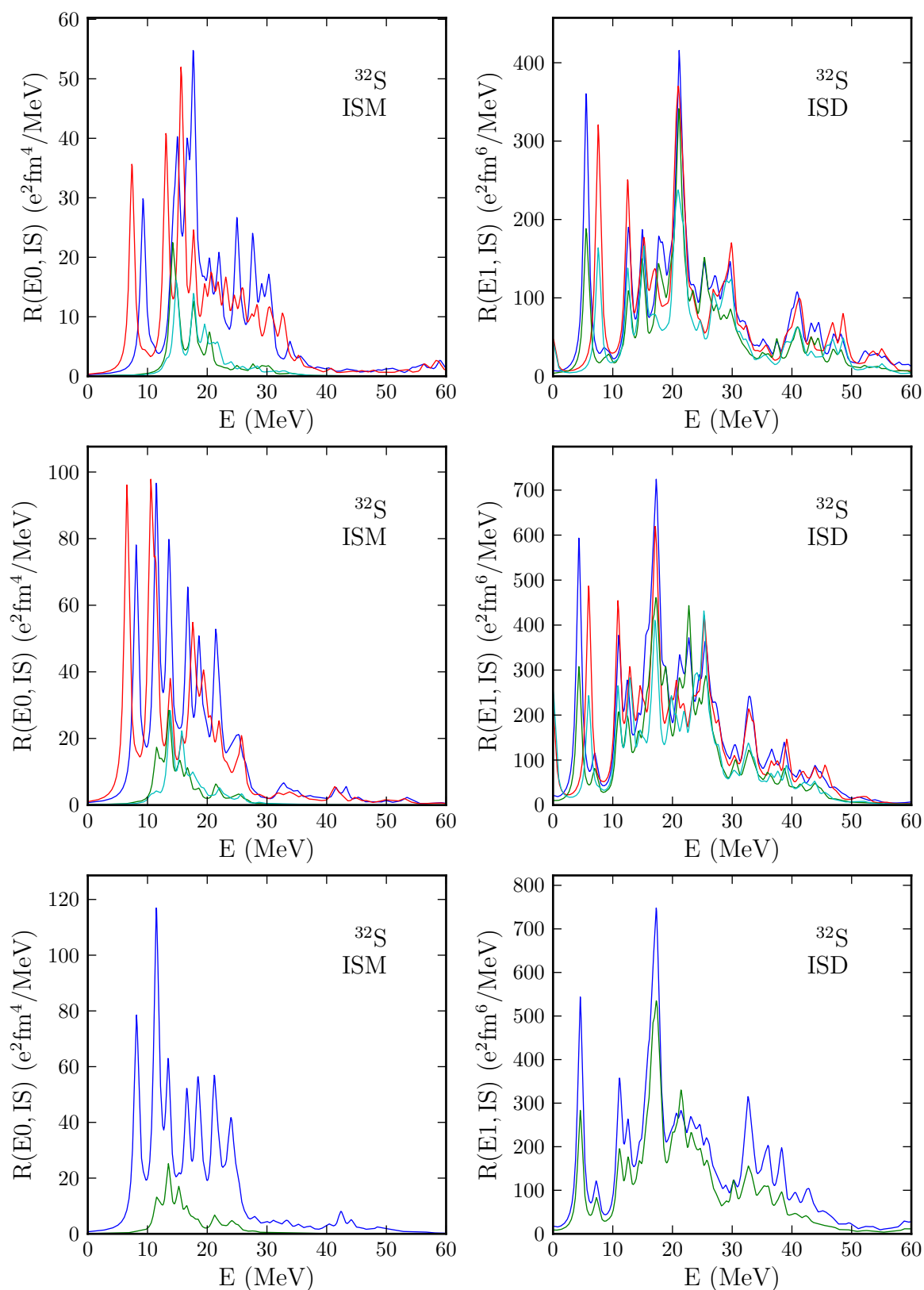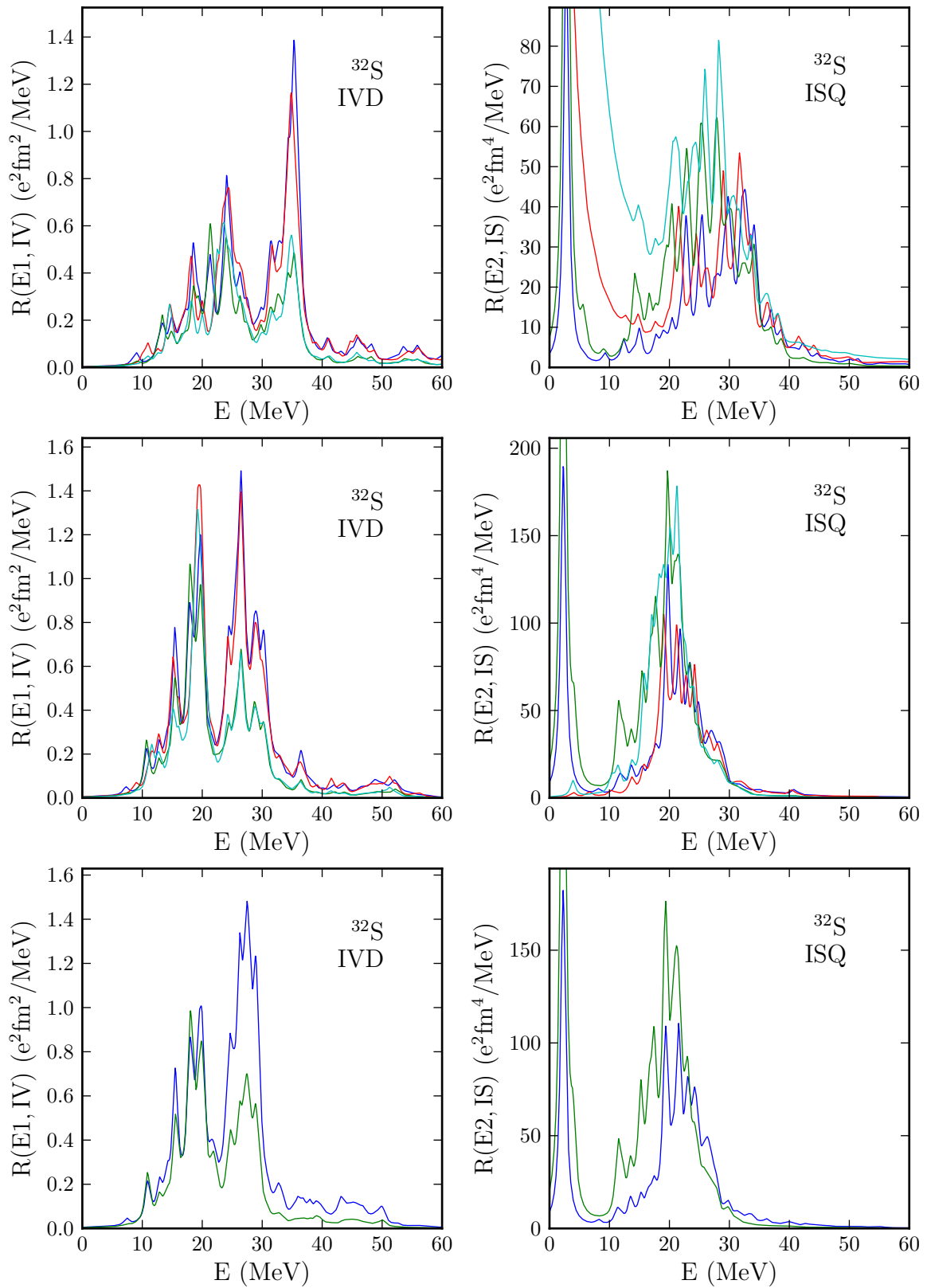
## 7.6. Comparison to Experimental Data

In this section, we compare our results to various data from experiment. Data on the isovector dipole resonance has been extracted directly from cross sections obtained from the CDFE database [CDF]. Where possible, the original publication is referenced, otherwise the citation key from the CDFE database is given. Measurements for the IVD resonance are made by photonuclear processes, $(\gamma,n)$ or $(\gamma,p)$. As shown in [RS80, appendix B], the dipole absorption cross section is proportional to the incident energy and the transition strength. The centroids and width given in tables 7.4, 7.6, 7.7-7.9 are given with respect to the cross sections, i.e.

$$E_{\text{cent}} = \frac{\sum_{E_{\min} \leq E_i \leq E_{\max}} E_i^2 \, B_i(E1)}{\sum_{E_{\min} \leq E_i \leq E_{\max}} E_i \, B_i(E1)} \quad . \tag{7.4}$$

Data on isoscalar transitions has been obtained from individual sources, where values for centroid energies and their widths have been given. Isoscalar transitions are usually measured by scattering with $\alpha$ particles, which can excite electric isoscalar transitions (see [Ber69, HvdW01]). As centroids are taken with respect to plots of sum-rule percentage (see also section 7.1), the same scaling as in eq. (7.4) also applies to this data

$$E_{\text{cent}} = \frac{\sum_{E_{\min} \leq E_i \leq E_{\max}} E_i^2 \, B_i(E\lambda)}{\sum_{E_{\min} \leq E_i \leq E_{\max}} E_i \, B_i(E\lambda)} \quad . \tag{7.5}$$

The rms-width is of the centroids $\Gamma_{\text{cent}}$ is given by

$$\Gamma_{\text{cent}} = \sqrt{\frac{\sum_{E_{\min} \leq E_i \leq E_{\max}} (E_i - E_{\text{cent}})^2 \, E_i \, B_i(E\lambda)}{\sum_{E_{\min} \leq E_i \leq E_{\max}} E_i \, B_i(E\lambda)}} \quad . \tag{7.6}$$

For each pair of measured values $E_{\text{cent}}$ and $\Gamma_{\text{cent}}$, we calculate $E_{\text{cent}}$ and $\Gamma_{\text{cent}}$ for the same energy window $E_{\min}$–$E_{\max}$ with our three interactions. Only the AVAP HF ground state is considered. $^{28}$Si is the only deformed nucleus where high quality data for isoscalar transitions is available. Due to the degenerate prolate and oblate states, we show one table for each of the two states. Table 7.3 shows the results for isoscalar transitions in the oblate state of $^{28}$Si$_o$ and table 7.4 shows results for the isovector dipole transition. Tables 7.5 and 7.6 show the same results for the prolate state $^{28}$Si$_p$. For the other deformed nuclei, only data for the IVD transition is available. It is shown in tables 7.7 ($^{12}$C), 7.8 ($^{20}$Ne) and 7.9 ($^{32}$S).

We can make the following observations:

- As already seen for spherical nuclei, the UCOM(VAR)$_{2b}$ interaction overestimates the centroid energies of most transitions. The S-SRG$_{3b}$ and S-UCOM(SRG)$_{3b}$ interactions agree much better with experiment

- In the case of $^{28}$Si, the question arises, if the centroid energies allow us to decide for one of the two possible ground state shapes. The values for the ISM transition are better reproduced by the prolate solution, however, as this is a breathing mode, the nucleir shape should not affect this transition very much.

The ISD transition should depend on the deformation, but its centroids are not well reproduced for both nuclei. Both, the ISQ and IVD centroids are well reproduced (withing less 1 MeV) for the oblate state, but not for the prolate state. This suggest, that the oblate state is the true ground state.

- A strong effect of the angular momentum projection can only be seen for the ISM transition in $^{28}$Si, where it leads to a much better agreement with the measured value.

- The rms-width of the transitions for deformed nuclei is usually reproduced quite well, and more often overestimated than underestimated. This is rather surprising, as the RPA does not take into account some processes which increase the width, like coupling to the continuum or configurations more complex than one-particle-one-hole excitations. This is also in contrast to spherical nuclei, where the width is underestimated more often.

- Our results for $^{12}$C agree well with the majority of the data. For small energy windows (smaller than 15 MeV), the width agrees well with experiment, but for larger windows (30 MeV), we overestimate the width.

- For $^{20}$Ne, our calculated values exceed the measured values by a few MeV. The width is reproduced well, but the energy windows of the experiments were not larger than 15 MeV. We get a similar picture for $^{32}$S.

| nucleus transition energy range | experiment or projected | | intrinsic | | reference or interaction |
|---|---|---|---|---|---|
| | $E_{\text{cent}}$ | $\Gamma_{\text{cent}}$ | $E_{\text{cent}}$ | $\Gamma_{\text{cent}}$ | |
| $^{28}\text{Si}_o$ | 17.3 | 3.0 | | | [YLC02, CLC$^+$09] |
| E0, IS | 16.1 | 2.1 | 16.4 | 2.4 | UCOM(VAR)$_{2b}$ |
| 8.0–22.5 | 14.1 | 2.9 | 14.7 | 2.4 | S-SRG$_{3b}$ |
| | 14.2 | 2.7 | 15.0 | 2.1 | S-UCOM(SRG)$_{3b}$ |
| $^{28}\text{Si}_o$ | 28.2 | 3.8 | | | [YLC02, CLC$^+$09] |
| E0, IS | 34.1 | 4.8 | 27.5 | 4.4 | UCOM(VAR)$_{2b}$ |
| 22.5–40.0 | 29.3 | 3.9 | 27.2 | 4.5 | S-SRG$_{3b}$ |
| | 29.3 | 4.0 | 27.0 | 4.4 | S-UCOM(SRG)$_{3b}$ |
| $^{28}\text{Si}_o$ | 21.2 | 6.4 | | | [YLC02, CLC$^+$09] |
| E0, IS | 26.6 | 9.7 | 18.4 | 5.1 | UCOM(VAR)$_{2b}$ |
| 8.0–40.0 | 23.7 | 8.1 | 16.1 | 4.8 | S-SRG$_{3b}$ |
| | 23.9 | 8.1 | 16.6 | 4.8 | S-UCOM(SRG)$_{3b}$ |
| $^{28}\text{Si}_o$ | 15.3 | 4.8 | | | [YLC02, CLC$^+$09] |
| E1, IS | 16.5 | 5.4 | 16.2 | 5.3 | UCOM(VAR)$_{2b}$ |
| 8.0–22.5 | 19.3 | 3.4 | 19.5 | 3.4 | S-SRG$_{3b}$ |
| | 19.3 | 3.4 | 19.3 | 3.5 | S-UCOM(SRG)$_{3b}$ |
| $^{28}\text{Si}_o$ | 27.6 | 3.0 | | | [YLC02, CLC$^+$09] |
| E1, IS | 30.2 | 6.3 | 29.3 | 5.7 | UCOM(VAR)$_{2b}$ |
| 22.5–40.0 | 29.8 | 5.4 | 29.5 | 5.5 | S-SRG$_{3b}$ |
| | 28.6 | 5.1 | 28.3 | 5.2 | S-UCOM(SRG)$_{3b}$ |
| $^{28}\text{Si}_o$ | 19.3 | 6.9 | | | [YLC02, CLC$^+$09] |
| E1, IS | 24.7 | 9.0 | 24.3 | 8.5 | UCOM(VAR)$_{2b}$ |
| 8.0–40.0 | 24.2 | 6.9 | 24.3 | 6.8 | S-SRG$_{3b}$ |
| | 24.4 | 6.4 | 24.5 | 6.3 | S-UCOM(SRG)$_{3b}$ |
| $^{28}\text{Si}_o$ | 16.6 | 3.5 | | | [YLC02, CLC$^+$09] |
| E2, IS | 19.4 | 2.7 | 19.0 | 3.0 | UCOM(VAR)$_{2b}$ |
| 8.0–22.5 | 16.8 | 2.0 | 17.5 | 2.7 | S-SRG$_{3b}$ |
| | 16.9 | 1.9 | 17.7 | 2.7 | S-UCOM(SRG)$_{3b}$ |
| $^{28}\text{Si}_o$ | 27.2 | 3.0 | | | [YLC02, CLC$^+$09] |
| E2, IS | 25.8 | 3.8 | 28.1 | 4.9 | UCOM(VAR)$_{2b}$ |
| 22.5–40.0 | 27.6 | 4.8 | 26.1 | 3.4 | S-SRG$_{3b}$ |
| | 28.0 | 4.8 | 26.2 | 3.3 | S-UCOM(SRG)$_{3b}$ |
| $^{28}\text{Si}_o$ | 18.5 | 4.7 | | | [YLC02, CLC$^+$09] |
| E2, IS | 23.7 | 4.6 | 25.8 | 6.0 | UCOM(VAR)$_{2b}$ |
| 8.0–40.0 | 18.3 | 4.5 | 19.8 | 4.8 | S-SRG$_{3b}$ |
| | 18.4 | 4.5 | 19.9 | 4.7 | S-UCOM(SRG)$_{3b}$ |

Table 7.3.: Comparison of calculated centroid energies and widths (in MeV) of $^{28}\text{Si}_o$ to experimental data.

| nucleus transition energy range | experiment or projected | | intrinsic | | reference or interaction |
|---|---|---|---|---|---|
| | centroid energy | width | centroid energy | width | |
| $^{28}$Si$_o$ | 22.0 | 3.1 | | | [V$^+$c] |
| E1, IV | 22.6 | 3.9 | 22.9 | 3.9 | UCOM(VAR)$_{2b}$ |
| 16.7–30.0 | 21.8 | 4.3 | 21.5 | 3.9 | S-SRG$_{3b}$ |
| | 21.8 | 4.4 | 21.6 | 4.0 | S-UCOM(SRG)$_{3b}$ |
| $^{28}$Si$_o$ | 23.0 | 6.4 | | | [I$^+$b] |
| E1, IV | 25.5 | 6.6 | 26.0 | 6.6 | UCOM(VAR)$_{2b}$ |
| 10.0–40.0 | 22.1 | 6.4 | 22.9 | 6.7 | S-SRG$_{3b}$ |
| | 22.5 | 6.4 | 23.2 | 6.7 | S-UCOM(SRG)$_{3b}$ |
| $^{28}$Si$_o$ | 22.5 | 3.4 | | | [GISY68] |
| E1, IV | 22.7 | 3.9 | 23.0 | 3.8 | UCOM(VAR)$_{2b}$ |
| 17.4–29.8 | 21.9 | 4.3 | 21.6 | 3.9 | S-SRG$_{3b}$ |
| | 22.0 | 4.4 | 21.7 | 4.0 | S-UCOM(SRG)$_{3b}$ |
| $^{28}$Si$_o$ | 22.2 | 3.3 | | | [PBJ$^+$83] |
| E1, IV | 24.1 | 4.7 | 24.3 | 4.5 | UCOM(VAR)$_{2b}$ |
| 17.0–33.1 | 23.3 | 5.4 | 23.6 | 5.5 | S-SRG$_{3b}$ |
| | 22.9 | 5.2 | 22.9 | 5.1 | S-UCOM(SRG)$_{3b}$ |
| $^{28}$Si$_o$ | 22.4 | 3.4 | | | [CHBF63] |
| E1, IV | 23.5 | 4.5 | 23.7 | 4.3 | UCOM(VAR)$_{2b}$ |
| 16.8–31.0 | 22.1 | 4.6 | 22.0 | 4.3 | S-SRG$_{3b}$ |
| | 21.9 | 4.5 | 21.7 | 4.2 | S-UCOM(SRG)$_{3b}$ |
| $^{28}$Si$_o$ | 22.5 | 3.3 | | | [GISY68] |
| E1, IV | 21.7 | 3.0 | 22.2 | 3.2 | UCOM(VAR)$_{2b}$ |
| 17.3–29.4 | 21.8 | 4.2 | 21.6 | 3.9 | S-SRG$_{3b}$ |
| | 21.8 | 4.3 | 21.6 | 3.9 | S-UCOM(SRG)$_{3b}$ |
| $^{28}$Si$_o$ | 21.5 | 2.5 | | | [V$^+$a] |
| E1, IV | 21.1 | 2.6 | 21.6 | 2.8 | UCOM(VAR)$_{2b}$ |
| 16.7–27.7 | 21.3 | 4.0 | 21.2 | 3.7 | S-SRG$_{3b}$ |
| | 20.6 | 3.7 | 20.7 | 3.4 | S-UCOM(SRG)$_{3b}$ |
| $^{28}$Si$_o$ | 21.4 | 2.6 | | | [VIK$^+$79] |
| E1, IV | 21.1 | 2.6 | 21.6 | 2.8 | UCOM(VAR)$_{2b}$ |
| 16.1–27.9 | 19.8 | 4.1 | 19.9 | 3.9 | S-SRG$_{3b}$ |
| | 20.0 | 4.0 | 20.1 | 3.8 | S-UCOM(SRG)$_{3b}$ |

Table 7.4.: Comparison of calculated centroid energies and widths (in MeV) of $^{28}$Si$_o$ to experimental data.

| nucleus transition energy range | experiment or projected | | intrinsic | | reference or interaction |
|---|---|---|---|---|---|
| | centroid energy | width | centroid energy | width | |
| $^{28}\text{Si}_p$ E0, IS 8.0–22.5 | 17.3 | 3.0 | | | [YLC02, CLC$^+$09] |
| | 18.9 | 2.6 | 15.2 | 2.6 | UCOM(VAR)$_{2b}$ |
| | 18.0 | 3.0 | 13.8 | 3.6 | S-SRG$_{3b}$ |
| | 18.3 | 2.9 | 14.2 | 3.5 | S-UCOM(SRG)$_{3b}$ |
| $^{28}\text{Si}_p$ E0, IS 22.5–40.0 | 28.2 | 3.8 | | | [YLC02, CLC$^+$09] |
| | 28.4 | 3.9 | 29.3 | 4.1 | UCOM(VAR)$_{2b}$ |
| | 29.1 | 5.1 | 26.7 | 3.2 | S-SRG$_{3b}$ |
| | 29.0 | 5.2 | 26.7 | 3.3 | S-UCOM(SRG)$_{3b}$ |
| $^{28}\text{Si}_p$ E0, IS 8.0–40.0 | 21.2 | 6.4 | | | [YLC02, CLC$^+$09] |
| | 24.0 | 5.8 | 17.9 | 6.3 | UCOM(VAR)$_{2b}$ |
| | 21.2 | 6.2 | 15.6 | 5.8 | S-SRG$_{3b}$ |
| | 21.5 | 6.1 | 16.2 | 5.8 | S-UCOM(SRG)$_{3b}$ |
| $^{28}\text{Si}_p$ E1, IS 8.0–22.5 | 15.3 | 4.8 | | | [YLC02, CLC$^+$09] |
| | 17.6 | 2.8 | 17.7 | 2.9 | UCOM(VAR)$_{2b}$ |
| | 17.5 | 3.6 | 18.5 | 3.5 | S-SRG$_{3b}$ |
| | 17.8 | 3.7 | 19.0 | 3.6 | S-UCOM(SRG)$_{3b}$ |
| $^{28}\text{Si}_p$ E1, IS 22.5–40.0 | 27.6 | 3.0 | | | [YLC02, CLC$^+$09] |
| | 29.9 | 4.5 | 28.7 | 4.5 | UCOM(VAR)$_{2b}$ |
| | 29.3 | 5.0 | 28.5 | 5.0 | S-SRG$_{3b}$ |
| | 29.8 | 5.1 | 28.9 | 4.9 | S-UCOM(SRG)$_{3b}$ |
| $^{28}\text{Si}_p$ E1, IS 8.0–40.0 | 19.3 | 6.9 | | | [YLC02, CLC$^+$09] |
| | 25.3 | 7.2 | 24.9 | 6.6 | UCOM(VAR)$_{2b}$ |
| | 24.5 | 7.4 | 23.8 | 6.6 | S-SRG$_{3b}$ |
| | 25.1 | 7.4 | 24.3 | 6.6 | S-UCOM(SRG)$_{3b}$ |
| $^{28}\text{Si}_p$ E2, IS 8.0–22.5 | 16.6 | 3.5 | | | [YLC02, CLC$^+$09] |
| | 17.0 | 3.4 | 16.0 | 3.6 | UCOM(VAR)$_{2b}$ |
| | 18.5 | 3.5 | 17.7 | 4.0 | S-SRG$_{3b}$ |
| | 19.1 | 3.4 | 18.2 | 3.9 | S-UCOM(SRG)$_{3b}$ |
| $^{28}\text{Si}_p$ E2, IS 22.5–40.0 | 27.2 | 3.0 | | | [YLC02, CLC$^+$09] |
| | 30.5 | 4.1 | 28.6 | 4.1 | UCOM(VAR)$_{2b}$ |
| | 26.8 | 4.2 | 25.7 | 3.1 | S-SRG$_{3b}$ |
| | 27.3 | 4.2 | 26.2 | 3.1 | S-UCOM(SRG)$_{3b}$ |
| $^{28}\text{Si}_p$ E2, IS 8.0–40.0 | 18.5 | 4.7 | | | [YLC02, CLC$^+$09] |
| | 27.8 | 6.7 | 25.5 | 6.8 | UCOM(VAR)$_{2b}$ |
| | 22.8 | 5.7 | 19.9 | 5.2 | S-SRG$_{3b}$ |
| | 23.0 | 5.6 | 20.1 | 5.1 | S-UCOM(SRG)$_{3b}$ |

Table 7.5.: Comparison of calculated centroid energies and widths (in MeV) of $^{28}\text{Si}_p$ to experimental data.

| nucleus transition energy range | experiment or projected | | intrinsic | | reference or interaction |
|---|---|---|---|---|---|
| | centroid energy | width | centroid energy | width | |
| $^{28}\mathrm{Si}_p$ | 22.0 | 3.1 | | | [V$^+$c] |
| E1, IV | 25.7 | 3.9 | 24.4 | 4.0 | UCOM(VAR)$_{2b}$ |
| 16.7–30.0 | 23.6 | 3.6 | 22.5 | 3.9 | S-SRG$_{3b}$ |
| | 23.9 | 3.5 | 22.8 | 3.9 | S-UCOM(SRG)$_{3b}$ |
| $^{28}\mathrm{Si}_p$ | 23.0 | 6.4 | | | [I$^+$b] |
| E1, IV | 29.9 | 6.0 | 28.2 | 6.4 | UCOM(VAR)$_{2b}$ |
| 10.0–40.0 | 25.1 | 5.2 | 23.6 | 5.5 | S-SRG$_{3b}$ |
| | 25.5 | 5.2 | 24.0 | 5.6 | S-UCOM(SRG)$_{3b}$ |
| $^{28}\mathrm{Si}_p$ | 22.5 | 3.4 | | | [GISY68] |
| E1, IV | 25.5 | 3.9 | 24.1 | 3.8 | UCOM(VAR)$_{2b}$ |
| 17.4–29.8 | 23.6 | 3.5 | 22.6 | 3.9 | S-SRG$_{3b}$ |
| | 23.7 | 3.3 | 22.6 | 3.7 | S-UCOM(SRG)$_{3b}$ |
| $^{28}\mathrm{Si}_p$ | 22.2 | 3.3 | | | [PBJ$^+$83] |
| E1, IV | 27.4 | 4.4 | 26.1 | 4.7 | UCOM(VAR)$_{2b}$ |
| 17.0–33.1 | 25.5 | 4.7 | 24.1 | 5.0 | S-SRG$_{3b}$ |
| | 25.3 | 4.4 | 24.0 | 4.8 | S-UCOM(SRG)$_{3b}$ |
| $^{28}\mathrm{Si}_p$ | 22.4 | 3.4 | | | [CHBF63] |
| E1, IV | 25.9 | 4.0 | 24.6 | 4.1 | UCOM(VAR)$_{2b}$ |
| 16.8–31.0 | 23.8 | 3.7 | 22.8 | 4.1 | S-SRG$_{3b}$ |
| | 24.2 | 3.7 | 23.1 | 4.1 | S-UCOM(SRG)$_{3b}$ |
| $^{28}\mathrm{Si}_p$ | 22.5 | 3.3 | | | [GISY68] |
| E1, IV | 24.7 | 3.7 | 23.5 | 3.5 | UCOM(VAR)$_{2b}$ |
| 17.3–29.4 | 23.2 | 3.2 | 22.2 | 3.7 | S-SRG$_{3b}$ |
| | 23.6 | 3.2 | 22.4 | 3.5 | S-UCOM(SRG)$_{3b}$ |
| $^{28}\mathrm{Si}_p$ | 21.5 | 2.5 | | | [V$^+$a] |
| E1, IV | 22.2 | 2.7 | 22.0 | 2.6 | UCOM(VAR)$_{2b}$ |
| 16.7–27.7 | 22.5 | 2.9 | 21.5 | 3.2 | S-SRG$_{3b}$ |
| | 22.8 | 2.8 | 21.7 | 3.1 | S-UCOM(SRG)$_{3b}$ |
| $^{28}\mathrm{Si}_p$ | 21.4 | 2.6 | | | [VIK$^+$79] |
| E1, IV | 22.2 | 2.8 | 22.0 | 2.6 | UCOM(VAR)$_{2b}$ |
| 16.1–27.9 | 22.5 | 2.9 | 21.5 | 3.2 | S-SRG$_{3b}$ |
| | 22.7 | 2.8 | 21.7 | 3.1 | S-UCOM(SRG)$_{3b}$ |

Table 7.6.: Comparison of calculated centroid energies and widths (in MeV) of $^{28}\mathrm{Si}_p$ to experimental data.

| nucleus transition energy range | experiment or projected | | intrinsic | | reference or interaction |
|---|---|---|---|---|---|
| | centroid energy | width | centroid energy | width | |
| $^{12}$C | 22.6 | 1.0 | | | [IKPS71] |
| E1, IV | 23.2 | 1.2 | 22.7 | 1.4 | UCOM(VAR)$_{2b}$ |
| 19.1–24.2 | 23.2 | 0.9 | 23.1 | 1.3 | S-SRG$_{3b}$ |
| | 23.2 | 0.7 | 22.9 | 1.2 | S-UCOM(SRG)$_{3b}$ |
| $^{12}$C | 26.7 | 5.0 | | | [I$^+$b] |
| E1, IV | 25.9 | 7.5 | 26.2 | 7.5 | UCOM(VAR)$_{2b}$ |
| 10.0–40.0 | 24.2 | 7.8 | 23.8 | 7.4 | S-SRG$_{3b}$ |
| | 24.2 | 7.6 | 23.8 | 7.2 | S-UCOM(SRG)$_{3b}$ |
| $^{12}$C | 24.2 | 2.5 | | | [KKK$^+$75] |
| E1, IV | 24.7 | 2.0 | 25.1 | 2.2 | UCOM(VAR)$_{2b}$ |
| 19.1–32.1 | 24.0 | 2.4 | 23.7 | 2.0 | S-SRG$_{3b}$ |
| | 24.4 | 2.6 | 24.0 | 2.2 | S-UCOM(SRG)$_{3b}$ |
| $^{12}$C | 24.8 | 3.2 | | | [FCB$^+$66] |
| E1, IV | 25.0 | 2.7 | 25.4 | 2.8 | UCOM(VAR)$_{2b}$ |
| 18.2–37.4 | 25.3 | 3.9 | 26.1 | 4.6 | S-SRG$_{3b}$ |
| | 25.6 | 4.0 | 26.4 | 4.7 | S-UCOM(SRG)$_{3b}$ |
| $^{12}$C | 23.8 | 2.4 | | | [BBJK69] |
| E1, IV | 22.4 | 3.7 | 22.8 | 4.1 | UCOM(VAR)$_{2b}$ |
| 12.1–30.7 | 20.6 | 4.2 | 20.4 | 4.1 | S-SRG$_{3b}$ |
| | 20.7 | 4.0 | 20.6 | 4.1 | S-UCOM(SRG)$_{3b}$ |
| $^{12}$C | 22.0 | 2.8 | | | [B$^+$] |
| E1, IV | 22.2 | 3.5 | 22.1 | 3.7 | UCOM(VAR)$_{2b}$ |
| 13.0–27.2 | 20.1 | 3.8 | 20.0 | 3.8 | S-SRG$_{3b}$ |
| | 20.4 | 3.7 | 20.2 | 3.8 | S-UCOM(SRG)$_{3b}$ |
| $^{12}$C | 24.1 | 2.5 | | | [KKK$^+$75] |
| E1, IV | 24.7 | 1.9 | 25.0 | 2.2 | UCOM(VAR)$_{2b}$ |
| 19.0–32.1 | 24.0 | 2.4 | 23.7 | 2.0 | S-SRG$_{3b}$ |
| | 24.3 | 2.6 | 23.9 | 2.3 | S-UCOM(SRG)$_{3b}$ |
| $^{12}$C | 24.7 | 4.1 | | | [ABC$^+$75] |
| E1, IV | 25.9 | 7.5 | 26.2 | 7.5 | UCOM(VAR)$_{2b}$ |
| 11.6–40.0 | 24.2 | 7.8 | 23.8 | 7.4 | S-SRG$_{3b}$ |
| | 24.2 | 7.6 | 23.8 | 7.2 | S-UCOM(SRG)$_{3b}$ |

Table 7.7.: Comparison of calculated centroid energies and widths (in MeV) of $^{12}$C to experimental data.

| nucleus transition energy range | experiment or projected | | intrinsic | | reference or interaction |
|---|---|---|---|---|---|
| | centroid energy | width | centroid energy | width | |
| $^{20}$Ne | 21.1 | 2.2 | | | [V$^+$b] |
| E1, IV | 24.3 | 2.9 | 23.4 | 3.0 | UCOM(VAR)$_{2b}$ |
| 16.1–28.4 | 23.5 | 3.2 | 22.0 | 3.5 | S-SRG$_{3b}$ |
| | 23.7 | 3.1 | 22.2 | 3.5 | S-UCOM(SRG)$_{3b}$ |
| $^{20}$Ne | 27.0 | 1.4 | | | [V$^+$b] |
| E1, IV | 26.4 | 1.5 | 26.1 | 1.4 | UCOM(VAR)$_{2b}$ |
| 23.4–29.2 | 25.9 | 1.6 | 26.1 | 1.6 | S-SRG$_{3b}$ |
| | 26.3 | 1.6 | 26.4 | 1.6 | S-UCOM(SRG)$_{3b}$ |
| $^{20}$Ne | 22.2 | 3.2 | | | [AMW81] |
| E1, IV | 24.3 | 2.9 | 23.4 | 3.0 | UCOM(VAR)$_{2b}$ |
| 16.1–28.4 | 23.5 | 3.2 | 22.0 | 3.5 | S-SRG$_{3b}$ |
| | 23.7 | 3.1 | 22.2 | 3.5 | S-UCOM(SRG)$_{3b}$ |
| $^{20}$Ne | 18.9 | 2.5 | | | [V$^+$b] |
| E1, IV | 24.3 | 2.9 | 23.4 | 3.0 | UCOM(VAR)$_{2b}$ |
| 15.4–28.4 | 23.4 | 3.2 | 22.0 | 3.5 | S-SRG$_{3b}$ |
| | 23.7 | 3.1 | 22.2 | 3.5 | S-UCOM(SRG)$_{3b}$ |

Table 7.8.: Comparison of calculated centroid energies and widths (in MeV) of $^{20}$Ne to experimental data.

| nucleus transition energy range | experiment or projected | | intrinsic | | reference or interaction |
|---|---|---|---|---|---|
| | centroid energy | width | centroid energy | width | |
| $^{32}$S | 21.9 | 3.5 | | | [I$^+$a] |
| E1, IV | 24.7 | 4.5 | 24.1 | 4.1 | UCOM(VAR)$_{2b}$ |
| 15.0–32.0 | 24.5 | 4.6 | 23.1 | 4.8 | S-SRG$_{3b}$ |
| | 24.6 | 4.3 | 23.2 | 4.5 | S-UCOM(SRG)$_{3b}$ |
| $^{32}$S | 26.9 | 2.0 | | | [VBB$^+$74] |
| E1, IV | 25.0 | 2.3 | 24.5 | 2.6 | UCOM(VAR)$_{2b}$ |
| 20.8–30.0 | 26.5 | 1.9 | 26.3 | 2.1 | S-SRG$_{3b}$ |
| | 26.8 | 2.0 | 26.5 | 2.2 | S-UCOM(SRG)$_{3b}$ |
| $^{32}$S | 21.4 | 3.3 | | | [VIK$^+$78] |
| E1, IV | 22.4 | 3.9 | 22.1 | 3.8 | UCOM(VAR)$_{2b}$ |
| 12.2–29.2 | 23.0 | 4.5 | 21.8 | 4.5 | S-SRG$_{3b}$ |
| | 23.9 | 4.4 | 22.6 | 4.6 | S-UCOM(SRG)$_{3b}$ |
| $^{32}$S | 22.1 | 3.8 | | | [VBB$^+$74] |
| E1, IV | 24.8 | 4.5 | 24.1 | 4.1 | UCOM(VAR)$_{2b}$ |
| 15.2–32.2 | 24.5 | 4.6 | 23.1 | 4.8 | S-SRG$_{3b}$ |
| | 24.6 | 4.3 | 23.2 | 4.5 | S-UCOM(SRG)$_{3b}$ |
| $^{32}$S | 21.8 | 3.5 | | | [VBB$^+$74] |
| E1, IV | 24.8 | 4.5 | 24.1 | 4.1 | UCOM(VAR)$_{2b}$ |
| 15.2–32.2 | 24.5 | 4.6 | 23.1 | 4.8 | S-SRG$_{3b}$ |
| | 24.6 | 4.3 | 23.2 | 4.5 | S-UCOM(SRG)$_{3b}$ |
| $^{32}$S | 23.3 | 5.3 | | | [I$^+$b] |
| E1, IV | 29.7 | 6.4 | 27.6 | 6.7 | UCOM(VAR)$_{2b}$ |
| 10.0–40.0 | 25.1 | 5.9 | 23.2 | 5.9 | S-SRG$_{3b}$ |
| | 25.4 | 5.8 | 23.6 | 5.9 | S-UCOM(SRG)$_{3b}$ |

Table 7.9.: Comparison of calculated centroid energies and widths (in MeV) of $^{32}$S to experimental data.

## 7.7. K-Components and Transition Densities

In this section, we take a closer look at a few selected peaks from figures 7.18-7.25. Since we focus on the low-lying ISD and ISQ transitions, which do not depend very much on the NN interaction, we only consider the S-SRG$_{3b}$ interaction.

To get a better picture of the oscillation patterns involved in the transitions, we first discuss the different oscillation modes. In deformed nuclei, the oscillation pattern is determined by the $K$ quantum-number. Oscillations with $K = 0$ are along the symmetry axis ($\beta$-vibrations), including breathing modes, while $K = 1$ and $K = 2$ oscillations are perpendicular to the symmetry axis. The $K = 1$ oscillations preserve the axial symmetry. Oscillations with $K = 1$ and $K = 2$ differ in their shape. For $K = 1$, the density increases in one hemisphere of the nucleus and decreases in the other, for $K = 2$, the density increases along one axis and decreases along the other, perpendicular axis ($\gamma$-vibrations).

The $K$-components of the projected transition strengths are shown in figures 7.28 to 7.32. Since every transition for $K \neq 0$ occurs twice, the corresponding markers have been doubled in height. It can be seen that peaks usually have one dominant $K$-component, and that there is an order in the energy. The $K = 2$ components alway have the highest energy, but for prolate nuclei, the $K = 0$ components have the lowest energy, followed by the $K = 1$ components. A $K = 0$ excitation corresponds to an oscillation on the long axis of a prolate nucleus, which does not require much energy, while a $K = 1$ excitation oscillates along a short axis, which requires more energy. For oblate nuclei, the long and short axes are reversed. Therefore, the $K = 1$ oscillations have a lower energy than the $K = 0$ oscil lations.

We will take a closer look at the following transitions: For $^{20}$Ne, we consider the low-lying ISD transition at $E = 3.1\,\text{MeV}$ (fig. 7.33), and the two low-lying ISQ transitions at $E = 2.4\,\text{MeV}$ (fig. 7.34) and $E = 10.3\,\text{MeV}$ (fig. 7.35), and the strongest $K = 2$ ISQ transition at $E = 21.0\,\text{MeV}$ (fig. 7.35). For the oblate $^{28}$Si$_o$, we show the strongest ISM transition at $E = 13.1\,\text{MeV}$ (fig. 7.37), the two low-lying ISD transitions at $E = 7.6\,\text{MeV}$ (fig. 7.38) and $E = 10.8\,\text{MeV}$ (fig. 7.39), the strongest IVD transition at $E = 17.7\,\text{MeV}$ (fig. 7.39) and the low-lying ISQ transition at $E = 2.3\,\text{MeV}$ (fig. 7.41). The transition densities for each energy are presented as a set of six plots. The upper left panel shows the total transition density, i.e. the sum of protons and neutrons, as a 2D plot in the $x$-$z$-plane. The upper right panel shows the same density as a 3D plot of the isosurface at $\rho = 0.4\,\rho_{\text{max}}$ (the coloring is only according to sign, but not to value). The middle row shows the neutron (left) and proton (right) transition density as 2D plots in the $x$-$z$-plane. The bottom row shows the ground-state density (left) and the sum of the ground-state density and the total transition density (right) as 2D plots in the $x$-$z$-plane. To assess the amount of center-of-mass movement or rotational motion, all 2D plots include the axes with $x = 0$ and $z = 0$. Additionally the center-of-mass of the state is marked by a $\times$. The $\times$ marker always correspond to the sum of the ground-state density and the transition density. In the middle row, only neutrons or protons are taken into account. The marker in the upper left and the lower right plot are identical. The lower left plot shows the marker for the ground-state density only, i.e. the center-of-mass always lies at the center.

The low-lying ISD state in $^{20}$Ne (figure 7.33) has center-of-mass contaminations, but is clearly dominated by true oscillation modes. The contributions are from a spurious state with zero energy. Taking into account the flatness of mean-field potentials in the central region, the impact of the center-of-mass contributions is most likely very small. The first low-lying ISQ state $^{20}$Ne (figure 7.34) obviously has strong rotational component and, therefore, may have sizable spurious contaminations. As this state has the lowest energy of all $K = 1$, $\Pi = +$ states, this is not surprising. Unfortunately, its rather high energy means that other states, which correspond to physical excitations, can also be contaminated. However, with respect to the transitions studied in this work, the $K = 1$, $\Pi = +$ mode only contributes to quadrupole transitions, which are dominated by the $K = 2$ mode. The impact of the spurious rotations is therefore small.[2] The next two ISQ states of $^{20}$Ne (figures 7.35 and 7.36) show no spurious contributions, as is expected for $K = 0$ and $K = 2$ modes. The $K = 2$ mode shows a $\gamma$-like oscillation, however, most other $K = 2$ states are of a more complex structure. The ISM state of $^{28}$Si$_o$ (figure 7.37) is a good example for a breathing mode, where the center of the nucleus exchanges mass with the outer regions. The two ISD states of $^{28}$Si$_o$ (figures 7.38 and 7.39) both have center-of-mass contributions, but other oscillation modes are dominant. We note that the lower energy oscillation has one node more than the higher-energy oscillation. In the IVD state (figures 7.40), protons and neutrons oscillate with opposite phase. As the neutron amplitude is larger than the proton amplitude, an overall density oscillation remains. The ISQ state of $^{28}$Si$_o$ shown in figure 7.41 clearly has sizable contributions from spurious rotations. As in $^{20}$Ne, this state has the lowest energy of all $K = 1$, $\Pi = +$ states.

---

[2]The spurious states could pose a problem for other transitions with contributions from the $K = 1$, $\Pi = +$ mode. A well known example is the isovector M1 scissor mode, where protons and neutrons oscillate against each other in a rotation-like motion, like opening and closing scissors.
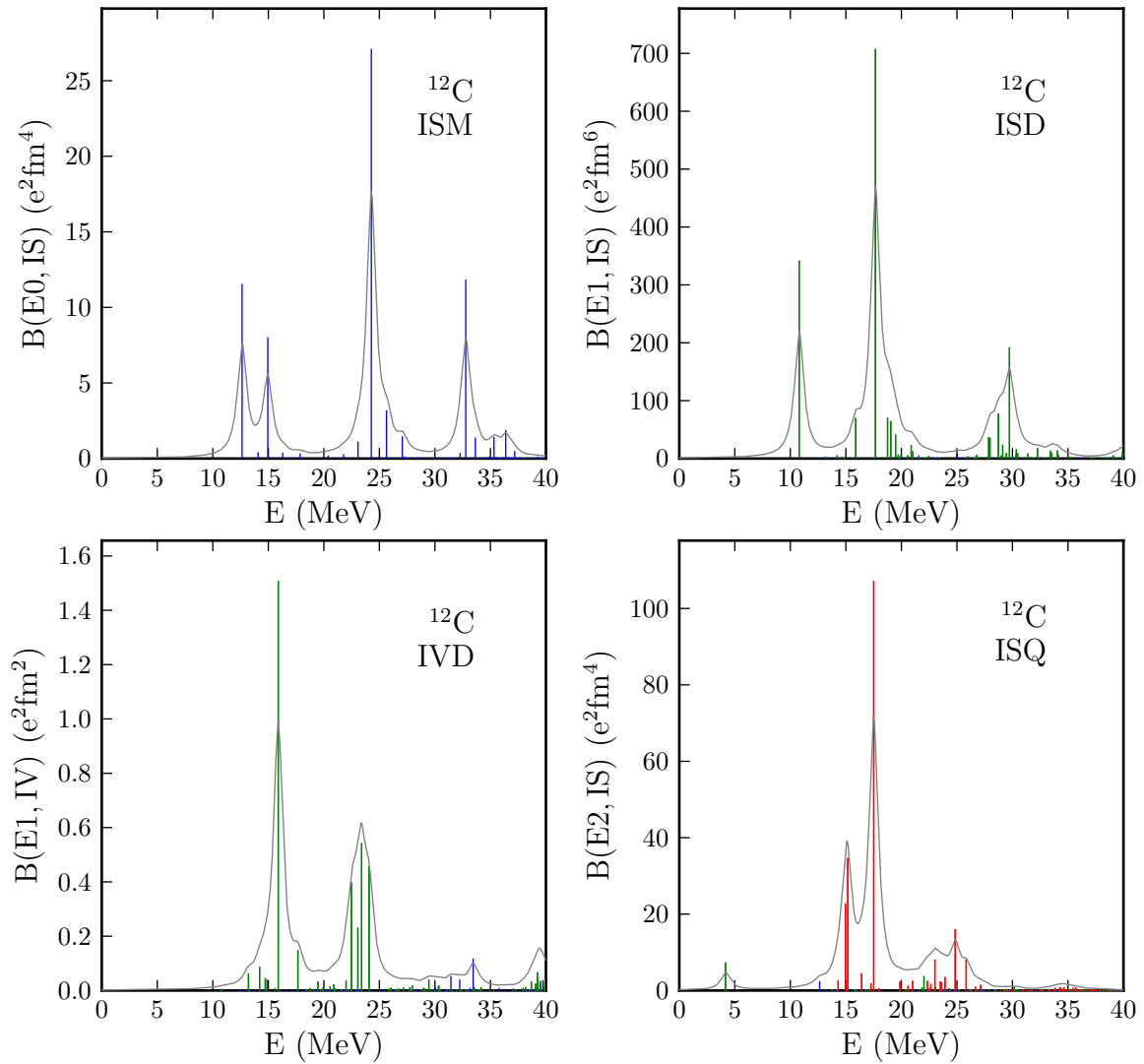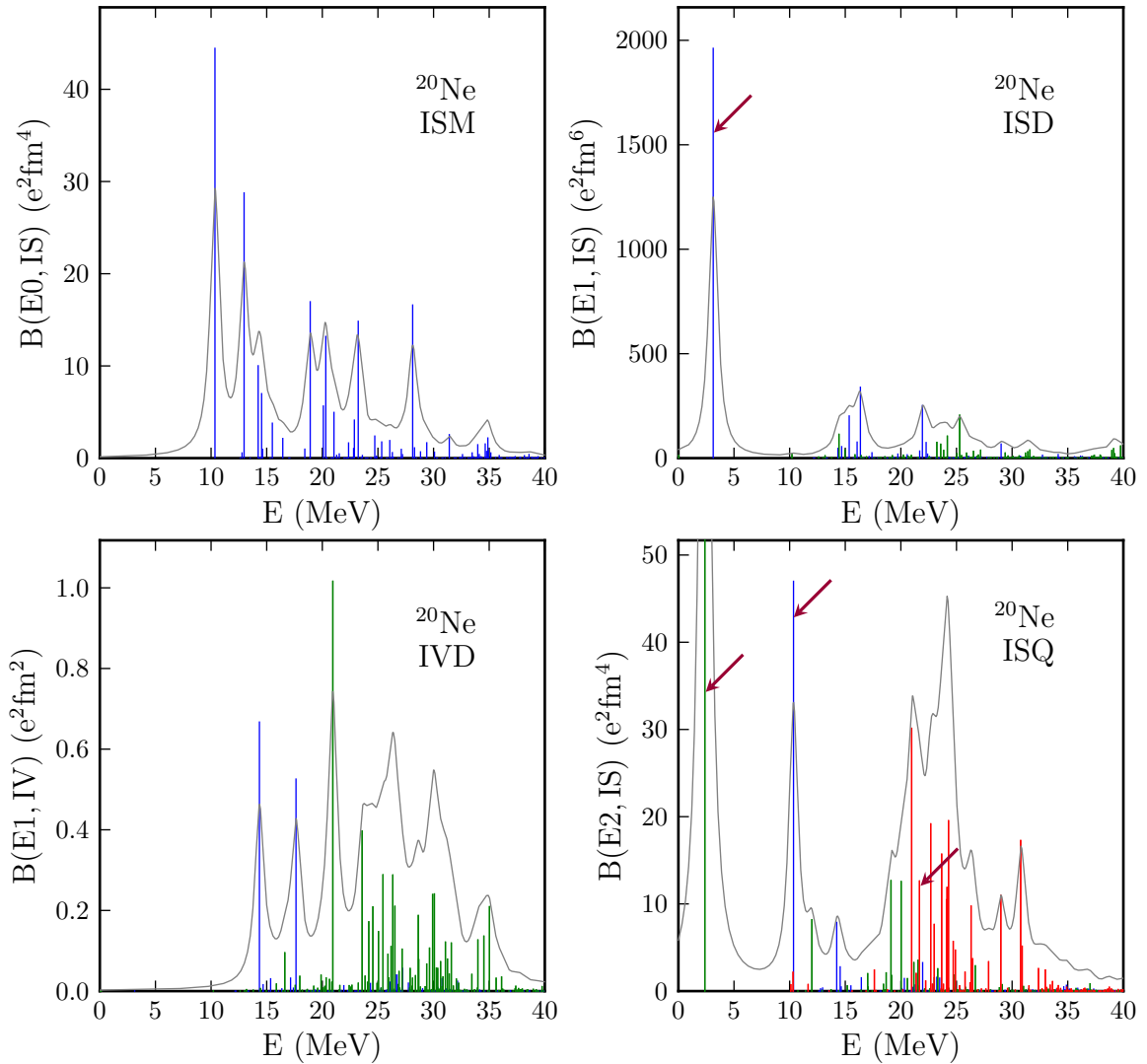
Figure 7.28.: ISM, ISD, IVD and ISQ transitions of $^{12}$C for the S-SRG$_{3b}$ interaction. Strength contributions from $k = 0$, $k = 1$, $k = 2$ and summed Lorentzian. Lorentzians in units of e$^2$fm$^x$/MeV, values according to tick labels.
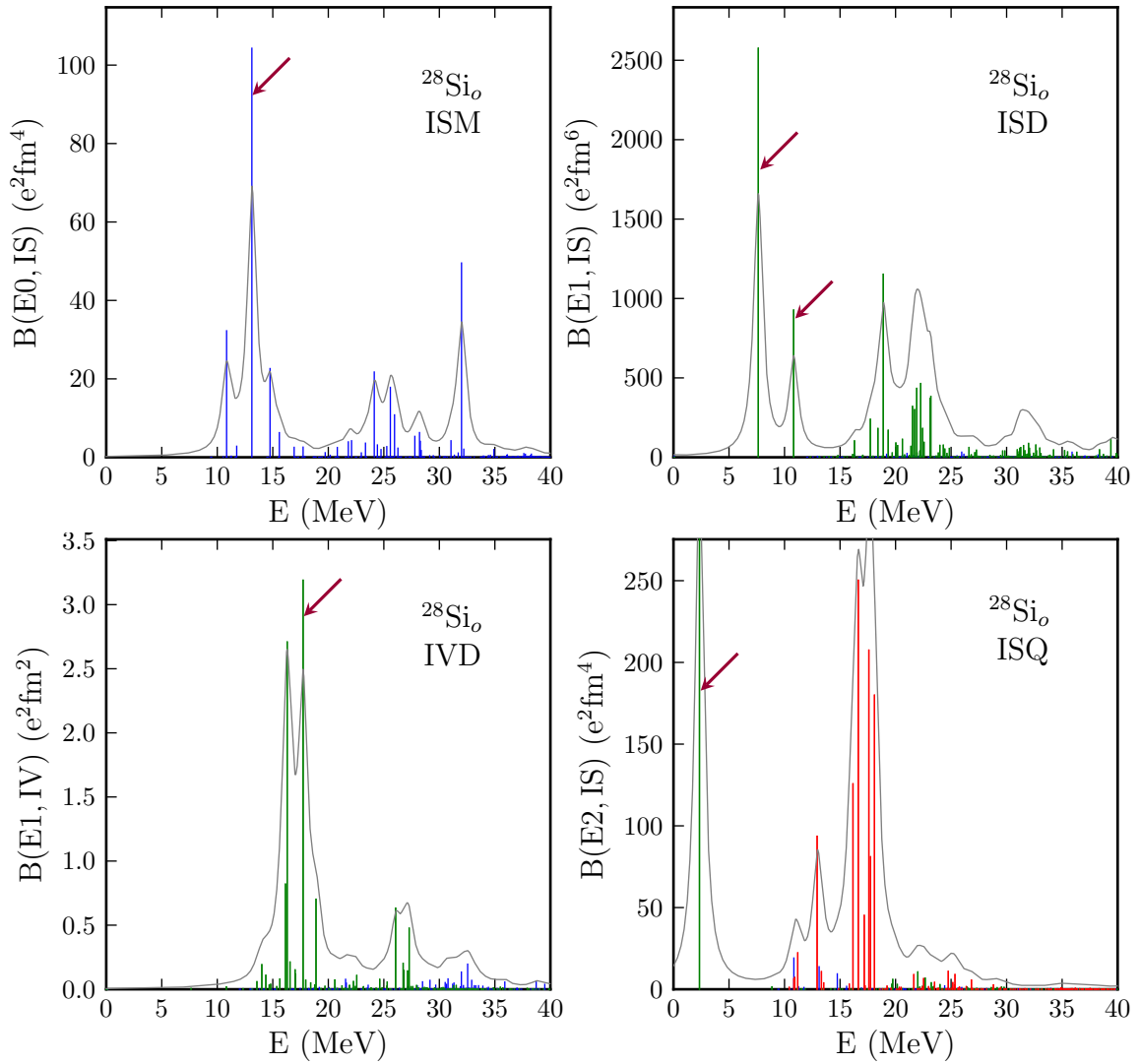
Figure 7.29.: ISM, ISD, IVD and ISQ transitions of $^{20}$Ne for the S-SRG$_{3b}$ interaction. Strength contributions from $k = 0$, $k = 1$, $k = 2$ and summed Lorentzian. Lorentzians in units of $e^2$fm$^x$/MeV, values according to tick labels. Arrows indicate transitions shown in figures 7.33-7.36.

Figure 7.30.: ISM, ISD, IVD and ISQ transitions of $^{28}\text{Si}_o$ for the S-SRG$_{3b}$ interaction. Strength contributions from $k = 0$, $k = 1$, $k = 2$ and summed Lorentzian. Lorentzians in units of $\text{e}^2\text{fm}^x/\text{MeV}$, values according to tick labels. Arrows indicate transitions shown in figures 7.37-7.41
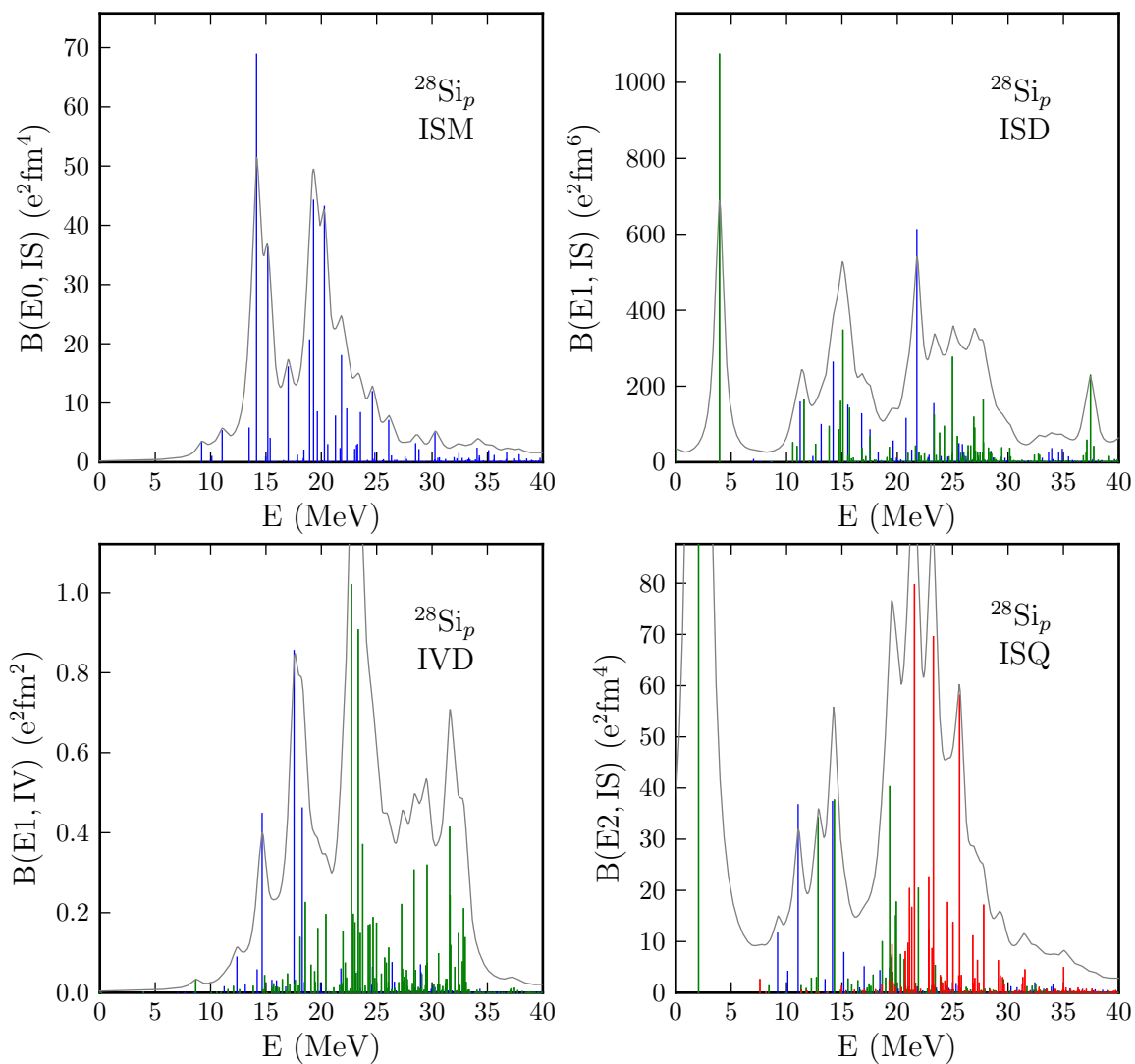
Figure 7.31.: ISM, ISD, IVD and ISQ transitions of $^{28}\text{Si}_p$ for the S-SRG$_{3b}$ interaction. Strength contributions from $k = 0$, $k = 1$, $k = 2$ and summed Lorentzian. Lorentzians in units of $\text{e}^2\text{fm}^x/\text{MeV}$, values according to tick labels.
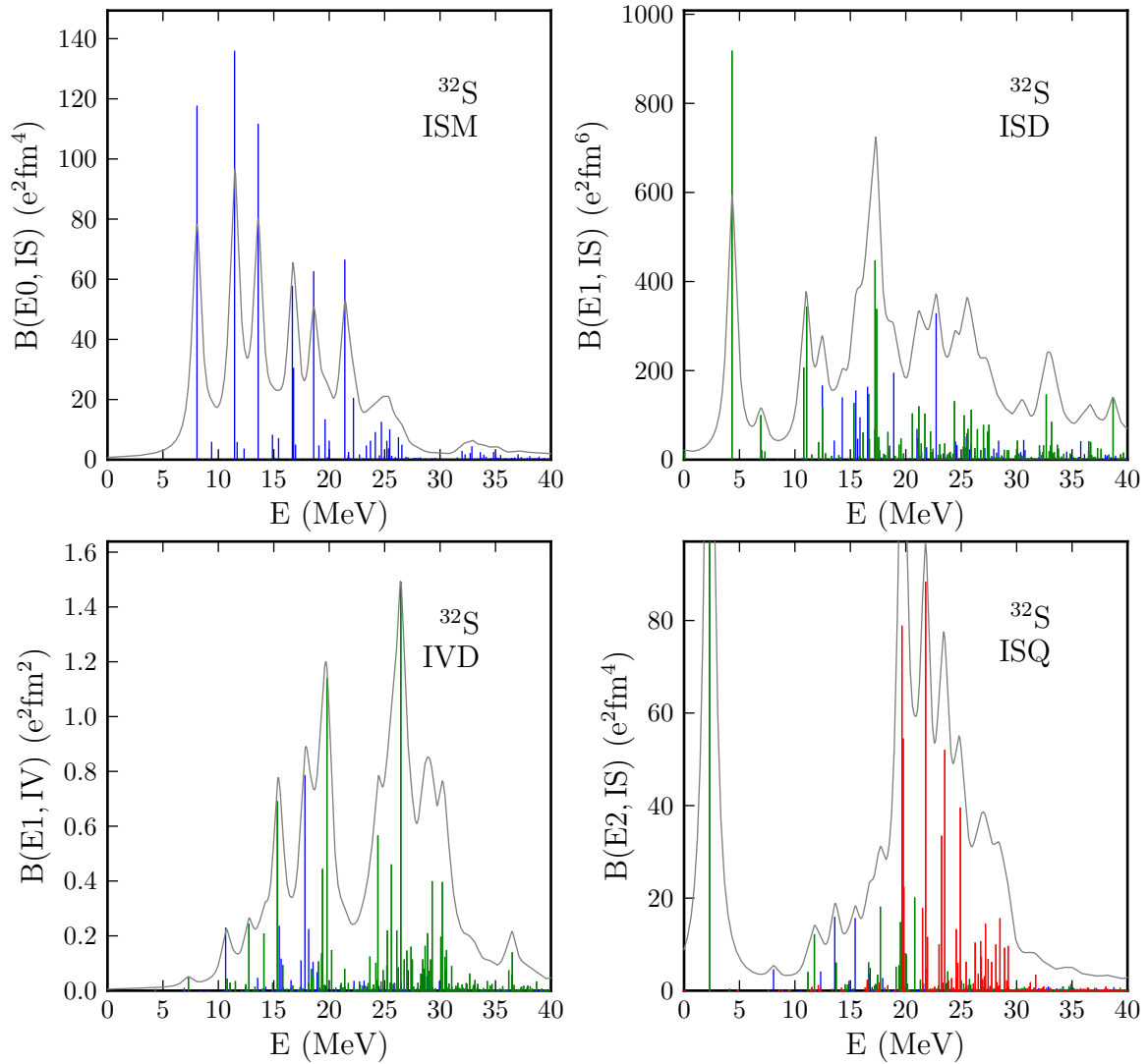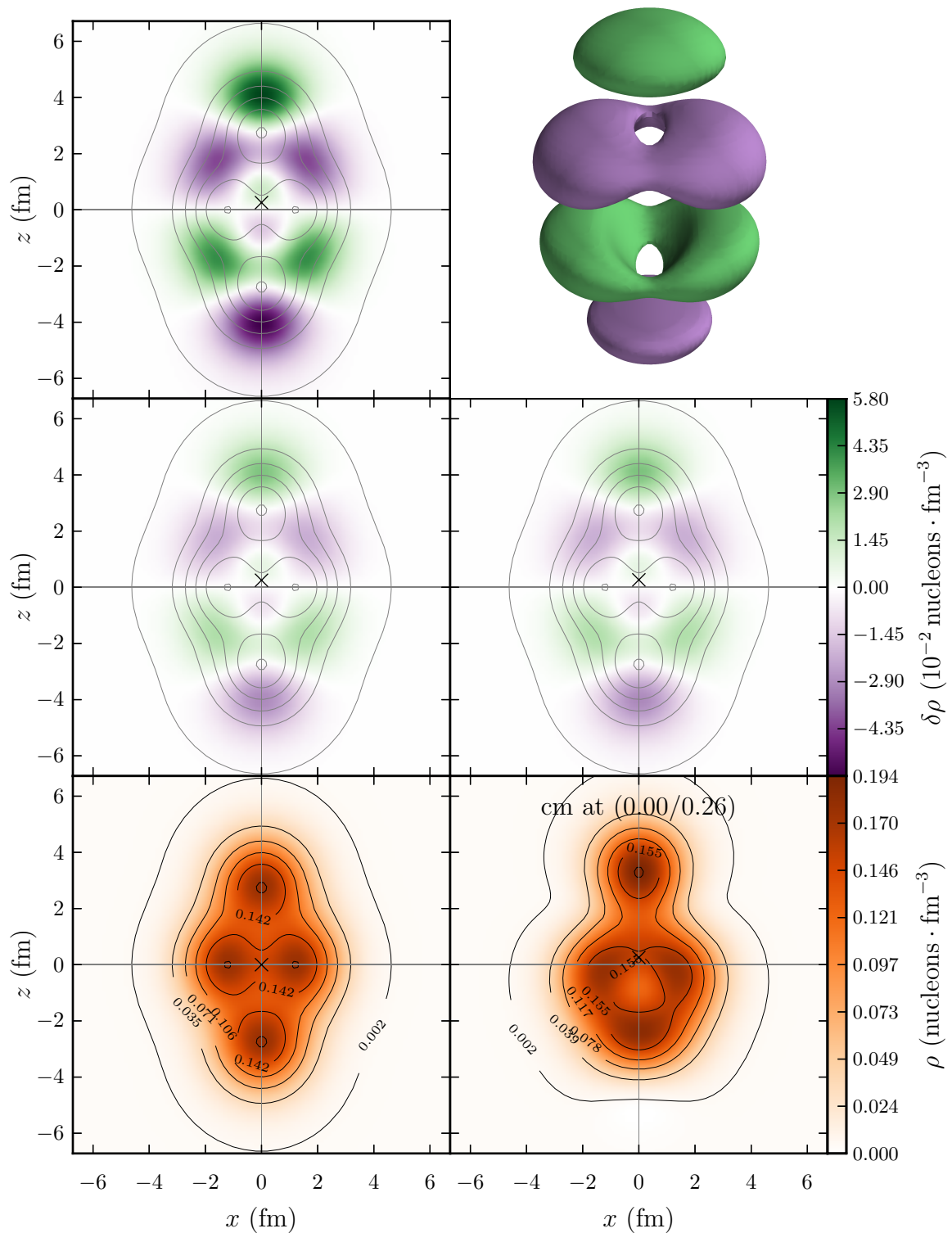
Figure 7.32.: ISM, ISD, IVD and ISQ transitions of $^{32}$S for the S-SRG$_{3b}$ interaction. Strength contributions from $k = 0$, $k = 1$, $k = 2$ and summed Lorentzian. Lorentzians in units of e$^2$fm$^x$/MeV, values according to tick labels.

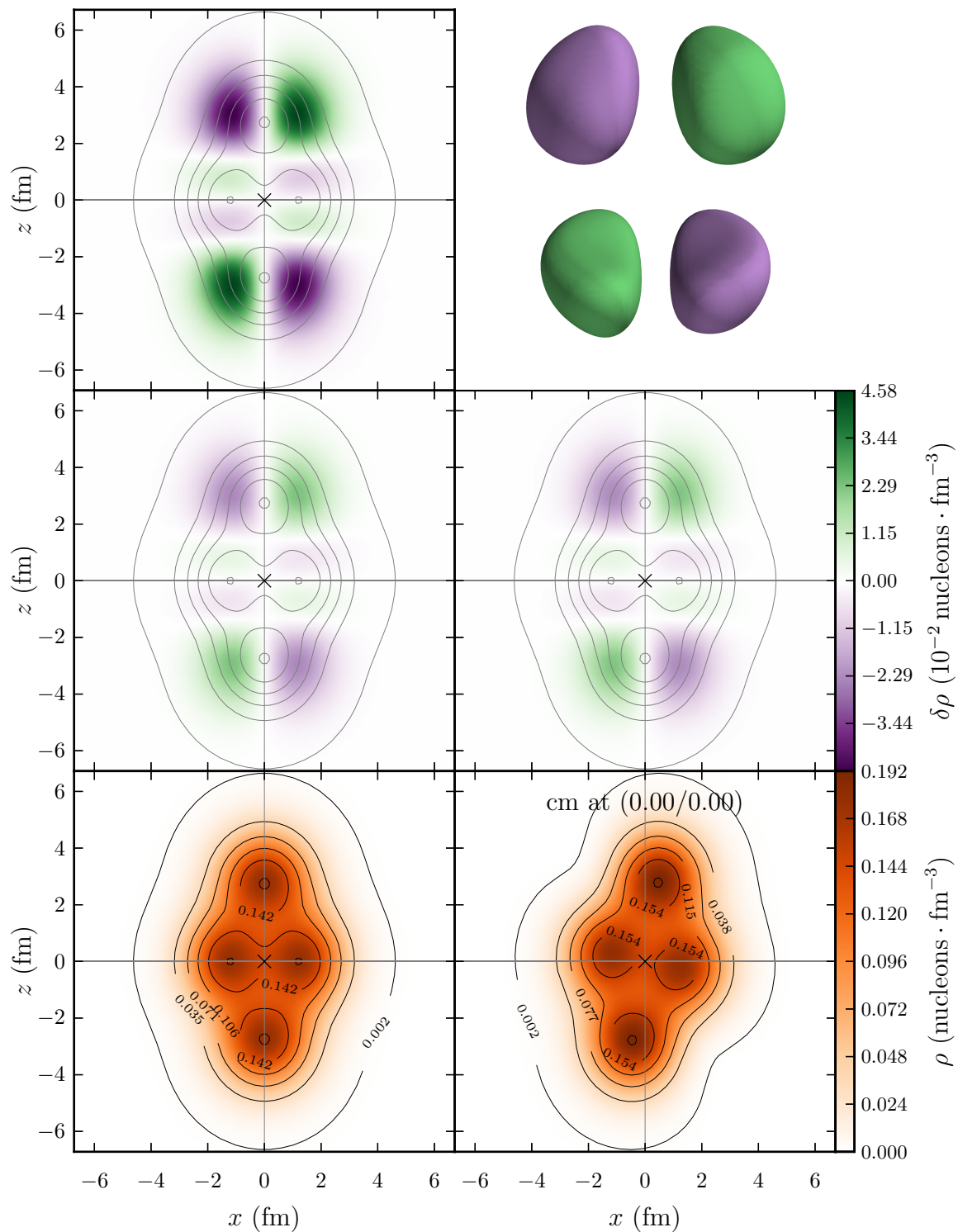Figure 7.33.: ISD $K = 0$, $\Pi = -$ transition densities of $^{20}$Ne at $E = 3.1$ MeV (see text).

Figure 7.34.: ISQ $K = 1$, $\Pi = +$ transition densities of $^{20}$Ne at $E = 2.4\,$MeV (see text).

Figure 7.35.: ISQ $K = 0$, $\Pi = +$ transition densities of $^{20}$Ne at $E = 10.3$ MeV (see text).
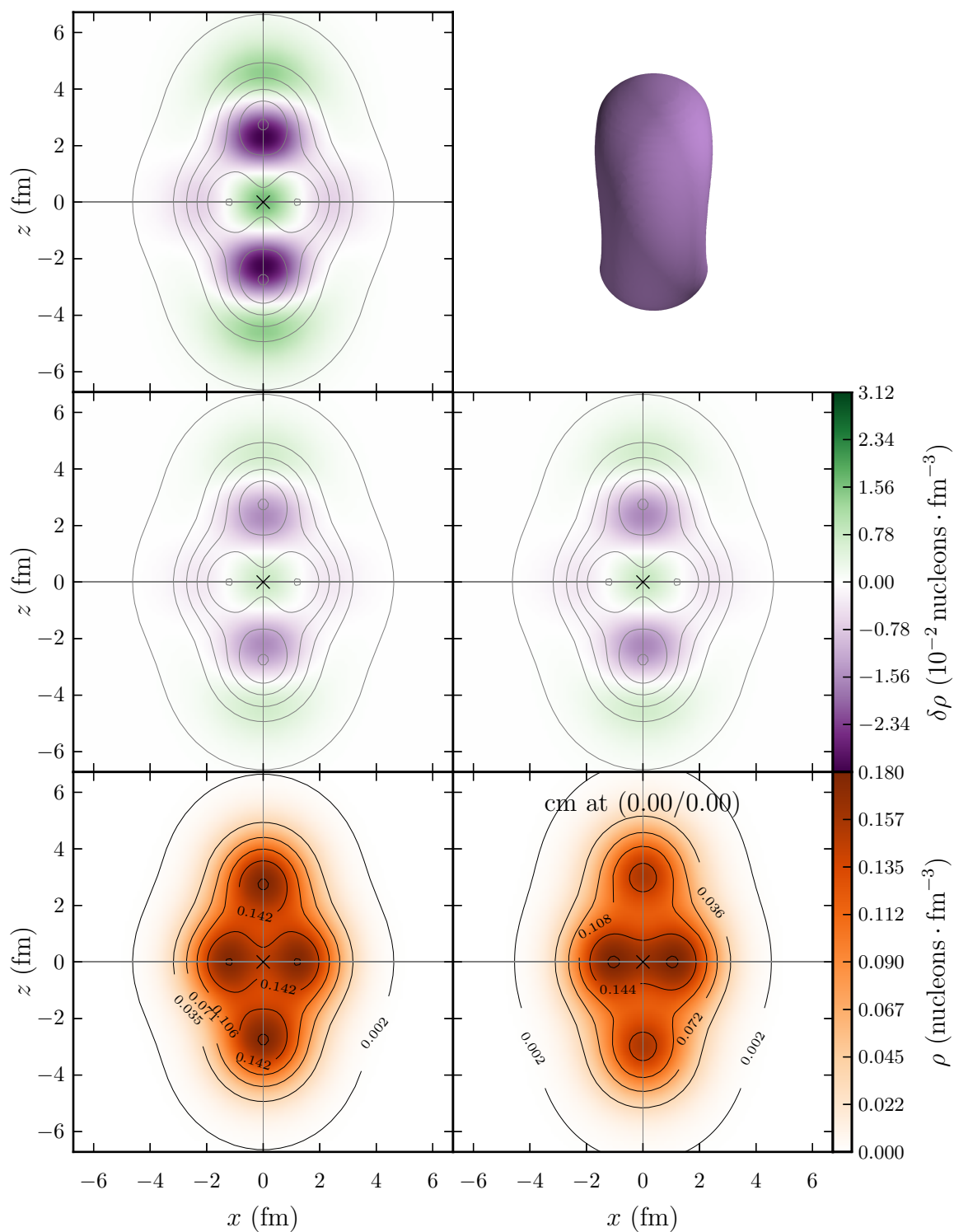
Figure 7.36.: ISQ $K = 2$, $\Pi = +$ transition densities of $^{20}$Ne at $E = 21.7\,\text{MeV}$ (see text).
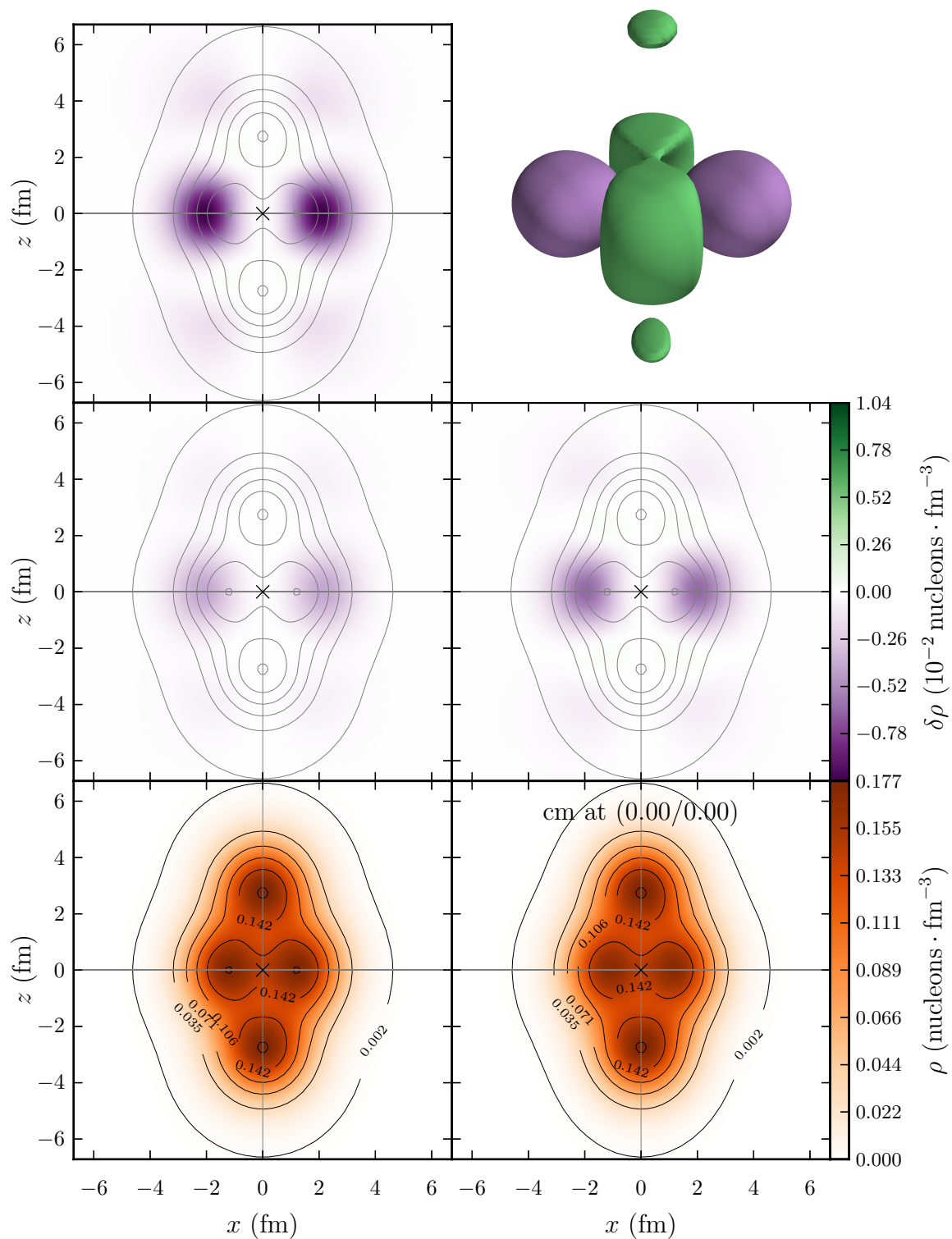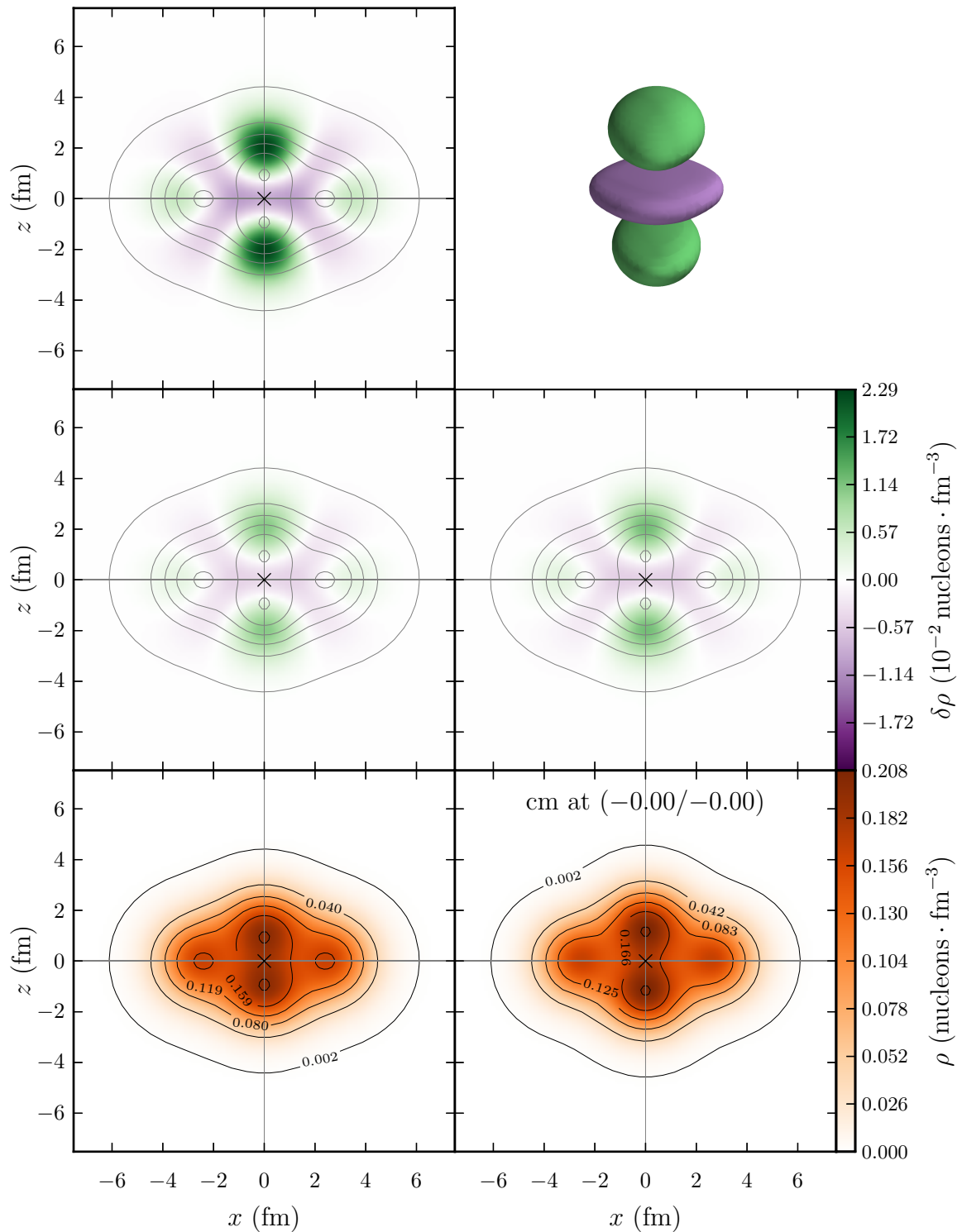
Figure 7.37.: ISM $K = 0$, $\Pi = +$ transition densities of $^{28}$Si$_o$ at $E = 13.1$ MeV (see text).
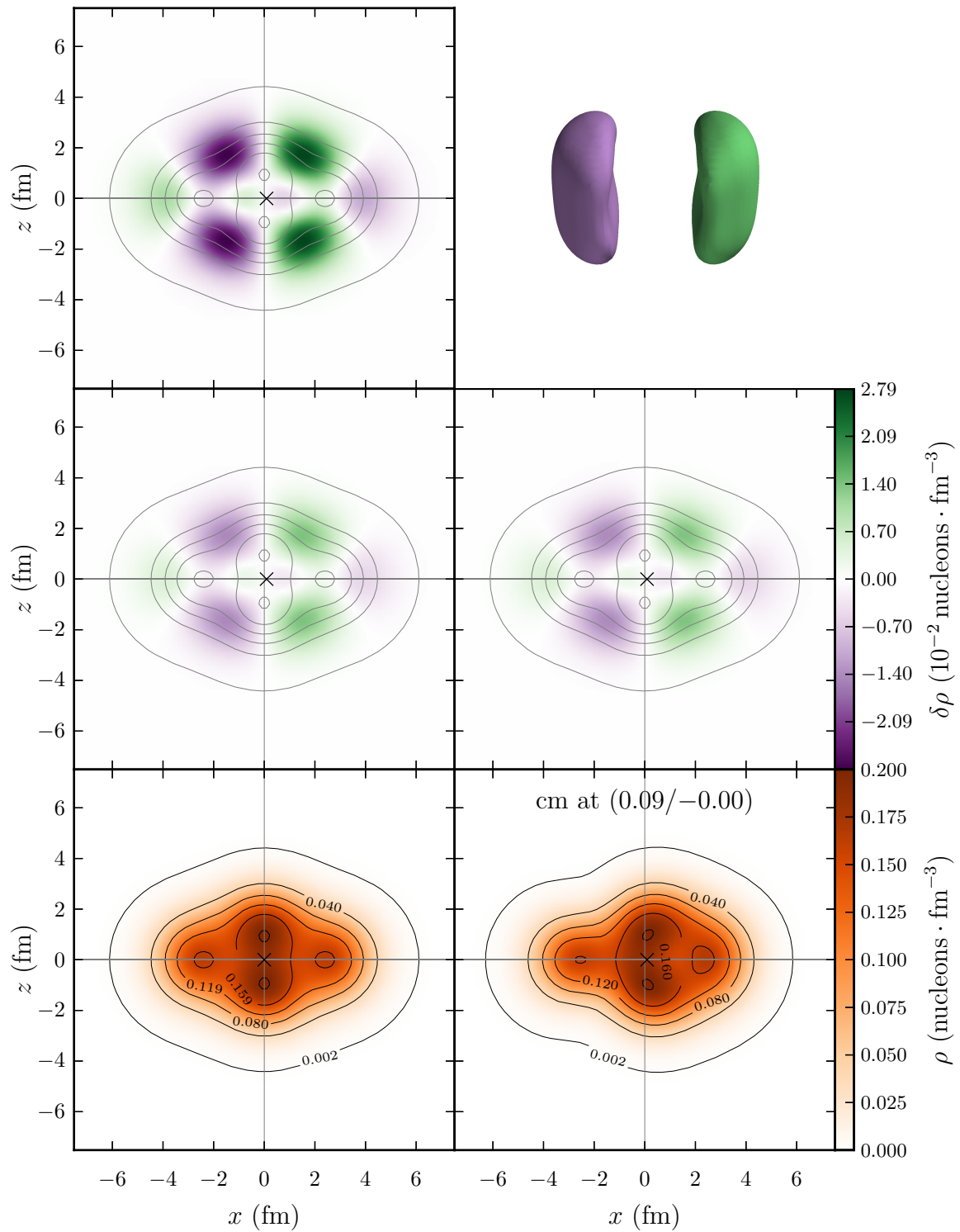
Figure 7.38.: ISD $K = 1$, $\Pi = -$ transition densities of $^{28}\mathrm{Si}_o$ at $E = 7.6\,\mathrm{MeV}$ (see text).

Figure 7.39.: ISD $K = 1$, $\Pi = -$ transition densities of $^{28}\mathrm{Si}_o$ at $E = 10.8\,\mathrm{MeV}$ (see text).

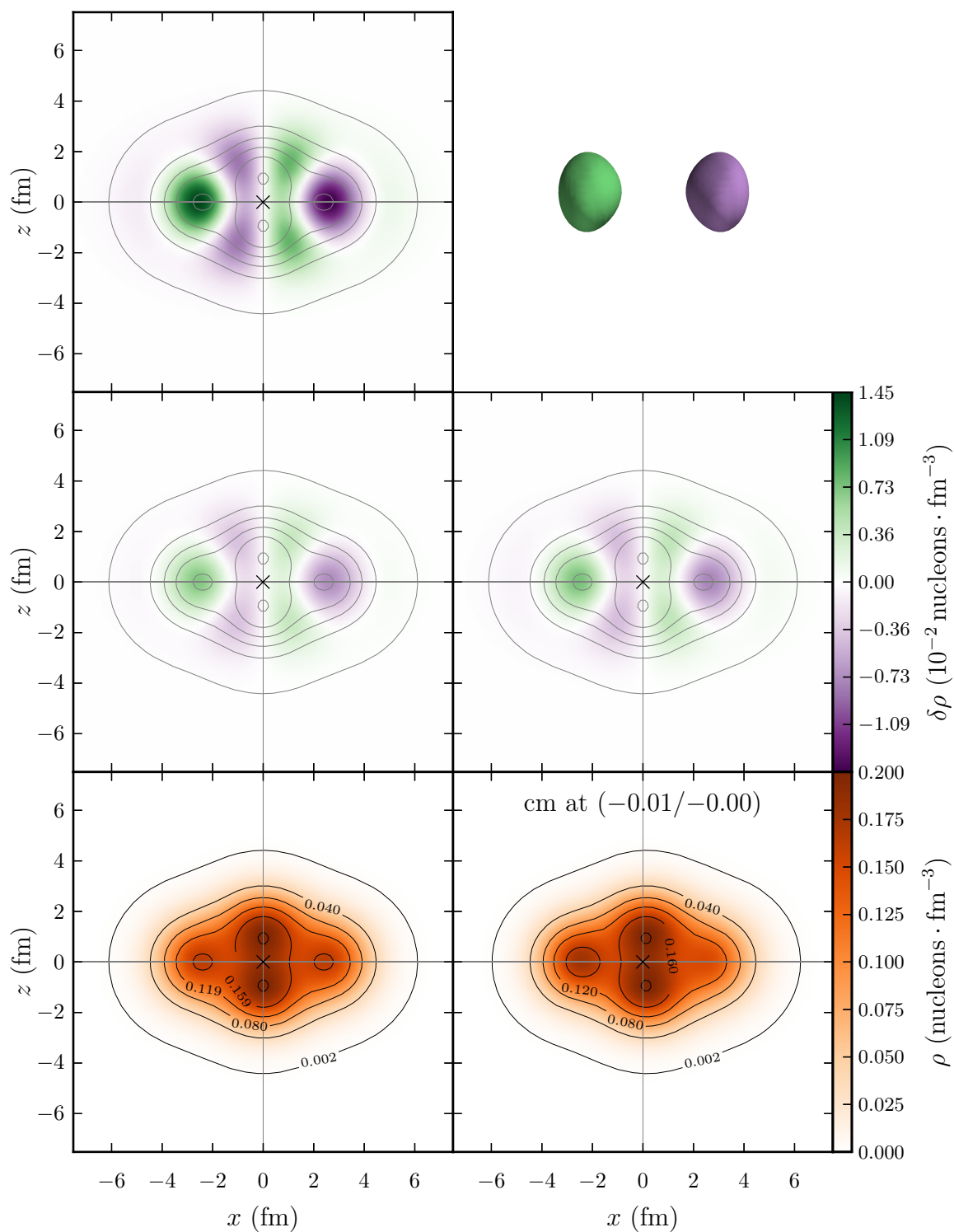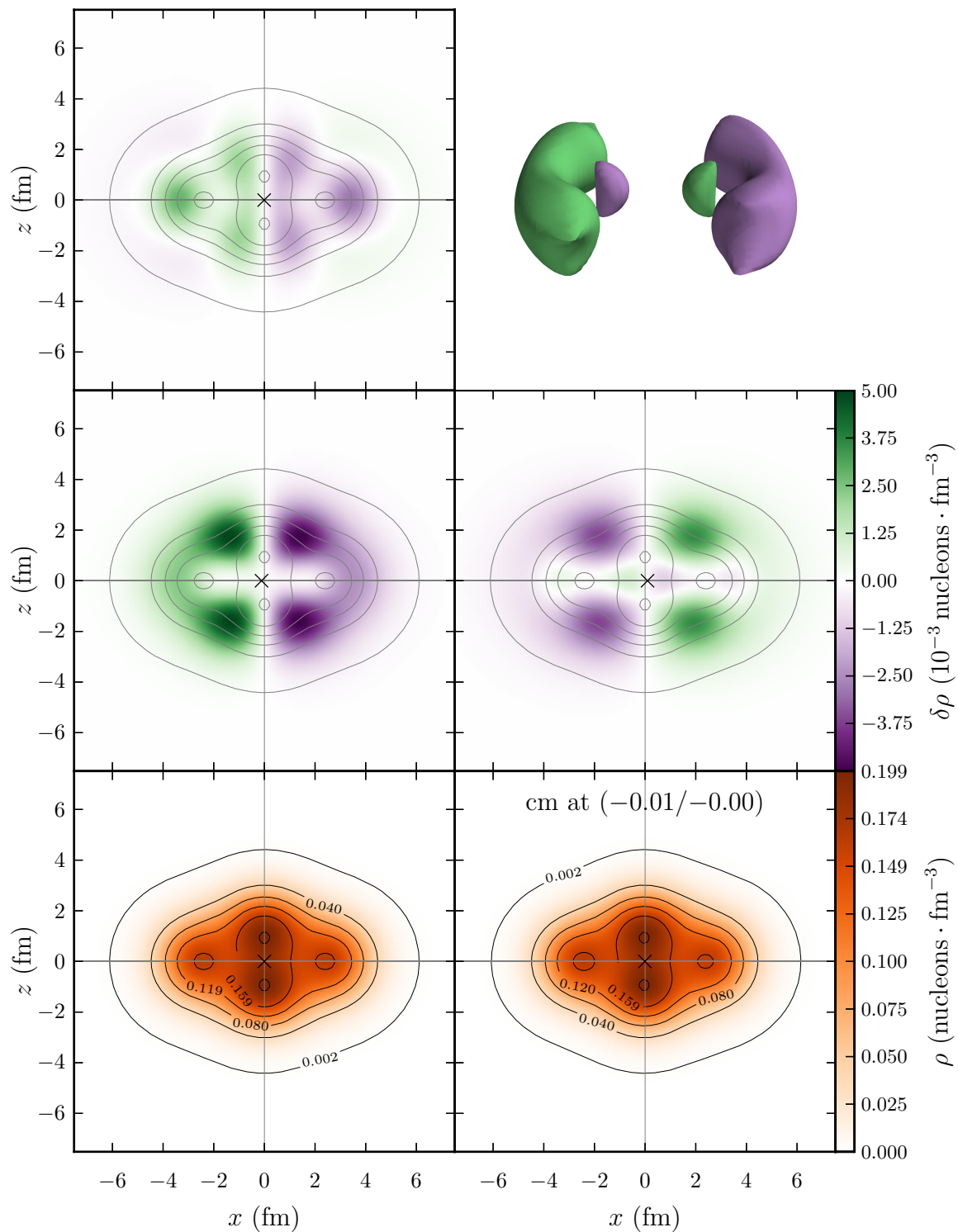Figure 7.40.: IVD $K = 1$, $\Pi = -$ transition densities of $^{28}\mathrm{Si}_o$ at $E = 17.7\,\mathrm{MeV}$ (see text).
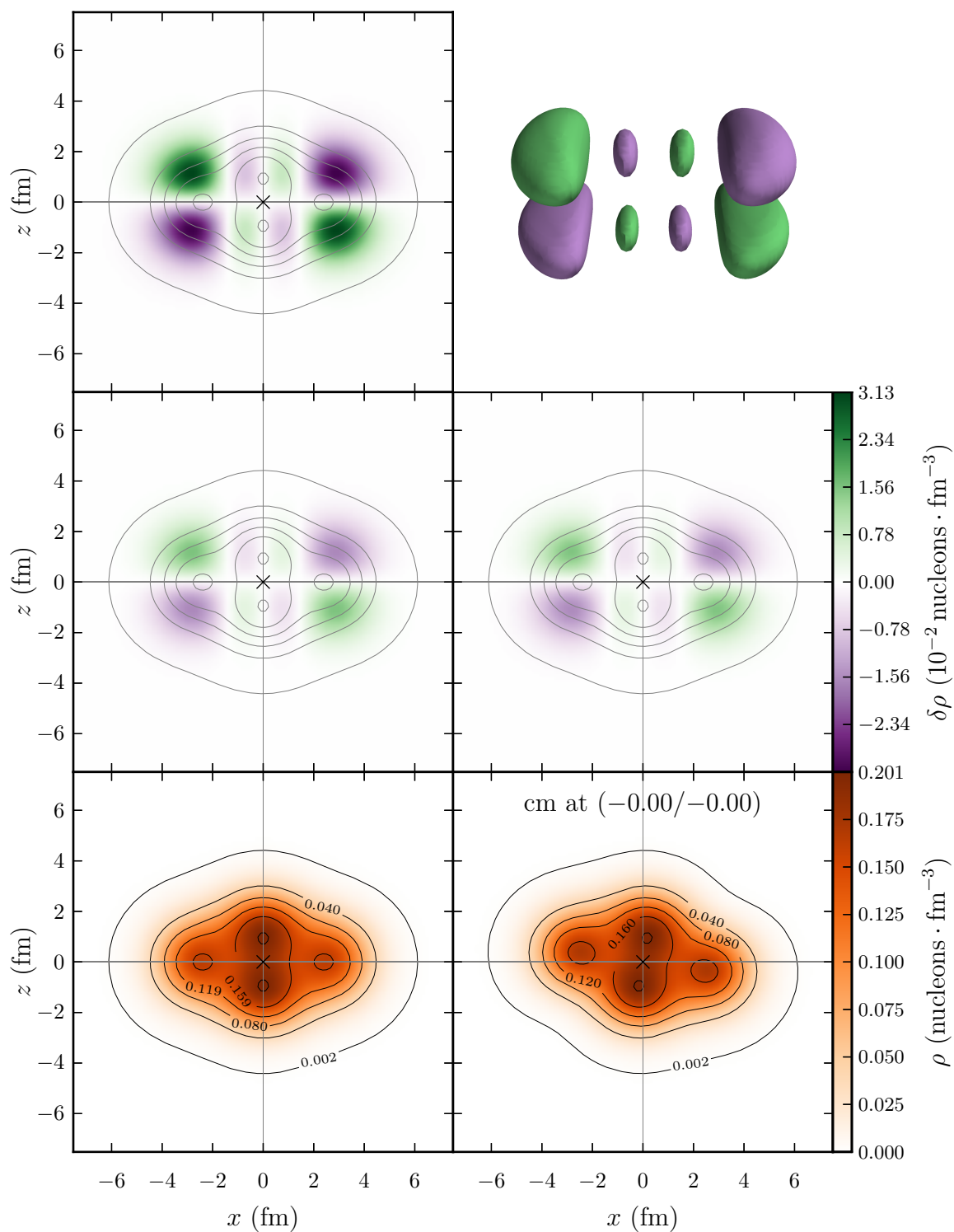
Figure 7.41.: ISQ $K = 1$, $\Pi = +$ transition densities of $^{28}\text{Si}_o$ at $E = 2.3\,\text{MeV}$ (see text).

## 7.8. Complex RPA Eigenvalues

As shown by [Tho60] (see also [Row70]), imaginary or complex RPA eigenvalues indicate an unstable HF ground state, i.e. the HF ground state used for the RPA is not the real HF minimum. For the nuclei studied in this work, complex eigenvalues appeared for $^{16}O$, $^{28}Si_o$ and $^{32}S$, regardless of the interaction used. The imaginary parts are shown in table 7.10. In each nucleus, only the first pair of eigenvalues is complex and the real parts are at the order of $10^{-10}$ MeV The values for $^{16}O$ and $^{28}Si_o$ are still close to zero, but the large value for $^{32}S$ cannot be dismissed. This indicates that at least $^{32}S$ has deformations that cannot be described by the axial-symmetric, parity-symmetric AVAP formalism used in this work. As a $K = 2$, $\Pi = +$ mode corresponds to a $\gamma$-vibration, $^{32}S$ may have a triaxial deformation. The $K = 1$, $\Pi = -$ mode corresponds to an oscillation pattern as seen in figure 7.38, which could indicate an octupole deformation.[3] This suggests the inclusion of triaxial quadrupole and octupole deformations and as a refinement of the current method.

| nucleus | $KP$ | Im($E$) | | |
| --- | --- | --- | --- | --- |
| | | UCOM(VAR)$_{2b}$ | S-SRG$_{3b}$ | S-UCOM(SRG)$_{3b}$ |
| $^{16}O$ | 11 | $1.02 \cdot 10^{-3}$ | $1.45 \cdot 10^{-4}$ | $3.84 \cdot 10^{-4}$ |
| $^{28}Si_o$ | 11 | $6.04 \cdot 10^{-2}$ | $5.58 \cdot 10^{-2}$ | $5.51 \cdot 10^{-2}$ |
| $^{32}S$ | 20 | $2.17 \cdot 10^{0}$ | $1.64 \cdot 10^{0}$ | $1.71 \cdot 10^{0}$ |

Table 7.10.: Imaginary parts of RPA eigenvalues, in MeV.

---

[3]In the case of $^{16}O$, this is consistent with *fermion molecular dynamics* (FMD) calculations [NFR05], where a tetrahedral structure (roughly four $\alpha$-nuclei in tetrahedral arrangement) with a lower projected ground-state energy was found.

# 8. Multi-Configuration Hartree-Fock

In the preceding chapters, we discussed the RPA as one possibility to build a more sophisticated many-body state on top of the HF results. In this chapter, we briefly discuss a different approach, referred to as *multi-configuration Hartree-Fock* (MCHF). The MCHF method is a special case of the *generator-coordinate method* (GCM).

## 8.1. Formalism

In the GCM, one makes the following ansatz for the many-body state $|\Psi\rangle$

$$|\Psi\rangle = \int f(a) |\Phi(a)\rangle \mathrm{d}a \quad , \tag{8.1}$$

where $|\Phi(a)\rangle$ are the so-called generating functions—more or less simple many-body state, which are defined by a parameter set $a$, the so-called generator coordinates. The integral goes over all these parameters and includes a weight function $f(a)$. The quality of the final many-body state $|\Psi\rangle$ depends entirely on the choice of $a$, $|\Phi(a)\rangle$ and $f(a)$. In the case of MCHF, the generating functions $|\Phi(a)\rangle$ are based on Slater determinants and $a$ is some quantity for which constrained HF calculations can be carried out. For deformed nuclei, the deformation parameter $\beta$ (or the mass quadrupole moment) is a natural choice for the generator coordinate, and for $|\Phi(\beta)\rangle$ one uses angular momentum projected HF states.

The weight function $f(\beta)$ is determined via the variational principle

$$\delta \frac{\langle \Psi | \hat{H} | \Psi \rangle}{\langle \Psi | \Psi \rangle} = 0 \quad . \tag{8.2}$$

This leads to the following integral equation, known as the *Hill-Wheeler equation* [HW53]

$$\int f(\beta') \langle \Phi(\beta) | \hat{H} | \Phi(\beta') \rangle \, \mathrm{d}\beta' = E \int f(\beta') \langle \Phi(\beta) | \Phi(\beta') \rangle \, \mathrm{d}\beta' \quad . \tag{8.3}$$

To handle (8.3) numerically, one can discretize $\beta$ to obtain a generalized eigenvalue problem

$$\sum_{\beta'} \langle \Phi_\beta | \hat{H} | \Phi_{\beta'} \rangle f_{\beta'} = E \sum_{\beta'} \langle \Phi_\beta | \Phi_{\beta'} \rangle f_{\beta'} \quad , \tag{8.4}$$

where the weight function $f$ is given by the eigenvectors and the energy of the many-body state $|\Psi\rangle$ by the eigenvalues. The calculation of the matrix elements $\langle \Phi_\beta | \hat{H} | \Phi_{\beta'} \rangle$

and $\langle \Phi_\beta | \Phi_{\beta'} \rangle$ has already been discussed in the context of angular-momentum projection (chapter 3.5). For the solution of the generalized eigenvalue problem, one can use the corresponding LAPACK routine. Depending on the actual states $|\Phi(\beta)\rangle$ used in the calculations, the solution of (8.4) can contain unphysical eigenvalues, which arise when basis states are linearly dependent. However, these states can be well identified, as they have very large (in theory infinite) eigenvalues, but the number of physical solutions is reduced. A prior orthogonalization, which leads to a non-hermitian (non-generalized) eigenvalue problem is not necessary.

## 8.2. Results

The results presented in this section are only proof-of-concept calculations. The basis used for the MCHF calculations consists of either 7 ($e_{\max} = 14$) or 10 ($e_{\max} = 10$) states selected from intermediate results of the AVAP process. Depending on the angular momentum projection, the MCHF states have different angular momentum. MCHF states with $J \neq 0$ are members of rotational bands (cf. chapter 5.5). In figures 8.1 to 8.4, we present our results for $^{20}$Ne and the oblate $^{28}$Si$_o$ in a similar fashion to those in chapter 5.5.

In some cases the description of rotational states is comparable to that in chapter 5.5. However, there are also examples for a much richer structure, which shows the higher complexity of the MCHF states. Some of the $0^+$ states already seem to be reproduced quite well.

Presently, the basis states are selected in a more or less random fashion. So far, the effect of the inclusion or deletion of single states on the results has not been investigated.—Since the calculation of the overlap matrix elements is the time consuming element, it would be interesting to calculate the overlap matrix for a very large basis and then solve the eigenvalue problem for all possible subsets of the initial basis. We can only conclude that the MCHF scheme is a very interesting approach and which is worth pursuing in future work.

Figure 8.1.: Ground-state rotational band and excited $0^+$ states of $^{20}$Ne for $e_{\max} = 10$. Experimental values from [SIM75, TCK$^+$98].



Figure 8.2.: Ground-state rotational band and excited $0^+$ states of $^{28}$Si$_o$ for $e_{\max} = 10$. Experimental values from [SIM75, End90, End98].
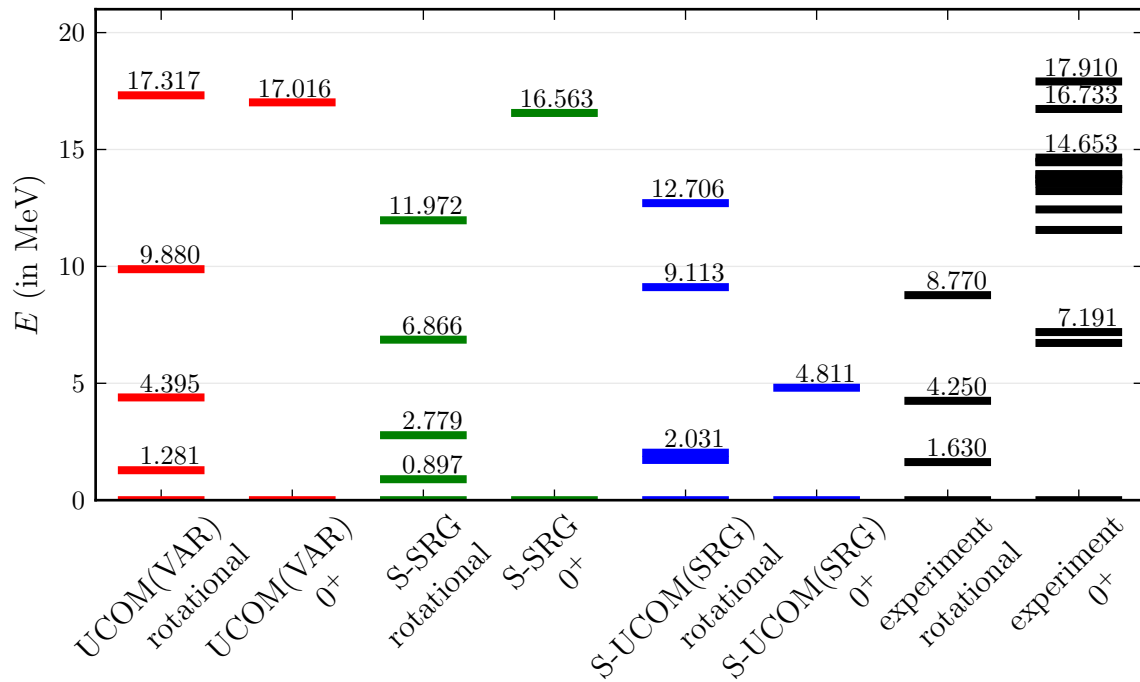
Figure 8.3.: Ground-state rotational band and excited $0^+$ states of $^{20}$Ne for $e_{\mathrm{max}} = 14$. Experimental values from [SIM75, TCK$^+$98].
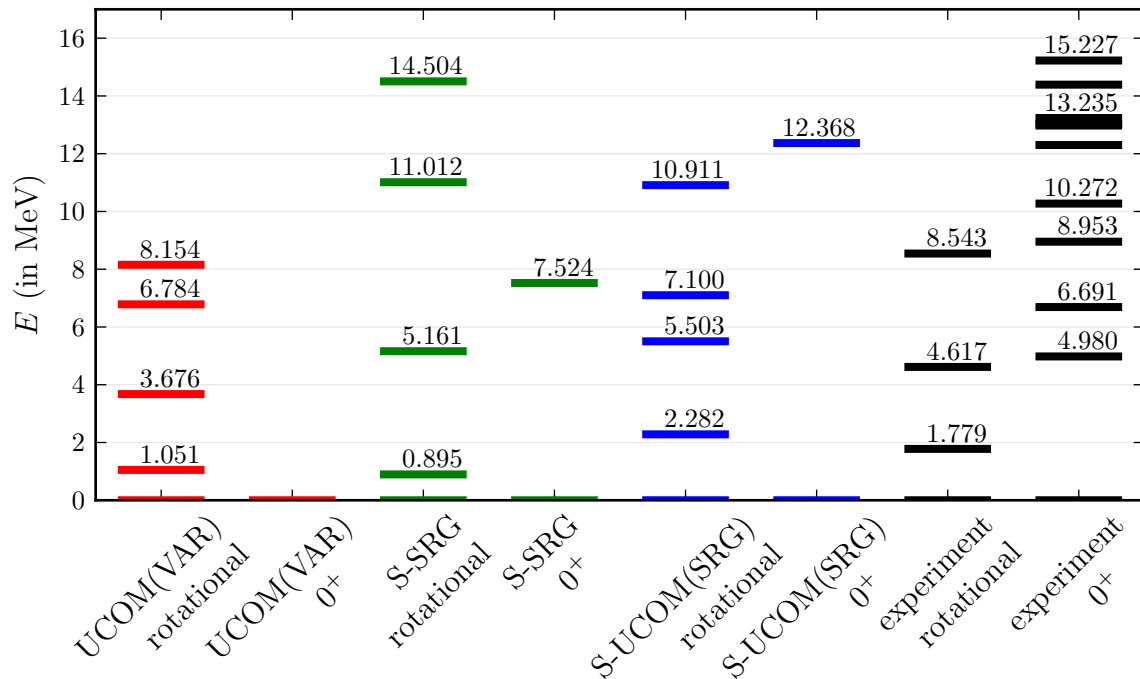


Figure 8.4.: Ground-state rotational band and excited $0^+$ states of $^{28}$Si$_o$ for $e_{\mathrm{max}} = 14$. Experimental values from [SIM75, End90, End98].
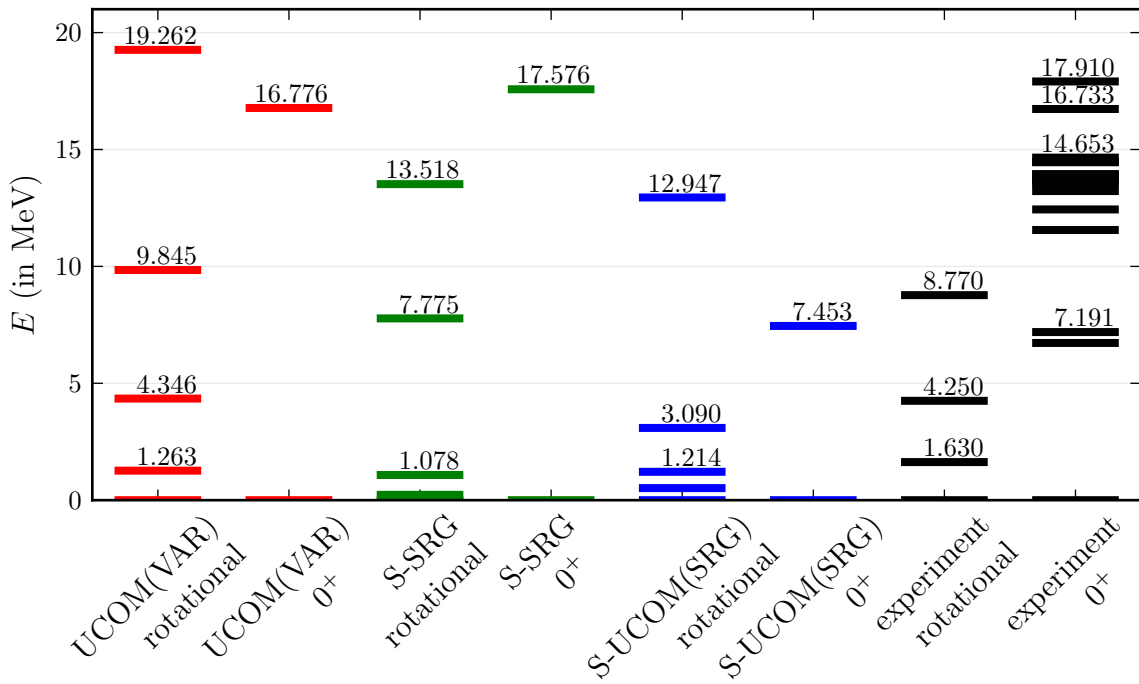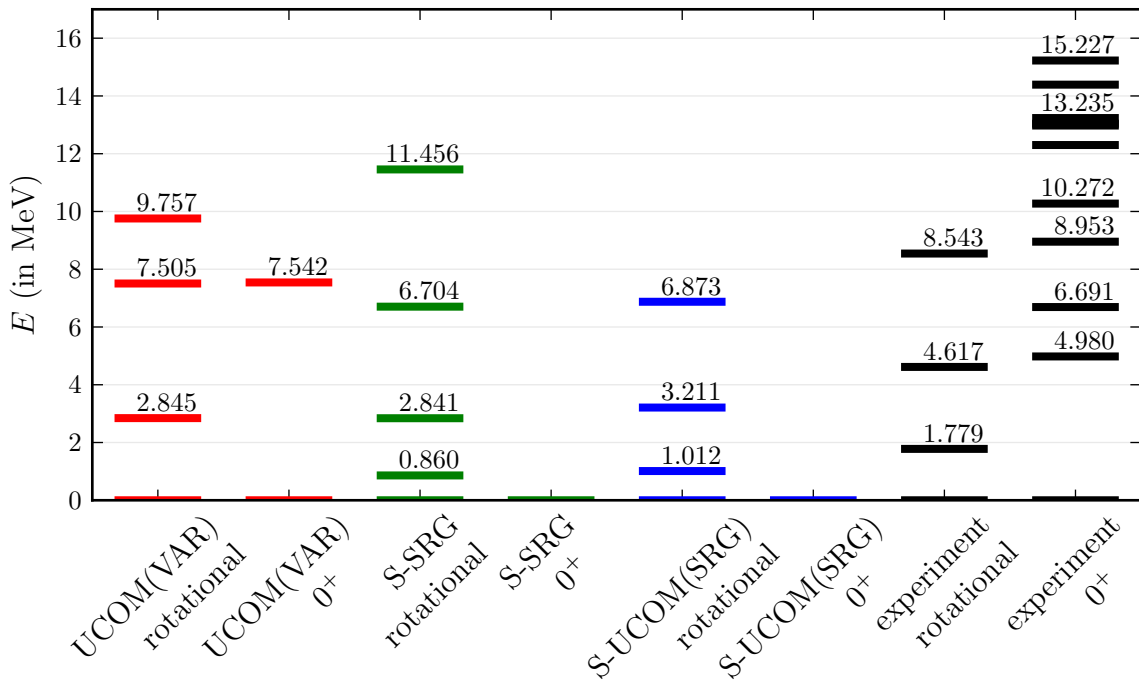
# 9. Conclusion and Outlook

This work is the first application of UCOM and SRG transformed interactions to deformed nuclei in an HF-RPA framework. Angular-momentum projection has been implemented in an exact formalism, without resorting to approximations for operators or overlap integrals. We employed an approximate *variation after projection* method based on constrained HF calculations. As seen in the case of $^{12}$C, this method has its limitations, but it has proven to be well suited for the studies carried out in this work.

The implementation is checked against published results for the Gogny D1S force, where it shows a very good agreement. For realistic interactions, we obtain well converged HF ground-state energies with respect to basis size and oscillator length. The largest convergence effect with respect to the oscillator length can be seen for the deformation parameter, where we reach a precision of about 5–10%. The effect of the AVAP approach compared to the PAV approach is found to be negligible with respect to ground-state energies or charge radii. However, the effect on the deformation parameter can reach up to 10%. The systematics of ground-state energies show, that angular-momentum projection has a visible effect and improves the agreement with experiment. However, as already seen in earlier studies with UCOM and SRG transformed interactions [RPP$^+$06, GRHR10], the binding energy per nucleon is underestimated by about 3–5 MeV, which is due to correlations which cannot be described by the angular-momentum projected mean-field. A study of the radii shows, that the S-SRG$_{3b}$ and S-UCOM(SRG)$_{3b}$ interactions, which include a three-body interaction, reproduce all radii within an rms-deviation of less than 7%. The oblate nuclei $^{12}$C and $^{28}$Si show the largest deviations, which leads to a slightly different systematic than the measured one. For both interactions, we saw a prolate state of $^{28}$Si within a few keV of the ground-state energy of the oblate state. However, the radius of the prolate state is even larger. The older UCOM(VAR)$_{2b}$ interaction, which is a pure two-body interaction, produces similar systematics, but at consistently lower radii, with an increasing difference for heavier nuclei. Currently, the number of nuclei studied is insufficient to decide whether deviations from the measured trend are just random fluctuations or a real physical effect. However, with increasing mass, pairing becomes more important and would have to be included in our approach. We also used the angular momentum projection to calculate rotational bands, where we get a rough agreement with experiment, on the order of 50%. The results are in better agreement to measured values than those obtained with the Gogny force, even though the Gogny force reproduces the nuclear binding energy within a few MeV. This shows that the validity of phenomenological interactions is questionable, if one goes beyond the binding energy.

Angular-momentum projected transition strengths in the RPA framework have been calculated for the first time. We study electric transitions of the isoscalar monopole,

isoscalar dipole, isovector dipole and isoscalar quadrupole type. The RPA formalism with deformation is compared to other RPA implementations and to a spherical RPA formalism, showing a reasonable agreement. Using the same basis sizes as for the HF calculations, we get well converged results for excitation energies of $E < 15\,\text{MeV}$. At higher energies, the finer details of peaks change with respect to basis size, but the position and width of giant resonances is stable up to excitation energies of $E \approx 30\,\text{MeV}$. However, as the RPA only includes one-particle one-hole excitations, and does not couple to the continuum, we do not expect the fine structure to be reproduced accurately, even if fully converged. Therefore, we can regard our results as well converged within the inherent limitations of the method. The angular-momentum projection only has a large effect on ISM transitions, where it improves the agreement with experimental data. But since there is currently only data for $^{28}\text{Si}$ available, more experimental data is needed. We presented the intrinsic transition densities as a tool to assess spurious center-of-mass and rotational contributions to the RPA excitations. While the spurious center-of-mass motion is very small, spurious rotations are not well separated from other states and, therefore, are likely to contaminate other states. However, among the transitions studied in this work, rotational modes, which have $K = 1$ and $\pi = +$, only contribute to quadrupole excitations, which are dominated by $K = 2$ modes. For some nuclei ($^{16}\text{O}$, $^{28}\text{Si}$ and $^{32}\text{S}$), we encountered imaginary RPA eigenvalues, which indicate unstable HF ground-states. This can mean, that the restrictions regarding axial-symmetry or parity are violated in these nuclei.

The present work provides many avenues for future studies. The HF and RPA methods can be extended by the inclusion of triaxial and parity violating deformations. Including triaxial deformations in the HF method would only require an initialization method that produces a state with triaxial deformation. Axial symmetry is not enforced on the HF level, so no changes are necessary. The integration for the angular momentum projection would have to be extended to include all Euler angles, which increases the computational effort considerably. To include triaxial shapes in the AVAP approach, additional constraints are required. Extending the RPA to triaxial deformation would further destroy the block structure of the A and B matrices. A major problem could occur for the angular-momentum projected transition strengths. The values of the weighting factors for the different $K$-components ($g_K$ in equation (3.12)) are no longer known and have to be calculated for each particle-hole excitation, which is very time consuming, as it involves the Hamiltonian.

Another possible extension would be to include pairing via Hartree-Fock-Bogoliubov and the Quasiparticle Random Phase Approximation. We did not study the effect of pairing in this work, but the vanishing pairing energy in the pure HFB approach, as seen for the Gogny force, does not exclude a pairing contribution if particle-number projection is taken into account, as it happens in the case of $^{24}\text{Mg}$ [RE10]. Of course the inclusion of full, ab-initio three-body forces also has to be mentioned. However, the computational effort required is still large for the basis sizes used in this work.

The MCHF approach discussed in chapter 8 also provides a very interesting field for further studies. Only proof-of-concept calculations of the energies have been carried out and no systematics with respect to the multi-configuration basis have been studied so far. In addition to the energy expectation values, other quantities definitely merit

further exploration. Currently, excited states can only be compared to measurements via their quantum numbers and energies. Knowledge regarding the matrix elements of transition operators would provide additional information to compare calculations to experimental data. MCHF calculations would also benefit from the inclusion of triaxial deformations, and the problems regarding the weighting factors of particle-hole excitations would not arise.

# A. Misc. Calculations

This appendix collects various calculations which are neither difficult nor provide any physical insight. However, since the formulae are crucial in obtaining the results presented in this thesis, the calculations are collected here.

## A.1. Radial Harmonic Oscillator Integral

We start with the expression for the radial part of the overlap for two harmonic oscillator wave-functions for an excitation of multipolarity $\lambda$. See e.g. [Suh07, eq. 6.23].

$$\mathcal{R}_{ab}^{\lambda} = \int_{0}^{\infty} g_{n_a l_a}(r) \, r^{\lambda} \, g_{n_b l_b}(r) \, r^2 \, \mathrm{d}r \tag{A.1}$$

The radial part of the wave function for a harmonic oscillator with oscillator length $b$ can be written as ([Suh07, eq. 3.42])

$$g_{nl}(r) = \sqrt{\frac{2n!}{b^3 \, \Gamma(n + l + \frac{3}{2})}} \left(\frac{r}{b}\right)^l \mathrm{e}^{-r^2/2\,b^2} L_n^{(l+\frac{1}{2})}(r^2/b^2) \quad . \tag{A.2}$$

The associate Laguerre polynomials are given by the explicit formula [BSMM98]

$$L_n^k(x) = \sum_{i=0}^{n} \frac{(-1)^i}{i!} \binom{n+k}{n-i} x^i \tag{A.3}$$

with the generalized binomial coefficient for real $n$ and $k$

$$\binom{n}{k} = \frac{\Gamma(n+1)}{\Gamma(k+1)\,\Gamma(n-k+1)} \quad . \tag{A.4}$$

Using the explicit notation of the radial wave function, the integral can be expressed as

$$\mathcal{R}_{ab}^{\lambda} = \int_{0}^{\infty} \frac{2}{b^3} \sqrt{\frac{n_a!\,n_b!}{\Gamma(n_a + l_a + \frac{3}{2})\,\Gamma(n_b + l_b + \frac{3}{2})}} \left(\frac{r}{b}\right)^{l_a+l_b} \mathrm{e}^{-r^2/b^2} \, r^{\lambda+2}$$

$$\times \sum_{i_a,i_b=0}^{n_a,n_b} \frac{(-1)^{i_a+i_b}\,\Gamma(n_a + l_a + \frac{3}{2})\,\Gamma(n_b + l_b + \frac{3}{2})}{i_a!\,i_b!\,(n_a - i_a)!\,(n_b - i_b)!\,\Gamma(l_a + i_a + \frac{3}{2})\,\Gamma(l_b + i_b + \frac{3}{2})} \left(\frac{r}{b}\right)^{2\,i_a+2\,i_b} \mathrm{d}r \quad , \tag{A.5}$$

where $\Gamma$-functions with integer arguments have been converted to factorials.

The $\Gamma$-functions in the denominator under the square root cancel partly with the $\Gamma$-functions in the numerator in the sum. After introducing $\tilde{r} = \frac{r}{b}$ and reshuffling the equation, we get

$$\mathcal{R}_{ab}^\lambda = b^\lambda \sqrt{n_a!\, n_b!\, \Gamma(n_a + l_a + \tfrac{3}{2})\, \Gamma(n_b + l_b + \tfrac{3}{2})}$$
$$\times \left[ \sum_{i_a, i_b=0}^{n_a, n_b} \frac{(-1)^{i_a + i_b}}{i_a!\, i_b!\, (n_a - i_a)!\, (n_b - i_b)!\, \Gamma(l_a + i_a + \tfrac{3}{2})\, \Gamma(l_b + i_b + \tfrac{3}{2})} \right.$$
$$\left. \times 2 \cdot \int_0^\infty \tilde{r}^{\,2\,i_a + 2\,i_b + \lambda + l_a + l_b + 2}\, e^{-\tilde{r}^2}\, d\tilde{r} \right] \quad . \tag{A.6}$$

The integral can be evaluated using the identity [BSMM98]

$$\int_0^\infty x^n\, e^{-ax^2}\, dx = \frac{\Gamma(\frac{n+1}{2})}{2\, a^{\frac{n+1}{2}}} \quad \text{for } n > -1 \text{ and } a > 0 \; . \tag{A.7}$$

As the final result, we get

$$\mathcal{R}_{ab}^\lambda = b^\lambda \sqrt{n_a!\, n_b!\, \Gamma(n_a + l_a + \tfrac{3}{2})\, \Gamma(n_b + l_b + \tfrac{3}{2})}$$
$$\times \sum_{i_a, i_b=0}^{n_a, n_b} \frac{(-1)^{i_a + i_b}\, \Gamma(i_a + i_b + \frac{\lambda + l_a + l_b + 3}{2})}{i_a!\, i_b!\, (n_a - i_a)!\, (n_b - i_b)!\, \Gamma(l_a + i_a + \tfrac{3}{2})\, \Gamma(l_b + i_b + \tfrac{3}{2})} \quad . \tag{A.8}$$

## A.2. Intrinsic Quadrupole Moment

The total static quadrupole moment of a nucleus is given by the sum of the static quadrupole moments of the single nucleons.

$$Q = \sqrt{\frac{16\pi}{5}} \sum_{i=1}^A \langle \alpha_i | \hat{Q}_{20} | \alpha_i \rangle \tag{A.9}$$

The quadrupole moment of a nucleon in a HF state can be calculated analytically in the HO basis. An arbitrary HF state $|\alpha\rangle$ is expanded to (chapter 4.2.1)

$$|\alpha\, m_t\rangle = \sum_a C_a^{\alpha\, m_t} \sum_{m_l, m_s} (l\, m_l\, \tfrac{1}{2}\, m_s | j\, m_j) |n\, l\, m_l\rangle \otimes |m_s\rangle \otimes |m_t\rangle \quad , \tag{A.10}$$

where we omitted the trivial spin and isospin quantum numbers. To avoid cluttering of the formulae, the $a$ dependence of $l$, $j$, $m_j$ and $n$ is not explicitly indicated.

The general quadrupole moment operator for a single nucleon is defined as

$$\hat{Q}_{20} = \hat{r}^2\, Y_{20}(\Omega) \quad . \tag{A.11}$$

In the HO basis, the matrix elements of the quadrupole operator can be expressed analytically. Using the integral form of the scalar product we get

$$\langle a | \hat{Q}_{20} | a' \rangle = \int_{-\infty}^\infty \Psi_a^*\, r^2\, Y_{20}(\Omega)\, \Psi_b\, r^2\, dr\, d\Omega \quad . \tag{A.12}$$

The static quadrupole moment is defined as the diagonal part of the quadrupole operator, but for completeness, all matrix elements are calculated.

Using the radial integral derived earlier (appendix A.1), we get

$$\langle a|\hat{Q}_{20}|a'\rangle = \int_{-\infty}^{\infty} g_a(r)\, Y_a^*(\Omega)\, r^2\, Y_{20}(\Omega)\, g_{a'}(r)\, Y_{a'}(\Omega)\, r^2\, \mathrm{d}r\, \mathrm{d}\Omega$$

$$= \mathcal{R}_{aa'}^{(2)} \int_{-\infty}^{\infty} Y_a^*(\Omega) Y_{20}(\Omega)\, Y_{a'}(\Omega) \mathrm{d}\Omega$$

$$= \mathcal{R}_{aa'}^{(2)}\, (-1)^{m_a}\, \frac{\hat{l}_a \hat{l}_{a'}}{\hat{2}\sqrt{4\pi}}\, (l_a\, {-}m_a\, l_{a'}\, m_{a'}|2\,0)\, (l_a\, 0\, l_{a'}\, 0|2\,0) \quad , \tag{A.13}$$

where we used Gaunt's formula ([Suh07, eq. 2.66]) to evaluate the integral.

Putting everything together, we end up with the following formula.

$$Q = \sqrt{\frac{16\pi}{5}} \sum_{i=1}^{A} \sum_{a\,a'} C_a^{\alpha_i\, m_t^{i}*}\, C_{a'}^{\alpha_i\, m_t^{i}}$$

$$\times \sum_{\substack{m_l\, m_s \\ m_l'\, m_s'}} (l\, m_l\, \tfrac{1}{2}\, m_s|j\, m_j)(l'\, m_l'\, \tfrac{1}{2}\, m_s'|j'\, m_j')\, \langle n\, l\, m_l|\hat{Q}_{20}|n'\, l'\, m_l'\rangle\, \langle m_s|m_s'\rangle\, \langle m_t^{i}|m_t^{i}\rangle \quad . \tag{A.14}$$

Using $\langle m_s|m_s'\rangle = \delta_{m_s, m_s'}$, the sum reduces to two elements.

$$Q = \sqrt{\frac{16\pi}{5}} \sum_{i=1}^{A} \sum_{a\,a'} C_a^{\alpha_i\, m_t^{i}*}\, C_{a'}^{\alpha_i\, m_t^{i}}$$

$$\times \Big( (l\, m_j{+}\tfrac{1}{2}\, \tfrac{1}{2}\, {-}\tfrac{1}{2}|j\, m_j)(l'\, m_j'{+}\tfrac{1}{2}\, \tfrac{1}{2}\, {-}\tfrac{1}{2}|j'\, m_j')\, \langle n\, l\, m_j{+}\tfrac{1}{2}|\hat{Q}_{20}|n'\, l'\, m_j'{+}\tfrac{1}{2}\rangle$$

$$+ (l\, m_j{-}\tfrac{1}{2}\, \tfrac{1}{2}\, \tfrac{1}{2}|j\, m_j)(l'\, m_j'{-}\tfrac{1}{2}\, \tfrac{1}{2}\, \tfrac{1}{2}|j'\, m_j')\, \langle n\, l\, m_j{-}\tfrac{1}{2}|\hat{Q}_{20}|n'\, l'\, m_j'{-}\tfrac{1}{2}\rangle \Big) \quad . \tag{A.15}$$

## A.3. Intrinsic 3D Nucleon Density

The single-particle operator $\hat{\rho}(\boldsymbol{r})$ gives the density at the point $\boldsymbol{r}$ in an A-body Hilbert space. It is defined as [RS80, eq. D.1]

$$\hat{\rho}(\boldsymbol{r}) = \sum_{i}^{A} \delta(\boldsymbol{r} - \hat{\boldsymbol{r}}_i) \quad . \tag{A.16}$$

The density of the A-body system is given by

$$\rho(\boldsymbol{r}) = \langle \Psi|\hat{\rho}(\boldsymbol{r})|\Psi\rangle \quad . \tag{A.17}$$

Applying the Slater-Condon rules leads to

$$\rho(\boldsymbol{r}) = \sum_{\alpha}^{A} \int \psi_\alpha^*(\boldsymbol{r}_\alpha)\, \delta(\boldsymbol{r} - \boldsymbol{r}_\alpha)\, \psi_\alpha(\boldsymbol{r}_\alpha)\, \mathrm{d}\boldsymbol{r}_\alpha$$

$$= \sum_{\alpha}^{A} \psi_\alpha^*(\boldsymbol{r})\, \psi_\alpha(\boldsymbol{r}) \quad . \tag{A.18}$$

To do the actual calculation, we express the result in terms of coupled HO wave functions.

$$\rho(\boldsymbol{r}) = \sum_{\alpha}^{A} \sum_{m_t} \sum_{a\,a'} C_a^{\alpha * m_t} C_{a'}^{\alpha m_t} \varphi_a^*(\boldsymbol{r}) \varphi_{a'}(\boldsymbol{r})$$
$$= \sum_{m_t} \sum_{a\,a'} \rho_{a\,a'}^{m_t} \varphi_a^*(\boldsymbol{r}) \varphi_{a'}(\boldsymbol{r})$$

$$\text{(A.19)}$$

The single particle wave functions are given by

$$\varphi_a(\boldsymbol{r}) = \sum_{m_l\,m_s} (l\,m_l\,\tfrac{1}{2}\,m_s|j\,m_j)\,\varphi_{nlm_l}(\boldsymbol{r})$$
$$\varphi_{nlm_l}(\boldsymbol{r}) = g_{nl}(r) \cdot Y_{lm_l}(\Omega)$$
$$= \sqrt{\frac{2n!}{b^3\,\Gamma(n+l+\tfrac{3}{2})}} \left(\frac{r}{b}\right)^l \mathrm{e}^{-r^2/2\,b^2} L_n^{(l+\frac{1}{2})}(r^2/b^2)\,Y_{lm_l}(\Omega) \quad, \qquad \text{(A.20)}$$

with $\Omega = \varphi, \theta$ and the oscillator length $b$.

# B. Three-Body Contact Interaction Matrix Elements

## B.1. Introduction

As discussed in section 2.3, we use a zero-range three-body contact interaction in the nuclear Hamiltonian. Due to the specific structure of this interaction, its contributions to the RPA and HF matrices and the HF ground-state energy can be reduced to density dependent matrix elements of a lower order. For the RPA, it can be reduced to a two-body matrix element, for the HF iterations to a one-body matrix element and the contribution to the HF ground-state energy reduces to a purely density dependent term, independent of the individual single-particle wave-functions. In the following, we carry out the necessary calculations.

Since the three-body interaction is defined in real-space coordinates, we have to work in a decoupled HO basis with quantum numbers $n$, $l$, $m_l$, $s$, $m_s$, $t$ and $m_t$. To reduce the number of indices, we combine $n$, $l$ and $m_l$ to one index $i$. As $s$ and $t$ are always $\frac{1}{2}$, we omit these quantum numbers and rename $m_s$ and $m_t$ to $s$ and $t$. The association of $i$, $s$ and $t$ to a specific state is depicted by subscripting them with the primed or unprimed letters $x$, $y$ and $z$. As usual, states in the coupled HO basis have the letters $a$, $b$, $c$ and states in the HF basis have the Greek letters $\alpha$, $\beta$, $\gamma$.

The anti-symmetric three-body matrix element in the uncoupled HO basis is given by

$$V_{x,y,z,x',y',z'} = V_3 \int \varphi^*_{i_x}(\boldsymbol{r})\, \varphi^*_{i_y}(\boldsymbol{r})\, \varphi^*_{i_z}(\boldsymbol{r})\, \varphi_{i'_x}(\boldsymbol{r})\, \varphi_{i'_y}(\boldsymbol{r})\, \varphi_{i'_z}(\boldsymbol{r}) \mathrm{d}\boldsymbol{r} \cdot \Delta_{\mathrm{AS}} \quad , \qquad (\mathrm{B.1})$$

with

$$\begin{aligned}
\Delta_{\mathrm{AS}} = \quad & st_{xx'}\, st_{yy'}\, st_{zz'} - st_{xx'}\, st_{yz'}\, st_{zy'} + st_{xz'}\, st_{yx'}\, st_{zy'} \\
& - st_{xz'}\, st_{yy'}\, st_{zx'} + st_{xy'}\, st_{yz'}\, st_{zx'} - st_{xy'}\, st_{yx'}\, st_{zz'} \quad ,
\end{aligned} \qquad (\mathrm{B.2})$$

and

$$st_{xx'} = \delta_{s_x, s_{x'}}\, \delta_{t_x, t_{x'}} \quad . \qquad (\mathrm{B.3})$$

## B.2. Two-body Matrix Element for RPA

The contribution of a three-body interaction to the RPA matrices in the HF basis is given by (6.10)

$$V_{\alpha,\beta,\alpha',\beta'} = \sum_{\gamma}^{A} V_{\alpha,\beta,\gamma,\alpha',\beta',\gamma} \quad , \tag{B.4}$$

which has the form of a two-body matrix element. If the three-body interaction is given in the uncoupled HO basis, the appropriate transformation has to be applied. A single HF state $|\alpha\rangle$ can be expressed in the uncoupled HO basis via

$$|\alpha\, t\rangle = \sum_{a} C_a^{\alpha t} |a\, t\rangle = \sum_{a,s} C_a^{\alpha t}\, cg_s^a\, |i\, s\, t\rangle \quad , \tag{B.5}$$

where we have to keep in mind, that the quantum numbers contained in $i$ are a subset of those included in $a$. To reduce the length of the formulae, we use a shorthand for the Clebsch-Gordan coefficients

$$cg_s^a = (l\, m{-}s\, \tfrac{1}{2}\, s | j\, m) \quad . \tag{B.6}$$

The complete matrix element is therefore given by

$$V_{\alpha,\beta,\alpha',\beta'} = \sum_{\substack{a,s_x,b,s_y \\ a',s_x',b',s_y'}} C_a^{\alpha t_\alpha}\, cg_{s_x}^a\, C_b^{\beta t_\beta}\, cg_{s_y}^b\, C_{a'}^{\alpha' t_\alpha'}\, cg_{s_x'}^{a'}\, C_{b'}^{\beta' t_\beta'}\, cg_{s_y'}^{b'}\, V_{x,y,x',y'} \quad , \tag{B.7}$$

with

$$V_{x,y,x',y'} = \sum_{\substack{i_z,s_z,t_z \\ i_z',s_z',t_z'}} \rho_{i_z i_z'}^{s_z t_z}\, st_{zz'}\, V_{x,y,z,x',y',z'} \quad , \tag{B.8}$$

where we already used that the density matrix is diagonal in $s$ and $t$. With a three-body contact interaction like (B.1), we can carry out the summation and derive a density dependent two-body matrix element.

Using eq. (B.1) and reordering the terms yields

$$V_{x,y,x',y'} = V_3 \int \varphi_{i_x}^*(\boldsymbol{r})\, \varphi_{i_y}^*(\boldsymbol{r})\, \varphi_{i_x'}(\boldsymbol{r})\, \varphi_{i_y'}(\boldsymbol{r}) \underbrace{\sum_{\substack{i_z,s_z,t_z \\ i_z',s_z',t_z'}} \rho_{i_z i_z'}^{s_z t_z}\, \varphi_{i_z}^*(\boldsymbol{r})\, \varphi_{i_z'}(\boldsymbol{r})\, st_{zz'}\, \Delta_{\mathrm{AS}}}_{\text{interesting part}}\, \mathrm{d}\boldsymbol{r} \quad . \tag{B.9}$$

We can now simplify the interesting part. The sum over $i_z$ and $i_z'$ can be carried out to give a density

$$\sum_{i_z,i_z'} \rho_{i_z i_z'}^{s_z t_z}\, \varphi_{i_z}^*(\boldsymbol{r})\, \varphi_{i_z'}(\boldsymbol{r}) = \rho^{s_z t_z}(\boldsymbol{r}) \tag{B.10}$$

and $st_{zz'}$ can be combined with $\Delta_{\mathrm{AS}}$ to give

$$\sum_{\substack{s_z,t_z \\ s_z',t_z'}} st_{zz'}\Delta_{\mathrm{AS}} = \sum_{s_z t_z}(st_{xx'}\, st_{yy'} - st_{xy'}\, st_{yx'})(1 - st_{xz} - st_{yz}) \quad . \tag{B.11}$$

We therefore have

$$\sum_{\substack{i_z,s_z,t_z \\ i_z',s_z',t_z'}} \rho_{i_z i_z'}^{s_z t_z}\, \varphi_{i_z}^*(\boldsymbol{r})\, \varphi_{i_z'}(\boldsymbol{r})\, st_{zz'}\Delta_{\mathrm{AS}}$$

$$= \left(\rho(\boldsymbol{r}) - \rho^{s_x t_x}(\boldsymbol{r}) - \rho^{s_y t_y}(\boldsymbol{r})\right)(st_{xx'}\, st_{yy'} - st_{xy'}\, st_{yx'}) \quad , \tag{B.12}$$

and for the complete two-body matrix element

$$V_{x,y,x',y'} = V_3 \int \varphi_{i_x}^*(\boldsymbol{r})\, \varphi_{i_y}^*(\boldsymbol{r})\, \varphi_{i_x'}(\boldsymbol{r})\, \varphi_{i_y'}(\boldsymbol{r})$$

$$\times \left(\rho(\boldsymbol{r}) - \rho^{s_x t_x}(\boldsymbol{r}) - \rho^{s_y t_y}(\boldsymbol{r})\right)(st_{xx'}\, st_{yy'} - st_{xy'}\, st_{yx'})\, \mathrm{d}\boldsymbol{r} \quad . \tag{B.13}$$

Inserting (B.13) into (B.7) yields the matrix element in the HF basis

$$V_{\alpha,\beta,\alpha',\beta'}$$

$$= V_3 \int \sum_{\substack{a,s_x,b,s_y \\ a',s_x',b',s_y'}} C_a^{\alpha t_\alpha}\, cg_{s_x}^a\, C_b^{\beta t_\beta}\, cg_{s_y}^b\, C_{a'}^{\alpha' t_\alpha'}\, cg_{s_x'}^{a'}\, C_{b'}^{\beta' t_\beta'}\, cg_{s_y'}^{b'}\, \varphi_{i_x}^*(\boldsymbol{r})\, \varphi_{i_y}^*(\boldsymbol{r})\, \varphi_{i_x'}(\boldsymbol{r})\, \varphi_{i_y'}(\boldsymbol{r})$$

$$\times \left(\rho(\boldsymbol{r}) - \rho^{s_x t_x}(\boldsymbol{r}) - \rho^{s_y t_y}(\boldsymbol{r})\right)(st_{xx'}\, st_{yy'} - st_{xy'}\, st_{yx'})\, \mathrm{d}\boldsymbol{r} \quad . \tag{B.14}$$

With the definition of spin dependent HF wave-functions

$$\psi_{\alpha t_\alpha}^s(\boldsymbol{r}) = \sum_a C_a^{\alpha t}\, cg_s^a\, \varphi_i(\boldsymbol{r}) \quad , \tag{B.15}$$

we can simplify (B.14) to

$$V_{\alpha,\beta,\alpha',\beta'}$$

$$= V_3 \int \sum_{\substack{s_1,s_2 \\ s_1',s_2'}} \psi_{\alpha t_\alpha}^{s_1 *}(\boldsymbol{r})\, \psi_{\beta t_\beta}^{s_2 *}(\boldsymbol{r})\, \psi_{\alpha' t_\alpha'}^{s_1'}(\boldsymbol{r})\, \psi_{\beta' t_\beta'}^{s_2'}(\boldsymbol{r})\left(\rho(\boldsymbol{r}) - \rho^{s_1 t_\alpha}(\boldsymbol{r}) - \rho^{s_2 t_\beta}(\boldsymbol{r})\right)$$

$$\times \left(\delta_{s_1 s_1'}\, \delta_{s_2 s_2'}\, \delta_{t_\alpha t_\alpha'}\, \delta_{t_\beta t_\beta'} - \delta_{s_1 s_2'}\, \delta_{s_1 s_2'}\, \delta_{t_\alpha t_\beta'}\, \delta_{t_\alpha t_\beta'}\right)\mathrm{d}\boldsymbol{r} \quad , \tag{B.16}$$

where we used that the $t$ quantum numbers are the same in all bases and renamed $s_x,\ldots$ to $s_1,\ldots$.

## B.3. One-body Matrix Element for HF

The contribution of a three-body interaction to the HF energy functional is given by eq. (4.13)

$$V_{a,a'} = \tfrac{1}{2}\sum_{b,c,b',c'} V_{a,b,c,a',b',c'}\, \rho_{bb'}\, \rho_{cc'} = \tfrac{1}{2}\sum_{s,s'} cg_s^a\, cg_{s'}^{a'}\, V_{x,x'} \quad , \tag{B.17}$$

with

$$V_{x,x'} = \sum_{\substack{i_z,s_z,t_z \\ i_z',s_z',t_z'}} \rho_{i_y i_y'}^{s_y t_y} \, st_{yy'} \, \rho_{i_z i_z'}^{s_z t_z} \, st_{zz'} \, V_{x,y,z,x',y',z'} \quad , \tag{B.18}$$

which has the form of a one-body matrix element (we already used that the density matrix is diagonal in $s$ and $t$). With a three-body contact interaction like (B.1), we can carry out the summation and derive a density dependent one-body matrix element.

We start with the result from section B.2, the density dependent two-body matrix element in the uncoupled HO basis (eq. (B.13))

$$\begin{aligned}
V_{x,x'} &= \tfrac{1}{2} \sum_{\substack{i_y,s_y,t_y \\ i_y',s_y',t_y'}} \rho_{i_y i_y'}^{s_y t_y} \, st_{yy'} \, V_{x,y,x',y'} \\
&= \tfrac{1}{2} V_3 \int \varphi_{i_x}^*(\boldsymbol{r}) \, \varphi_{i_x'}(\boldsymbol{r}) \sum_{\substack{i_y,s_y,t_y \\ i_y',s_y',t_y'}} \rho_{i_y i_y'}^{s_y t_y} \, st_{yy'} \, \varphi_{i_y}^*(\boldsymbol{r}) \, \varphi_{i_y'}(\boldsymbol{r}) \\
&\quad \times \left( \rho(\boldsymbol{r}) - \rho^{s_x t_x}(\boldsymbol{r}) - \rho^{s_y t_y}(\boldsymbol{r}) \right) \left( st_{xx'} \, st_{yy'} - st_{xy'} \, st_{yx'} \right) \mathrm{d}\boldsymbol{r} \quad . \tag{B.19}
\end{aligned}$$

The sum over $i_y$ and $i_y'$ can be carried out to give a density

$$\sum_{i_y,i_y'} \rho_{i_y i_y'}^{s_y t_y} \, \varphi_{i_y}^*(\boldsymbol{r}) \, \varphi_{i_y'}(\boldsymbol{r}) = \rho^{s_y t_y}(\boldsymbol{r}) \tag{B.20}$$

and $st_{yy'}$ can be combined with the other Kronecker deltas to give

$$\sum_{\substack{s_y,t_y \\ s_y',t_y'}} st_{yy'}(st_{xx'} \, st_{yy'} - st_{xy'} \, st_{yx'}) = \sum_{s_y t_y} st_{xx'}(1 - st_{xy}) \quad . \tag{B.21}$$

The matrix element then reads

$$\begin{aligned}
V_{x,x'} &= \tfrac{1}{2} V_3 \int \varphi_{i_x}^*(\boldsymbol{r}) \, \varphi_{i_x'}(\boldsymbol{r}) st_{xx'} \tag{B.22} \\
&\quad \times \sum_{s_y,t_y} \rho^{s_y t_y}(\boldsymbol{r}) \left( \rho(\boldsymbol{r}) - \rho^{s_x t_x}(\boldsymbol{r}) - \rho^{s_y t_y}(\boldsymbol{r}) \right) (1 - st_{xy}) \, \mathrm{d}\boldsymbol{r} \quad .
\end{aligned}$$

Inserting (B.22) into (B.17) gives the matrix element in the coupled HO basis

$$\begin{aligned}
V_{a,a'} &= \tfrac{1}{2} V_3 \int \sum_{s_1} \varphi_a^{s_1 *}(\boldsymbol{r}) \, \varphi_{a'}^{s_1'}(\boldsymbol{r}) t_{aa'} \tag{B.23} \\
&\quad \times \sum_{s_2,t_2} \rho^{s_2 t_2}(\boldsymbol{r}) \left( \rho(\boldsymbol{r}) - \rho^{s_1 t_a}(\boldsymbol{r}) - \rho^{s_2 t_2}(\boldsymbol{r}) \right) (1 - s_{12} t_{a2}) \, \mathrm{d}\boldsymbol{r} \quad ,
\end{aligned}$$

with spin-dependent coupled HO wave functions

$$\varphi_{a t_a}^s(\boldsymbol{r}) = \sum_s cg_s^a \, \varphi_i(\boldsymbol{r}) \quad . \tag{B.24}$$

For time-reversal invariant systems, i.e. $\rho^s(\boldsymbol{r}) = \frac{1}{2}\rho(\boldsymbol{r})$, the second line of eq. B.23 can be simplified considerably

$$
\begin{aligned}
\sum_{s_2,t_2} & \rho^{s_2 t_2}(\boldsymbol{r}) \left( \rho(\boldsymbol{r}) - \rho^{s_1 t_a}(\boldsymbol{r}) - \rho^{s_2 t_2}(\boldsymbol{r}) \right) (1 - s_{12} t_{a2}) \\
&= \sum_{t_2} \rho^{t_2}(\boldsymbol{r}) \left( \rho(\boldsymbol{r}) - \tfrac{1}{2}\rho^{t_a}(\boldsymbol{r}) - \tfrac{1}{2}\rho^{t_2}(\boldsymbol{r}) \right) (1 - \tfrac{1}{2} t_{a2}) \\
&= \rho^2(\boldsymbol{r}) - \tfrac{1}{2}\rho(\boldsymbol{r})\rho^{t_a}(\boldsymbol{r}) - \tfrac{1}{2}\rho^{t_a{}^2}(\boldsymbol{r}) - \tfrac{1}{2}\rho^{-t_a{}^2}(\boldsymbol{r}) \\
&\quad - \tfrac{1}{2}\rho^{t_a}(\boldsymbol{r})\rho(\boldsymbol{r}) + \tfrac{1}{2}\rho^{t_a{}^2}(\boldsymbol{r}) \\
&= \rho^2(\boldsymbol{r}) - \rho(\boldsymbol{r})\rho^{t_a}(\boldsymbol{r}) - \tfrac{1}{2}\rho^{-t_a{}^2}(\boldsymbol{r}) \\
&= \tfrac{1}{2}\left( \rho^2(\boldsymbol{r}) - \rho^{t_a{}^2}(\boldsymbol{r}) \right) \quad,
\end{aligned}
\tag{B.25}
$$

resulting in the matrix element

$$
V_{a,a'} = \tfrac{1}{4}V_3 \int \sum_{s_1} \varphi_a^{s_1*}(\boldsymbol{r})\, \varphi_{a'}^{s_1'}(\boldsymbol{r}) \left( \rho^2(\boldsymbol{r}) - \rho^{t_a{}^2}(\boldsymbol{r}) \right) \delta_{t_a t_a'}\, \mathrm{d}\boldsymbol{r} \quad.
\tag{B.26}
$$

## B.4. Ground State Contribution

The contribution of a three-body interaction to the HF ground-state energy is given by eq. (4.12)

$$
\begin{aligned}
E_{\mathrm{HF}} &= \tfrac{1}{6} \sum_{a,b,c,a',b',c'} \rho_{aa'}\, \rho_{bb'}\, \rho_{cc'}\, V_{abca'b'c'} \\
&= \tfrac{1}{6} \sum_{\substack{i_x,s_x,t_x \\ i_x',s_x',t_x'}} \sum_{\substack{i_y,s_y,t_y \\ i_y',s_y',t_y'}} \sum_{\substack{i_z,s_z,t_z \\ i_z',s_z',t_z'}} \rho_{i_x i_x'}^{s_x t_x}\, st_{xx'}\, \rho_{i_y i_y'}^{s_y t_y}\, st_{yy'}\, \rho_{i_z i_z'}^{s_z t_z}\, st_{zz'}\, V_{x,y,z,x',y',z'} \quad,
\end{aligned}
\tag{B.27}
$$

where we already used that the density matrix is diagonal in $s$ and $t$. With a three-body contact interaction like (B.1), we can carry out the summation and derive a purely density dependent contribution.

We start with the result from section B.3, the one-body matrix element in the uncoupled HO basis (eq. (B.22))

$$
\begin{aligned}
E_{\mathrm{HF}} &= \tfrac{2}{6} \sum_{\substack{i_x,s_x,t_x \\ i_x',s_x',t_x'}} \rho_{i_x i_x'}^{s_x t_x}\, st_{xx'}\, V_{x,x'} \\
&= \tfrac{1}{6} V_3 \int \sum_{\substack{i_x,s_x,t_x \\ i_x',s_x',t_x'}} \rho_{i_x i_x'}^{s_x t_x}\, \varphi_{i_x}^*(\boldsymbol{r})\, \varphi_{i_x'}(\boldsymbol{r}) st_{xx'} \\
&\quad \times \sum_{s_y,t_y} \rho^{s_y t_y}(\boldsymbol{r}) \left( \rho(\boldsymbol{r}) - \rho^{s_x t_x}(\boldsymbol{r}) - \rho^{s_y t_y}(\boldsymbol{r}) \right) (1 - st_{xy})\, \mathrm{d}\boldsymbol{r} \quad.
\end{aligned}
\tag{B.28}
$$

The sum over $i_y$ and $i'_y$ again gives a density, resulting in

$$E_{\text{HF}} = \tfrac{1}{6} V_3 \int \sum_{\substack{s_1,t_1 \\ s_2,t_2}} \rho^{s_1 t_1}(\boldsymbol{r}) \, \rho^{s_2 t_2}(\boldsymbol{r}) \left( \rho(\boldsymbol{r}) - \rho^{s_1 t_1}(\boldsymbol{r}) - \rho^{s_2 t_2}(\boldsymbol{r}) \right) (1 - st_{12}) \, \mathrm{d}\boldsymbol{r} \quad . \quad (\text{B.29})$$

For time-reversal invariant systems ($\rho^s(\boldsymbol{r}) = \tfrac{1}{2}\rho(\boldsymbol{r})$), the densities can be simplified to

$$\sum_{\substack{s_1,t_1 \\ s_2,t_2}} \rho^{s_1 t_1}(\boldsymbol{r}) \, \rho^{s_2 t_2}(\boldsymbol{r}) \left( \rho(\boldsymbol{r}) - \rho^{s_1 t_1}(\boldsymbol{r}) - \rho^{s_2 t_2}(\boldsymbol{r}) \right) (1 - st_{12})$$

$$= \sum_{t_1,t_2} \rho^{t_1}(\boldsymbol{r}) \, \rho^{t_2}(\boldsymbol{r}) \left( \rho(\boldsymbol{r}) - \tfrac{1}{2} \rho^{t_1}(\boldsymbol{r}) - \rho^{\frac{1}{2} \, t_2}(\boldsymbol{r}) \right) (1 - \tfrac{1}{2} t_{12})$$

$$= \rho^{p2}(\boldsymbol{r}) \left( \rho(\boldsymbol{r}) - \rho^p(\boldsymbol{r}) \right) \tfrac{1}{2} + \rho^{n2}(\boldsymbol{r}) \left( \rho(\boldsymbol{r}) - \rho^n(\boldsymbol{r}) \right) \tfrac{1}{2} + \rho^p(\boldsymbol{r}) \, \rho^n(\boldsymbol{r}) \tfrac{1}{2} \rho(\boldsymbol{r})$$

$$= \tfrac{3}{2} \rho^p(\boldsymbol{r}) \, \rho^n(\boldsymbol{r}) \, \rho(\boldsymbol{r}) \quad , \qquad\qquad (\text{B.30})$$

resulting in an energy contribution of

$$E_{\text{HF}} = \tfrac{1}{4} V_3 \int \rho^p(\boldsymbol{r}) \, \rho^n(\boldsymbol{r}) \, \rho(\boldsymbol{r}) \, \mathrm{d}\boldsymbol{r} \quad . \qquad\qquad (\text{B.31})$$

# C. Definitions, Conventions and Acronyms

## C.1. Units and Constants

In this work, all quantities are expressed in natural units $\hbar = c = 1$. The conversion factor to standard units is given by $\hbar c = 197.327053\,\mathrm{MeV\,fm}$.

The nucleon properties are:

neutron mass $m_n = 939.56563\,\mathrm{MeV}$

proton mass $m_p = 938.27231\,\mathrm{MeV}$

nucleon mass $m_N = 938.91897\,\mathrm{MeV}$

proton charge radius $m_p = 0.876\,\mathrm{fm}$

## C.2. Operators, Vectors etc.

| | |
|---|---|
| $\hat{x}$ | generic operator |
| $\boldsymbol{x}$ | generic vector |
| $\hat{\boldsymbol{x}}$ | generic vector operator |
| $\mathsf{X}$ | generic matrix |
| $\hat{X}^{[k]}$ | irreducible $k$-body part of many-body operator |
| $\hat{a}_x^\dagger,\ \hat{a}_x$ | creation and annihilation operators in HF basis |
| $\hat{c}_x^\dagger,\ \hat{c}_x$ | creation and annihilation operators in HO basis |
| $m,\ n$ | as index of creation or annihilation operators: state above Fermi level |
| $i,\ j,\ k$ | as index of creation or annihilation operators: state below Fermi level |
| $(j_1\,m_1\,j_2\,m_2|J\,M)$ | Clebsch-Gordan coefficient |
| $\begin{pmatrix} j_1 & j_2 & J \\ m_1 & m_2 & M \end{pmatrix}$ | Wigner 3j-symbol |
| $D_{KM}^J(\beta)$ | Wigner rotation matrix (D-matrix) |
| $d_{KM}^J(\beta)$ | reduced Wigner rotation matrix (d-matrix) |
| $\hat{P}_{KM}^J$ | angular-momentum projection operator |

## C.3. Quantum Numbers and Related Symbols

Small letters denote single-particle quantum numbers, capital letters denote quantum numbers of many-body states.

| | |
|---|---|
| $e$ | major harmonic oscillator quantum number |
| $n$ | radial harmonic oscillator quantum number |
| $l, m_l$ | orbital angular-momentum quantum number and projection |
| $j, m_j, m, k$ | total angular-momentum quantum number and projection |
| $s, m_s$ | spin and spin-projection |
| $t, m_t$ | isospin and isospin-projection |
| $J, M, M_J$ | total angular-momentum quantum number and projection |
| $K$ | projection of total angular-momentum on nuclear symmetry axis |
| $N$ | neutron number |
| $P$ | proton number |
| $A$ | nucleon number |

## C.4. Acronyms

| | |
|---|---|
| AMP | angular-momentum projection |
| AVAP | approximate variation after projection |
| EWSR | energy-weighted sum rule |
| GCM | generator coordinate method |
| HF | Hartree-Fock |
| HO | harmonic oscillator |
| ISD | isoscalar dipole |
| ISM | isoscalar monopole |
| ISQ | isoscalar quadrupole |
| IVD | isovector dipole |
| MCHF | multi-configuration Hartree-Fock |
| NEWSR | non-energy-weighted sum rule |
| NN | nucleon-nucleon |
| PAV | projection after variation |
| ph | particle-hole |
| QBA | quasi-boson-approximation |
| RPA | Random Phase Approximation |
| SRG | Similarity Renormalization Group |
| UCOM | Unitary Correlation Operator Method |

# Bibliography

[ABC⁺75]  J. Ahrens, H. Borchert, K. H. Czock, H. B. Eppler, H. Gimm, H. Gundrum, M. Kroning, P. Riehn, G. Sita Ram, A. Zieger, and B. Ziegler. Total nuclear photon absorption cross sections for some light elements. *Nucl.Phys.*, A251:479, 1975.

[AMW81]  P. D. Allen, E. G. Muirhead, and D. V. Webb. The photoneutron cross section of $^{20}$Ne. *Nucl.Phys.*, A357:171, 1981.

[AR08]  Daniel Pena Arteaga and Peter Ring. Relativistic RPA in axial symmetry. *Physical Review C*, 77:034317, 2008.

[AS04]  B. K. Agrawal and S. Shlomo. Consequences of self-consistency violations in hartree-fock random-phase approximation calculations of the nuclear breathing mode energy. *Phys. Rev. C*, 70:014308, Jul 2004.

[AWT03]  G. Audi, A.H. Wapstra, and C. Thibault. The AME2003 atomic mass evaluation: (II). Tables, graphs and references. *Nuclear Physics A*, 729(1):337–676, 2003.

[B⁺]  N. A. BURGOV et al. ZHETF,45,1694(1963).

[BBJK69]  N. Bezic, D. Brajnik, D. Jamnik, and G. Kernel. Total photonuclear cross sections for $^{12}$C, $^{14}$N, $^{16}$O and $^{19}$F in the region of the giant resonance. *Nucl.Phys.*, A128:426, 1969.

[Ber69]  A.M. Bernstein. Isoscalar transition rates from the $(\alpha, \alpha')$ reaction. *Advances in Nuclear Physics*, 3, 1969.

[BM69]  Aage Bohr and Ben R. Mottelson. *Nuclear Structure Volume 1*. W.A. Benjamin, Inc., 1969.

[BM75]  Aage Bohr and Ben R. Mottelson. *Nuclear Structure Volume 2*. W.A. Benjamin, Inc., 1975.

[Bri66]  D.M. Brink. The alpha-particle model of light nuclei. In *Many-Body Description of Nuclear Structure and Reactions*, volume 36 of *International School of Physics "Erico Fermi"*, pages 247–277, 1966.

[BSMM98]  Ilja N. Bronstein, K. A. Semendjajew, Gerhard Musiol, and Heiner Muehlig. *Taschenbuch der Mathematik, CD-ROM Version*. Verlag Harri Deutsch, 1st edition, 1998.

*Bibliography*

[Cal10]     Angelo Calci. *Ab initio nuclear structure with SRG-transformed chiral NN plus NNN interactions*. Master thesis, Technische Universität Darmstadt, 2010.

[CDF]       Centre for photonuclear experiments data. http://cdfe.sinp.msu.ru/index.en.html.

[CGBQ00]    G Colò, N Van Giai, P.F Bortignon, and M.R Quaglia. On dipole compression modes in nuclei. *Physics Letters B*, 485(4):362–366, 2000.

[CHBF63]    J. T. Caldwell, R. R. Harvey, R. L. Bramblett, and S. C. Fultz. $(\gamma, n)$ cross sections for $^{16}$O and $^{28}$Si. *Phys.Letters*, 6:213, 1963.

[CLC$^{+}$09]   X. Chen, Y.-W. Lui, H.L. Clark, Y. Tokimoto, and D.H. Youngblood. Giant resonances in $^{24}$Mg and $^{28}$Si from 240 MeV $^{6}$Li scattering. *Physical Review C*, 80:014312, 2009.

[DG80]      J. Dechargé and D. Gogny. Hartree-fock-bogolyubov calculations with the $D1$ effective interaction on spherical nuclei. *Phys. Rev. C*, 21:1568–1593, Apr 1980.

[Dob11]     Jacek Dobaczewski. Current developments in nuclear density functional methods. *Journal of Physics: Conference Series*, 312(9):092002, 2011.

[Edm60]     A.R. Edmonds. *Angular Momentum in Quantum Mechanics*. Princeton University Press, 1960.

[EGM05]     E. Epelbaum, W. Glöckle, and Ulf-G. Meißner. The two-nucleon system at next-to-next-to-next-to-leading order. *Nuclear Physics A*, 747(2–4):362–424, 2005.

[EM03]      D. R. Entem and R. Machleidt. Accurate charge-dependent nucleon-nucleon potential at fourth order of chiral perturbation theory. *Phys. Rev. C*, 68:041001, Oct 2003.

[End90]     P.M. Endt. Energy levels of A = 21–44 nuclei (VII). *Nuclear Physics A*, 521(0):1–400, 1990.

[End98]     P.M. Endt. Supplement to energy levels of A = 21–44 nuclei (VII). *Nuclear Physics A*, 633(1):1–220, 1998.

[ENG$^{+}$02]   E. Epelbaum, A. Nogga, W. Glöckle, H. Kamada, Ulf-G. Meißner, and H. Witała. Three-nucleon forces from chiral effective field theory. *Phys. Rev. C*, 66:064001, Dec 2002.

[ER04]      J.L. Egido and L.M. Robledo. 10 Angular momentum projection and quadrupole correlations effects in atomic nuclei. In Georgios Lalazissis, Peter Ring, and Dario Vretenar, editors, *Extended Density Functionals in Nuclear Structure Physics*, volume 641 of *Lecture Notes in Physics*, pages

269–302. Springer Berlin / Heidelberg, 2004. 10.1007/978-3-540-39911-7_10.

[FCB+66] S. C. Fultz, J. T. Caldwell, B. L. Berman, R. L. Bramblett, and R. R. Harvey. Photoneutron cross sections for $^{12}$C and $^{27}$Al. *Phys.Rev.*, 143:790, 1966.

[FHH+92] G. Fricke, J. Herberz, Th. Hennemann, G. Mallot, L. A. Schaller, L. Schellenberg, C. Piller, and R. Jacot-Guillarmod. Behavior of the nuclear charge radii systematics in the $s$ - $d$ shell from muonic atom measurements. *Phys. Rev. C*, 45:80–89, Jan 1992.

[GISY68] B. I. Goryachev, B. S. Ishkhanov, V. G. Shevchenko, and B. A. Yurev. Structure of $(\gamma, n)$ cross sections in $^{28}$Si, $^{32}$S, and $^{40}$Ca. *Yadern.Fiz.*, 7:1168, 1968.

[GRHR10] A. Günther, R. Roth, H. Hergert, and S. Reinhardt. Systematics of binding energies and radii based on realistic two-nucleon plus phenomenological three-nucleon interactions. *Phys. Rev. C*, 82:024319, Aug 2010.

[GS81] Nguyen Van Giai and H. Sagawa. Monopole and dipole compression modes in nuclei. *Nuclear Physics A*, 371(1):1–18, 1981.

[Gün11] Anneke Günther. *Nuclear Structure with Unitarily Transformed Two-Body plus Phenomeological Three-Body Interactions*. PhD thesis, Technische Universität Darmstadt, 2011.

[Her08] Heiko Hergert. *An Ab-Initio Approach to Pairing Phenomena Using Modern Effective Interactions*. PhD thesis, Technische Universität Darmstadt, 2008.

[HG07] S. Hilaire and M. Girod. Large-scale mean-field calculations from proton to neutron drip lines using the D1S gogny force. *The European Physical Journal A - Hadrons and Nuclei*, 33:237–241, 2007. 10.1140/epja/i2007-10450-2.

[HPR11] H. Hergert, P. Papakonstantinou, and R. Roth. Quasiparticle random-phase approximation with interactions from the similarity renormalization group. *Phys. Rev. C*, 83:064317, Jun 2011.

[HvdW01] M.N. Harakeh and A. van der Woude. *Giant Resonances*, volume 24 of *Oxford Studies In Nuclear Physics*. Oxford Science Publications, 2001.

[HW53] David Lawrence Hill and John Archibald Wheeler. Nuclear constitution and the interpretation of fission phenomena. *Phys. Rev.*, 89:1102–1145, Mar 1953.

[I+a] B. S. ISHKHANOV et al. J,PL,9,162,1964.

[I⁺b]      B. S. ISHKHANOV et al. R,MSU-INP-2002-27/711,2002.

[IKPS71]   B. S. Ishkhanov, I. M. Kapitonov, I. M. Piskarev, and V. G. Shevchenko. Structure of the $^{12}$C($\gamma$, n) cross section in the giant resonance region. *Yad.Fiz.*, 14:253, 1971.

[KKK⁺75]   U. Kneissl, E. A. Koop, G. Kuhl, K. H. Leister, and A. Weller. The quasimonoenergetic photon facility at the giessen 65 MeV electron linear accelerator. *Nucl.Instrum.Methods*, 127:1, 1975.

[Lan10]    Joachim Langhammer. *Consistent chiral three-nucleon interactions in nuclear structure.* Master thesis, Technische Universität Darmstadt, 2010.

[LB68]     H.A. Lamme and E. Boeker. Exact and approximate angular momentum projection for light nuclei. *Nuclear Physics A*, 111:492, 1968.

[Löw55]    Per-Olov Löwdin. Quantum theory of many-particle systems II. *Physical Review*, 97:1490, 1955.

[LPD⁺10]   C. Losa, A. Pastore, T. Dossing, E. Vigezzi, and R.A. Broglia. Linear response of light deformed nuclei investigated by self-consistent QRPA. *Physical Review C*, 81:064307, 2010.

[Mac01]    R. Machleidt. High-precision, charge-dependent bonn nucleon-nucleon potential. *Phys. Rev. C*, 63:024001, Jan 2001.

[Man75]    H.J. Mang. The self-consistent single-particle model in nuclear physics. *Physical Reports*, 18:325, 1975.

[ME10]     R Machleidt and D R Entem. Nuclear forces from chiral EFT: the unfinished business. *Journal of Physics G: Nuclear and Particle Physics*, 37(6):064041, 2010.

[NFR05]    Thomas Neff, Hans Feldmeier, and Robert Roth. Clusters and shell-structure in light nuclei. *AIP Conference Proceedings*, 764(1):387–392, 2005.

[PBJ⁺83]   R. E. Pywell, B. L. Berman, J. W. Jury, J. G. Woodworth, K. G. McNeill, and M. N. Thompson. Photoneutron cross sections for the silicon isotopes. *Phys.Rev.*, C27:960, 1983.

[PG08]     S. Peru and H. Goutte. Role of deformation on GR within the QRPA and the gogny force. *Physical Review C*, 77:044313, 2008.

[PHPR12]   P. Papakonstantinou, H. Hergert, V.Yu. Ponomarev, and R. Roth. Low-energy dipole strength and the critical case of $^{48}$Ca. *Physics Letters B*, 709(3):270–275, 2012.

[PPHR06]   N. Paar, P. Papakonstantinou, H. Hergert, and R. Roth. Collective multipole excitations based on correlated realistic nucleon-nucleon interactions. *Phys. Rev. C*, 74:014318, Jul 2006.

[PPRW11]   P. Papakonstantinou, V. Ponomarev, R. Roth, and J. Wambach. Isoscalar dipole coherence at low energies and forbidden E1 strength. *The European Physical Journal A - Hadrons and Nuclei*, 47:1–10, 2011. 10.1140/epja/i2011-11014-7.

[PRP07]   P. Papakonstantinou, R. Roth, and N. Paar. Nuclear collective excitations using correlated realistic interactions: The role of explicit random-phase approximation correlations. *Phys. Rev. C*, 75:014310, Jan 2007.

[RE10]   Tomás R. Rodríguez and J. Luis Egido. Triaxial angular momentum projection and configuration mixing calculations with the gogny force. *Phys. Rev. C*, 81:064323, Jun 2010.

[Rei08]   Sabine Reinhardt. *Comparison and Connection of the Similarity Renormalization Group and the Unitary Correlation Operator Method*. Diploma thesis, Technische Universität Darmstadt, 2008.

[RGER02]   R. Rodríguez-Guzmán, J.L. Egido, and L.M. Robledo. Correlations beyond the mean field in magnesium isotopes: angular momentum projection and configuration mixing. *Nuclear Physics A*, 709(1-4):201–235, 2002.

[RHP+05]   R. Roth, H. Hergert, P. Papakonstantinou, T. Neff, and H. Feldmeier. Matrix elements and few-body calculations within the unitary correlation operator method. *Phys. Rev. C*, 72(3):034002, Sep 2005.

[RLC+11]   Robert Roth, Joachim Langhammer, Angelo Calci, Sven Binder, and Petr Navrátil. Similarity-transformed chiral $NN + 3N$ interactions for the *Ab Initio* description of $^{12}$C and $^{16}$O. *Phys. Rev. Lett.*, 107:072501, Aug 2011.

[RNF10]   Robert Roth, Thomas Neff, and Hans Feldmeier. Nuclear structure in the framework of the unitary correlation operator method. *Progress in Particle and Nuclear Physics*, 65(1):50–93, 2010.

[RNHF04]   R. Roth, T. Neff, H. Hergert, and H. Feldmeier. Nuclear structure based on correlated realistic nucleon–nucleon potentials. *Nuclear Physics A*, 745(1–2):3–33, 2004.

[Rob10]   L. M. Robledo. Remarks on the use of projected densities in the density-dependent part of skyrme or gogny functionals. *Journal of Physics G: Nuclear and Particle Physics*, 37(6):064020, 2010.

[Rod12]   Tomás R. Rodríguez. personal communication, 5 2012.

[Row70]   D.J. Rowe. *Nuclear Collective Motion*. Methuen and Co. Ltd., 1970.

[RPP+06]   R. Roth, P. Papakonstantinou, N. Paar, H. Hergert, T. Neff, and H. Feld-meier. Hartree-fock and many body perturbation theory with correlated realistic *NN* interactions. *Phys. Rev. C*, 73:044312, Apr 2006.

[RS80]   Peter Ring and Peter Schuck. *The Nuclear Many-Body Problem.* Texts and Monographs in Physics. Springer Berlin Heidelberg, 1980.

[Sid98]   Roger B. Sidje. EXPOKIT: Software package for computing matrix exponentials. *ACM Transactions on Mathematical Software*, 24(1):130–156, March 1998.

[SIM75]   R.O. Sayer, J.S. Smith III, and W.T. Milner. Rotational and quasirotational bands in even-even nuclei. *Atomic Data and Nuclear Data Tables*, 15(2):85–110, 1975.

[SKTdS94]   V. G. J. Stoks, R. A. M. Klomp, C. P. F. Terheggen, and J. J. de Swart. Construction of high-quality *NN* potential models. *Phys. Rev. C*, 49:2950–2962, Jun 1994.

[Sky59]   T.H.R. Skyrme. The effective nuclear potential. *Nuclear Physics*, 9(4):615–634, 1958–1959.

[Spe81]   R.H. Spear. Static quadrupole moments of first $2^+$ states in the 2s-1d shell: A review of experiment and theory. *Physical Reports*, 73:369, 1981.

[SR00]   Javid A. Sheikh and Peter Ring. Pairing correlations and particle-number projection methods. *Nuclear Physics A*, 665:71, 2000.

[Sto05]   N.J. Stone. Table of nuclear magnetic dipole and electric quadrupole moments. *Atomic Data and Nuclear Data Tables*, 90(1):75–176, 2005.

[Suh07]   Jouni Suhonen. *From Nucleons to Nucleus.* Theoretical and Mathematical Physics. Springer Berlin Heidelberg, 2007.

[TCK+98]   D.R. Tilley, C.M. Cheves, J.H. Kelley, S. Raman, and H.R. Weller. Energy levels of light nuclei, A = 20. *Nuclear Physics A*, 636(3):249–364, 1998.

[TGPO00]   F. Tondeur, S. Goriely, J. M. Pearson, and M. Onsi. Towards a hartree-fock mass formula. *Phys. Rev. C*, 62:024308, Jul 2000.

[Tho60]   D.J. Thouless. Stability conditions and nuclear rotations in the hartree-fock theory. *Nuclear Physics*, 21(0):225–232, 1960.

[Tho61]   D.J. Thouless. Vibrational states of nuclei in the random phase approximation. *Nuclear Physics*, 22(1):78–95, 1961.

[Tri12]   Richard Trippel. personal communication, 2 2012.

[V+a]   V. V. VARLAMOV et al. J,IZV,67,656,2003.

[V⁺b]      V. V. VARLAMOV et al. MSU-INP-99-40/598(1999).

[V⁺c]      V. V. VARLAMOV et al. YAD.KONST.,1,52(1993).

[VBB⁺74]   A. Veyssiere, H. Beil, R. Bergere, P. Carlos, A. Lepretre, and A. de Miniac. A study of the photoneutron contribution to the giant dipole resonance of s-d shell nuclei. *Nucl.Phys.*, A227:513, 1974.

[VIK⁺78]   V. V. Varlamov, B. S. Ishkhanov, I. M. Kapitonov, Z. L. Kocharova, and V. I. Shvedunov. Investigation of the proton decay channel of the $^{32}$S giant resonance. *Yad.Fiz.*, 28:590, 1978.

[VIK⁺79]   V. V. Varlamov, B. S. Ishkhanov, I. M. Kapitonov, A. N. Panov, and V. I. Shvedunov. Investigation of the contribution from various configurations to giant dipole resonance of the $^{28}$Si nucleus. *Izv.Akad.Nauk*, SSSR:Ser.Fiz. 43, 186, 1979.

[VJV87]    H. De Vries, C.W. De Jager, and C. De Vries. Nuclear charge-density-distribution parameters from elastic electron scattering. *Atomic Data and Nuclear Data Tables*, 36(3):495–536, 1987.

[WKB73]    W.T. Weng, T.T.S. Kuo, and G.E. Brown. Electric-dipole sum rule and two-body correlations in nuclei. *Physics Letters B*, 46(3):329–333, 1973.

[WSS95]    R. B. Wiringa, V. G. J. Stoks, and R. Schiavilla. Accurate nucleon-nucleon potential with charge-independence breaking. *Phys. Rev. C*, 51:38–51, Jan 1995.

[YLC02]    D. H. Youngblood, Y.-W. Lui, and H. L. Clark. Isoscalar giant resonances in $^{28}$Si and the mass dependence of nuclear compressibility. *Phys. Rev. C*, 65:034302, Feb 2002.

## Danksagung

An erster Stelle bedanke ich mich bei Prof. Dr. Robert Roth für die Annahme als Doktorand und die Gelegenheit, diese Arbeit zu verfassen. Er ließ mir immer genügend Freiraum, um mich auf die selbstständige Forschungsarbeit zu konzentrieren. Prof. Dr. Gabriel Martínez-Pinedo danke ich für die Übernahme des Zweitgutachtens. Eskendr Gebrerufael, Christina Stumpf, Richard Trippel und Roland Wirth danke ich für die angenehme Arbeitsatmosphäre während der Fertigstellung dieser Arbeit.

## Erklärung zur Dissertation

Hiermit versichere ich, die vorliegende Dissertation ohne Hilfe Dritter nur mit den angegebenen Quellen und Hilfsmitteln angefertigt zu haben. Alle Stellen, die aus Quellen entnommen wurden, sind als solche kenntlich gemacht. Diese Arbeit hat in gleicher oder ähnlicher Form noch keiner Prüfungsbehörde vorgelegen.

Darmstadt, den 19. Juni 2012

## Lebenslauf

### Persönliche Daten

Bastian Erler

geboren am 12.10.1982

in Frankfurt am Main

### Bildungsweg

| | |
|---|---|
| 06/2002 | Abitur an der Herderschule, Frankfurt am Main |
| 07/2002-04/2003 | Zivildienst beim Malteser Hilfsdienst, Frankfurt am Main |
| 10/2002-03/2003 | Fernstudium der Physik im FiPS Programm der Technischen Universität Kaiserslautern |
| 04/2003-01/2009 | Studium der Physik an der TU Darmstadt |
| 09/2005-09/2006 | Auslandsaufenthalt am Nihon University College of Science and Technology in Tokio, Japan |
| 07/2007-03/2008 | Forschungsaufenthalt im Rahmen der Diplomarbeit am Tokyo Institute of Technology in Tokio, Japan |
| 08/2007-07/2008 | Anfertigung der Diplomarbeit *Ladungszustände von Ionenstrahlen in Gastargets* |
| 01/2009 | Diplom in Physik, Gesamtnote: sehr gut |
| 02/2009-07/2012 | Promotionsstudium an der TU Darmstadt und Anfertigung der Dissertation |
| seit 02/2009 | Wissenschaftlicher Mitarbeiter am Institut für Kernphysik |